Magnetic Fields in Star-Forming Molecular Clouds

A Polarimetric Study of Magnetic Fields in Star-Forming Molecular Clouds

By

Brenda Christine Matthews, B.A.Sc., M.Sc.

A Thesis
Submitted to the School of Graduate Studues
in Partial Fulfilment of the Requirements
for the Degree
Doctor of Philosophy

McMaster University

© Brenda Matthews, September 2001

DOCTOR OF PHILOSOPHY (2001) McMaster University

(Physics and Astronomy) Hamilton, Ontario

TITLE: A Polarimetric Study of Magnetic Fields in Star-Forming Molecular Clouds

AUTHOR: Brenda Matthews, B.A.Sc., M.Sc.

SUPERVISOR: Dr. Christine D. Wilson

NUMBER OF PAGES: xix, 285

Abstract

I have used a recently commissioned, highly sensitive polarimeter at the James Clerk Maxwell Telescope to probe the magnetic field geometries of six star-forming regions within 500 pc of the Sun. For five of the regions, these are the first data produced of emission polarization from dust grains aligned by local magnetic fields. The variations in the polarization pattern across the clouds have been compared to predicted patterns from various models of magnetized molecular clouds. In several regions, particularly OMC-3 in the Orion A cloud, the polarization data are very consistent with predictions of a recently developed model of filamentary molecular clouds threaded by helical fields. The regions of NGC 2068 and LBS 23N could also contain helical magnetic field geometries. Although NGC 2024 is successfully modeled by a helical field, this geometry is not consistent with existing data of the line-of-sight magnetic field, which is not probed by polarization measurements. Instead, I suggest that the field geometry in NGC 2024 is that of an expanding ionization front from the associated HII region, bent around the dense ridge of star-forming cores. Prior to this work, most regions were thought to contain an ordered magnetic field component which was essentially unidirectional. Only one region in my sample contains a distribution of polarization vectors which could support such a geometry; in this cloud, Barnard 1, I have estimated the three-dimensional field strength and orientation associated with this "uniform" field and find a significant fraction of the field lies in the plane of the sky. This solution applies only to low column densities and not to the denser cores within Barnard 1, which do not exhibit alignment with the low density material. In short, this work reveals that unidirectional field geometries are not supported on intermediate scales within molecular clouds. Furthermore, no single mag-

netic field geometry is applicable in all molecular clouds; in each region, local environments and the associated physics must be taken into account.

For my Family... Here's to all the great times we've had,

and all the great times to come...

Co-Authorship

The original work in this thesis is contained in Chapters 3 through Chapter 7. At the beginning of each chapter, I have indicated whether the article contained within is a reprint, preprint or draft of a paper which has yet to be submitted. I hereby grant irrevocable, non-exclusive licence to McMaster University and the National Library of Canada to reproduce this material as part of the thesis.

The project, observing proposals and articles were developed in collaborative effort with my supervisor, Christine Wilson. I was the Principle Investigator and wrote all the observing proposals for this project, with the exception of the data obtained toward the regions of NGC 2024, NGC 2071 and LBS 23N, for which the observing proposal was developed with the Canadian Consortium for Star-Forming Studies, of which I am a member. Chapters 3, 6 and 7 were written entirely by me, although the work contained therein is a result of collaborative input with my supervisor, C. Wilson. J. Fiege was a collaborator on the work presented in Chapters 4 and 5. He developed the models (based on his models of filamentary molecular clouds as developed in his Ph.D. thesis) to which we compare the data. All parts of Chapter 4 were written by me. Chapter 5, however, was written in collaboration with J. Fiege and G. Moriarty-Schieven. I have prefaced that chapter with a detailed breakdown of the distribution of written work. All data reduction and analysis presented in Chapter 5 was completed by me.

Acknowledgement

I am grateful to many people for their support and assistance in the execution of this project. First and foremost, I wish to thank my supervisor, Christine Wilson, who has been so generous as to allow me to select my own project, write my own proposals, travel extensively for observing runs and provide me with excellent and timely encouragement and feedback on this thesis which has prevented this train from slipping off the rails. Her willingness to allow me to attend many international conferences to present my work I consider an enormous factor in the success of this thesis and its author.

Jason Fiege has been an indispensible resource on the state of all things magnetic inside molecular clouds and his willingness to collaboratively generate models for my data has greatly increased the impact of my observational work. Jane Greaves has gone above and beyond her duties as the JCMT polarimetry scientist in discussing my data and providing feedback on my papers. Similarly, Tim Jenness deserves credit for great forebearance in fielding my endless questions about why SCUBA software does what it does and why it doesn't do it better! Ralph Pudritz, Doug Johnstone and Gerald Moriarty-Schieven have also contributed to the ideas presented within this work. I am grateful to the various JCMT TACs who granted me sufficient time to execute this large project and the NRC who covered most of the costs associated with my observing in Hawaii.

On a more personal level, thanks to all my officemates in ABB 253: Dean McLaughlin, Tracy Webb, Andy Rorabeck, Marcel VanDalfsen, Waldemar Okon, Dave Lepischak and especially Glen Petitpas, who's had to put up with me the longest! Marcel's LaTex expertise has been critical in solving some pretty obscure problems with generating this thesis.

Finally, I want to acknowledge my parents, brother and sister, who have always encouraged me, and have the insight to think academia is cool. To my grandmother,

who has never wavered in her support of my pursuing my goals, even if they take me a few thousand kilometres away, I want to express my love and gratitude for showing me the real meaning of “young at heart”.

Table of Contents

List of Tables

List of Figures

Chapter 1

Introduction

While gazing into a dark, clear sky, one could be forgiven for thinking that stars are the most abundant, brightest objects in our Galaxy. Limited as we are by the range of our optical receptors, we are confined to view directly only a tiny fraction of the electromagnetic spectrum, that known as visible light. Figure 1.1 is an image of the well-known constellation of Orion.

Figure 1.1: The Constellation of Orion
The winter constellation of Orion is familiar to many astronomers, amateur and professional alike. The bright stars visible at optical wavelengths are only a small portion of the stars within this constellation. Many more are embedded so deeply in an associated molecular cloud that they are completely undetectable at wavelengths shorter than 60 μm.

Nature however yields small hints about the presence of other types of objects in the sky, for there are regions which are conspicuous by the absence of stars. These regions are called "dark clouds". The clouds are dark because they contain micron-scale particles of frozen carbon, silicon and other compounds (called "dust grains") which effectively absorb starlight. The absorption is strongest at shorter wavelengths. Figure 1.2 shows a series of images of the Barnard 68 dark cloud in Ophiuchus taken at wavelengths ranging from optical to near-infrared.

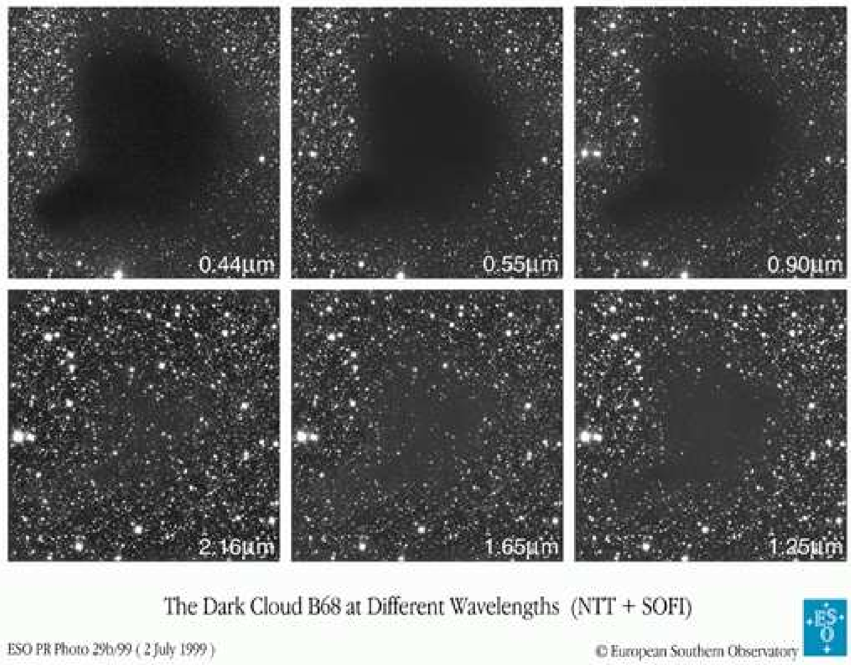

Figure 1.2: A Dark Cloud at Multiple Wavelengths
This series of observations, from the Very Large Telescope (VLT), show the dark cloud Barnard 68 (B68) at six different wavelengths. As the wavelength increases, the dust opacity drops, eventually permitting detection of the stars behind the cloud. The amount of obscuration toward the central part of the cloud is equivalent to 35 magnitudes in the visual. B68 is virtually devoid of forming stars, so the bulk of the objects seen at 2.2 μm lie behind the cloud.

Were we able to don a pair of magic glasses tunable to different wavelengths of light, the average person would be fascinated by the changed appearance of the sky. As one adjusted the glasses to wavelengths longer than the optical, the stars so familiar to us would gradually become fainter. At the same time, other stars would begin to appear, many of them within the regions which appear so completely dark on a clear night. One would also become aware of emission from "fluffy" or "clumpy" looking objects and their emission would eventually become so bright and extended that individual objects within them could not be distinguished. In fact, such magic glasses do exist, in the form of infrared telescopes. Unfortunately, due to high emission from the Earth's own atmosphere in this regime, astronomical observations at wavelengths between approximately 15-200 μm require that these telescopes be launched into space or placed aboard aircraft to observe above the stratosphere.

In 1983, the InfraRed Astronomical Satellite (IRAS) was launched into high orbit around the Earth. It performed an all-sky survey of the sky at four wavelengths either difficult or impossible to observe from the ground. The results of this mission were so fantastic that they are still being utilized by astronomers today. IRAS revealed a complexity within dark clouds which is remarkable. For instance, Figure 1.3 shows the region of Orion as it was seen by IRAS. Note that no stars are visible, and the emission is dominated by clumpy structures which are very large in spatial extent. The emission arises from tiny dust grains at a temperature of about 100 K. The emission from dust is a continuum blackbody. The presence of gas between the stars had been previously known, but IRAS provided an all-sky guide to where dense gas (and hence dust) is located.

In the post-IRAS period, much research has been dedicated to the study of molecular clouds, not only because they are complicated, dynamic objects, but also because they are the birthplace of all stars, and particularly Giant Molecular Clouds, where the entire population of massive stars is born. These studies involve the search for the mechanism which provides the support of molecular clouds against their own gravity and how stars are formed in their interiors. It is now generally accepted that magnetic fields play a significant role in both these processes.

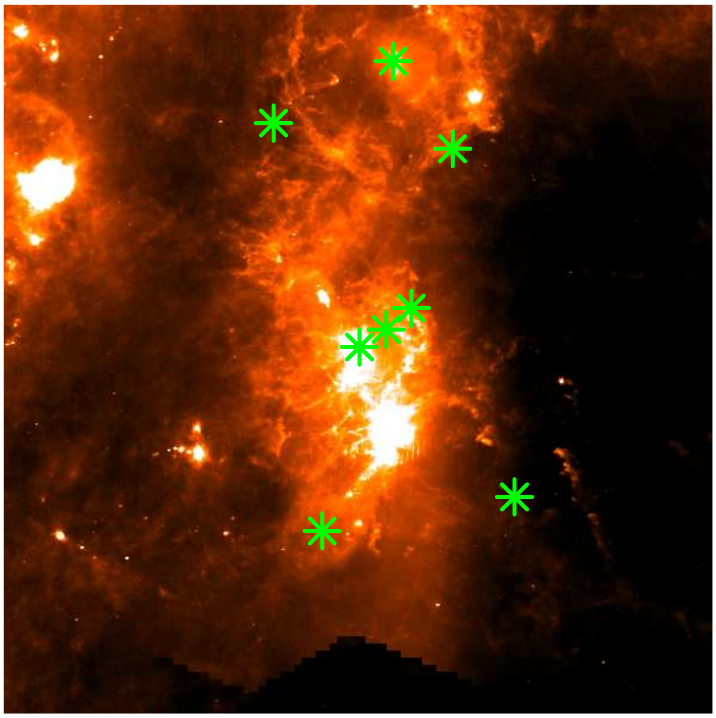

Figure 1.3: Orion in the Infrared

The region of Orion looks very different in the infrared than in the optical image of Figure 1.1. This image shows emission from dust at 60 μm as imaged by the IRAS (Infrared Astronomical Satellite). The dust traces regions of dense gas and is very effective at absorbing starlight at optical and shorter wavelengths. Eight of Orion's stars have been drawn in green to illustrate their positions.

This thesis probes the geometry of these magnetic fields within molecular clouds through detections of polarized light emitted from dust grains aligned by the field. The goals are to determine how prevalent large-scale ordered magnetic fields are within molecular clouds, to test existing theories for magnetic field geometries and, where possible, derive the three-dimensional magnetic field geometry. In the following chapter, I provide background on the role of magnetic fields in molecular clouds and why polarimetry is the primary observational tool for probing the geometry of the field. I then explain the importance of the timing of my thesis as a critical part of our evolving understanding of magnetic fields in molecular clouds and discuss the instrumentation used and regions selected for my project. The original work begins in Chapter 3 in which the initial analysis of my first observations is presented. A more extensive analysis of these data is produced in Chapter 4. Regions within a second Orion molecular cloud are analyzed in Chapters 5 and 6. Finally, in Chapter 7, I present data toward the Barnard 1 dark cloud in Perseus. The conclusions drawn from this thesis and my planned future work are summarized in Chapter 8.

Chapter 2

Magnetic Fields in Galactic Molecular Clouds

In this chapter, I will provide some background on molecular cloud physics and explain briefly why magnetic fields are believed to play an important role in their support against gravitational collapse. I will then introduce the evidence existing for the presence of magnetic fields in molecular clouds and the various means by which they can be detected. Finally, I will briefly discuss the motivation for this project, introduce the instrumentation utilized, and then provide some background on the regions I have chosen to observe.

2.1 Molecular Cloud Physics

Molecular clouds are the largest definable structures within galaxies, often containing masses as high as $10^{4-7} M_{\odot}$, comparable at the high end to globular clusters in galactic halos. Molecular gas comprises approximately 50% of the mass of the interstellar medium (ISM) in our Galaxy, but less than 20% of the volume. The number densities of hydrogen molecules in these clouds range from $n \sim 10^2$ cm^{-3} to $> 10^6$ cm^{-3}, significantly higher than the tenuous atomic medium, where the number density of hydrogen atoms ranges from 1-100 cm^{-3}. The densities permit some portion of the gas to become self-shielding to external ultraviolet (UV) and cosmic ray radiation. The gas cools, which permits density to increase further. The end product of this process (although the details are not completely understood) is the creation of stars and star clusters from the very densest cores of molecular gas.

Objects containing molecular gas are generally categorized as either *dark clouds* or *Giant Molecular Clouds* (GMCs). All molecular clouds actually appear dark in the optical, so the term dark cloud is somewhat misleading. The main difference between these two classes of molecular cloud is their ability to form massive ($M > 5M_{\odot}$) stars. Because GMCs may be up to 10^4 times more massive than typical dark clouds, they have the reservoirs of gas required to form massive stars. Hence, they often are associated with optically visible indicators of recent, massive star formation, such as HII regions and reflection nebulae. They usually have higher star formation efficiencies than dark clouds. However, dark clouds are in fact more likely to form bound clusters than GMCs since they do not suffer the same disruptive influences of high internal motions, stellar winds, shocks and supernovae as GMCs.

Molecular clouds were identified before their connection to star formation was evident. In the early 1930's, molecules such as CH, CH^+ and CN were discovered in stellar spectra (Dunham 1937; Adams 1943; Adams 1941; Swings & Rosenfeld 1937; McKellar 1940; Douglas & Herzberg 1941), but molecular hydrogen (H_2) itself was not discovered until 1970 (Carruthers 1970). Observations of H_2 are difficult since the absence of a permanent dipole moment means no radiation is produced from its lower rotational level. Early measurements were done in absorption against the UV radiation background. Direct evidence for its existence in molecular clouds was thus difficult to detect. Its presence was inferred due to the fact that the ratio of HI to extinction is lower toward dark clouds than diffuse clouds. Bok (1955) inferred that the missing hydrogen was in molecular form.

The study of molecular clouds progressed rapidly following the discovery of tracer molecules, which could be used to infer the distribution of H_2, even though their component atoms constitute just 2% of the mass of the molecular cloud (H_2 molecules account for 70% with helium atoms making up the balance). The most important of

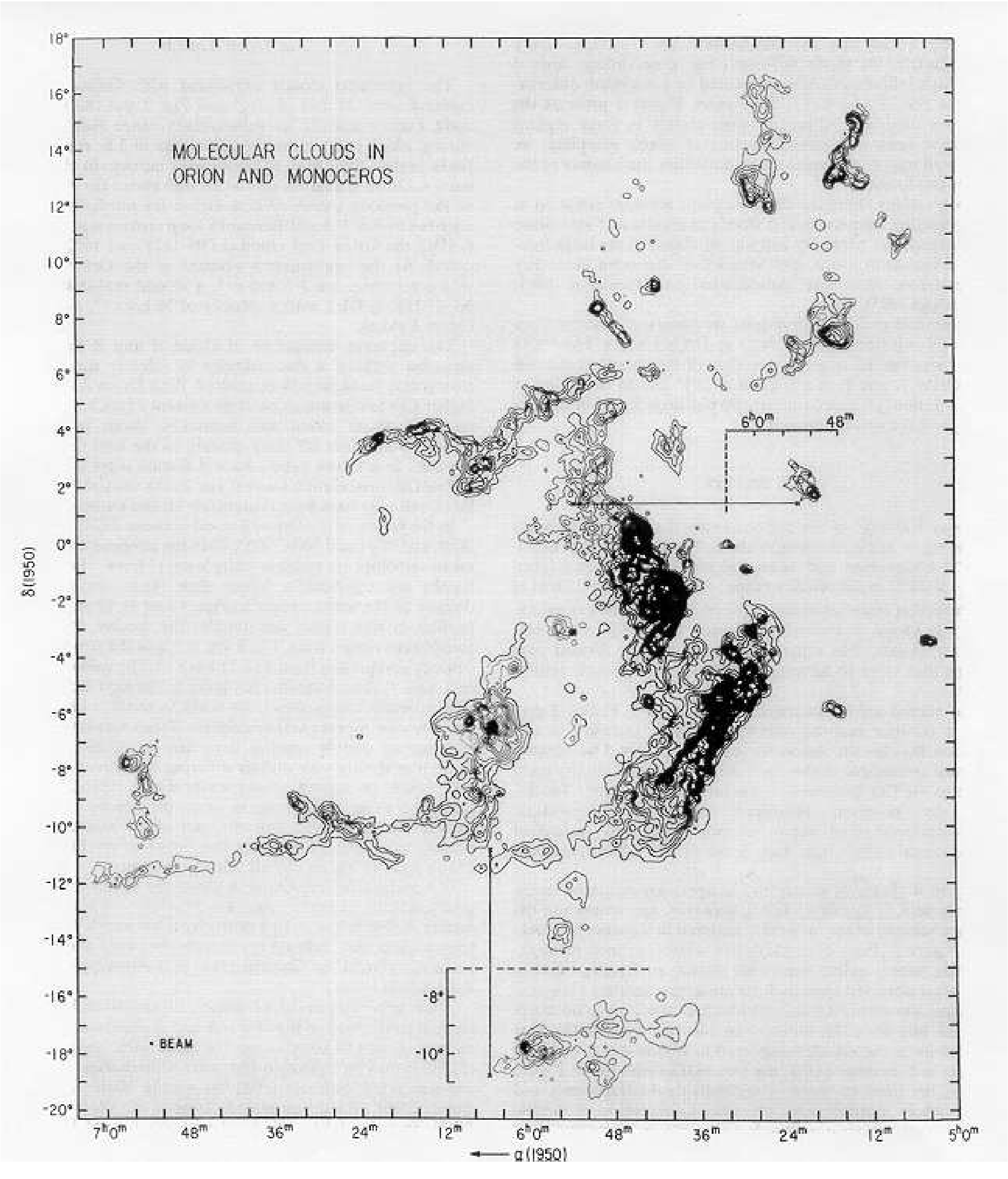

Figure 2.1: Molecular Clouds in Orion and Monoceros
CO is an effective tracer of molecular gas structure, but becomes optically thick quickly. Therefore, rarer isotopes of CO are typically used to measure the mass. The Orion A cloud is centred at roughly $\alpha(1950) = 05^{\mathrm{h}}36^{\mathrm{m}}$, $\delta(1950) = -6°$. The Orion B cloud lies to the northwest, centred at roughly $\alpha(1950) = 05^{\mathrm{h}}48^{\mathrm{m}}$, $\delta(1950) = -2°$. (reprinted from Maddalena et al. (1986)).

these molecules is carbon monoxide (CO, discovered by Wilson et al. (1970) in the Orion nebula) and its various isotopes, which can effectively map gas of densities from 10^3 cm^{-3} to 10^5 cm^{-3}. This was closely followed by the discovery of the CN radical (Jefferts et al. 1970) and CS (Penzias et al. 1971), also in Orion. The presence of H_2 was thus established based on the densities required to collisionally excite CO (10^3 cm^{-3}) and CS (10^4 cm^{-3}) (Elmegreen 1985). A variety of tracer molecules now exist to probe molecular gas up to densities $> 10^8$ cm^{-3}. These include NH_3, CS, CN, HCN, H_2CO and HCO^+ to name only a few.

The usefulness of each molecule as a probe of gas structure and mass is limited by how quickly it becomes optically thick (CO, which is easily excited and very abundant, is thus a poor tracer of mass), critical density and the temperature required for thermal excitation. For this reason, each molecular tracer gives information about a restricted range of physical conditions within clouds bounded by limits on density and temperature and the abundance of the molecule itself.

2.1.1 What Prevents Global Collapse of Molecular Clouds?

Interest in the study of molecular clouds increased greatly once they were identified as the birthplaces of stars. The IRAS satellite and ground-based submillimetre and millimetre telescopes conclusively connected these two phenomena (see Elmegreen (1985) and Shu et al. (1987) and references therein). Once the first surveys of forming stars were done in dark and molecular clouds, it became essential to understand how molecular clouds were able to sustain themselves over their 10^8 yr lifetimes, since arguments based on the virial theorem suggested that all molecular clouds should be undergoing global collapse.

Application of the virial theorem to molecular clouds can be used to estimate the *Jean's mass*, the minimum cloud mass, M, required for collapse under a cloud radius, R, and initial uniform density, ρ_0.

The self-gravity of a sphere is given by the gravitational energy:

$$U = -\frac{3}{5}a\frac{GM^2}{R} \tag{2.1}$$

(where a is a constant of order unity accounting for the degree of uniformity in the cloud) while an estimate of the clouds internal energy is:

$$K = \frac{3}{2}\eta kT \tag{2.2}$$

where G is the gravitational constant, k is the Boltzmann constant, T is the kinetic temperature, and η is the total number of particles, given by:

$$\eta = \frac{M}{\mu m_H}. \tag{2.3}$$

Under the virial theorem, the condition for collapse is

$$2K < |U|. \tag{2.4}$$

Substitution of equations (2.1), (2.2) and (2.3) into equation (2.4) and $R^3 = 3M/(4\pi\rho_0)$ yields an expression for the Jean's mass:

$$M_J = \left(\frac{5kT}{Ga\mu m_H}\right)^{3/2}\left(\frac{3}{4\pi\rho_0}\right)^{1/2}. \tag{2.5}$$

Typical values of temperature (10 K) and density (320 cm^{-3}) for molecular clouds (Goldsmith & Langer 1978) yield a Jean's mass of $\sim 30M_\odot$, which is many orders of magnitude less than a dark cloud ($\sim 10^4 M_\odot$) or a GMC ($\sim 10^{6-7} M_\odot$). By this reasoning, all molecular clouds should be undergoing global collapse in a free-fall time:

$$t_{ff} = \left(\frac{3\pi}{32}\frac{1}{G\rho_0}\right)^{1/2}, \tag{2.6}$$

which yields $\sim 10^6$ yr for the density assumed above. Thus, the star-forming efficiency (the ratio of mass in stars versus gas) should be very high. Instead, the efficiencies range from a $\leq$ a few percent in dark clouds such as Barnard 1 (Bachiller et al. 1990) and Taurus (Mizuno et al. 1995) to higher values for cluster forming regions in ρ Ophiuchus (4%, Liseau et al. 1999; $>$ 25%, Wilking & Lada 1983; Lada & Wilking 1984) and Orion A (10%, Carpenter 2000). In addition, based on the ages of associated star clusters and populations of molecular clouds, their ages range from 10^5 - 10^8 yr. The lower end is bounded by the formation time for molecules themselves, and the upper end by cluster ages (Elmegreen 1985).

2.1.2 Magnetic Fields as a Source of Global Support

Based on these simple relationships, it is evident that molecular clouds must rely on mechanisms other than thermal motions in the gas for their internal support. Clues to the nature of this support are obtained from observations of molecular line profiles. Line emission provides much information about the cloud structures. Doppler shifting of the lines reveals kinematic information and distances. Measurements of lines across clouds can reveal whether clouds are rotating as well as other bulk motions of the gas. Collapse produces observational features in spectra. But one of the most vital pieces of information, the velocity dispersion in the gas, is revealed by the line widths. The measurement of line widths across a variety of clouds reveals a correlation between line width and cloud size described by the empirical "size-linewidth" relation:

$$\sigma(\mathrm{kms}^{-1}) = 1.10\mathrm{L}(\mathrm{pc})^{0.38} \tag{2.7}$$

where σ is the total velocity dispersion and L is the region size (Larson 1981).

In fact, the total linewidths measured in molecular clouds are nonthermal, which is to say that they are too wide to be attributable to simply thermal motions in the gas. Based on the velocity dispersions of the gas, σ, the kinetic energy of a cloud is:

$$K = \frac{3}{2}M\sigma^2. \tag{2.8}$$

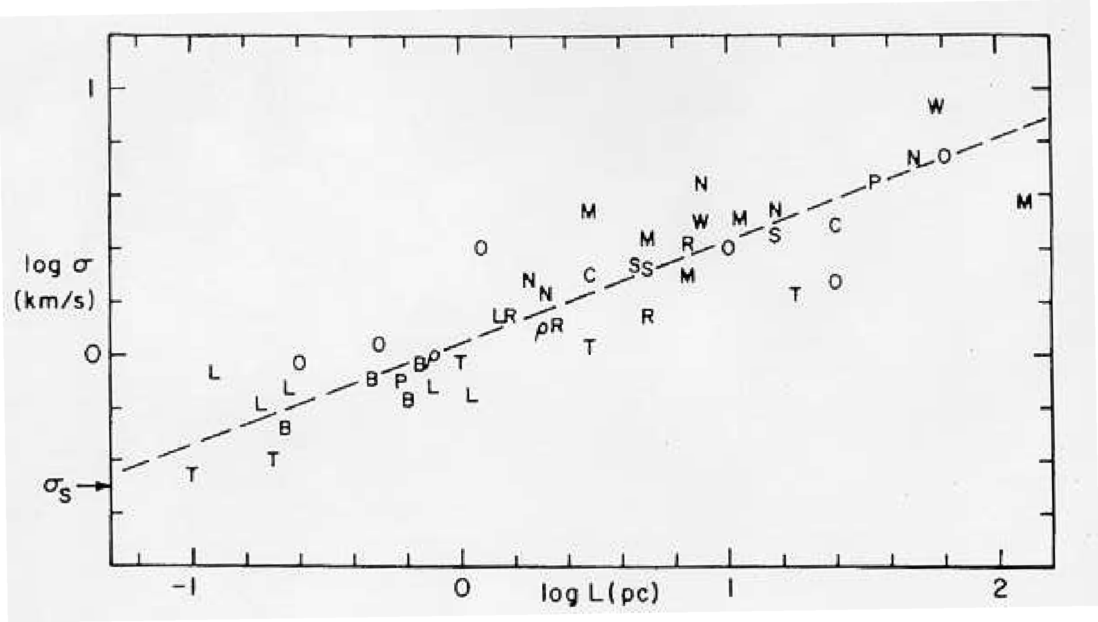

Figure 2.2: Size-linewidth Relation

There exists a strong correlation between the linewidth measured in molecular clouds and their size. The relation is independent of region and class of cloud. The labels on these data points refer to the region within which the cloud is located: O – Orion complex, M – M17, W – W3 (all GMCs); P – Perseus, C – Cepheus, ρ – ρ Ophiuchus, T – Taurus, L – Lynds clouds, B – Barnard objects (all dark clouds); N – HII regions associated with NGC objects, S – HII regions associated with Shapley objects, and R – reflection nebulae. (reprinted from Larson (1981))

The column density, N, of the cloud is given by:

$$N = \frac{M}{\mu m_H \pi R^2} \tag{2.9}$$

and the number density of particles, n_0, by:

$$n_0 = \frac{\rho_0}{\mu m_H}. \tag{2.10}$$

Using the self-gravity of a sphere (equation 2.1), equations (2.9) and (2.10) and the virial theorem, σ can be expressed in terms of N and n_0 as:

$$\sigma = \left[\frac{3\pi a}{20}\frac{G\mu m_H N^2}{n_0}\right]^{1/2}. \tag{2.11}$$

Using $\mu = 2.33$ as the mean atomic weight and the relation between the extinction and column density to be $A_V = N/(2\times10^{21}\ \mathrm{cm}^{-2})$ as given by Spitzer (1978), substitution of values gives:

$$\sigma = 7 \times A_V n_0^{-1/2}\ \mathrm{km\ s}^{-1}. \qquad (2.12)$$

Substitution of average values for a GMC of $A_V \sim 10$ and $n_0 \sim 10^3\ \mathrm{cm}^{-3}$ yields a linewidth of 2.2 km s^{-1}. However, based on the temperatures of ~ 15 K, the thermal component is only $\sqrt{kT/\mu m_H} \approx 0.23$ km s^{-1}. So, there is a significant nonthermal component to the linewidth. Despite this fact, the linewidths are still insufficient to provide support for the clouds on global scales; by the virial equation, a linewidth of 2 km s^{-1} is sufficient to support just $\sim 10^4 M_\odot$ of gas at density $10^3\ \mathrm{cm}^{-3}$. This is still several orders of magnitude less than the mass of a GMC. Nevertheless, the nonthermal components of the linewidths are indications of turbulent, or random, motions in the gas, which provides evidence for another source of support.

The presence of magnetic fields can provide support to a molecular cloud if the gas-field coupling is strong enough. The ionization fraction of the gas is what determines the strength of the coupling, and the estimated ionization fraction in clouds of 10^{-7} is sufficient for the gas to respond to the presence of the field. The magnetic field thus acts as a pressure which resists the collapse of the cloud. The field lines can be thought of as elastic bands; if the gas motions deform the bands, a restoring force acts to hold the original shape of the field lines. The support is strongest perpendicular to field lines (in the case of a unidirectional field) and the field offers no resistance to collapse along field lines.

Myers & Goodman (1988) compare the observed magnetic field strengths (derived from the line of sight components detected through Zeeman splitting) toward 14 molecular cloud cores to those predicted assuming equipartition between gravitational, kinetic and magnetic energies. The derived expression for the field strength is

$$B_{eq} \approx \frac{2}{8\ln 2}\left(\frac{5}{G}\right)^{1/2}\frac{\Delta v^2}{R} \tag{2.13}$$

where G is the gravitational constant, Δv is the observed line width and R is the radius of the cloud. Figure 2.3 shows that there is strong agreement between the observed and predicted values. Similar studies have yielded the same conclusion (Crutcher et al. 1999; Basu 2000). The range of clouds surveyed in mass and density shows that this energetic balance could be universal in star-forming clouds.

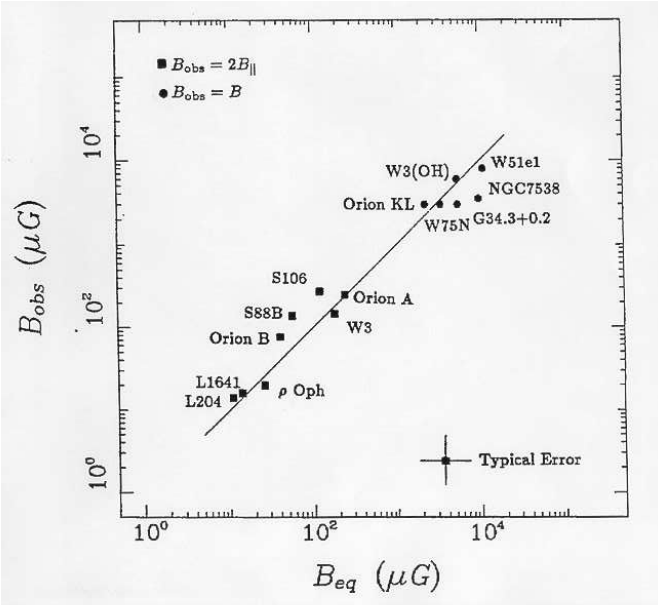

Figure 2.3: Observed vs. Predicted Magnetic Field Strengths in 14 Cores
Comparison of the observed magnetic field strengths, derived from the line-of-sight field strength, to that predicted for equipartition between magnetic, gravitational and kinetic energies reveals a strong agreement. The regions included span a factor of 10^3 in mass. (reprinted from Myers & Goodman (1988))

2.2 Detection of Magnetic Fields through Polarized Light

Even before it was known how inefficiently dark clouds and GMCs form stars, magnetic fields were detected in the atomic ISM. In fact, more than five decades have passed since the discovery that starlight is polarized (Hiltner 1949; Hall 1949). That interstellar dust grains were related to the polarization being observed was immediately evident, since the degree of polarization was strongly correlated with reddening, which was already established to be due to interstellar dust. The polarization of starlight was immediately attributed to partial absorption of the unpolarized starlight by dust grains, which must be aligned to produce a net polarization for the observer. The problem quickly shifted to a determination of the source of the grain alignment. Below I discuss why the alignment traces the magnetic field, and then the different methods by which magnetic fields can be observed.

2.2.1 Non-magnetic Sources of Alignment

Gold (1952) considered large scale bulk motions as a source of the alignment of dust grains, wherein each grain is continuously imparted angular momentum due to collisions with gas atoms. He found that a succession of impacts caused the grains to spin with their longest projected axes oriented with the streaming gas. However, the starlight transmitted by clouds revealed that the grains are in fact polarized with the E-vector in the plane of the shortest projected axes of the grains. Since the Galactic polarization pattern is observed to lie in the plane of the Galaxy (see Figure 2.4), streaming motions could not produce the pattern unless they were oriented perpendicular to the disk. Streams of photons were also considered, but in addition to having inadequate momentum, the photons move in the plane of the Galaxy, which would result in polarization perpendicular to the plane, which is not observed (Hildebrand 1988a).

Photons however possess both linear and angular momentum. While the linear momentum of a photon produces a change in the angular momentum of a grain of $\Delta L = f \times a \times (h\nu)/c$ where ν is the frequency of the radiation, c is the speed of light, a is the radius of the grain along its longest axis, and f is a factor of order unity

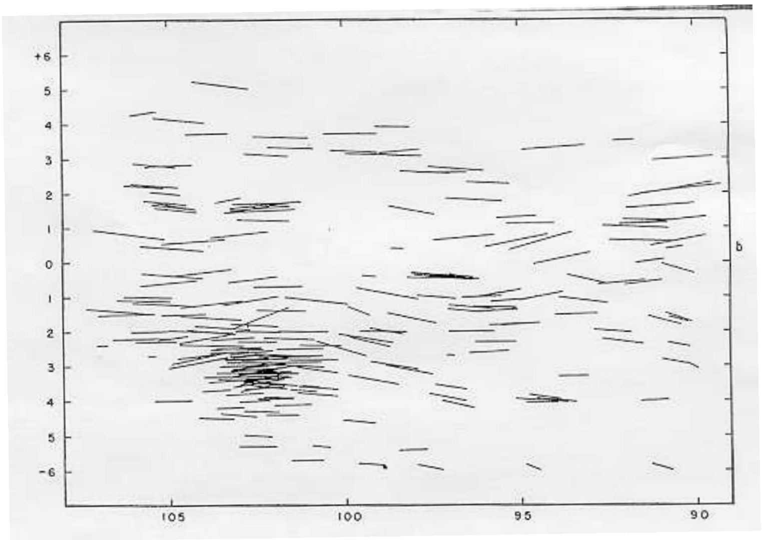

Figure 2.4: Polarization Along the Galactic Plane
This subset of the total polarization data set toward 841 background stars produced by Hiltner (1951) illustrates that polarization is observed to lie along the Galactic plane. Therefore, mechanisms should predict alignment of dust grains consistent with these data.

which depends on the shape of the grain (e.g. $f = 1/\sqrt{3}$ for a cylindrical grain), the angular momentum possesses only a tiny effect which produces $\Delta L = h/(2\pi)$. Although the linear momentum will dominate whenever $\lambda < 2\pi af$, the cumulative effect of angular momentum in a region with a strong radiation field can become large. For every UV photon a dust grain absorbs, it will emit several hundred far-infrared photons, each producing a change of $h/(2\pi)$ in a random direction. Thus, even if streaming could align the grains, the release of angular momentum is more than enough to overwhelm any alignment, unless the streaming velocities are greater than thermal (Harwit 1970; Purcell & Spitzer 1971).

Even alignment by ferromagnetic grains was found to be implausible in the diffuse ISM, although its dependence of the ratio of field strength to gas temperature suggests it could be more effective in dense molecular cores (Lazarian et al. 1997). If grains are made of pure iron and are as large as 1 μm (typical grain sizes are ~ 0.2 μm), a rotational kinetic energy as low as kT can prevent alignment (Spitzer & Tukey 1951). Most importantly however, ferromagnetic alignment would position the long axes of grains along the field in the plane of the sky, which does not agree with the expected configuration. In the case of the large scale polarization in the Galaxy, the position angle measured would be perpendicular to the Galactic plane, not parallel as observed.

To date, no plausible theory of grain alignment has been put forth which does not imply alignment by the magnetic field.

2.2.2 Magnetic Sources of Alignment

2.2.2.1 The Davis-Greenstein Mechanism

Whether or not grains become aligned depends on whether the aligning torques acting on the grains are sufficient to overcome the disordering effect of collisions by gas molecules. In 1951, Davis and Greenstein proposed a mechanism for alignment by which "paramagnetic relaxation" of thermally spinning grains gradually removes the components of angular rotation perpendicular to the magnetic field. Since grains are generally charged, they are paramagnetic with a magnetization, $\mathbf{M}$, which can respond to an external field, $\mathbf{B}$. If the grain spins with angular velocity $\boldsymbol{\Omega}$, then there exists a component of $\mathbf{M}$ in the direction $\boldsymbol{\Omega} \times \mathbf{B}$. A torque is exerted on the grain given by $\mathbf{M} \times \mathbf{B}$ which ceases only with the alignment of $\boldsymbol{\Omega}$ and $\mathbf{B}$. The original timescales required for alignment of the spin axes of the grains with the magnetic field were on the order of $> 10^6$ yr (Davis & Greenstein 1951).

Purcell (1979) illustrated that the spin axis of a grain aligns with the grain's principal axis (that of maximum rotational inertia) on very short timescales (i.e. ~ 1 yr for spins of 10^5 rad s^{-1} produced by random impacts on the grains) due to internal damping processes. This damping reduces the grain's rotational kinetic energy, $J^2/(2I)$ where J is the angular momentum and I is the moment of inertia, to its minimum value by increasing I to the maximum possible value. Hence, a grain's spin axis is perpendicular to its longest dimensions irrelevant of the alignment mechanism.

One of the major difficulties with the Davis-Greenstein mechanism was that the timescale on which random gas motions would be expected to destroy alignment (10^5 yr) was less than the timescale required to align the grains in the first place. Thus, the degree of alignment was limited to the amount which could be achieved before gas damping removed it. Purcell (1979) presented an amendment to the Davis and Greenstein mechanism which removed the constraint that alignment was limited to the time required for gas damping. In this picture, grains can be imparted with kinetic energies of rotation much greater than that which can result only from random collisions with gas molecules. Under the Davis-Greenstein model of stochastic excitation, each grain's rotational energy is $3kT/2$ where T is a temperature between the true temperatures of the gas and the grains (10-100 K, Hildebrand 1988b).

Rotational kinetic energy can be added to a grain by photoemission or the formation and ejection of hydrogen molecules (Hollenbach & Salpeter 1971). Under these acceleration mechanisms, the rotational energies achieved can be comparable to $T \sim 10000$ K. Due to irregularities in grain structures, certain sites on the grain surface will be more favorable for hydrogen molecule formation. The formation and ejection of H_2 at these sites can provide a net torque to the grain, spinning it up to speeds much greater than thermal. This mechanism is called the *Purcell Rocket Mechanism* and is a method of achieving *suprathermal rotation.* The effectiveness of alignment under suprathermal rotation is therefore the lifetime of irregularities on the grain surface. This mechanism can also act to provide grain rotation only in regions were there is sufficient atomic hydrogen available to create H_2. In the densest parts of molecular clouds, this condition is not expected to be satisfied (see Lazarian et al. 1997, for example).

A further hinderance to rapid alignment in dense clouds was removed by the theory of superparamagnetic damping due to grains with abnormally high magnetic susceptibilities. The creation of such grains is attributed to collisions, which can produce small clumps of material such as iron or iron oxide (Spitzer & Tukey 1951). Very small ($<< 1$ μm), pure clumps of such compounds within a grain will consist of only one domain and enhance the magnetic susceptibility up to 10^6 times that of the grains assumed by Davis and Greenstein. Due to such high values, the timescales for alignment between the spin axes of these grains and the magnetic field is considerably shortened increasing the alignment. Hildebrand (1988b) has calculated the relaxation time (at $T = 10$ K) for paramagnetic damping to be $\sim 9.5 \times 10^6/[B(\mu\mathrm{G})]^2$ yr. For superparamagnetic (SPM) grains, the timescales are significantly shorter, by a factor of $\sim 10^3$ (Lazarian et al. 1997).

2.2.2.2 Radiative Alignment

In this mechanism, the alignment is driven by radiative torques produced by photons distributed anisotropically in space. The actions of the torques align the short axes of the grains with the magnetic field. Primarily, radiative torques are determined by grain geometry, and the suprathermal spin up produced is expected to be long-lived (Draine & Weingartner 1996). The radiative effects can also act to align the grains on timescales shorter than the Davis-Greenstein mechanism. In this model, the spinning grain precesses around the magnetic field direction, being subject to the same paramagnetic effects as discussed by Davis & Greenstein (1951), although the paramagnetic dissipation is not absolutely required. Since the grains precess, the net alignment effect has the longest projected axis perpendicular to the local B_{pos} field component, just as in the case of the Davis-Greenstein mechanism (Draine & Weingartner 1997).

The effectiveness of radiative torques depend on the grain size quite strongly.

Draine & Weingartner (1996) find that radiative torques dominate Purcell torques in diffuse clouds for grains with effective radii greater than 0.2 μm. The radiative torques are expected to be minimal inside quiescent dark clouds, but have been shown to be effective in star-forming GMCs, such as M17 (Draine & Weingartner 1996).

2.2.2.3 Efficiency of Alignment Mechanisms in Dark Clouds

Lazarian et al. (1997) do a comparison of the likely alignment mechanisms with absorption polarimetry data toward the dark cloud L1755 in Ophiuchus. While they cannot determine whether Purcell or radiative torques dominate in the outer regions of L1755, they do find that the Davis-Greenstein mechanism alignment with SPM grains is very inefficient. In addition, they find that *all* the mechanisms above are unlikely to be efficient in the interior of the L1755 cloud due to insufficient spin. However, we note that Lazarian et al. (1997) have assumed that the angular velocity contributed by the Purcell Rocket Mechanism is approximately equal to the thermal component; it could be many times greater (Purcell 1979).

One of the reasons why all methods could fail inside L1755 is that it is a dark cloud and relatively quiescent. In an active, massive star-forming GMC, atomic hygrogen may be more abundant due to the presence of shocks (due to outflows from young stellar objects and recent supernovae). These mechanisms can dissociate H_2 and hence enhance alignment due to the Purcell Rocket Mechanism (Johnson 1982). Additionally, once stars have formed within clouds, they can be a source of anisotropic radiation fields on the nearby grains, thereby inducing radiative alignment. It is not clear, however, how deeply the emission from a single young star can penetrate into the surrounding cloud.

2.2.3 Methods of Observation

Magnetic fields are inherently three dimensional. They can only be measured by their effects on observable matter. Dust polarimetry provides information on the field projected onto the *plane of the sky*, denoted B_{pos} (or sometimes $B_{\perp}$). While Zeeman splitting of atomic and molecular lines could in principle provide information on all three dimensions of the field, sensitivity limits constrain this method to a probe of the field along the *line of sight*, denoted B_{los} (or $B_{||}$).

2.2.3.1 Absorption of Background Starlight

It was through this mechanism that polarization of the interstellar medium was first discovered by Hiltner (1949) and Hall (1949). Unpolarized light from stars at further distance than the clouds containing aligned dust grains is polarized by passage through the grains. The grains act as dichroic polarizers, absorbing the plane of polarization parallel to their longest axes. This is schematically illustrated in Figure 2.5. Thus, the absorption is *selective* and the transmitted light has a preferential polarization aligned with the shortest axes of the grains, expected to align with the local B_{pos}, as discussed above.

Polarimetry provides information on the direction of the magnetic field component B_{pos}, but no information on the field strength. The degree of polarization measured depends on several factors, all of which are not directly or easily measureable. These include the field strength, degree of alignment, the grain properties (composition, size, shape) and the optical depth of the absorbing material. The interpretation of absorption polarization data in the infrared ($2\ \mu$m $< \lambda < 60\ \mu$m) is further complicated by scattering and some emission from the grains.

Until recent developments of sensitive bolometric array cameras, this method was the best available for probing B_{pos}. However, since this method requires a

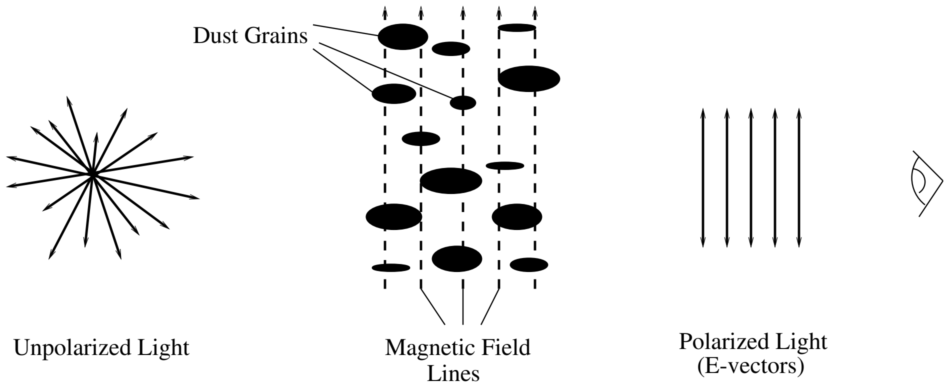

Figure 2.5: Selective Absorption of Background Starlight
Dust grains aligned by a magnetic field absorb light with components of the electric field vector oriented with their long axes. Since dust grains preferentially align with their long axes perpendicular to the local field, the transmitted light is polarized parallel to the field direction in the dust cloud.

background star, it is restricted primarily to the atomic ISM, and is effective only near the edges of molecular clouds where the optical depth is relatively small. Its effectiveness can be extended somewhat by observing at longer wavelengths into the near-infrared, where the dust is less opaque (as illustrated by Figure 1.2).

2.2.3.2 Thermal Emission from Dust Grains

Dust grains emit blackbody radiation according to their kinetic temperature. In the case of elongated, spinning, aligned grains, this emission is polarized. As in the case of absorption, the degree of polarized light emitted depends on the field strength, degree of alignment, how effectively the grains have been spun up, and the shapes and composition of the grains (their dielectric properties). Hence, information is provided on the direction of B_{pos} alone. One advantage to emission polarimetry is that dust emission at far-infrared and submillimetre wavelengths is typically optically thin, so the degree of polarization is independent of optical depth. Additionally, at these wavelengths ($\lambda > 60\,\mu$m), scattering and absorption effects are negligible, making interpretation of the position angles of the polarization vectors much more straight forward (Hildebrand 1988b). This means that measurements of polarized light at $\lambda > 60\ \mu$m samples the vector sum of the polarization through the depth of an emitting cloud.

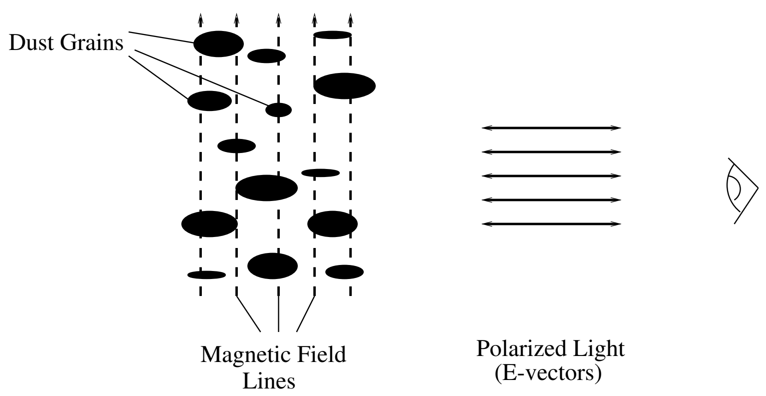

Figure 2.6: Thermal Emission from Aligned Grains
At wavelengths longer than $\lambda \sim 60\ \mu$m, emission from the dust grains themselves becomes the dominant source of polarized light. Elongated grains align with the magnetic field in precisely the same manner as Figure 2.5, but the emission is along the same grain axes as the absorption in the previous case. Therefore, the light emitted is perpendicular to the local B_{pos} field direction near the grains. Interpretation of the field direction from the polarization data is very straight forward, *if* one believes that the magnetic field direction is constant through the depth of the cloud.

Figure 2.6 shows the geometry of the alignment of the dust grains by a unidirectional magnetic field and the preferred plane of the emitted polarized light. It is important to remember that interpretation of a magnetic field direction as 90° offset from the measured plane of polarization implicitly assumes that the plane-of-sky field direction is constant throughout the depth of a cloud. Note that if near-infrared absorption and submillimetre emission polarization could be obtained toward the same region and sample the same dust grain population (which is generally unlikely to be the case due to sensitivity to different temperatures and densities), then the polarizations measured should be orthogonal (Hildebrand 1988b).

It is worth mentioning that to date, the results of polarimetry at far-infrared and submillimetre wavelengths (emission) do not generally agree with those at optical and near-infrared wavelengths (absorption). This may not be a surprising result since these two methods generally probe dust grain populations at different temperatures and densities. The near-infrared polarimetry by selective absorption suggests that grains are not aligned at $A_V >> 1.3$ mag, whereas the emission polarimetry indicates the presence of grains with a high degree of alignment in very dense interiors of clouds (often at $A_V > 40$ mag).

Lazarian et al. (1997) explain this as a selection effect. The near-infrared observations sample the total sample of grains (essentially up to the wavelength of the radiation) along the line of sight and are used typically toward dark, quiescent clouds. On the contrary, long wavelength emission polarization data have generally concentrated on the densest cores within active massive star-forming regions (partly due to limited sensitivity). These regions are often warm ($T \sim$ 25-100 K) and far from equilibrium. Therefore, direct comparison of background starlight polarization and thermal emission polarimetry must be done with some care.

2.2.3.3 Zeeman splitting of Spectral Lines

Zeeman splitting is detected by measuring circular polarization within a spectral line. It was first detected by Verschuur (1968). Since then, Zeeman splitting of HI has been the main method of probing the line of sight component of the magnetic field, B_{los}, toward atomic (diffuse) interstellar clouds. HI is not an effective probe within molecular clouds since most hydrogen is in molecular form. Instead, Zeeman splitting of the OH molecular transitions at 18 cm has been detected toward just over a dozen dark clouds, although many more have been surveyed without detection (see Crutcher 1999 for a summary). The OH molecule probes densities up to $\sim 10^4$ cm^{-3}. In order to sample the field in dense cores of GMCs, observation of the

Zeeman effect in CN (Crutcher et al. 1999) and CCS (Levin et al. 2000) have been made.

2.2.3.4 Faraday Rotation

Faraday rotation refers to the rotation of the plane of polarization of light due to interaction with a charged plasma. As light passes through the ISM, it may encounter regions of high electron density (n_e) over many parsecs. The change in the position angle ($d\theta$) is a function of λ^2, and thus Faraday rotation is typically measured toward long wavelengths. It has been primarily been used to probe the electron density of the atomic ISM via the relation:

$$\frac{d\theta}{d(\lambda^2)} \propto \int n_e B_{los} dl \tag{2.14}$$

where dl is the depth of the medium. Faraday rotation was first observed in radiation from pulsars (Manchester 1974), for which the line of sight field strength, B_{los}, can be assessed independently.

2.2.3.5 Synchrotron Emission

Generated in diffuse clouds with high energy electrons accelerated by magnetic fields, synchrotron emission was first observed by Dombrovsky (1954) at optical wavelengths, but more typically is observed in the radio (Mayer et al. 1957). Sensitive bolometer cameras can now detect this source of polarization between 350-850 μm; the Crab Nebula has been mapped in polarized emission at 850 μm (Greaves et al. 2001).

As in the case of thermal emission from grains, the polarization electric field vector arising from synchrotron radiation should lie orthogonal to the local B_{pos} direction where the emission was generated and hence be orthogonal also to polarimetry via selective absorption. This relationship has been observed in the spiral arms of the Milky Way (Berkhuijsen et al. 1964). Within dense clouds at submillimetre wavelengths, synchrotron emission will generally be overwhelmed by thermal emission from dust grains. However, if a synchrotron source lies behind a dense cloud, it can be used to estimate Faraday rotation through the cloud. Such sources (away from the dense clouds) can also be used as calibrators to ensure polarimeters are working correctly.

2.3 Previous Polarimetry of Molecular Clouds

The reader should be convinced that:

- magnetic fields exist in the interstellar medium,
- magnetic fields align dust grains,
- aligned dust grains generate polarized light, and
- polarization may be through absorption or emission, dependent on wavelength.

Absorption polarization using background stars is limited to clouds of low to moderate optical depth. However, toward tenuous systems of clouds, the polarization maps produced can illustrate a large-scale mean direction for the polarization. For example, Figure 2.7 presents a polarization map made toward the Lynds 1641 cloud (Orion A) at 500 pc and Taurus, the nearest star-forming cloud at 140 pc. However, it is not obvious that there exists a relation between polarization vectors and dense gas, since polarization data do not align preferentially either parallel or perpendicular to structures within the clouds.

Goodman et al. (1995) mapped polarization in near-infrared absorption from many dark clouds and found that, even where background starlight was still visi-

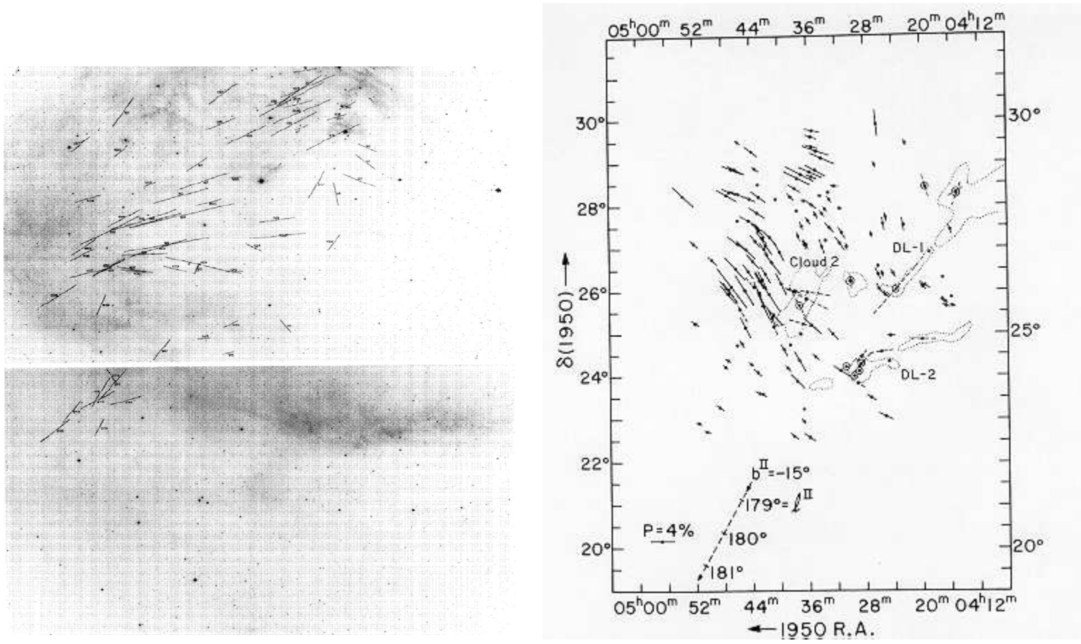

Figure 2.7: Absorption Polarimetry of the Orion A and the Taurus Clouds Using background starlight, Vrba et al. (1988) and Moneti et al. (1984) have measured the large scale polarizations toward the L1641 cloud (associated with the Orion A GMC) and the Taurus Dark Cloud, respectively. The Orion A map was done at optical wavelengths, and the Taurus map contains both optical and near-infrarad polarization data. The Taurus map also shows the global gas structure by dotted lines. Note that there is no distinctive alignment between the gas structures and the polarization. Vectors lie both parallel and perpendicular to filamentary structures.

ble, the degree of polarization did not continue to rise with increasing extinction. The different behaviors between stars observed through diffuse clouds and dark clouds is shown in Figure 2.8. From these data, it was determined that there is a threshold extinction beyond which near-infrared polarimetry is not an effective probe of magnetic field geometries. This decline in polarization percentage has been attributed to several potential causes: absence of magnetic field within the clouds, turbulence, geometry of fields, field tangling, ineffective alignment mechanisms, and changing grain shapes (e.g. spheroidal grains cannot polarize light) or compositions. Regardless of the cause of the drop in the degree of polarization (or the "polarization percentage"), absorption polarimetry clearly has its limits as a probe of field structure within dense gas. The effective limit due to availability of background starlight is $A_V \approx 2$ mag for optical polarimetry and $A_V > 40$ mag for the near-infrared, although the believable measurements fall far short of these extinction limits (Goodman et al. 1995). Figure 2.8 shows that, even in the near-infrared, the polarization stops rising around an extinction of $A_V \approx 1.3$ mag (Weintraub et al. 2000).

At high extinctions, the flattening of the polarization percentage has been attributed to the presence of poorly polarizing, or "bad" grains, generally separating by extinction regimes in which the polarization data effectively probe the magnetic field (good grains) from those where it does not (bad grains) (Goodman et al. 1995; Arce et al. 1998; Weintraub et al. 2000). Grains may be poorly polarizing for several reasons. They may become spherical (or too large) by agglomeration processes as density increases, rendering them more difficult to align; or they may alter composition with different density and temperature regimes. The presence of such bad grains does not imply that no magnetic field is present; it merely sets a threshold as to where polarization data can reliably be expected to trace that field.

In dense clouds, emission polarization and Zeeman splitting are the techniques used to probe the geometry of magnetic fields, but both have been restricted to only the brightest regions until recent developments of bolometric cameras with large fields of view, which has greatly advanced our potential to measure the field geometry in the plane of the sky.

The earliest detection of polarized emission in the far infra-red was made by Cudlip et al. (1982) toward the OMC-1 region of Orion. Two years later, the first submillimetre polarization data were obtained, also in Orion (Hildebrand et al. 1984). Polarization percentages were in the range of 1-2 %. Single bolometer polarimetry began in the 1990s (e.g. Flett & Murray 1991), resulting in important observations of polarized emission from aligned dust grains. Through laborious ob-

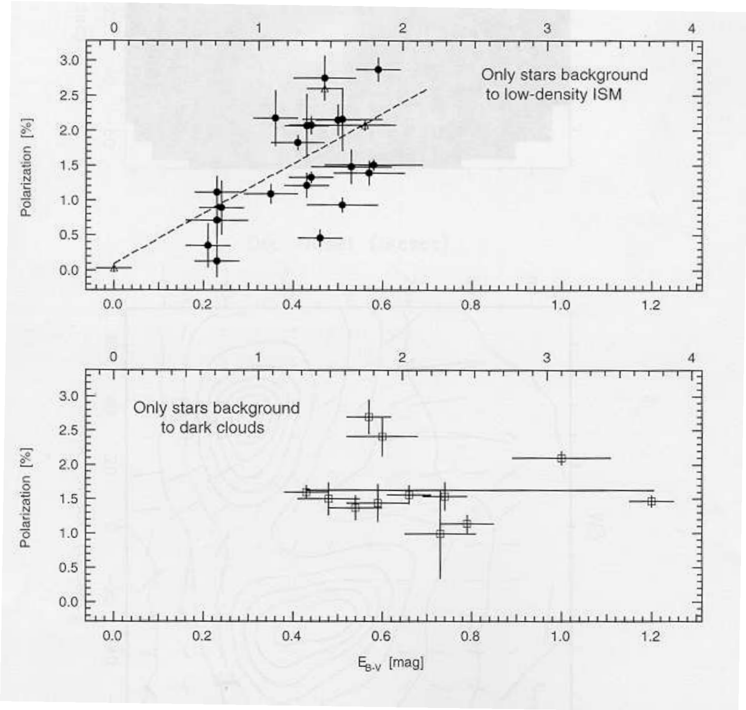

Figure 2.8: Relation between Near-infrared Polarization and Extinction
These plots show the observed relation between the polarization percentage in K-band (2.2 μm) and extinction ($A_V = 3.1E(B-V)$). The dashed line is a least square fit to the stars background to low-density gas in the ISM: $p_K = (0.09\pm0.06)+(3.58\pm0.13)E(B-V)$ with a correlation coefficient of 0.68. The solid line fit to stars background to dark clouds gives $p_K = (1.61\pm0.13)+(0.03\pm0.15)E(B-V)$ with correlation coefficient 0.79. (Figure reprinted from Arce et al. (1998) as presented by Weintraub et al. (2000).)

servations with many pointings, these instruments (such as the Stokes polarimeter aboard the Kuiper Airborne Observatory) produced impressive maps of variations in polarization across bright molecular cloud cores. A compilation of KAO observations was recently published by Dotson et al. (2000). The MILLIPOL polarimeter also produced some 1.3 mm polarimetry at Kitt Peak Observatory (Leach et al. 1991). The James Clerk Maxwell Telescope (JCMT) used the single UKT14 bolometer for polarimetry, and even this less sophisticated predecessor to the current SCUBA (Submillimetre Common User Bolometric Array) detector made the JCMT the leading world facility for submillimetre polarimetry. Due to limited sensitivity, these early observations were confined to only the brightest cores of molecular clouds (i.e. $>$ 5 Jy), since typically cores are polarized at only the 2-3% level. The first polarimetric map of a pre-stellar core was obtained by Greaves et al. (1994). Maps were achieved only through long integrations with multiple pointings; for example, the ρ Ophiuchus A core containing the protostellar source VLA 1623 was mapped by Holland et al. (1996). These data, shown in Figure 2.9, required 12 hours of integration time to complete.

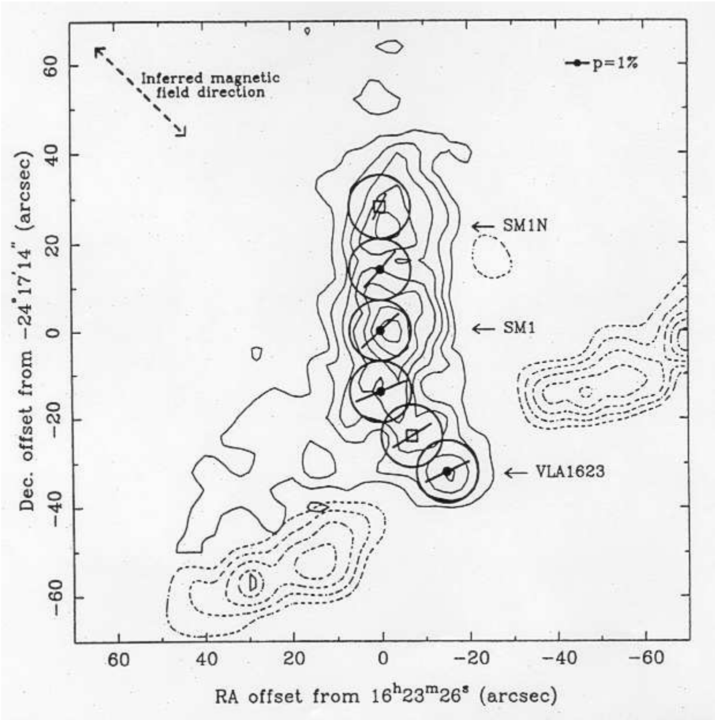

Figure 2.9: Early JCMT Polarization Map made with the UKT14 Single Bolometer.
Polarization measurements at 800 μm toward six positions along the ρ Ophiuchus A core containing the classic protostar VLA 1623 were made at the JCMT. These data required six telescope pointings and 12 hours to observe. The magnetic field direction is inferred by rotating the vectors by 90°. (reprinted from Holland et al. (1996))

2.4 Current Theoretical Models of Magnetic Field Geometries

Models of formation mechanisms for molecular cloud structures (particularly filaments) typically take one of two forms. The first involves the creation of structure arising as density fluctuations in the ISM (e.g. filamentary structures arising from MHD turbulence simulations, see Vazquez-Semadeni et al. 2000 for a review). The second involves equilibrium solutions assuming reasonably stable cloud configurations. The most extensively developed example of the latter group is the model of Fiege & Pudritz (2000a), in which filamentary clouds are confined by helical fields (i.e. fields with both poloidal and toroidal components). The toroidal field acts to confine the gas and is compressive at all radii. This model has been used to generate testable polarization patterns (Fiege & Pudritz 2000b). The predicted polarization patterns differ depending on three parameters: the flux-to-mass ratios in the poloidal and toroidal directions and the concentration parameter, which sets the radius of pressure truncation (Fiege & Pudritz 2000b). Figure 2.10 shows some simulated patterns for different variations in these parameters.

A helical field geometry is not the only current model for magnetic fields in molecular clouds. An hourglass geometry has been measured in the OMC-1 core of Orion A. In addition, numerical simulations of turbulence are used to predict field geometries (and polarization patterns) within molecular clouds. Many simulations of turbulence have been limited to two dimensions and do not include self-gravity; this presents difficulties for modeling magnetic fields and turbulence which are inherently three-dimensional phenomena. The ISM is viewed in these models as a magnetized, turbulent, self-gravitating, compressible fluid in which density enhancements are transient. Many such simulations (even in two dimensions) have been successful at producing filamentary structures with the highest density fluctuations at the interface between colliding streams of gas (see Vazquez-Semadeni et al. 2000). Computational power is now making three-dimensional simulations

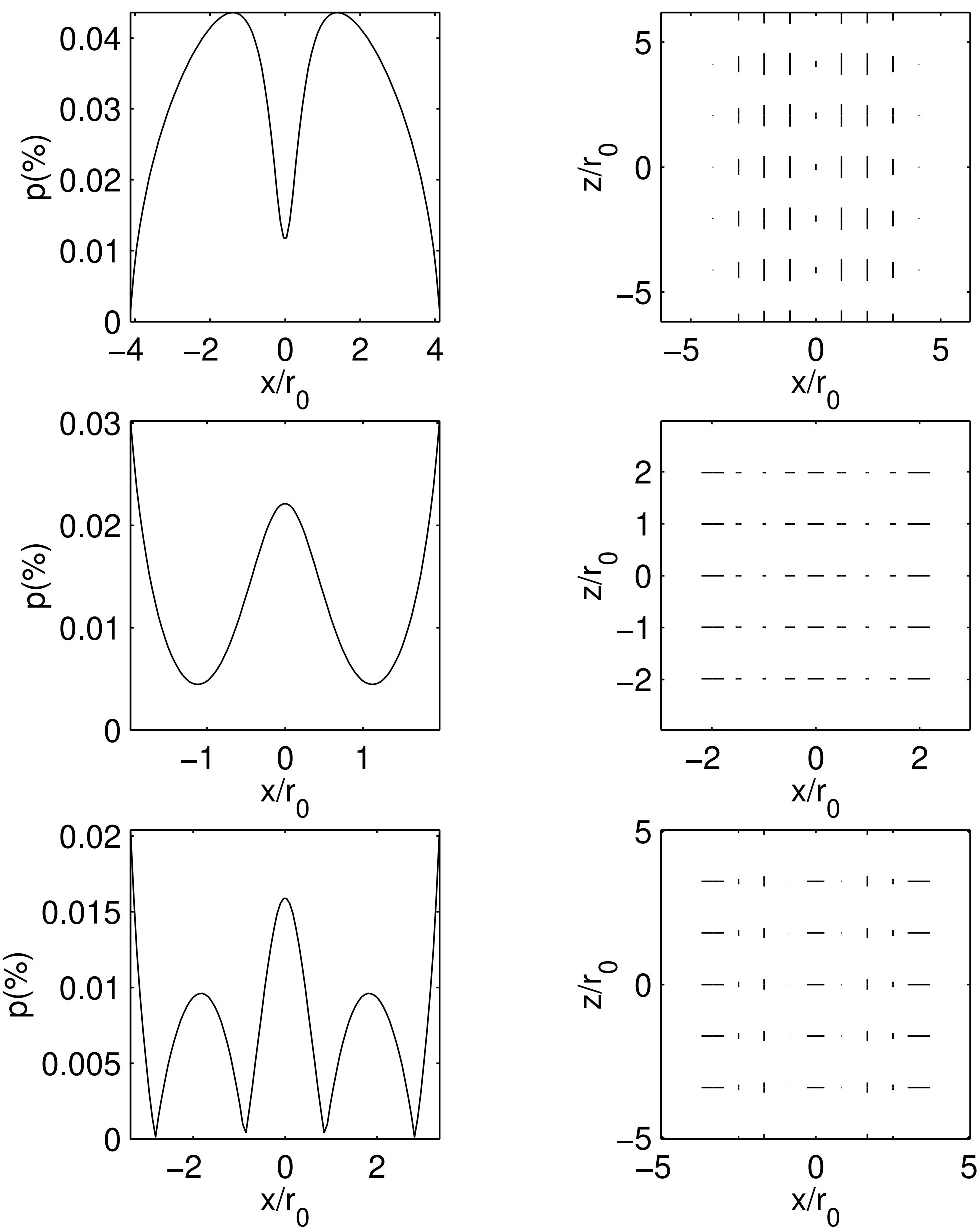

Figure 2.10: Polarization Patterns for Filaments Threaded with Helical Fields The variations of polarization percentage and position angle are illustrated for three different cases of a filament threaded by a helical field. In each case, the filament lies entirely in the plane of the sky and the axis is defined by $x = 0$. The top two panels show a toroidally dominated field pattern; the centre shows a poloidally dominated pattern while the bottom panel shows a mixed pattern which is neither toroidal nor poloidally dominated. (reprinted from Fiege & Pudritz (2000b))

manageable. An example of a recent magnetized, three-dimensional simulation of cores formed through supersonic turbulence is shown in Figure 2.11.

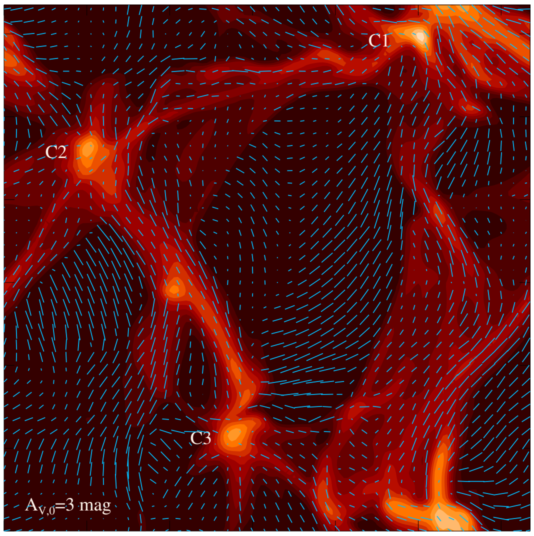

Figure 2.11: Magnetized Turbulent Flows and Core Formation
This 3D MHD simulation illustrates the formation of cores C1, C2 and C3 due to infall along super-sonic turbulent flows in a region of average density 320 cm^{-3} and turbulent velocity 3.0 km s^{-1}. The selected cores have masses of $\sim 60 M_{\odot}$ and gas densities reaching 10^5 cm^{-3}. Polarization vectors are overlain on top of the gas structures. This simulation assumes grains are effectively aligned only to a maximum extinction of $A_V = 3$ mag. (reprinted from Padoan et al. (2001))

Polarization maps can be difficult to interpret since one can imagine more than one three-dimensional magnetic field geometry which can produce the same two-dimensional polarization pattern. The possible sources of a given pattern therefore cannot be easily deduced from the polarization data directly, without making some simplifying assumptions about the geometry of the field.

In past work, most polarization data has been analyzed using the relation between the alignment of individual dust grains to magnetic fields and the relative orientation of the polarization produced. Hence, absorption polarization studies have been interpreted as tracing the magnetic field directions (in the plane of the sky) directly, while emission polarization vectors are rotated by 90° to yield the magnetic field's geometry. For example, the far-infrared/submillimetre data of Schleuning (1998) in Orion A's OMC-1 core is interpreted in this way (see Figure 2.12).

However, there is an assumption implicit in these interpretations; the plane-of-sky magnetic field direction is assumed to be constant through the whole depth of the cloud so that all dust grains are aligned not only with the local field, but also with each other. In fact, it is this special case which was diagrammed in Figures 2.5 and 2.6 of §2.2.3.1. What is measured at the telescope is a net polarization through the entire cloud, in essence a weighted vector average of all the polarization vectors along a particular line of sight. In the case of a varying magnetic field, simply rotating polarization vectors can produce completely incorrect interpretations of the field geometry.

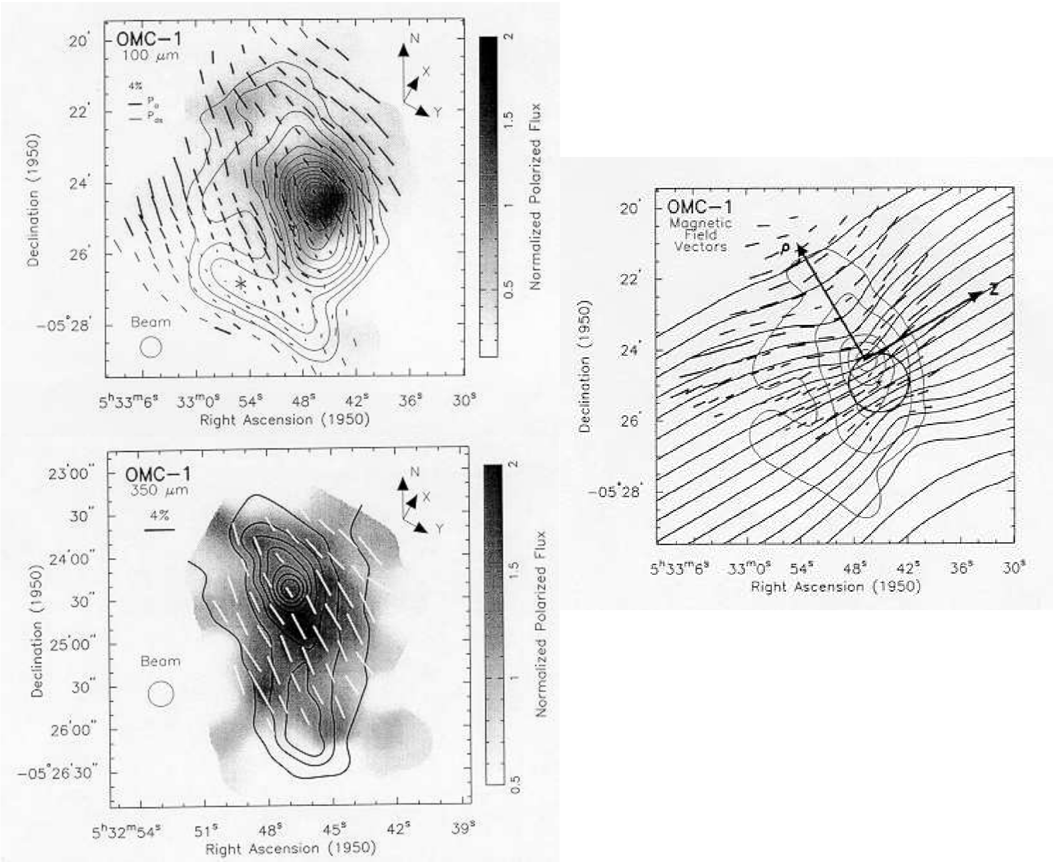

Figure 2.12: Submillimetre Polarization toward the OMC-1 core
100 and 350 μm polarization vectors measured with the KAO and CSO polarimeters. Strong agreement exists between the two wavelengths. A mean magnetic field direction was inferred from these data by rotation of the vectors by 90°. These images are reproduced from Schleuning (1998).

Within several protostellar and massive cores, rotation of field lines to estimate the magnetic field geometry has produced an "hourglass" configuration, in which the field lines appear to be drawn into an hourglass shape. When this "pinching" of field lines is centred on a known protostar or young stellar object, then this field geometry has been interpreted in terms a dragging inward of magnetic field lines along with infalling gas toward the accreting object. Perhaps the best illustration of this geometry is the massive OMC-1 core of Orion A, shown in Figure 2.12. This signature of infalling gas has been identified in several smaller cores, such as NGC 1333 IRAS 4A (Girart et al. 1999). This orderly picture of the field geometry near OMC-1 is not mirrored on smaller scales where interferometric polarization observations show subsets of ordered vectors grouped together but each subset oriented in different directions (Rao et al. 1998).

2.5 The Motivating Goals of this Thesis

The state of the models for magnetized star-forming clouds had, by 1998, reached a point at which well-sampled polarimetric maps over several parsec scales were required to test their predictions. The timely commissioning of the SCUBA polarimeter for large-scale imaging in the fall of 1998 was most advantageous and, thanks to enthusiasm on the part of the community to exploit its potential fully, placed me in the position to obtain some of the largest spatial scale emission polarization maps of the dense interiors of molecular clouds yet produced. In several regions, these maps are the first indications of the presence of aligned grains and hence magnetic fields.

In addition to confirming the presence of magnetic fields within star forming clouds, the polarization maps can be compared to predicted polarization patterns (e.g. Figure 2.10) for various magnetic field geometries (unidirectional, helical, hourglass). The JCMT's rather large resolution (although excellent for a single dish) of $15''$ unfortunately prohibits comparison of polarization data to single protostellar core models at the distance of Orion. However, this limitation ensures that in such regions, the polarization detected is arising primarily from the filamentary structure and not the cores themselves.

Both polarimetry and Zeeman splitting observations are time-consuming and challenging in most regions. However, polarimetry has met with more general success than Zeeman measurements in molecular clouds. Hence, the observation of many clouds for polarized emission can provide better information on candidate regions for extensive Zeeman study, in order to concentrate telescope time where success is most likely.

2.6 Observing Polarized Light at the JCMT

2.6.1 The JCMT and SCUBA

The introduction of sensitive submillimetre bolometric arrays has greatly enhanced our ability to probe magnetic field geometries inside molecular clouds. The foremost such instrument is the polarimeter created for use with the SCUBA (Submillimetre Common User Bolometer Array) detector at the James Clerk Maxwell Telescope (JCMT). This polarimeter was commissioned for imaging polarimetry in 1998.

With its 15 m antenna, the JCMT is the largest telescope in the world designed to work in the submillimetre part of the spectrum. It is situated at 4092 m (13400 ft), near the summit of Mauna Kea in Hawaii. Figure 2.13 shows a picture of the JCMT without its protective membrane, which is a Goretex sheet that acts to shield the telescope from wind during observing. The resolving power of the telescope is 14-15$''$ at 850 μm. This is roughly comparable to the size of a protostellar core in the Orion GMC at 500 pc distance (1 parsec = 3.1×10^{13} km).

Figure 2.13: The James Clerk Maxwell Telescope
A view of the JCMT with the Goretex membrane rolled back. It is the largest telescope in the world designed to work in the submillimetre regime of the electromagnetic spectrum. During operation, the protective membrane, transparent to submillimetre waves, is rolled down in front of the antenna. This acts as a windblind which greatly increases the stability of the telescope.

The SCUBA detector consists of two bolometric arrays operating in two continuum wavebands centred on 450 and 850 μm (667 and 353 GHz respectively). The bandwidths at both wavelengths are $\sim$ 40 GHz. Observations are obtained simultaneously at these two wavelengths, although owing to higher atmospheric noise, irregularity in the beam and difficulty with measurement of instrumental polarizations, the 450 μm polarization data are not useful at present. SCUBA is mounted at the Nasmyth focus of the JCMT, since the size and weight of the instrument prohibit its placement inside the receiver cabin where it would also be subject to tipping with the motion of the telescope.

The 850 μm array consists of 37 bolometers arranged in a hexagonal array (see Figure 2.14). Since the feeds are circular, there are gaps between the bolometers. A SCUBA observation at a fixed pointing of the telescope would thus leave some regions unobserved. To create a fully sampled image, a series of 16 exposures of 1 s

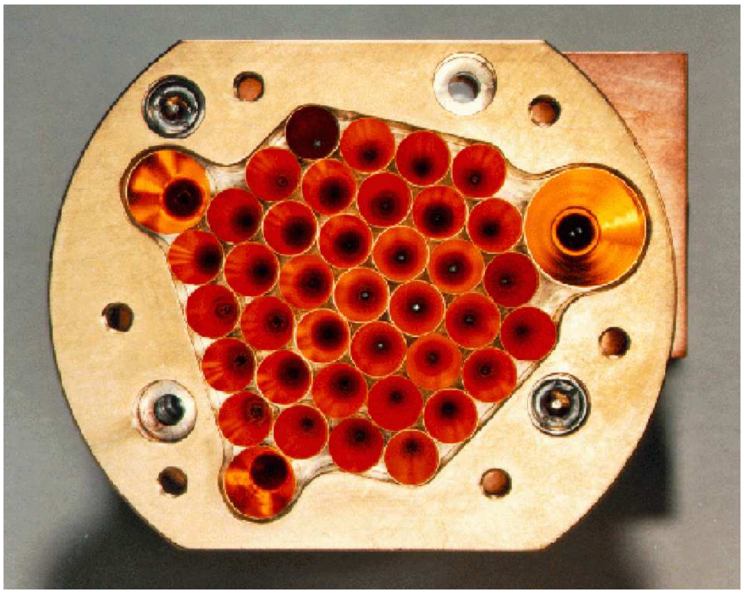

Figure 2.14: SCUBA's Long Wavelength Bolometer Array
The 850 μm array consists of 37 bolometers, each with a separate feedhorn as shown here. Three photometric feeds permit single bolometer observations at 1.1, 1.3 and 2.0 mm, but these are not done simultaneously with the 850 μm observations. The array's footprint on the sky spans a diameter of roughly $2.3'$. To fill in the spaces between the bolometers, the array position must be shifted during each observation. This method is called "jiggle mapping".

each are taken with each observation offset by $6.18''$ in a hexagonal pattern (shown in Figure 2.15).

2.6.2 The SCUBA Polarimeter

The SCUBA polarimeter utilizes a rotating half waveplate and a fixed analyzer. The polarimeter is described in detail in Murray et al. (1997). The waveplate introduces a half-wavelength phase lag between the so-called "fast-axis" and the plane orthogonal to this axis. The waveplate is an achromatic half-wave retarder in which plates of birefringent quartz are used to retard one plane of polarization with respect to the orthogonal plane. The phase difference is achieved by precise cutting of the plate's thickness. In the SCUBA array waveplate, several monochromatic

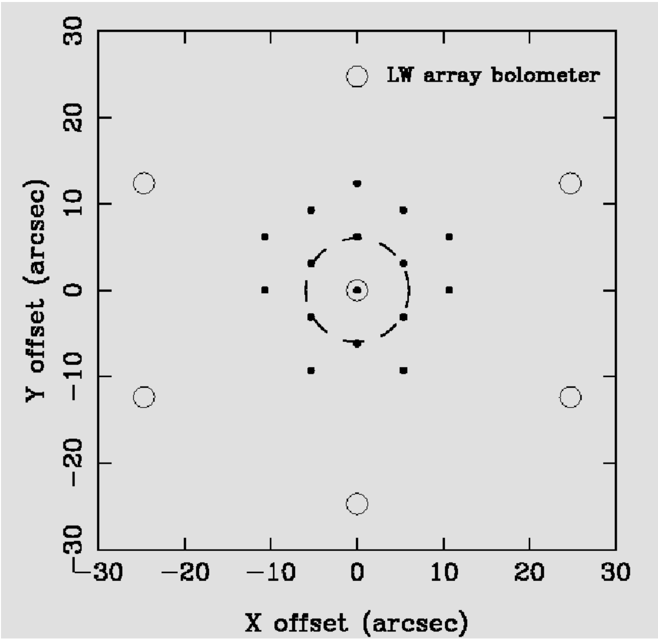

Figure 2.15: 16-pt Jiggle Pattern
This 16 point jiggle pattern is used to produce a fully sampled image with the long wavelength (850 μm) array. The changes in the location of the observation are achieved by jiggling the secondary mirror.

plates are used together, oriented with different directions of the "fast axis", so the waveplate is serviceable over a wide range of wavelengths. Transmission losses due to quartz absorption are around 15%, at 850 μm, but are larger at 450 μm (see Table 2.1). Reflections at the quartz surfaces are reduced using polypropylene coatings. In operation, the waveplate is cycled through 16 positions, each 22.5° apart, during a single observation. A 16-point jiggle map is made at each position.

The analyzer is a photo-lithographically etched grid of 6 micron spacing, which transmits only one plane of polarization by absorbing photons with an electric field component parallel to the grid lines. Therefore, as the waveplate rotates, the analyzer produces a modulated signal. Linear polarization naturally contains two periods within 360° (i.e. the fluxes measured at position angles offset by 180° are equal).

The optical path of light through the polarizer is shown in Figure 2.17. Incoming

Figure 2.16: Polarimeter Mounted in the SCUBA Optical Path
The polarimeter must be manually mounted in the SCUBA optical path in front of the cryostat window for each observing session. SCUBA is contained in the big, red cryostat behind the polarimeter.

light travelling in the $+\hat{z}$ direction is incident on the half-wave plate. The waveplate acts to select out one polarization direction according to the angle δ. The analyzer then selects the component of light transmitted from the waveplate along one constant direction. Note that in the absence of the analyzer, unpolarized incoming light with electric field vectors in random directions would produce a uniformly strong signal regardless of the position of the waveplate, since unpolarized light will always have some component along δ.

However, with the analyzer present, only that component of light along the transmission axis (shown as a dashed line in Figure 2.17) will be passed through to SCUBA. Thus, a sinusoidal pattern will naturally result, reflecting the angle selected by the waveplate. If the waveplate angle is equal to the transmission axis of the analyzer, then a signal of $E\cos\delta$ will be transmitted. If the angle is orthogonal to the axis of transmission, then the transmitted signal will be zero. The polarizer is sensitive to linear polarization only. As the waveplate rotates by some angle δ, the

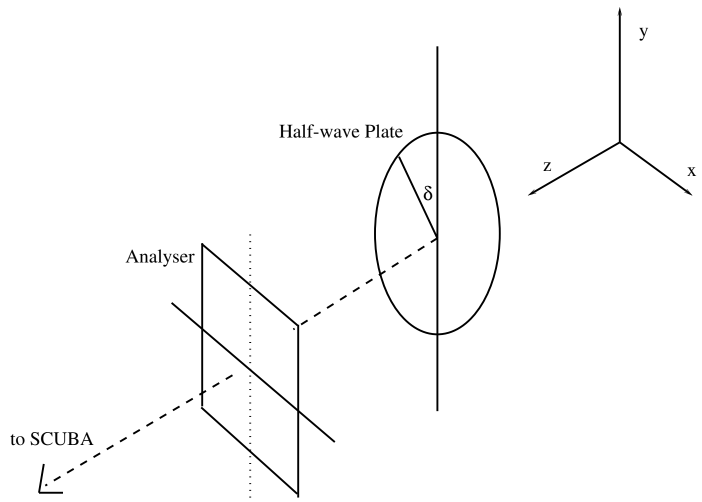

Figure 2.17: Optical Path of Light Through the Polarimeter
The path of incoming light along $+\hat{z}$ into SCUBA is illustrated. Light travels through the half-wave plate, which transmits light with electric field vectors with components parallel to δ. The light then passes through the analyzer, which is fixed and transmits along one axis only. The transmission axis is shown as a dotted line.

selected position angle on the sky is actually changed by 2δ, as illustrated in Figure 2.18.

The flux density measured as a function of the waveplate angle, δ, is given by

$$S(\delta) = \frac{1}{2}\left[I_0 + I_p\left(1 + \cos(4\delta - 2\theta)\right)\right] \tag{2.15}$$

where the polarization position angle is θ measured with respect to the analyzer axis and I_0 and I_p are the unpolarized and polarized intensities respectively. The minimum measured signal is thus $I_0/2$. The 1/2 factor takes into account that the analyzer always hinders one plane of polarization from being transmitted. (Cameras designed specifically for polarimetry usually measure both planes of polarization using two separate detector arrays.) The polarized intensity is thus a modulation about

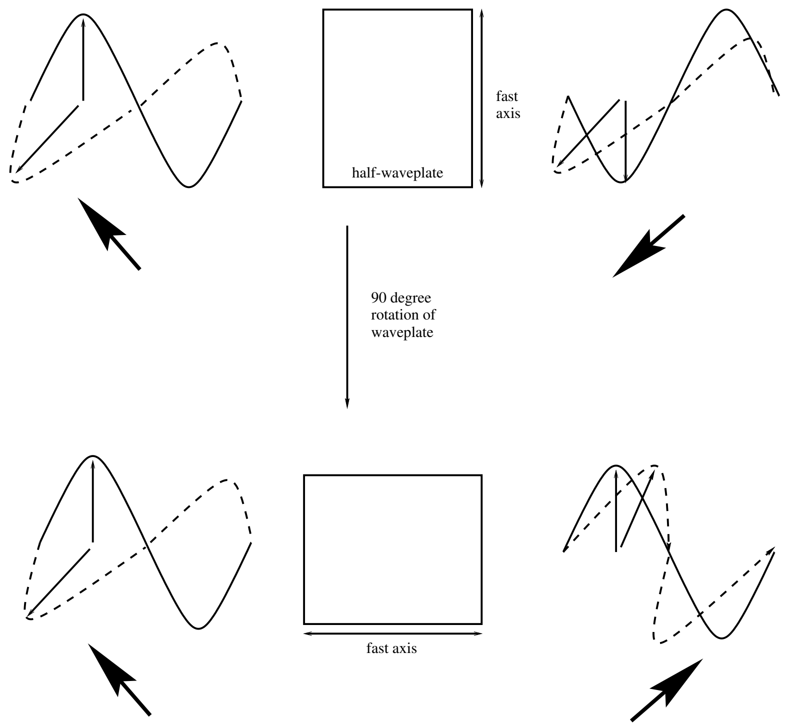

Figure 2.18: Polarization Angle Response to Waveplate Rotation.
An illustration of the response of the measured polarization vector to waveplate rotation. The incoming radiation vector is shown at the left. When the waveplate is rotated through 90°, the output angle (at right) has rotated by 180°. The vectors shown at the right are indistinguishable to the polarizer. An angle of 135° is equivalent to 315° in linear polarization.

the mean intensity and the first maximum occurs at $\delta = \theta/2$ and then subsequently every 90° in the cycle.

The signal detected can be expressed as two Stokes' parameters: Q and U where

$$Q = I_p \cos(2\theta) \tag{2.16}$$

and

$$U = I_p \sin(2\theta). \tag{2.17}$$

λ (μm)	mean PME (%)	ϕ (degrees)	η (%)
350	96	+9	—
450	98	+7	$\sim 60\%$
750	99	+1	—
850	97	-5	$> 85\%$ (pre-1998)

Table 2.1: Polarimeter Performance of the Array Waveplate.
This chart illustrates the mean polarization modulation efficiency (PME), the direction of the fast axis, ϕ, and the transmission efficiency, η. A second analyzer was used to create a linearly polarized signal from Saturn. (reprinted from Greaves et al. 2001b.)

Polarization data are typically displayed in vector format, where the length of the vector represents p, the polarization percentage (i.e. the ratio of polarized to unpolarized flux):

$$p = \frac{\sqrt{Q^2 + U^2}}{I_0} \times 100\%. \tag{2.18}$$

The uncertainty in p is denoted dp and is given by:

$$dp = \frac{\sqrt{(dQ^2)Q^2 + (dU^2)U^2}}{p}. \tag{2.19}$$

A small correction must be made to p, particularly in the case of low signal to noise data. Since p is forced to be positive, values which are in fact zero may falsely appear as signal. To remedy this, the value of p is "debiased" by subtraction of the uncertainty dp:

$$p_{db} = \sqrt{p^2 - (dp^2)}. \tag{2.20}$$

Even when not specified as p_{db}, all polarization percentages discussed in this dissertation have been debiassed in this manner.

The position angle of the polarization on the plane of the sky is denoted θ (as above):

$$\theta = \frac{1}{2}\arctan\left(\frac{U}{Q}\right). \qquad (2.21)$$

with an uncertainty of

$$\begin{aligned} d\theta &= 0.5\frac{dp}{p} \text{ radians} && (2.22)\\ &= 0.5/\sigma_p \text{ radians} && (2.23)\end{aligned}$$

where σ_p is the signal-to-noise in polarization percentage. Some caution must be exercised when determining θ, since both U and Q must be chosen from the correct quadrant.

To deduce the polarized signal, the Stokes' parameters must be detected. In our first data paper (Chapter 3), subtraction of waveplate positions was used. Q was deduced from $S(0) - S(45)$, and U was deduced from $S(22.5) - S(67.5)$. With improved software, the data of subsequent papers (Chapters 4 - 7) were used to deduce Stokes' parameters through fitting to the sinusoidal pattern produced by waveplate rotation.

2.6.2.1 Instrumental Polarization

Unfortunately, along with polarizations measured from astronomical sources, there is instrumental polarization (IP) which must be assessed and removed from the data. Because SCUBA is mounted on the Nasmyth platform, the degree of IP should be constant. In fact, the IP arises primarily from the weave of the JCMT's protective membrane, owing to a small difference between the thread spacing in the vertical and horizontal directions. The effects are most acute at 450 μm since this is the closest wavelength to the thread spacing of 500 μm. Unfortunately, rolling back

λ (μm)	p_{IP} (%)	θ_0 (degrees)	source	epoch
Array Waveplate (central array bolometer)				
350	0.82 ± 0.13	100 ± 4	Saturn	Oct 1997 + Aug 1999
450	3.60 ± 0.41	114 ± 3	Mars/Uranus	Oct 1997
750	1.16 ± 0.04	97 ± 1	Saturn	Oct 1997 + Aug 1999
850	1.09 ± 0.06	161 ± 2	Mars/Uranus	1997-99 (25 days)
Array Waveplate (off-centre bolometers)				
450	3.26 ± 0.23	100 ± 2	Saturn	Jul 1998 (6 bols)
850	0.92 ± 0.05	163 ± 2	Mars/Uranus/Saturn	1997-99 (4 days, 36 bols)

Table 2.2: Instrumental Polarizations for SCUBA Arrays.
The 850 μm waveband has been the most extensively tested of all SCUBA's potential array frequencies. The 450 μm band suffers the highest IP effects due to the similarity of the wavelength to the thread spacing in the JCMT windblind. All data discussed in this work are 850 μm observations. (reprinted from Greaves et al. (2001b).)

the membrane is only possible if wind-speeds are very low and it is not typically done; a more interesting option is to add an orthogonal sheet of Goretex in the beam to cancel these effects, but this is not yet a standard practice (Greaves et al. 2001). The effects are less evident at 850 μm, where all the data presented in this thesis are taken.

The instrumental polarizations were measured using planets, which are assumed to be unpolarized. Table 2.2 shows that at 850 μm, the IP values are $\sim$ 1% at angles of $\sim 160°$ (east of north). The values reported are for zero elevation. In fact, the effective θ_{IP} values are $\theta_0 + \text{elevation}$ (see Table 2.2). The p_{IP} values are also affected by telescope elevation, but these effects are much less significant than those of θ_{IP}.

2.6.2.2 Sensitivity Limits of the SCUBA Polarimeter

The high degree of sensitivity in SCUBA is mirrored in the polarimeter, with some attenuation due to the imperfect transmission through the waveplate. The previous single bolometer detector, UKT14, was limited to a polarized flux of 100 mJy at 800 μm (Murray et al. 1997). If the source is 2% polarized, then the total flux would have to be 5 Jy in order to detect it with this polarimeter. SCUBA's polarimeter is much more sensitive. The faintest sources detected have fluxes of about 0.2 Jy beam^{-1} and polarizations of a few percent, resulting in polarized fluxes of approximately 4 mJy (Greaves et al. 2001), almost two orders of magnitude improvement over UKT14.

High sensitivity not only permits detection of significantly fainter compact objects (such as protostars and Active Galactic Nuclei), but also allows observations of more extended, tenuous material within molecular clouds. The JCMT's resolution of 14-15$''$ at 850 μm is insufficient to probe variations across compact protostellar cores at Orion's distance, which are generally only poorly resolved at best (cores in closer dark clouds will be better sampled). Interferometers are more appropriate for the study of such sources. However, observations have shown that the interiors of molecular clouds are complex, with significant filamentary structures of significantly higher densities than the mean densities of the clouds. These dense "clumps" or "filaments" are where pre-protostellar cores form. SCUBA's polarimeter now permits the study of the magnetic fields in extended dense gas, providing a probe into the pre-existing conditions for star formation.

2.7 Background on the Regions Observed

My goal is to compare the magnetic field geometries as inferred from dust emission polarimetry in several different star-forming regions within some clouds, as well as sampling different clouds with varying masses, star formation histories and ages.

The choice of which regions to observe with the SCUBA polarimeter was motivated by several factors. With the ultimate goals of testing newly developed models for filamentary molecular clouds, it was important that several of the regions

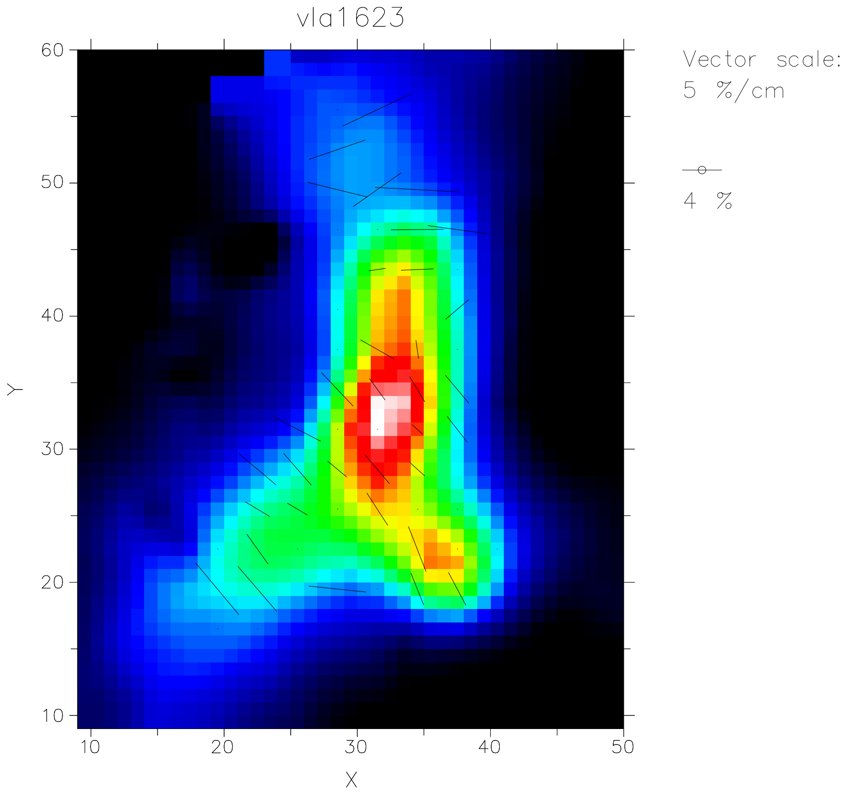

Figure 2.19: SCUBA Observation of VLA 1623
These data were taken of the ρ Ophiuchus core containing VLA 1623, the prototype of the class 0 source of protostars (André et al. 1993), by J. Greaves as part of the commissioning of the SCUBA polarimeter. These polarization data were obtained in 25 minutes of observing at a single SCUBA position. This illustrates the increased senstivity and field of view when compared with the earlier polarization map of this region (see Figure 2.9) which took 12 hours to produce.

studied be clearly filamentary. In order to compare magnetic field geometries in different star-forming environments, it was essential that more than one cloud be observed. Other, more practical, constraints included the proximity and brightness of the region, the presence of pre-existing data, and the amount of time required to achieve a high quality map. In several cases, our data represent the first emission polarimetry observed toward the region. Only one region observed (NGC 2024 in Orion B) has pre-existing maps of the polarized thermal emission from dust, and the field strength toward both NGC 2024 and the Barnard 1 cloud in Perseus has been measured through Zeeman splitting of the OH molecule. Some background of each region discussed in this work is presented below.

2.7.1 OMC-3 in Orion A

The Orion A GMC is by far the most extensively studied star-forming region. GMCs are not only dynamically interesting objects in their own right, but they are also the loci of the formation of massive stars. Within Orion, star-formation is ostensibly an ongoing process. The optically visible nebula M42 or "The Great Nebula in Orion" has been observed for centuries. Only recently, with the development of infrared and submillimetre astronomy, has it been recognized that very high numbers of embedded objects, many stars in the process of accreting material from the molecular cloud, exist beyond the range of optical telescopes. Within the Orion A cloud (already discussed in the context of molecular clouds in §2.1), observations of CO have revealed a dense gas stucture denoted the Integral-shaped Filament (Bally et al. 1987). Figure 2.20 shows the CO emission from part of the Integral-shaped Filament.

Shortly before I embarked on this project, a large portion of the Integral-shaped Filament was mapped using the (then) recently commissioned SCUBA scan-mapping mode at the JCMT (Johnstone & Bally 1999). Figure 2.21 shows the dust continuum map at 850 μm, as well as a smaller 1.3 mm dust emission map by Chini et al. (1997) on which condensations and boundaries between OMC-2 and OMC-3 are labelled. The OMC-2 and OMC-3 regions both lie to the north of the very bright central object on the 850 μm map, which is the OMC-1 core. With a view toward testing new theories about the field structure of filamentary gas, the most often studied region of OMC-1 was supplanted by the northern region of the filament, a region denoted OMC-3. This region does not contain a highly massive core (OMC-1 has a mass of 2200 $M_{\odot}$), nor does an HII region lie in the foreground (see Figure 2.22).

The OMC-1 region has been studied in polarization at many wavelengths (Cudlip et al. 1982; Hildebrand et al. 1984; Leach et al. 1991; Schleuning et al. 1997; Schle-

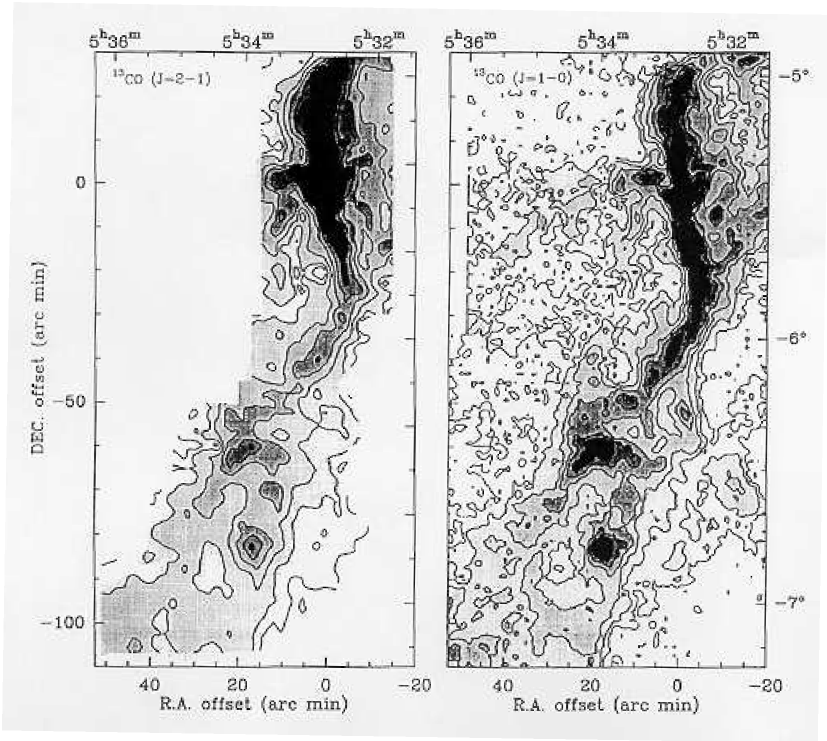

Figure 2.20: The Integral-shaped Filament of Orion A
Observations in CO trace the gas distribution of the Integral-shaped Filament. The right panel shows the ^{13}CO $J = 1 - 0$ map of Bally et al. (1987); the left map shows ^{13}CO $J = 2 - 1$ emission (Castets et al. 1990). Contour levels range from 5 to 25 K km s^{-1} in steps of 5 K km s^{-1}. The dominant structure of the gas is clearly filamentary. The bulk of the filament has been observed with SCUBA at 850 μm (see Figure 2.21).

uning 1998; Coppin et al. 2000; Dotson et al. 2000), but most have concentrated on the bright compact objects within this core. Some optical polarization data have been taken toward the periphery of the Orion A cloud by Vrba et al. (1988) and toward the Orion Nebula (Breger 1976). Histograms of the position angles measured over these two regions are shown in Figure 2.23. There exists reasonably good agreement between these two data sets regarding the mean polarization orientation (and hence the magnetic field if it is assumed to remain constant over the depth of the cloud). In this case, a mean field direction is taken to be equivalent to the polarization directions. Table 2.3 summarizes the derived field orientation from these two data sets plus the emission data toward OMC-1 shown in Figure 2.12 (Schleuning 1998).

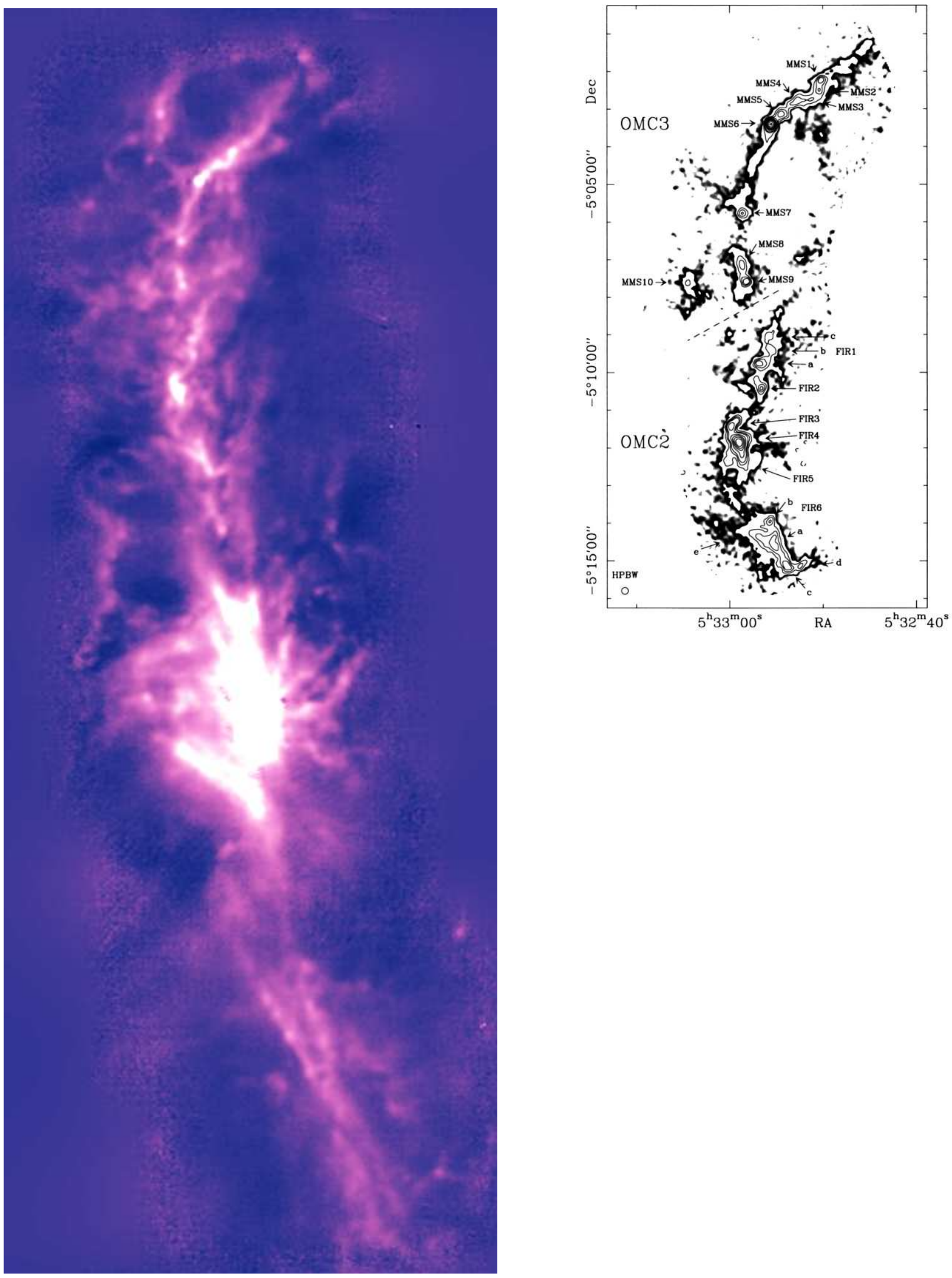

Figure 2.21: Dust continuum emission from Integral-shaped Filament. The spatially extensive map on the left was produced with SCUBA at the JCMT in scan-mapping mode. The existence of this map enabled the selection of a region to be mapped with the polarimeter and rendered the observations more effective due to information about flux levels and extended structure. (Data provided by D. Johnstone.) The right panel shows a 1.3 mm map from IRAM of the northern regions of OMC-2 and OMC-3 (a subset of the 850 μm map area north of the bright central core) in which several compact cores were identified (Chini et al. 1997).

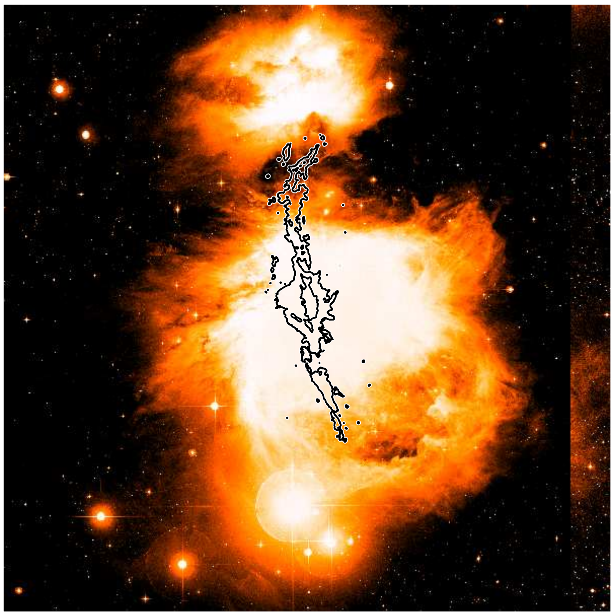

Figure 2.22: The Integral Filament and Optical Emission
Comparison of the Integral Filament structure in dust emission (Johnstone & Bally 1999) with the optical emission from the Palomar All Sky Survey shows that the OMC-3 region at the northern tip of the filament does not lie along the line of sight toward either the M42 HII region to the south or the NGC 1977 HII region at the north.

The data assembled in Table 2.3 were interpreted as evidence that a unidirectional magnetic field oriented at $\sim 120°$ (east of north) threaded the entire Orion A cloud (Schleuning 1998). If this is indeed the case, then all polarimetry data at 850 μm should show a position angle of 30° (east of north), regardless of which part of the cloud is observed. With a view toward testing this assertion, plus a chance to test a new model for filamentary clouds threaded by helical fields, OMC-3 was chosen as the primary target of our study. The data set of Johnstone & Bally (1999) revealed a shallow density profile along the whole filament in which OMC-3 is located. The density follows a power law with an index of -2 in radial displacement from the filament axis, and this behavior is predicted by the helical field model of Fiege & Pudritz (2000a).

There is yet one more piece of evidence in support of a helical field geometry in

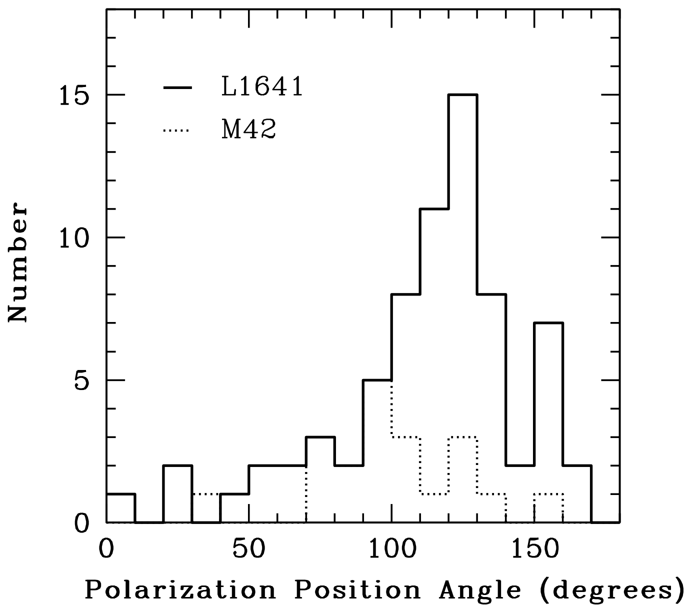

Figure 2.23: Optical Polarimetry toward L1641 and M42
The distributions of position angle in absorption polarization data toward the periphery of the Orion A cloud (a.k.a. Lynds 1641, or L1641) and toward bright stars in the HII region M42. These data sets both probe the field geometry near the periphery of the molecular cloud, since the HII region is a blister nebula on the near side of Orion A and the L1641 data are restricted to regions where background stars are visible though Orion A. (Data from Vrba et al. (1988) and Breger (1976).)

Orion A. Zeeman measurements of atomic hydrogen's 21 cm line were made by Heiles (1987). These data, shown in Figure 2.24, show a reversal of the line of sight field direction across the Orion A cloud. These data were later re-interpreted as evidence for an expanding shell around λ Orionis, the star at the centre of the Eridanus Loop (Heiles 1997). However, the HI Zeeman data probe the atomic envelope of the Orion A cloud and may not be indicative of the internal field structure.

2.7.2 Four Regions in Orion B

In 1998, a group of Canadian astronomers interested in star formation undertook a long term project of observing large regions of several nearby molecular clouds at the JCMT. The Orion B GMC was among those selected for detailed study, including polarization work on three bright cores and filamentary structures. As part of this

Region	Mean θ (degrees E of N)	Mean Field Inferred (degrees E of N)	Method of Observation
M42	100	100	absorption (optical)
L1641	120	120	absorption (optical)
OMC-1	30	120	emission (100 and 350 μm)

Table 2.3: Existing Polarization Data toward Orion A
Data obtained toward three different regions of Orion A show good agreement in their inferred mean magnetic field directions. These data have been taken jointly as evidence of a unidirectional field threading the entire Orion A cloud.

consortium, my principle task has been to obtain these polarization data, reduce and analyze them.

The regions selected for polarization mapping by the Consortium include NGC 2024, an active star-forming ridge in Orion B south and NGC 2071 and LBS 23N, regions of known star formation within the Orion B north cloud. NGC 2071 is a massive single clump with several cores within dominated by a single outflow but containing many young stellar objects. Although less massive, it is thus similar to the OMC-1 core in Orion A. The LBS 23N region is a string of cores with little obvious filamentary structure. NGC 2024 is the only one of these regions for which previous emission polarimetry or Zeeman splitting measurements have been done. Figure 2.25 shows the 100 μm polarization toward this core as measured with the KAO. The data were re-reduced by Dotson et al. (2000). Zeeman data also exist toward this region; they are presented in Figure 2.25.

The data of these three regions are presented in Chapter 5. Following these observations, and the success of observations of OMC-3, a fourth region of Orion B was observed. This filament, associated with the reflection nebula NGC 2068, has a complex filamentary structure, evidence for several star-forming cores and outflows, and several potential cores in a pre-protostellar phase. No previous polarization or Zeeman data exist toward this region. These data are examined in Chapter 6.

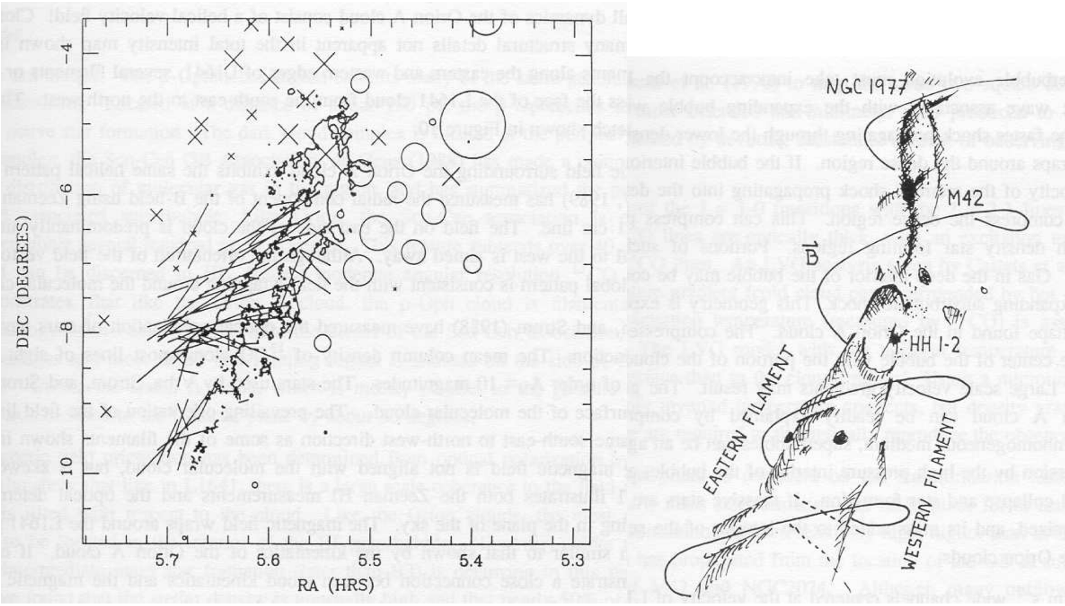

Figure 2.24: Zeeman measurements in HI near the L1641 Cloud
Heiles (1987) measured Zeeman splitting of atomic hydrogen in the atomic envelope of the Orion A cloud. These data indicate a mean field strengh of 10 μG and were originally interpreted as indications of a helical field geometry as indicated on the right. (Circles indicate field oriented toward the observer; crosses indicate field oriented away fromt the observer. Their size is a function of field strength.) The optical polarization data of Vrba et al. (1988) are also plotted on this image. The schematic illustration of Orion A is taken from Bally (1989).

2.7.3 Barnard 1

Barnard 1 (B1) is the only dark cloud contained in the sample of clouds presented in this work. This cloud lies within the Perseus complex of molecular clouds. It is also the closest region to the Sun at 350 pc (Borgman & Blaauw 1964). Along with Barnard 1, five other star-forming clouds are associated with Perseus: Barnard 5, IC 348, L1448, L1455 and NGC 1333. Since B1 is not part of a GMC, its mass and extinction are lower than those clouds observed in Orion. Its mass contained in regions of gas with density $> 10^3$ cm^{-3} is just 1200 $M_\odot$, and the density is seen to increase toward the centre of the cloud. Its total area as traced in CS ($J = 1 - 0$) is just 2 pc $\times$ 5 pc. The stellar to gas mass ratio in B1 is very low, estimated by Bachiller et al. (1990) to be just 0.5%, negligibly small even when compared to

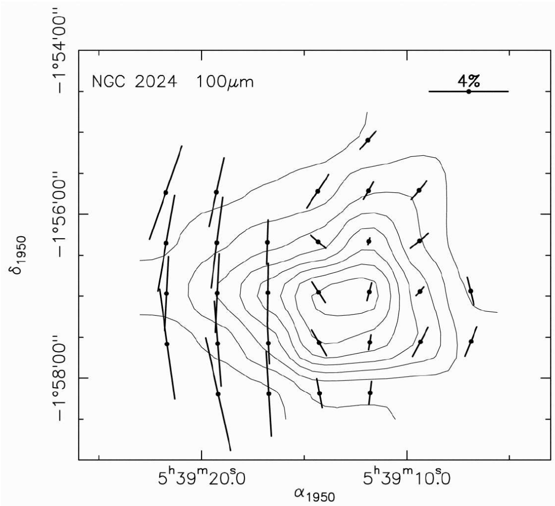

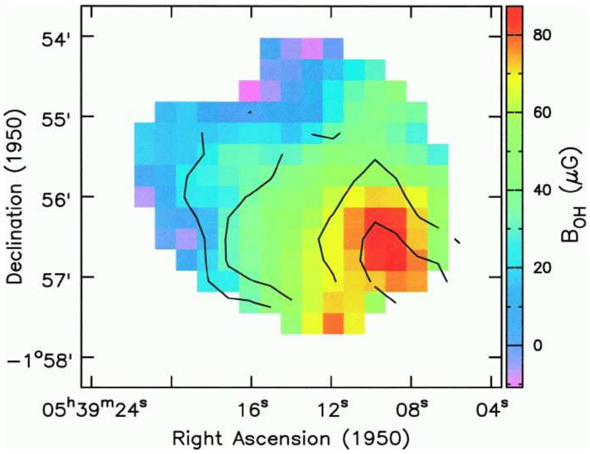

Figure 2.25: NGC 2024: Polarization and Zeeman Data
Left: The 100 μm map, produced as part of a compilation of all polarization data made with the Kuiper Airborne Observatory (Dotson et al. 2000), shows the NGC 2024 cloud core in Orion B. The flux contours range from 20% to 90% of the peak in steps of 10%. Some variation in the polarization position angles is observed across the core, but there is no evidence of the hourglass field geometry detected by Schleuning (1998) in OMC-1 of Orion A. *Right:* B_{los} toward the northern part of the NGC 2024 core, as measured by Zeeman splitting of OH at 18 cm (Crutcher et al. 1999).

Taurus, where it is a few percent. The observed rotation velocities within B1 are insufficient to support the cloud against collapse by a factor of ~ 8 (Bachiller et al. 1990). The ages of embedded but optically visible objects LkHα 327 and LkHα 328 are between 4-6 $\times 10^6$ yr (Cohen & Kuhi 1979). Based on this, Bachiller et al. (1990) conclude that another mechanism must be providing substantial support to this cloud.

The largest molecular core, referred to as the "main core" in the literature (see Figure 2.26), contains several peaks and has been observed for evidence of Zeeman splitting. In fact, B1 is one of the very few dark clouds to be detected in surveys for the Zeeman effect. The first published detection of Zeeman splitting in a dark cloud was within B1 (Goodman et al. 1989). A field strength of -27 ± 4 μG was measured

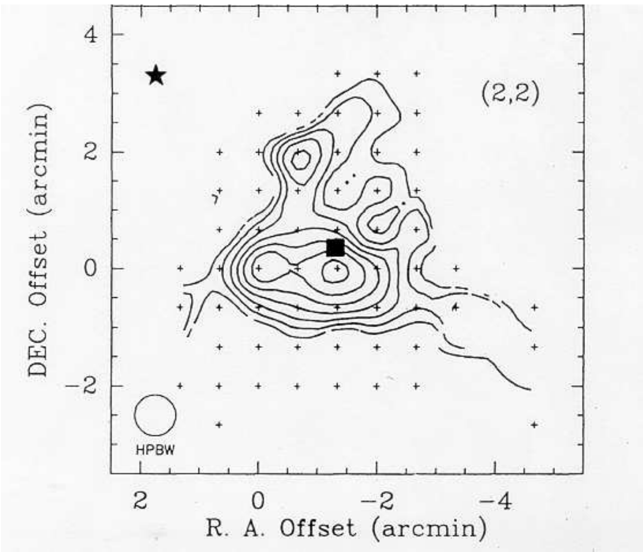

Figure 2.26: Ammonia Emission in the B1 Main Core
Ammonia emission from the B1 main core reveals several cores of molecular gas. The densities traced by the NH_3 (2,2) transition are high ($> 10^4$ cm^{-3}), and the cores identified in this transition are good candidates for dense, protostellar cores. The square marks the position of IRAS 03301+3057 and the star is the optically visible LkHα 327. This image has been reprinted from Bachiller et al. (1990).

toward the position of the bright molecular core coincident with IRAS 03301+3057 (Goodman et al. 1989). Two other detections were made in the cloud: -12 ± 5 μG was measured 4$'\!.$2 southwest of the IRAS source and -13 ± 6 μG was measured toward a fainter OH peak 12$'$ north of the IRAS source (see Goodman et al. 1990 and Crutcher et al. 1994). The negative sign indicates that the field is oriented toward the observer. A survey of 12 dark clouds for evidence of Zeeman splitting yielded only one solid detection – toward B1 – with the 140 ft. Green Bank Telescope (Crutcher et al. 1993). In that observation, toward the IRAS source 03301+3057, a field strength of -19 ± 4 μG was measured. These measurements are summarized in Figure 2.27.

In addition to the Zeeman data, polarization of background starlight from the Perseus cloud was measured by Goodman et al. (1990). Their map is presented in Figure 2.28. The distribution of polarization position angles measured is bimodal, with weaker vectors aligned along the cloud's projected major axis and stronger vec-

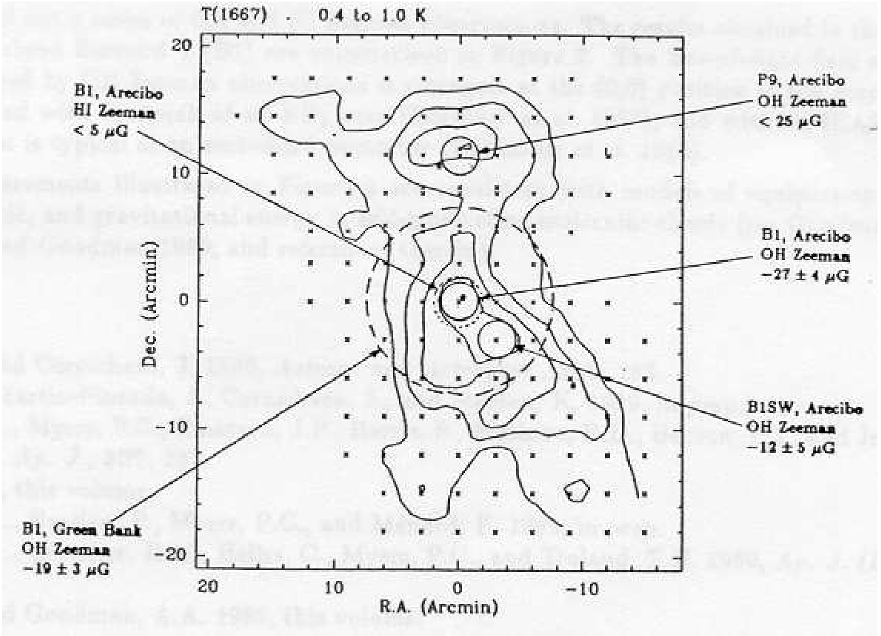

Figure 2.27: Zeeman splitting measurements toward the B1 main core Several detections of B_{los} have been made in B1. The measurements made with Arecibo are independent, while the Green Bank data sample a larger area owing to the smaller telescope dish. The HI data likely sample the field at the outer envelope of the cloud only. (reprinted from Goodman et al. (1990))

tors lying roughly perpendicular to the first population, as shown by the histogram of Figure 2.29. Goodman et al. (1990) hypothesized that two emitting clouds of differing magnetic field orientations could be superimposed along the line of sight. Previous evidence for a second gas cloud along the line of sight to Perseus and B1 at a distance of 200 pc were presented by Cernicharo et al. (1985).

Recently, some submillimetre and millimetre observations have been made toward the main core at the centre of Barnard 1. These data, obtained with SCUBA at the JCMT and the Nobeyama Millimetre Array, reveal a binary pair of sources which are likely protostellar based on their spectral energy distributions (Hirano et al. 1999). Most of B1 remains unobserved in dust continuum emission, and our polarization maps, discussed in Chapter 7 are the first toward this region.

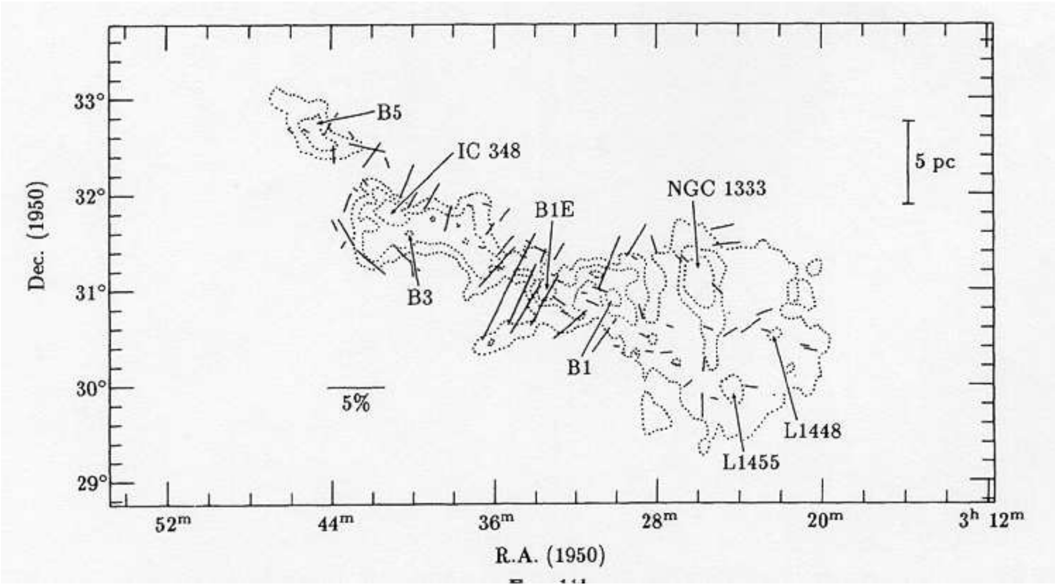

Figure 2.28: Optical Polarization in the Perseus Cloud Complex.
Taken from Goodman et al. (1990), this image shows the optical polarization data toward the whole Perseus complex. The polarization data are plotted over ^{13} CO $J = 1 - 0$ integrated intensity contours from Bachiller & Cernicharo (1986). The contours lie at 2, 6 and 10 K km s^{-1}. The length scale assumes a distance of 350 pc to the Perseus complex. Two distinct orientations of vectors are observed, one lying approximately parallel to the long axis of the complex; the other perpendicular to it.

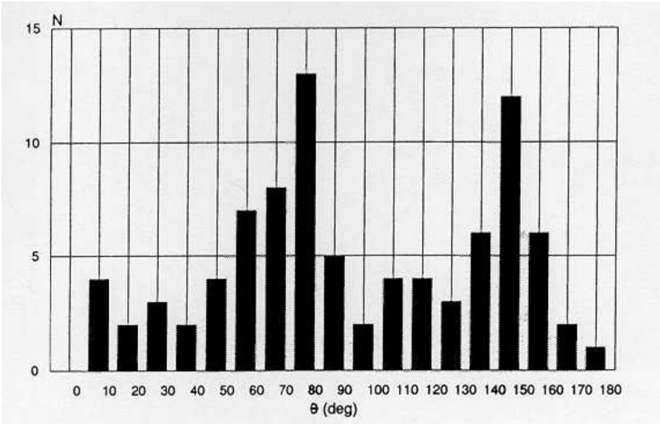

Figure 2.29: A Bimodal Distribution of θ in Perseus.
Two distinct populations of position angle are seen in the map of Figure 2.28. Gaussian fits were made to the populations above and below $\theta = 105°$ as discussed in the text. These data are interpreted as support for two different clouds lying along the line of sight to Perseus. (reprinted from Goodman et al. (1990))

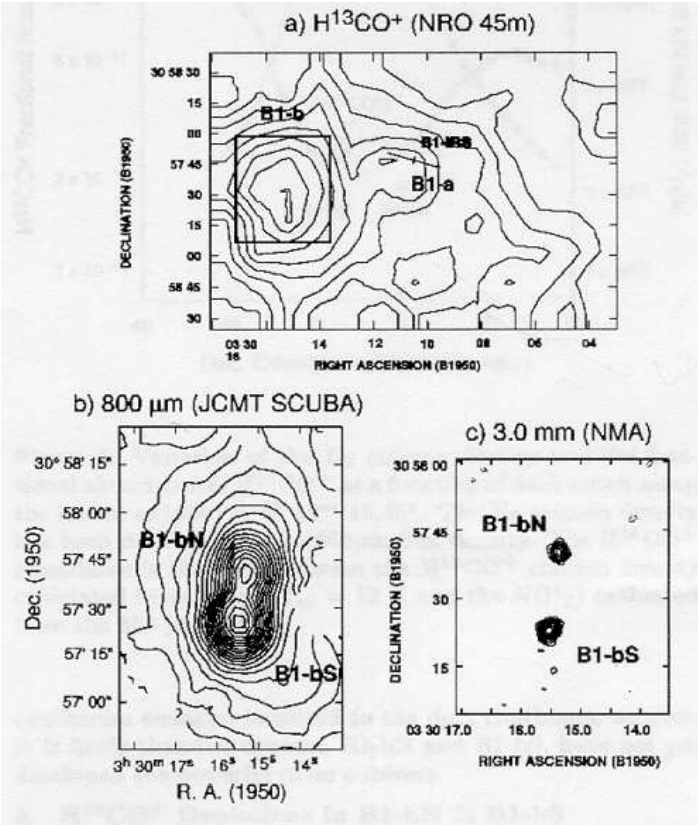

Figure 2.30: Submillimetre and Millimetre Observations toward the B1 main core

Molecular observations with the Nobeyama Radio Observatory identify several peaks in the B1 main core. Higher resolution data with SCUBA and then the Nobeyma Millimetre Array reveal dust condensations associated with the "B1-b" core. The resolved dust image at 3 mm reveals two distinct protostellar sources. (reprinted from Hirano et al. (1999))

Bibliography

Adams, W. S., 1941. *ApJ* **93**, 11.

Adams, W. S., 1943. *ApJ* **97**, 105.

Arce, H. G., Goodman, A. A., Bastien, P., Manset, N., & Sumner, M., 1998. *ApJ Letters* **499**, L93.

Bachiller, R. & Cernicharo, J., 1986. *A&A* **166**, 283.

Bachiller, R., del Rio Alvarez, S., & Menten, K. M., 1990. *A&A* **236**, 461.

Bally, J., 1989. The structure and kinematics of star forming clouds. In *Low Mass Star Formation and Pre-main Sequence Objects*, pp. 1.

Bally, J., Stark, A. A., Wilson, R. W., & Langer, W. D., 1987. *ApJ Letters* **312**, L45.

Basu, S., 2000. *ApJ Letters* **540**, L103.

Berkhuijsen, E. M., Brouw, W. N., Muller, C. A., & Tinbergen, J., 1964. *Bull. Astr. Inst. Netherlands* **17**, 465.

Bok, B. J., 1955. *AJ* **60**, 146.

Borgman, J. & Blaauw, A., 1964. *Bull. Astron. Inst. Netherlands* **17**, 358.

Breger, M., 1976. *ApJ* **204**, 789.

Carpenter, J. M., 2000. *AJ* **120**, 3139.

Carruthers, G. R., 1970. *ApJ Letters* **161**, L81.

Castets, A., Duvert, G., Dutrey, A., Bally, J., Langer, W. D., & Wilson, R. W., 1990. *A&A* **234**, 469.

Cernicharo, J., Bachiller, R., & Duvert, G., 1985. *A&A* **149**, 273.

Chini, R., Reipurth, B., Ward-Thompson, D., Bally, J., Nyman, L. ., Sievers, A., & Billawala, Y., 1997. *ApJ Letters* **474**, L135.

Cohen, M. & Kuhi, L. V., 1979. *ApJS* **41**, 743.

Coppin, K. E. K., Greaves, J. S., Jenness, T., & Holland, W. S., 2000. *A&A* **356**, 1031.

Crutcher, R. M., 1999. *ApJ* **520**, 706.

Crutcher, R. M., Mouschovias, T. C., Troland, T. H., & Ciolek, G. E., 1994. *ApJ* **427**, 839.

Crutcher, R. M., Roberts, D. A., Troland, T. H., & Goss, W. M., 1999. *ApJ* **515**, 275.

Crutcher, R. M., Troland, T. H., Goodman, A. A., Heiles, C., Kazes, I., & Myers, P. C., 1993. *ApJ* **407**, 175.

Crutcher, R. M., Troland, T. H., Lazareff, B., Paubert, G., & Kazès, I., 1999. *ApJ Letters* **514**, L121.

Cudlip, W., Furniss, I., King, K. J., & Jennings, R. E., 1982. *MNRAS* **200**, 1169.

Davis, L. J. & Greenstein, J. L., 1951. *ApJ* **114**, 206.

Dombrovsky, V. A., 1954. *Dokl. Akad. Nauk SSSR*.

Dotson, J. L., Davidson, J., Dowell, C. D., Schleuning, D. A., & Hildebrand, R. H., 2000. *ApJS* **128**, 335.

Douglas, A. E. & Herzberg, G., 1941. *ApJ* **94**, 381.

Draine, B. T. & Weingartner, J. C., 1996. *ApJ* **470**, 551.

Draine, B. T. & Weingartner, J. C., 1997. *ApJ* **480**, 633.

Dunham, T., 1937. *PASP* **49**, 26.

Elmegreen, B. G., 1985. Molecular clouds and star formation - an overview. In *Protostars and Planets II*, pp. 33–58.

Fiege, J. D. & Pudritz, R. E., 2000a. *MNRAS* **311**, 85.

Fiege, J. D. & Pudritz, R. E., 2000b. *ApJ* **544**, 830.

Flett, A. M. & Murray, A. G., 1991. *MNRAS* **249**, 4P.

Girart, J., Crutcher, R. M., & Rao, R., 1999. *ApJ Letters* **525**, L109.

Gold, T., 1952. *MNRAS* **112**, 215.

Goldsmith, P. F. & Langer, W. D., 1978. *ApJ* **222**, 881.

Goodman, A. A., Bastien, P., Menard, F., & Myers, P. C., 1990. *ApJ* **359**, 363.

Goodman, A. A., Crutcher, R. M., Heiles, C., Myers, P. C., & Troland, T. H., 1989. *ApJ Letters* **338**, L61.

Goodman, A. A., Jones, T. J., Lada, E. A., & Myers, P. C., 1995. *ApJ* **448**, 748.

Goodman, A. A., Myers, P. C., Bastien, P., Crutcher, R. M., Heiles, C., Kazes, I., & Troland, T. H., 1990. The magnetic field in the perseus molecular cloud complex. In *IAU Symp. 140: Galactic and Intergalactic Magnetic Fields*, Volume 140, pp. 319.

Greaves, J., Holland, W., Jenness, T., Moriarty-Schieven, G., Chrysostomou, A., Berry, D., Murray, A., Nartallo, R., Ade, P., Gannaway, F., Haynes, C., Tamura, M., Momose, M., & Morino, J., 2001. *MNRAS in preparation.*

Greaves, J. S., Murray, A. G., & Holland, W. S., 1994. *A&A* **284**, L19.

Hall, J. S., 1949. *Science* **109**, 166.

Harwit, M., 1970. *Nature* **226**, 61.

Heiles, C., 1987. Interstellar magnetic fields. In *ASSL Vol. 134: Interstellar Processes*, pp. 171.

Heiles, C., 1997. *ApJS* **111**, 245.

Hildebrand, R. H., 1988a. *Astrophysical Letters and Communications* **26**, 263.

Hildebrand, R. H., 1988b. *QJRAS* **29**, 327.

Hildebrand, R. H., Dragovan, M., & Novak, G., 1984. *ApJ Letters* **284**, L51.

Hiltner, W. A., 1949. *Science* **109**, 165.

Hiltner, W. A., 1951. *ApJ* **114**, 241.

Hirano, N., Kamazaki, T., Mikami, H., Ohashi, N., & Umemoto, T., 1999. Discovery of two extreme young protostars in barnard 1. In *Star Formation 1999, Proceedings of Star Formation 1999, held in Nagoya, Japan, June 21 - 25, 1999, Editor: T. Nakamoto, Nobeyama Radio Observatory, p. 181-182*, pp. 181.

Holland, W. S., Greaves, J. S., Ward-Thompson, D., & Andre, P., 1996. *A&A* **309**, 267.

Hollenbach, D. & Salpeter, E. E., 1971. *ApJ* **163**, 155.

Jefferts, K. B., Penzias, A. A., & Wilson, R. W., 1970. *ApJ Letters* **161**, L87.

Johnson, P. E., 1982. *Nature* **295**, 371.

Johnstone, D. & Bally, J., 1999. *ApJ Letters* **510**, L49.

Lada, C. J. & Wilking, B. A., 1984. *ApJ* **287**, 610.

Larson, R. B., 1981. *MNRAS* **194**, 809.

Lazarian, A., Goodman, A. A., & Myers, P. C., 1997. *ApJ* **490**, 273.

Leach, R. W., Clemens, D. P., Kane, B. D., & Barvainis, R., 1991. *ApJ* **370**, 257.

Levin, S. M., Langer, W. D., Kuiper, T. B. H., Velusamy, T., & Crutcher, R. M., 2000. Measuring the magnetic field strength in l1498 with zeeman splitting observations of ccs. In *American Astronomical Society Meeting*, Volume 197, pp. 1016.

Liseau, R., White, G. J., Larsson, B., Sidher, S., Olofsson, G., Kaas, A., Nordh, L., Caux, E., Lorenzetti, D., Molinari, S., Nisini, B., & Sibille, F., 1999. *A&A* **344**, 342.

Maddalena, R. J., Moscowitz, J., Thaddeus, P., & Morris, M., 1986. *ApJ* **303**, 375.

Manchester, R. N., 1974. *ApJ* **188**, 637.

Mayer, C. H., McCullough, T. P., & Sloanaker, R. M., 1957. *ApJ* **126**, 468.

McKellar, A., 1940. *PASP* **52**, 187.

Mizuno, A., Onishi, T., Yonekura, Y., Nagahama, T., Ogawa, H., & Fukui, Y., 1995. *ApJ Letters* **445**, L161.

Moneti, A., Helfer, H. L., McMillan, R. S., Perry, M. L., & Pipher, J. L., 1984. *ApJ* **282**, 508.

Murray, A. G., Nartallo, R., Haynes, C. V., Gannaway, F., & Ade, P. A. R., 1997. An imaging polarimeter for scuba. In *The Far Infrared and Submillimetre Universe.*, pp. 405.

Myers, P. C. & Goodman, A. A., 1988. *ApJ Letters* **326**, L27.

Padoan, P., Goodman, A., Draine, B., Juvela, M., Nordlund, A., & Rögnvaldsson, O., 2001. *ApJ submitted.*

Penzias, A. A., Solomon, P. M., Wilson, R. W., & Jefferts, K. B., 1971. *ApJ Letters* **168**, L53.

Purcell, E. M., 1979. *ApJ* **231**, 404.

Purcell, E. M. & Spitzer, L. J., 1971. *ApJ* **167**, 31.

Rao, R., Crutcher, R. M., Plambeck, R. L., & Wright, M. C. H., 1998. *ApJ Letters* **502**, L75.

Schleuning, D. A., 1998. *ApJ* **493**, 811.

Schleuning, D. A., Dowell, C. D., Hildebrand, R. H., Platt, S. R., & Novak, G., 1997. *PASP* **109**, 307.

Shu, F. H., Adams, F. C., & Lizano, S., 1987. *ARA&A* **25**, 23.

Spitzer, L., 1978. *Physical processes in the interstellar medium.* New York Wiley-Interscience, 1978. 333 p.

Spitzer, L. J. & Tukey, J. W., 1951. *ApJ* **114**, 187.

Swings, P. & Rosenfeld, L., 1937. *ApJ* **86**, 483.

Vazquez-Semadeni, E., Ostriker, E. C., Passot, T., Gammie, C. F., & Stone, J. M., 2000. Compressible mhd turbulence: Implications for molecular cloud and star formation. In *Protostars and Planets IV*, pp. 3.

Verschuur, G. L., 1968. *The Observatory* **88**, 15.

Vrba, F. J., Strom, S. E., & Strom, K. M., 1988. *AJ* **96**, 680.

Weintraub, D. A., Goodman, A. A., & Akeson, R. L., 2000. Polarized light from star-forming regions. In *Protostars and Planets IV*, pp. 247.

Wilking, B. A. & Lada, C. J., 1983. *ApJ* **274**, 698.

Wilson, R. W., Jefferts, K. B., & Penzias, A. A., 1970. *ApJ Letters* **161**, L43.

Chapter 3

The First Polarimetry of OMC-3 in Orion A

This chapter is a reprint of the article "Magnetic Fields in Star-Forming Molecular Clouds I. The First Polarimetry of OMC-3 in Orion A" by B.C. Matthews and C.D. Wilson, which was published in The Astrophysical Journal, volume 531 on 10 March 2000.

Abstract

The first polarimetric images of the OMC-3 region of the Orion A filamentary molecular cloud are presented. Using the new imaging polarimeter on SCUBA at the James Clerk Maxwell Telescope, we have detected polarized thermal emission at 850 μm from dust along a $6'$ length of the dense filament. The polarization pattern is highly ordered and is aligned with the long axis of the filament throughout most of the region, diverging only near the southern boundary by $30 - 50°$. If the polarization arises from thermal emission of dust grains aligned via either paramagnetic inclusions or radiative torques, this configuration indicates a plane-of-sky magnetic field which is normal to the filament along most of its length. The mean percentage polarization is 4.2% with a 1σ dispersion of 1%. This region is part of the integral-shaped filament, and active star formation is ongoing along its length, with only two of nine dust condensations in our field lacking evidence of outflow activity. The outflow directions do not appear to be consistently correlated with the direction of the plane-of-sky field or the filament structure itself. Depolarization toward the filament centre, previously detected in many other star-forming cores and protostars, is also evident in our data.

3.1 Introduction

It is now well established that magnetic fields play a significant role in the evolution of molecular clouds and their associated star formation (see Heiles et al. 1993 and references therein). At a distance of 500 pc, the Orion complex is the closest star forming region that is undergoing massive star formation, and as such, has been the object of intense study. Many studies have focused on the region known as OMC-1, a massive cloud core which lies behind the Orion Nebula (M42). This core is embedded in the integral-shaped filament, identified in the ^{13}CO $J = 1-0$ transition by Bally et al. (1987) and most recently mapped at 850 and 450 μm by Johnstone & Bally (1999). The OMC-3 region lies at the northern tip of the filament (Bally et al. 1987), near the HII region NGC 1977 (see Kutner et al. 1976). Molecular studies reveal the dust temperatures to be considerably cooler (T $\sim$ 20-25 K) in the OMC-3 region than in OMC-1 (Chini et al. 1997).

Dust condensations in OMC-3 were identified in 1.3 mm continuum by Chini et al. (1997). An evolutionary sequence has been suggested, with source ages declining as one moves north along the filament. Reipurth et al. (1999) have done a VLA search at 6 cm for compact sources in the region and report no sources coincident with the positions of MMS1 and MMS4, two of the most northern condensations identified by (Chini et al. 1997). Additionally, there is no outflow associated with either source (Yu et al. 1997; Chini et al. 1997; Castets & Langer 1995). These results suggest that these objects may in fact be in a pre-collapse phase, since outflows are known to be associated with the earliest phases of collapse (Shu et al. 1987).

Goodman et al. (1995) illustrated that measurements of polarization of background starlight in the optical and near-infrared are not effective tracers of magnetic field structure in dense molecular gas due to poor alignment and/or amorphous dust grain structure. At submillimetre and millimetre wavelengths, aligned, rotating grains produce polarized thermal emission. Draine & Weingartner (1996) and

Draine & Weingartner (1997) have shown that radiative torques are highly effective at aligning grains of specific sizes ($\sim$0.2 μm). Lazarian et al. (1997) suggest that the effects of radiative torques could be comparable to paramagnetic inclusions (Purcell 1975; Purcell 1979; Spitzer & McGlynn 1979) at aligning grains in the star-forming interstellar medium. Both these mechanisms result in grains aligned with their long axes perpendicular to the magnetic field.

In this paper, we present 850 μm imaging polarimetry of OMC-3. These data represent the first polarimetry of this active star-forming region and are also some of the first obtained with the new imaging polarimeter at the James Clerk Maxwell Telescope (JCMT). This is the first publication from a project designed to study magnetic field structure in a variety of molecular clouds in different phases of star formation. In §2, we describe the polarimeter and the observing and reduction techniques; in §3, a mosaic of OMC-3 is presented and discussed; §4 summarizes the results thus far.

3.2 Observations and Data Reduction

The observations were taken from 1998 September 5 to 7 using the new imaging polarimeter on SCUBA (Submillimetre Common User Bolometric Array) at the JCMT. These nights were stable, with τ(225 GHz) ranging from 0.05 to 0.07 during the period of observations. Calibration of the polarizer was performed on 1998 September 5 using the Crab Nebula, for which percentage polarization $p = 19.3\pm4\%$ and position angle $\theta = 155\pm\ 5°$ were measured.

The polarimeter consists of a rotating quartz half-waveplate and a fixed analyzer which are used to measure linear polarization of thermal emission. The waveplate introduces a phase-lag of one half wavelength between the plane of polarization along the 'fast axis' and the orthogonal plane. Rotation of the plate changes the angle between the fast axis and the plane of the incoming source polarization, so a varying component of the polarized emission is retarded. The analyzer is a photolithographically etched grid of 6 μm spacing which transmits only one plane of polarization (by absorbing photons with an **E**-component parallel to the wires) to SCUBA. The detector thus sees a modulated signal as the waveplate rotates. The variations are used to deduce the percentage polarization and polarization position angle of the source.

Seven pointing centres were observed along the OMC-3 filament, four the first night and only three (slightly shifted in position) on subsequent nights to provide better coverage of low signal-to-noise regions. Data for each pointing centre were co-added to create seven maps of I, $Q = q/I$ and $U = u/I$, where I, q and u are Stokes' parameters. Each polarization cycle consists of 16 integrations at 22.5° rotation intervals (i.e. 4 independent measurements at each angle) in 8 minutes integration time. The brightest source, MMS6, was observed for only 6 cycles, or 48 minutes integration time. Observations centred on MMS1 and MMS4 required $\sim$3 hours integration time. The sensitivity of the SCUBA detector yielded polarization measurements on sources of 0.5 Jy beam^{-1} at the 6σ level for 4% polarized flux.

For each polarization cycle map, the standard preliminary reduction was done. This included subtraction of sky levels as well as instrumental polarization (IP) for each bolometer. Polarizations less than 1% are unreliable, since the IP has been found to vary by $\pm$0.5% for about 30% of the bolometers. The average IP for all off-axis bolometers is $0.88 \pm 0.06\%$ @ 166$\pm$ 2° while the IP of the central bolometer is $1.08 \pm 0.10\%$ @ 158$\pm$ 3°. After correction for source rotation across the array, the Stokes' parameters were calculated by comparing measurements offset by 45° in waveplate rotation (90° on the sky). The I, Q and U maps for each pointing centre were averaged, and standard deviations were derived by comparing the individual data sets. The maps were then binned spatially by a factor of two to yield $6''$ (approximately half-beamwidth) sampling.

At this point, it was necessary to diverge from the standard reduction technique to make mosaics of the I, Q and U maps before calculating the percentage polarization p and position angle θ. Mosaicing was done using the MAKEMOS tool in Starlink's CCDPACK (a UK based software package). Variances were used to weight the overlapping data values, and variances were also generated for the map. The calculation of p (and its uncertainty) is given by:

$$p = \sqrt{Q^2 + U^2}; \quad dp = p^{-1}\sqrt{[dQ^2Q^2 + dU^2U^2]}. \tag{3.1}$$

A bias exists which tends to increase the p value, even when Q and U are consistent with $p = 0$, because p is forced to be positive. The polarization percentages were debiased according to the expression:

$$p_{db} = \sqrt{p^2 - dp^2}. \tag{3.2}$$

The position angle can then be calculated by the following relations:

$$\theta = 0.5\arctan(U/Q); \quad d\theta = 28.6^\circ/\sigma_p \tag{3.3}$$

where σ_p is the ratio p_{db}/dp.

The p_{db} values were then thresholded such that $p_{db} \leq 100\%$ and $\sigma_p \geq 2.5$. The position angles can of course take on any value, but we note that offsets of 180° cannot be distinguished in linear polarization.

3.3 Results

3.3.1 The Polarization Pattern

Figure 3.1 shows the OMC-3 filament in 850 μm continuum (coloured greyscale) overlaid with polarization vectors. Only vectors up to 20% are plotted on the figure;

27 vectors in total were omitted. The blue contours indicate where $\sigma_p = 6$ and $\sigma_p = 10$. By equation (3.3), the vectors enclosed by these contours have $d\theta \leq 5°$ and $d\theta \leq 3°$, respectively. No vectors have $\sigma_p < 2.5$, so no plotted vector has $d\theta > 12°$.

The polarization vectors are well-ordered along the filament with the best alignment in the northern region between the sources MMS1 and MMS6 (as identified by Chini et al. 1997, see Figure 3.1). Since the vectors show a high degree of ordering, it is tempting to think that they are uniform across the field. However, extraction of data subsets centred on each of the four "regions" indicated in Figure 3.1 illustrates that this is not the case. The distribution of θ in each region is fit by either 1 or 2 Gaussians by minimizing chi-squared. The position angle (mean and dispersion) of each of these Gaussians is noted on the figure, as well as the reduced chi-squared of each fit.

The dispersions in θ are relatively narrow, when compared with the sample presented in Myers & Goodman (1991) for 26 dark cloud regions. If a single gaussian is fit to every subregions' distribution (regardless of the goodness-of-fit), it is found that Regions A through D have dispersions of 8, 8, 9 and 12° respectively. Such low dispersions were identified only for dark clouds without clusters, i.e. less than 15 associated stars in 1 pc^2 (Myers & Goodman 1991), yet OMC-3 has condensation density of 135 pc^{-2} (taking 9 sources in a $6' \times 30''$ area). According to the Myers & Goodman model of uniform and non-uniform field components, this result implies either a low ratio of non-uniform to plane-of-sky uniform components of the magnetic field, or a low number of magnetic field correlation lengths along the line of sight. To implement their analysis fully will require measurement of the line-of-sight component of the magnetic field toward several positions in OMC-3.

It is interesting to compare the changes in the position angle of the filament on the sky with the change in orientation of the polarization vectors. The filament's

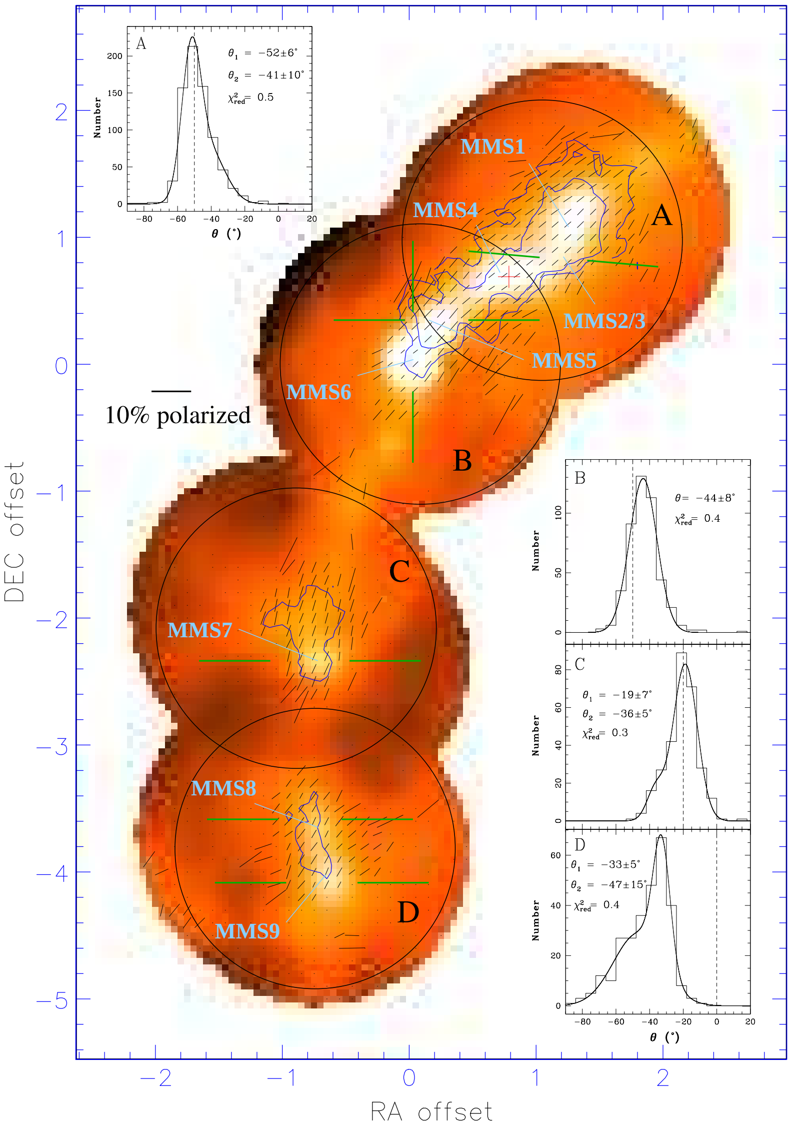

Figure 3.1: The Polarization Pattern of OMC-3

850 μm polarized emission along OMC-3. The coordinates are arcminute offsets from the position of MMS6, $\alpha_{1950} = 5^{\mathrm{h}}32^{\mathrm{m}}55.6^{\mathrm{s}}$ and $\delta_{1950} = -5°03'\,25''$. Colour greyscale indicates variations in uncalibrated I, with a range of -2 to 3 σ. Polarization vectors (to a maximum of 20%) are overlain. All vectors shown have $\sigma_p > 2.5$. Blue contours indicate bounds of $\sigma_p = 6$ and $\sigma_p = 10$ respectively. These bounds also indicate where $d\theta < 5°$ and $d\theta < 3°$ respectively. The condensations of Chini et al. (1997) are labelled MMS1 through MMS9, and outflow orientations are shown in green. The red cross shows the centre of the cut shown in Figure 3.2. Subregions, labelled A through D, are identified, and the distributions of position angle for each are shown in the histograms. Position angles are grouped to 6° bin widths. To test the form of the distributions, binning was also done with widths of 3° and 12°. The only cases in which the distributions were not consistent were Regions A and D with a 12° bin width. In these cases, the double Gaussian profile did not produce a fit to the data. Nevertheless, all single Gaussian fits for these two regions produced reduced chi-squared values > 1; hence, single Gaussians are poor fits to these distributions. The parameters of the fits are noted on each figure, as well as the reduced chi-square values. The dashed lines represent the mean position angle of the *filament* in each region.

orientation can be traced easily due to the positions of the condensations themselves, which without exception are embedded within it. Measuring an angle E of N, three main segments of OMC-3 can be distinguished. From MMS1 to MMS6, the filament is at an angle of $\sim 130°$ ($-50°$); this area is covered by Regions A and B as denoted on Figure 3.1. These histograms reveal that the peaks fit to these distributions agree with the position angle of the filament to within $10°$. The situation is similar for Region C, which contains MMS7, the only IRAS source in OMC-3 (05329−0505). The angle of the filament steepens from MMS6 to MMS7 to $\sim 160°$ ($-20°$). The distribution of θ exhibits two peaks in position angle. The strongest peak is in fact at $-19 \pm 7°$ which indicates excellent alignment with the filament. (The uncertainty represents the 1σ dispersion in the distribution.) However, a second peak exists at $-36 \pm 5°$. Finally, from MMS7 through MMS9, the filament aligns north-south (position angle $0°$). None of the polarization vectors exhibit such an angle; instead, the distribution is double peaked at $-33 \pm 5°$ and $-47 \pm 15°$. Since the maximum uncertainty associated with any value of θ is $12°$, Region D is the only one where no alignment exists between the filament and the polarization pattern.

In short, the polarization, and hence inferred field direction (in the plane of the sky), $B_\perp$, changes as one moves along OMC-3. $B_\perp$ is predominantly perpendicular to the filament along most of its length, diverging by $30 - 50°$ from the filament only in the southernmost part of OMC-3. These results are roughly consistent with the work of Schleuning (1998), which also established $B_\perp$ perpendicular to the filament direction in OMC-1. The field direction does not appear to be affected by the presence of the dust condensations, but rather is aligned with the structure of the filament itself. At a resolution of $15''$ (7500 A.U.), these data simply may not have enough resolution to detect the details of fields associated with the starless cores or protostellar envelopes and their associated outflows.

3.3.2 The Influence of Outflows?

Many previous works have noted that the inferred $B_\perp$ field direction from long wavelength polarization is oriented either parallel (e.g. IRAS 16293, Tamura et al. 1993; NGC 1333, Minchin et al. 1995; Tamura et al. 1995) or perpendicular (e.g. VLA 1623, Holland et al. 1996) to the observed protostellar outflow direction. The relative orientations of the outflows in OMC-3 are illustrated by the green lines on Figure 3.1, as measured by Chini et al. (1997) and Yu et al. (1997) using ^{12}CO $J = 2 - 1$ and H_2 shocks, respectively, to identify outflow signatures. With the exception of MMS6, the outflows are aligned E-W. Hence, in Regions A-C, the outflows are perpendicular neither to the filament nor the $B_\perp$-field. In Region D, they are aligned perpendicular to the filament, but are offset from $B_\perp$ by $\sim 30-50°$; however, it is possible that we may be detecting a superposition of the magnetic fields of the filament and the outflow(s). Reipurth et al. (1999) suggest that MMS9 is in fact the driving source for the most powerful outflow in the OMC-3 region. If the evolutionary sequence proposed by Chini et al. (1997) is correct, then MMS9's outflow may have had sufficient time to alter the magnetic field in its vicinity.

These results suggest that the field of the filament alone does not determine the outflow direction. Thus, there must be other relevant factors which determine the stucture of a protostellar system. Were these data interpreted as a uniform field along which material had collapsed, one would naively expect protostellar disks to be aligned parallel to the filament, and outflows perpendicular to it but aligned with the ambient field; however, this is not observed.

3.3.3 Percentage Polarization

The distribution of p_{db} along the filament exhibits a mean value of 4.2%, with a 1σ dispersion of 1%. Values up to 100% are allowed, but only those $< 20\%$ (i.e. all but 27) are plotted on Figure 3.1 since larger values are unlikely to be physical. The rms dp and σ_p values of unplotted data are 15% and 2.9, compared to 2.5% and 7.3 for all values of p with $\sigma_p > 2.5$. Polarizations up to 11.9% have been detected with $\sigma_p \sim 7$.

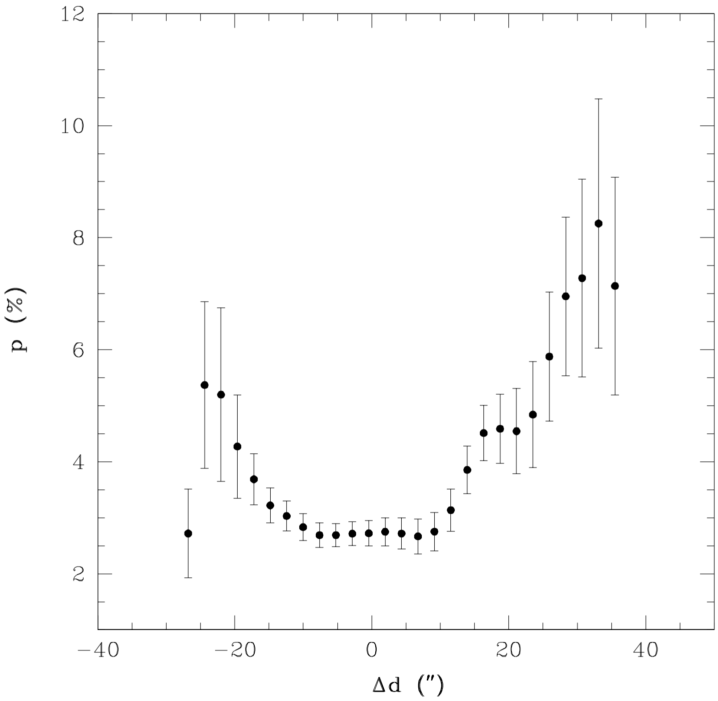

Figure 3.2: Depolarization Across the MMS4 core
Variation in p_{db} along a line perpendicular to the filament. These data are centred on $\alpha_{1950} = 5^{\mathrm{h}}32^{\mathrm{m}}52.5^{\mathrm{s}}$ and $\delta_{1950} = -5°02'\ 46''$, the position of the source MMS4 identified by Chini et al. (1997) and identified by the red cross in Figure 3.1. The cut is centred on MMS4, and Δd is the offset perpendicular to the filament. The plot clearly shows a reduction in polarization toward the centre of the filament. The error bars represent the uncertainty associated with each interpolated data point. The depolarization effect cannot be accounted for merely by the increasing noise in regions of low signal. Only data points with $\sigma_p > 2.5$ were used.

Several authors have discussed whether observations of decreased polarization percentage toward regions of higher flux are due to changes in physical conditions or averaging of small scale variations in a large beam. Figure 3.2 shows the percentage polarization along a cut perpendicular to the filament through MMS4 (indicated by the red cross in Figure 3.1), which has the highest σ_p in our data set. Although the uncertainties are increasing toward the edge of the filament, the data show a clear trend of decreasing polarization percentage toward the filament's centre. These changes could be due to changes in either grain properties or field strength, but they have also been suggested as an observable signature of helical fields (Fiege & Pudritz 2000). The interpretation of this depolarization effect will be discussed more fully in a forthcoming paper.

3.4 Summary

Submillimetre wavelength polarimetry with the JCMT has revealed a highly ordered polarization pattern along the filament known as OMC-3. These data indicate that $B_{\perp}$is perpendicular to the filament along most of its length, diverging only in the most southern regions by between $30 - 50°$. The outflows which have been observed in OMC-3 are aligned with neither the ambient field nor the filament in any consistent way. The field of the filament is thus unlikely to be the dominant factor in determining the configuration of the protostellar systems embedded within it. The mean percentage polarization is 4.2%, with a 1σ dispersion of 1%. Values as high as 11.9% have been measured with $\sigma_p \sim 7$. A depolarization effect is measured toward the denser parts of the filament.

The authors would like to thank J. Greaves, T. Jenness, G. Moriarty-Schieven and A. Chrysostomou at the JCMT for their assistance with problems both large and small during and especially after observing, and the referee for an insightful and thorough review. BCM would like to thank J. Fiege for many constructive conversations and MATLAB expertise. The research of BCM and CDW is supported through grants from the Natural Sciences and Engineering Research Council of Canada. The JCMT is operated by the Joint Astronomy Centre on behalf of the Particle Physics and Astronomy Research Council of the UK, the Netherlands Organization for Scientific Research, and the National Research Council of Canada.

Bibliography

Bally, J., Stark, A. A., Wilson, R. W., & Langer, W. D., 1987. *ApJ Letters* **312**, L45.

Castets, A. & Langer, W. D., 1995. *A&A* **294**, 835.

Chini, R., Reipurth, B., Ward-Thompson, D., Bally, J., Nyman, L. ., Sievers, A., & Billawala, Y., 1997. *ApJ Letters* **474**, L135.

Draine, B. T. & Weingartner, J. C., 1996. *ApJ* **470**, 551.

Draine, B. T. & Weingartner, J. C., 1997. *ApJ* **480**, 633.

Fiege, J. D. & Pudritz, R. E., 2000. *MNRAS* **311**, 85.

Goodman, A. A., Jones, T. J., Lada, E. A., & Myers, P. C., 1995. *ApJ* **448**, 748.

Heiles, C., Goodman, A. A., McKee, C. F., & Zweibel, E. G., 1993. Magnetic fields in star-forming regions - observations. In *Protostars and Planets III*, pp. 279.

Holland, W. S., Greaves, J. S., Ward-Thompson, D., & Andre, P., 1996. *A&A* **309**, 267.

Johnstone, D. & Bally, J., 1999. *ApJ Letters* **510**, L49.

Kutner, M. L., Evans, N. J., & Tucker, K. D., 1976. *ApJ* **209**, 452.

Lazarian, A., Goodman, A. A., & Myers, P. C., 1997. *ApJ* **490**, 273.

Minchin, N. R., Sandell, G., & Murray, A. G., 1995. *A&A* **293**, L61.

Myers, P. C. & Goodman, A. A., 1991. *ApJ* **373**, 509.

Purcell, E. M., 1975. pp. 155. The Dusty Universe.

Purcell, E. M., 1979. *ApJ* **231**, 404.

Reipurth, B., Rodríguez, L. F., & Chini, R., 1999. *AJ* **118**, 983.

Schleuning, D. A., 1998. *ApJ* **493**, 811.

Shu, F. H., Adams, F. C., & Lizano, S., 1987. *ARA&A* **25**, 23.

Spitzer, L. & McGlynn, T. A., 1979. *ApJ* **231**, 417.

Tamura, M., Hayashi, S. S., Yamashita, T., Duncan, W. D., & Hough, J. H., 1993. *ApJ Letters* **404**, L21.

Tamura, M., Hough, J. H., & Hayashi, S. S., 1995. *ApJ* **448**, 346.

Yu, K., Bally, J., & Devine, D., 1997. *ApJ Letters* **485**, L45.

Chapter 4

The Depolarization Effect in the OMC-3 Filament of Orion A

This chapter is a preprint of the article "Magnetic Fields in Star-Forming Molecular Clouds II. The Depolarization Effect in the OMC-3 Filament of Orion A" by B.C. Matthews, C.D. Wilson and J.D. Fiege which has been accepted for publication in The Astrophysical Journal. It is currently in press. This paper contains both observational and theoretical work. I wrote the proposals for this work, did the observing, and reduced and analyzed the data. J. Fiege contributed the theoretical models for a bent filament and two crossed filaments, as well as the cublic spline fitting routine used to fit the axis of the OMC-3 filament. The article was written by me, but I am grateful to both C. Wilson and J. Fiege for careful editing of the manuscript. In this chapter, our use of the term "uniform field" refers to a unidirectional, ordered field component, which would produce a unidirectional projected field on the plane of the sky and hence a polarization pattern in which all vectors lie at the same polarization angle.

Abstract

Polarized 850 μm thermal emission data of the region OMC-3 in the Orion A molecular cloud are presented. These data, taken in 1998 with the SCUBA polarimeter mounted on the James Clerk Maxwell Telescope, have been re-reduced using improved software. The polarization pattern is not suggestive of a uniform field structure local to OMC-3, nor does the orientation of the vectors align with existing polarimetry maps of the OMC-1 core $20'$ to the south. The depolarization toward

high intensity regions cannot be explained by uniform field geometry except in the presence of changing grain structure, which is most likely to occur in regions of high density or temperature (i.e. the embedded cores). The depolarization in fact occurs along the length of the filamentary structure of OMC-3 and is not limited to the vicinity of the bright cores. Such a polarization pattern is predicted by helical field models for filamentary clouds. Along $\sim 75\%$ of the filament's length, the polarization vectors correlate strongly with the filament axis, a signature of a toroidally dominated helical magnetic field; however, near the southern cores, the vectors are offset in direction by $90°$ from the gas structure of the Integral-shaped Filament, as traced by dust. We present three scenarios to explain the observed polarization pattern of OMC-3 in terms of a helical field geometry. A helical field which is toroidally dominated in the north and poloidally dominated in the south could wrap the filament. A criss-crossing of two filamentary structures could produce the observed offset in polarization vectors, or the filament could be bent into the plane of the sky. Qualitative models incorporating a helical field geometry are presented for each of the latter two cases.

4.1 Introduction

One of the outstanding questions in the study of star formation concerns the relative importance of magnetic fields in the formation and evolution of clouds, cores and finally protostars. Magnetic fields are thought to provide support against gravitational collapse on large scales, even regulating the filamentary structures observed within molecular clouds (e.g. Fiege & Pudritz 2000a; Carlqvist & Kristen 1997; Nakamura et al. 1993). The process of ambipolar diffusion has been proposed to regulate the collapse of dense cores to form protostars (see Shu, Adams, & Lizano 1987). However, some magnetic field must be retained within the protostellar system, since models predict that protostellar outflows are collimated by magnetic fields (e.g. Pudritz 1985; Uchida & Shibata 1985; Shu et al. 1994; Fiege & Henriksen 1996). Girart et al. (1999) present polarization observations of the CO $J = 2 - 1$ line from outflow of the NGC 1333 IRAS 4A which predict the same magnetic field direction as their dust polarimetry at 1.3 mm, at least very close to the outflow source. Further from the source, the outflow is not aligned with the inferred field direction, and this could be due to interaction between the field and outflow. Alignment between the outflow and the field of the outflow has been observed in NGC 2024 FIR 5 (Greaves, Holland, & Ward-Thompson 2001) using polarized spectral line observations. The most common method of estimating field strengths has been the detection of Zeeman splitting of atomic and molecular lines. Measurement of Zeeman splitting of the HI 21 cm line provides direct evidence for magnetic fields on very large scales in the Galaxy and in the envelopes of molecular cloud complexes such as Orion A (Heiles 1987). Similar observations with molecular species within dense cores has proven challenging, with detections toward only 15 cloud cores (Crutcher 1999). The sensitivity does not yet exist to measure the Zeeman effect in more tenous regions of molecular clouds, where the current generation of polarizers are beginning to probe.

Emission from aligned, spinning dust grains is anisotropic and hence polarized.

Polarization data reveal no direct information about the field strength, since the degree of polarization is dependent on other factors such as grain shape, composition, and degree of alignment. The degree of polarization is in essence a measure of how effectively the grains have been "sped up" (Hildebrand et al. 1999). Even in theories where the grain spin is induced by a mechanism other than the magnetic field, such as the radiation field (Draine & Weingartner 1996) or the production of H_2 on the grain surface (Purcell 1979), the magnetic field is expected to provide the alignment. Because of this, continuum polarization data are the principal means of probing the geometry of the magnetic field. Each individual dust grain produces polarized emission perpendicular to its local field direction. All polarization data probe only the plane-of-sky component of the three dimensional magnetic field (perhaps vexingly denoted $B_\perp$, or B_{pos}), but the polarization vectors measured may be either *parallel or perpendicular* to $B_\perp$, depending on whether the polarization data are due to absorption of background light by dust grains ($\lambda < 25$ μm), or thermal emission from the grains themselves ($\lambda > 25$ μm). Hildebrand (1988) contains a thorough review. At far-infrared and submillimetre wavelengths, dust emission is optically thin toward all but the densest cores. Therefore, observations represent the sum of polarizations contributed by all dust grains through the depth of the cloud along a line of sight.

Where field geometries are simple and the direction of the magnetic field does not vary through the cloud depth, the polarized emission detected is perpendicular to the mean magnetic field and the latter can be inferred simply by rotating the polarization vectors by 90°. If the field has a more complex, non-uniform geometry, then interpretation becomes more difficult. In such cases, it is best to compare directly the polarization maps with polarization patterns predicted from a physical model of a magnetized cloud. For example, the Integral-shaped Filament of Orion A is clearly filamentary, so core models are inappropriate. Fiege & Pudritz (2000a) present a model for a filamentary cloud in which a helical magnetic field threads the filament and plays an important role in determining the radial density structure. This model predicts an r^{-2} density profile, which has been observed in several clouds, including the Integral-shaped Filament (Johnstone & Bally 1999) and several clouds in Cygnus (Lada et al. 1999; Alves et al. 1999). Fiege & Pudritz (2000c) present predicted polarization patterns for cases in which the field is either poloidally or toroidally dominated.

Polarimeters aboard the Kuiper Airborne Observatory (KAO), at the Caltech Submillimeter Observatory (CSO) and the James Clerk Maxwell Telescope (JCMT) have detected far-infrared and submillimetre polarization toward many Galactic molecular clouds (Schleuning et al. 1997; Dowell et al. 1998; Schleuning 1998; Aitken et al. 2000; Coppin et al. 2000; Dotson et al. 2000; Matthews & Wilson 2000), although until recently, limitations on detector sensitivity restricted observations to bright and/or compact, usually massive, cores. Detections of polarized thermal emission from dust have now been made toward individual protostellar envelopes (Girart et al. 1999; Holland et al. 1996) and starless cores (Ward-Thompson et al. 2000). Dotson et al. (2000) contains a summary of all regions toward which polarized emission at 100 μm was detected with the KAO. Among these sources is OMC-1, a 2000 $M_\odot$ core embedded in the Orion A Integral-shaped Filament. These data, along with 350 μm data from the CSO's Hertz polarimeter, are presented by Schleuning (1998). The polarization pattern observed in OMC-1 has been interpreted as evidence for an hourglass magnetic field geometry, expected if the field is being dragged inward with the gas as the core collapses.

Matthews & Wilson (2000) (hereafter Paper I) presented submillimetre emission polarization data of OMC-3, a $6'$ portion of the Integral-shaped Filament of Orion A, located approximately $20'$ north of OMC-1. In this follow-up to Paper I, we present an improved polarimetry map as well as a broader discussion of the depolarization observed across the filament. Additionally, we present three possible explanations for the observed polarization pattern, two of which require extensions of the Fiege &

Pudritz (2000c) models. Each of these can potentially explain the $\sim 90°$ offset from the filament axis observed for polarization vectors near OMC-3's southern boundary in terms of magnetic field geometry. The observations and data reduction techniques are described in §4.2. The polarization data are analyzed in §4.3. The polarization pattern is interpreted in § 4.4, and § 4.5 contains a discussion and summary.

4.2 Observations and Data Reduction

Using the SCUPOL polarimeter on the SCUBA detector, 850 μm maps of polarized thermal emission from dust were obtained on 5 to 7 September 1998 at the James Clerk Maxwell Telescope[1]. The data set, polarimeter, and general reduction techniques are described in Paper I, Greaves et al. (2000), and Greaves et al. (2001). We have re-reduced the data appearing in Paper I using the Starlink software package POLPACK, designed specifically for polarization data obtained with bolometric arrays. The method of reduction remains consistent with our previous analysis, but the new software permits easier binning and filtering of data to extract a higher quality map. Additionally, noisy bolometers have been removed from the data and estimates of the instrumental polarization (IP) have been updated.

At 850 μm, the sky is highly variable on timescales of seconds. This variability must be measured and removed from the data. Chopping removes the effects of slow sky variability; however, fast variations remain in the data, requiring sky subtraction using array bolometers devoid of significant flux. Typically, we have used between one and four bolometers (less than the number used in the reduction of Paper I), depending on the filling factor of the emission across the detector array. It is very difficult to select sky bolometers based on jiggle map data, since bolometers which

[1]The JCMT is operated by the Joint Astronomy Centre on behalf of the Particle Physics and Astronomy Research Council of the UK, the Netherlands Organization for Scientific Research, and the National Research Council of Canada.

appear devoid of flux may in fact have negative fluxes if the chop position contained significant emission. This is highly probable in regions of extended emission such as OMC-3. To aid in the identification of bolometers for sky subtraction, we referred to the Johnstone & Bally (1999) scan maps to compare our source and chop position fluxes. If the difference between these two was approximately zero, the bolometers at those locations were candidates for use in sky subtraction. We note that this method will not be generally available in other regions where pre-existing scan maps may not exist. This method prompted us to exclude from sky subtraction some bolometers used in Paper I.

The methods of sky subtraction are discussed in detail in Jenness et al. (1998). Prior to sky subtraction, images were made to examine the flux in each bolometer, since bolometers used for sky subtraction should not have negative values (produced if one has chopped onto a location with significant flux, for example). If three bolometers are used, then the signal per second in those three bolometers is averaged and subtracted from each bolometer in the map. Clearly, one should be left with zero flux on average in the sky bolometers. If there is evidence that these bolometers were not completely empty, an estimate of the total flux removed from the map (by summing all the 1s removals) can be made and a fraction of that flux is added back into each bolometer such that the total flux is distributed equally over all 37 bolometers. This assures that the total flux in the map before sky subtraction is the same as after sky subtraction. In the re-reduction for this paper, the mean sky level was added back into the data for OMC-3, thereby avoiding a systematic overestimation of polarization percentage due to underestimates of the total intensity, I. For example, in Paper I, a bolometer which contains a flux almost one quarter that of the MMS8 peak was used for sky subtraction. In the extreme case where Q and U are unaffected by the sky removal, this implies that the polarization percentage would be overestimated by a factor of 1.3.

When dealing with extended sources, such as those in OMC-3, the observing technique of chopping from source to a reference position can produce systematic error, since the reference position may not be devoid of flux and may be polarized. Appendix 4A discusses the possible impact such a reference, or chop, position could have on the measured polarization vectors. We particularly want to investigate the so-called "depolarization effect" which refers to the trend, observed in many regions, of measuring lower polarization percentages at positions of high total intensity emission. However, we find that, rather than underestimating the "true" source polarization percentage at high intensity, in fact, chopping onto a region of polarized emission can produce a systematic increase in polarization percentage for regions of low intensity. The degree of increase varies depending on the ratios between the polarized and total fluxes at the reference and source positions. Such an effect would, of course, appear qualitatively identical to the observed "polarization holes". In the scenario we describe, the polarizations at high intensity are most representative of the correct polarization percentage in the source. Similarly, position angles can be adversely affected if the polarized emission from the source and reference positions are oriented differently. Thus, where chopping introduces systematic error, the most reliable polarization percentages and position angles will be observed toward the highest flux positions. For the OMC-3 data set, assuming the reference position is not significantly more polarized than the source, the analysis of Appendix 4A suggests that even in the faintest regions of the OMC-3 map, the maximum error in the position angles introduced by chopping should range from $10-20\%$. The slopes of log-log plots of polarization percentage versus intensity observed should not be steeper than -0.3.

As discussed above, the removal of sky noise is a critical part of reducing SCUBA polarimetry data. Appendix 4B contains a comparison of reductions with and without sky subtraction for different observations of the same region. Discrepant results are only obtained if no sky subtraction is performed. In fact, whereas non-sky subtracted data tend to show high uniformity in the polarization vectors across the image, the mean polarization position angle differs greatly from one observation to another toward the same region. Once sky subtraction is applied to each map, all the resultant polarization patterns show similar trends.

It is also instructive to subdivide the entire data set and compare one section to another to check for consistency within the data set. For OMC-3, there are a total of 69 individual polarization observations, basically centred on four different positions (see Table 4.1). We divided the data evenly, so that the S/N per area in the map is maintained across each subset (of 34 and 35 observations respectively). The sky conditions were extremely stable over all three nights, meaning differences in the optical depth should have minimal effects on the S/N of the maps. Polarization maps were then generated for each subset separately, binned to $12''$ and compared. Of the data vectors which had absolute uncertainties in polarization percentage, dp, less than 1.4% and signal-to-noise in polarization percentage, σ_p, greater than 4.2 (values consistent with uncertainties in $dp < 1\%$ and $\sigma_p > 6$ in the total map), there were 190 vectors in common between the maps. Appendix 4C contains maps of each subset of data. These maps illustrate that the same general polarization pattern is produced with each subset. Comparison of the percentage polarization data for the 190 vectors in common between the maps reveals that 70% of them show insignificant differences between each other (i.e. $(p_1 - p_2)/(dp_1 + dp_2) < 3$ where we have assumed the errors are correlated in estimating the upper limit on the uncertainty in the difference). The largest discrepencies are seen in the lower intensity regions.

The data presented in this work have lower noise than those in Paper I. Binning the data to $12''$ instead of $6''$ increases the signal-to-noise across the whole map by a factor of 2, since binning is executed in both dimensions. Data are not thresholded by an upper bound on polarization percentage as was done for Paper I. Instead, thresholding is done on total intensity, uncertainty in polarization percentage, and signal-to-noise of polarization percentage. Vectors with low polarization percentage

Pointing Centre		Chop Throw	Chop P.A.	Number of
R.A. (J2000)	Dec. (J2000)	($''$)	(E of N)	Times Observed
$05^h35^m19\overset{s}{.}3$	$-05°00'36\overset{''}{.}9$	150	30°	6
$05^h35^m18\overset{s}{.}2$	$-05°00'21\overset{''}{.}8$	150	30°	17
$05^h35^m23\overset{s}{.}5$	$-05°01'32\overset{''}{.}2$	150	100°	6
$05^h35^m26\overset{s}{.}5$	$-05°03'57\overset{''}{.}4$	150	100°	9
$05^h35^m27\overset{s}{.}5$	$-05°03'32\overset{''}{.}5$	150	90°	9
$05^h35^m26\overset{s}{.}5$	$-05°05'31\overset{''}{.}4$	150	65°	8
$05^h35^m27\overset{s}{.}5$	$-05°05'21\overset{''}{.}5$	150	65°	14

Table 4.1: Observing Parameters for Jiggle Mapping

are suspect due to uncertainties in IP values of $\pm 0.5\%$, as well as potential sidelobe contamination (see Greaves et al. 2001). For our regions, polarization percentages less than 0.5% are not believable due to sidelobe effects. Thus, to account for these two effects, we reject all vectors with polarization percentage less than 1%. The number of vectors presented in this work is less than that of Paper I, due to higher binning, but the data quality has increased so that we present polarization data toward regions of low total intensity, particularly between the cores MMS6 and MMS7. The mean polarization percentage in Paper I was 4.2%; the data presented here have a mean of 5.0%. This increase is due to the polarization vectors present in regions originally used for sky subtraction. Their high polarization percentages (particularly in the southern region) inflates the new average. We note that even the bolometers used for sky subtraction in this analysis could also contain polarized flux; however, we have utilized Appendix 4A to estimate the potential effects on our data to be minimal under certain assumptions about the relative polarizing power off and on the bright peaks.

The most substantial change in the polarization pattern from Paper I is in the southern region of the map. As Figure 4.1 shows, the vectors are on average $-30°$ shifted compared with Paper I. This shift is not exhibited in other regions of the map, and we performed several tests to eliminate potential sources of the shift.

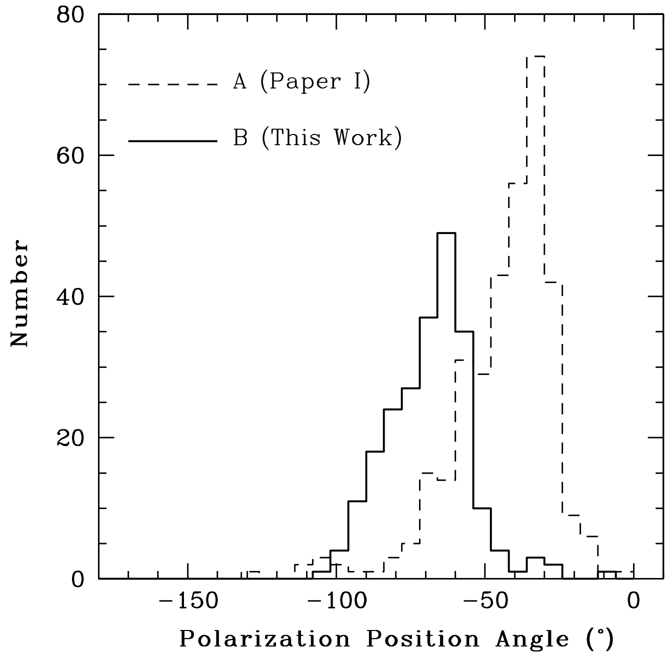

Figure 4.1: Comparison of position angle distributions in the MMS8-9 region. We show the distribution of position angles for the southern part of the OMC-3 map as presented in Paper I (distribution A) and this work (distribution B). Distribution A can be fit by two Gaussians of means $-33°$ and $-47°$ (with standard deviations of $5°$ and $15°$ respectively). Distribution B can be fit by two Gaussians of means $-63°$ and $-82°$ (with standard deviations of $7°$ and $9°$ respectively). The vectors are on average shifted by $-30°$ by the improved data reduction techniques of POLPACK. The effect is restricted to the MMS8-9 region.

Using the same bolometers as in Paper I, we still produce distribution B of Figure 4.1. We have also tested the effects of the addition of the mean sky flux level back into the map after the removal of sky noise, and the distribution remains unchanged. It is re-assuring that the distribution of vectors we present in this paper is robust against these changes in the reduction procedure and that sky subtraction in POLPACK is not producing the shift. The remaining substantive difference between the reductions we have run for this work and those of Paper I is the use of the POLPACK software itself. Since Paper I was published before POLPACK was available, the Paper I solution was the result of a "brute force" reduction, which used straight subtraction of fluxes at different waveplate positions to generate the Q and U Stokes' parameters. This method required substantial thresholding to remove data of poor quality and extract the polarization percentages and position angles. Generation of Q and U by subtraction meant that the expected sinusoidal dependence of the flux with waveplate position was not required. In POLPACK, the flux variations with waveplate positions are fit with a sinusoidal distribution and Q and U are extracted from the fit. This method also permits an internal estimation of errors by comparison of equivalent waveplate positions (i.e. $0, 90, 180$ and $270°$ waveplate positions all measure a position angle of $0°$ on the sky).

The southern region of OMC-3 is distinquished from the rest of the filament by the presence of extended emission of significant unpolarized intensity on either side of the filament. If the solutions for Q and U were under or over-estimated due to extreme values in some bolometers, and these were then used for sky subtraction, then this would explain the systematic shift in the vectors when comparing the results of Paper I and this work. It is not the specific bolometer used which affected the data, but how the Stokes' parameters were generated which led to the systematic shift. When POLPACK was used to generate Q and U, they were determined from a best fit to the predicted sinusoidal pattern, thus providing a much more sophisticated and robust means of extracting the polarization data. We are confident that the angles presented in this work are a correct representation of the polarization features in this region.

4.3 850 μm Polarization Data

4.3.1 A Non-Uniform Field across OMC-3

In Paper I, we presented maps of the distribution of position angle across four regions of OMC-3's filament. Based on Gaussian fits to those distributions, we showed that the position angles changed as one moved down the filament. In our re-reduced data set, shown in Figure 4.2, data are binned to 12$''$ sampling and bad bolometers have been removed, thereby increasing the signal-to-noise in all regions. The only significant difference is the shift of the southern vectors to more negative angles as discussed in § 4.2.

OMC-3 contains ten embedded cores as identified by Chini et al. (1997), some of which show evidence that protostellar collapse has already begun. However, the polarization pattern is not deflected by the presence of the dense cores, but is continuous along the filament, as is also observed in the ridge of cores in the NGC 2024 region of Orion B (Matthews, Fiege & Moriarty-Schieven 2001). This could suggest that the cores, which have presumably formed by the fragmentation of the filament, have preserved much of the highly ordered magnetic structure of the parent filament (Fiege & Pudritz 2000b). While this may be the case, it is also likely that, no matter what the field structure in the cores, the JCMT's 14$''$ beam is insufficient to resolve it, since the polarization pattern we observe appears to be dominated by the larger filamentary structure.

It is possible to quantify our argument that the polarization pattern traces primarily the filament, rather than the dense cores embedded within it. The filament's

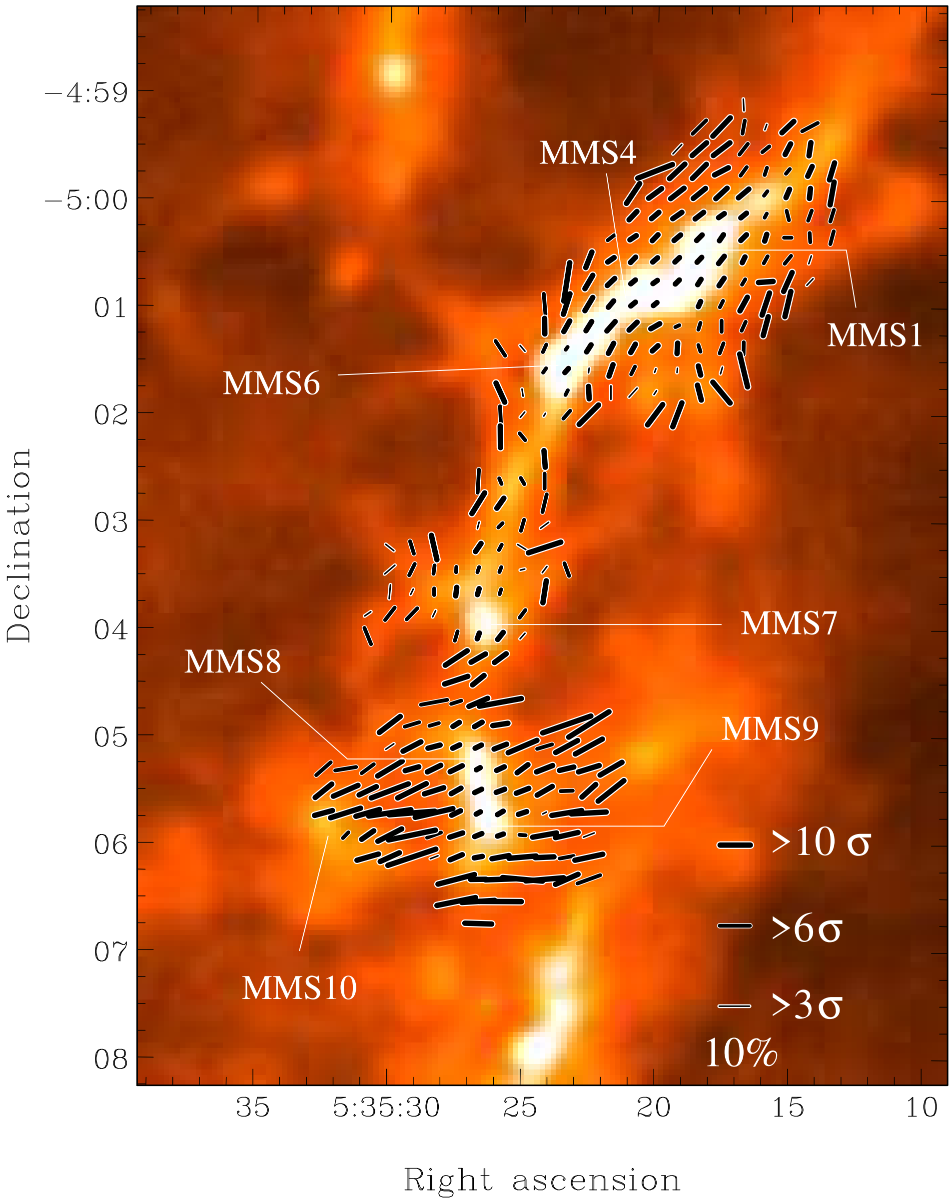

Figure 4.2: 850 μm polarization pattern across OMC-3.
A portion of the 850 μm intensity map of Johnstone & Bally (1999) is shown in coloured greyscale. The greyscale range is -1.5 to 3.5σ. The polarization mapping covers only a portion of the area shown. Polarization data were sampled at $3''$ and have been binned to $12''$ (slightly less than the JCMT 850 μm beamwidth of $14''$). The polarization vectors plotted all have percentage polarization $> 1\%$, an uncertainty in polarization percentage $< 1\%$ and a total intensity three times that of the sky bolometer level and $\sim 10\%$ of the faintest peak, MMS7. The thinnest vectors have a signal-to-noise in polarization percentage, $\sigma_p > 3$, while the medium thickness vectors have $\sigma_p > 6$. Most vectors are bold and have $\sigma_p > 10$. These vectors are accurate in position angle to better than 10°, 4.8° and 2.9°, respectively. The central region of MMS7 and the region south of MMS6 are devoid of vectors since the polarization percentages there are less than 1%. The mean polarization percentage of the plotted vectors is 5.0% in 286 vectors. The coordinates of the map are J2000.

axis was located by fitting a low order Chebyshev polynomial to the coordinates of the surface flux (or column) density maxima, equally spaced along the spine. A low order fit is desirable since the spine is then defined by a smooth curve which represents the global structure of the filament rather than responding in a noisy fashion to each small dense structure traced by dust. We then compared the orientation of each polarization vector with the *local* orientation of the filament. Orthogonal cuts at each position along the filament were made, and the position angle of the axis was compared to the position angles of polarization vectors lying along these radial cuts. Figure 4.3 presents histograms of the offset angles between polarization vectors and the filament orientation along its length. Along most of OMC-3, these distributions are centred on zero (although the FWHM are large). We fit Gaussians to these distributions and found mean offsets of 15°, 4° and 1° with σ of 26°, 21° and 29° for regions MMS1-4, MMS5-6 and the coreless-MMS7 regions respectively. South of MMS7, Figure 4.2 shows there is a shift in the vector orientation as the polarization pattern becomes increasingly misaligned with the fitted north-south spine of the filament. The distribution of offsets around MMS8 and MMS9 range from $\sim 60 - 90°$. A Gaussian fit to this distribution yields a mean offset of 86°. So, these vectors are virtually perpendicular to the filament.

Aside from the basic orientations of the polarization pattern discussed above, we note here that at the periphery of the detected polarization data, there are several locations in Figure 4.2 where the vectors appear to orient themselves along faint, extended dust structures. For example, south of MMS4 lie two small condensations of dust pointed southward. Note that the polarization data lie north-south in this region. Also, east of MMS6, a faint lane of dust extends to the north-east, toward the bright source at R.A. $05^{\rm h}35^{\rm m}29\overset{\rm s}{.}9$, DEC. $-04°58'52\overset{''}{.}7$ (J2000). The region surrounding MMS8 and MMS9 exhibits vector orientation aligned around $-70°$ (east of north). This is where the filament appears widest in OMC-3, with bright peaks at the east (MMS10, Chini et al. 1997) and west boundary of the polarization data.

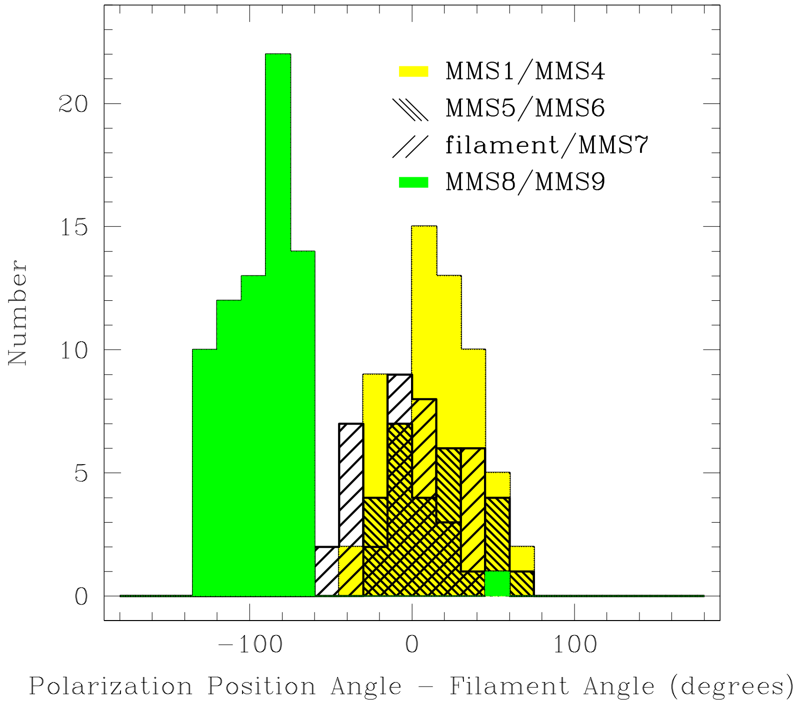

Figure 4.3: Filament-vector Offsets
The relative angles between the filament orientation and the position angles of polarization vectors (with $\sigma_p > 6$) along radial cuts to the filament are shown for four regions of the OMC-3 map. Only vectors with $\sigma_p > 6$ are used. The filament orientation is derived from a cubic spline fit to the intensity of OMC-3. For three of the four subregions, the offsets are centred around zero. For the region around MMS8 and MMS9, a Gaussian fit to this profile yields a mean and standard deviation of $-94° \pm 19°$.

The suggestion of alignment of polarization vectors with extended faint dust lanes and the data presented in Figure 4.3 for the region from MMS1 to MMS7 provide strong support for a correlation between the polarization pattern and dense gas as traced by dust in that part of the filament.

4.3.2 Depolarization Along the Filament Spine

Diminished polarization percentage toward bright peaks is routinely observed in extended massive cores, such as those of OMC-1 at 100 and 350 μm (Schleuning 1998) and even in interferometric maps of the protostellar source NGC 1333 IRAS4A

(Girart et al. 1999). In Paper I we briefly discussed the depolarization observed for a perpendicular cut across MMS4. We can now generalize this result for the whole OMC-3 region. Figure 4.4 plots the polarization percentage of vectors with $\sigma_p > 6$ versus the ratio of the intensity to the peak in the map where the intensities are estimated from the polarization data. This figure clearly shows that depolarization toward higher intensities is a general result in our data set. The same behavior is observed in three regions of Orion B (Matthews, Fiege, & Moriarty-Schieven 2001).

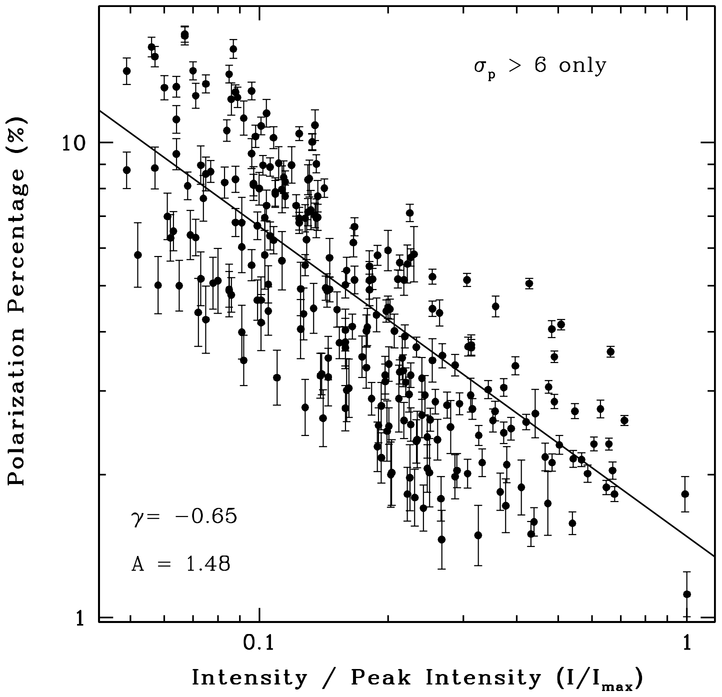

Figure 4.4: Polarization versus Intensity
A logarithmic plot of polarization percentage versus intensity (scaled by the maximum intensity point) reveals that higher intensities have systematically lower polarizations. Values plotted are those on Figure 4.2 which have $\sigma_p > 6$. The decreasing trend cannot be accounted for by the uncertainties shown here. A χ^2 power law fit of the form $p = A \times I^\gamma$ yields the A and γ parameters recorded on the log-log plot. A slope of -0.65 effectively characterizes these data.

Examination of Figure 4.4 raises the question of whether the diminished polarization could be a systematic effect at low values of total intensity. The polarization percentage, p, is derived from the Stokes' parameters Q and U where

$p = \sqrt{Q^2 + U^2}/I$. When I is small and $Q \propto I$ and $U \propto I$ are even smaller, noise effects can lead to gross overestimates of p. Systematic effects can also be introduced by significant polarization in the chop position, or reference beam, of the observation, or in the bolometers selected for sky subtraction (see Appendix 4A).

Figure 4.5 shows the depolarization toward the filament axis for regions containing bright cores as well as the coreless region between MMS6 and MMS7. These plots are generated using lines perpendicular to the fitted slope of the OMC-3 filament discussed in § 4.3.1. The polarization percentage versus (the magnitude of) the radial distance from the filament axis along these "radial cuts" are plotted. No interpolation is done; each plotted point is a true data point on Figure 4.2. Most of the cores (with the exception of MMS4) show increasing polarization at greater radial distances. The trend of declining polarization toward the axis is not limited to the bright cores embedded in the filament. Figure 4.5 shows that depolarization persists along the length of the filament spine, even in a region devoid of bright cores between MMS6 and MMS7. The depolarization becomes deeper as one moves southward, including the coreless region. The fact that depolarization is observed along the entire length of OMC-3 is further evidence that the polarization pattern is a feature of the filament itself and does not require the presence of dense, cold cores. Additionally, depolarization along the filament suggests that any model of the polarized emission from magnetized filamentary clouds must be able to explain the presence of depolarization toward the central axis.

Thus, we conclude that the depolarization effect is a feature of the filament, not the dense cores, although steeper depolarization may be observed near cores due to augmented effects of field tangling on scales smaller than the beam or more distinct grain changes. While the depolarization effect is a signature of a helical field, we do not suggest that field geometry is the sole means by which such an effect could be produced. Other factors which can produce a depolarization hole include systematic effects (i.e. chopping onto polarized emission as discussed in Appendix 4A),

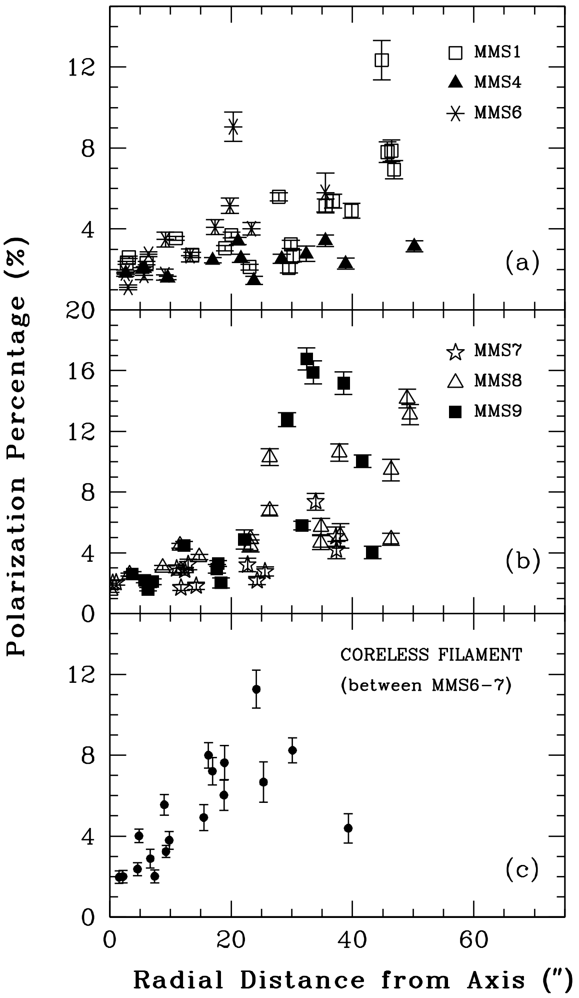

Figure 4.5: Polarization versus radial distance from the axis
Plots showing the polarization percentages as a function of radial distance from the filament axis toward different regions of OMC-3. Depolarization is exhibited toward the filament axis in all cases. Panels (a) and (b) show data around all six distinguishable cores. Panel (c) shows the coreless region between MMS6 and MMS7. The depolarization effect is particularly strong for MMS8 and MMS9. Only vectors with $\sigma_p > 6$ are used.

although we do not think the flux levels in these maps could reproduce the depth of depolarization we observe. One possible explanation could be that the grain physics is changing with proximity to the axis of the filament, i.e. with density or optical depth (Hildebrand et al. 1999). If the degree of alignment or spin rate changes with density, then the grains near the central axis could exhibit a lesser degree of polarization. At higher column densities, the grains could become more spherical through agglomeration processes, thereby rendering them unpolarizable. If these changes are present at the densities and temperatures characteristic of the centre of the filament, this too could explain, or at least contribute to, the depolarization effect.

4.3.3 Can Faraday Rotation Account for Depolarization?

Faraday rotation occurs if a linearly polarized wave encounters a plasma containing a magnetic field (i.e. the ISM). A linearly polarized wave can be decomposed into two circularly polarized waves of opposite orientations. These components propagate with different phase velocities in the plasma, if there is a component of the magnetic field along the line of sight. The net effect will be one of depolarization if the cloud is optically thin and field strength and electron densities are such that Faraday rotation is significant. Since thermal dust emission toward all molecular regions (with the exception of the central regions of dense collapsing cores) is optically thin, the net polarized emission measured by the telescope will be a sum over all emitting grains subject to different degrees of Faraday rotation depending on the different pathlengths through which they traveled through the cloud. Thus, vector addition of Faraday rotated emission from the far side of a cloud and virtually unaffected emission from the near side of the cloud could produce a net polarization vector of zero.

The plane of polarization of the linearly polarized wave rotates as it passes through the plasma by an amount:

$$\Delta\theta = RM\ \lambda^2 \qquad \text{radians} \tag{4.1}$$

where λ is the wavelength of the observation in meters and RM is the rotation measure, given by:

$$RM = (8.1 \times 10^5) \int n_e B_{||} dr \qquad \text{rad m}^{-2} \tag{4.2}$$

where $B_{||}$ is the magnetic field strength along the line of sight in Gauss; n_e is the number of elections per cm^{-3}; and $\int dr$ is the path length in parsecs (Kraus 1986). Although we cannot deduce a rotation measure from our data, it is useful to demonstrate that Faraday rotation has a negligible effect on the orientation of polarization vectors presented in Figure 4.2. The analysis can be broken into two parts: the possible effects of Faraday rotation in the ambient, diffuse ISM toward Orion; and within Orion A itself.

In the former case, we can derive $\Delta\theta$ at 850 μm by using the median value deduced from 81 extra-galactic sources at the high-longitude boundaries of the Canadian Galactic Plane Survey at 21 cm. For the vast majority of these sources, RM values between -400 and 50 rad m^{-2} have been measured, with a median value of -163 rad m^{-2} (Brown 2001). For $\lambda = 850$ μm, this RM implies an angular change of -1.2×10^{-4} rad or $-0.007°$ of rotation along the whole line of sight through the Galaxy. Thus, any rotation effects of the ISM between the Sun and Orion, a mere 500 pc away, are negligible.

Within the Orion A cloud, an estimate of Faraday rotation is more difficult to deduce. Measurements have been made of the field strength toward the dense (10^6 cm^{-3}) CN core of OMC-1 of $B_{||} = -0.36 \pm 0.08$ mG (Crutcher et al. 1999). Since the CN measurements sample gas up to 100 times denser than that sampled on large scales along OMC-3 at 850 μm, it is unlikely that the field strengths local to the gas sampled by our data would exceed 35 μG at 10^4 cm^{-3}. Assuming an ionization fraction of 10^{-4} (i.e. Ungerechts et al. 1997), implies that $n_e \approx 1$ cm^{-3} local to the gas sampled by the JCMT. At its widest point, the filament in OMC-3 is approximately 225$''$ which corresponds to 0.5 pc. If its depth is of comparable scale, and if $B_{||}$ and n_e are assumed to be constant, equation (4.2) yields $RM = 14$ rad m^{-2} within the OMC-3 filament. Since the OMC-3 filament is clearly denser than the ambient molecular region around it, we assume it would be the strongest source of Faraday rotation, having higher n_e and $B_{||}$ values than its surroundings. Substitution in equation (4.1) yields $\Delta\theta = 6 \times 10^{-4}$ degrees of rotation for the polarimetric angle through OMC-3. In regions denser than 10^4 cm^{-3}, rotation would be proportionally higher, although the depth (dr) of such regions would become progressively smaller. Hence we conclude that the effects of Faraday rotation cannot be responsible for the depolarization effect observed in OMC-3.

4.4 Interpreting the Polarization Pattern

As we concluded in Paper I, the re-reduction of data toward OMC-3 reveals no evidence for the presence of a uniform field on large scales across the filament since there are two distinct subsets of data – one aligned with and one orthogonal to the filament. Our analysis shows that along $\sim$ 75% of the OMC-3's projected length, the polarization pattern follows the orientation of the filament, becoming misaligned only south of MMS7. Further analysis reveals that the depolarization effect toward OMC-3 is a global feature of the region, existing along the entire length of the spine. Therefore, any theoretical models for this filament should support variations in field geometry and explain the depolarization effect in the absence of embedded cores.

In the far-infrared and submillimetre regimes, theoretical modelling of dust grains suggests that each grain along a line of sight contributes thermal radiation polarized perpendicular to the local direction of the magnetic field in the plane of the sky (Hildebrand 1988). As a result, polarimetry observations have often been interpreted by rotating the observed electric field vector orientations by 90° to estimate the magnetic field direction. However, since magnetic fields are inherently three dimensional, there may exist different configurations which can produce similar two dimensional polarization patterns. Since models of magnetized filamentary clouds are now available (Fiege & Pudritz 2000a; Carlqvist & Kristen 1997; Nakamura et al. 1993), a reasonable approach is to vary magnetic field parameters in a model and then generate the expected polarization pattern to compare to observations (Fiege & Pudritz 2000c). Note that the Fiege & Pudritz model employs an axisymmetric magnetic field, so that the field is helical in general. However, their model is also consistent with filaments threaded by purely poloidal fields, although such a geometry is not supported by this data set (see §4.5).

Some basic successes of the Fiege & Pudritz model include its prediction of an r^{-2} density profile for filaments, which has been observed in Orion A (Johnstone & Bally 1999) and two dark clouds in Cygnus (Alves et al. 1999; Lada et al. 1999). The model also predicts that the depolarization observed along the axis of the filament is a natural result of the helical field geometry and does not rely on poorly polarizing or poorly aligned grains at high optical depths although the field geometry certainly does not preclude the existence of such effects. The basic idea is that polarization contributions from the poloidally dominated axis of the filament partially cancel the contributions from the toroidally dominated envelope. The cancellation is greatest along the axis, creating the depolarization observed. However, we note that poorly polarizing or unaligned grains could act in concert with the helical field to amplify the depolarization.

The northern region of OMC-3 bears a strong resemblance to the inner regions of the Type 1 models of Fiege & Pudritz (2000c), for which $B_{z,S}/B_{\phi,S}$, the ratio of the poloidal to toroidal field components at the surface of the filament, ≤ 0.1. Note that B_z/B_ϕ is at a minimum at the surface of the filament and is typically

> 1 in the central regions. The models presented in Fiege & Pudritz (2000c) use a maximum polarization percentage of 10%, on the order of what we observe in OMC-3 and in three regions of Orion B (Matthews et al. 2001). Also, the width of the expected polarization hole predicted by the Fiege & Pudritz (2000c) model varies with $B_{z,S}/B_{\phi,S}$, increasing as a function of filament diameter as the relative poloidal strength increases. According to these models, the ratio of the width of the polarization hole to the filament diameter should be 0.5 or less for Type 1 filaments. Therefore, more sensitive measurements with longer chop throws (or no chopping at all) should detect a decline in polarization percentage at larger radial distances from the filament, if there is no significantly magnetized medium external to the filament. The only region where this effect is suggested by our data is between MMS6 and MMS7. Figure 4.5c shows depolarization toward the axis and a single vector of declining polarization percentage at approximately 35$''$ from the axis. Figure 4.2 shows that there are smaller polarizations below the $\sigma_p = 6$ level, but these are not preferentially further from the filament than those of Figure 4.5c.

Polarization vectors perpendicular to the filament axis are predicted for poloidally dominated field patterns (see Fig. 1 of Fiege & Pudritz 2000c). For filaments symmetric about a central axis, only vectors parallel or perpendicular to filament axes are expected (Fiege & Pudritz 2000c). Paper I reported a misalignment of the polarization vector position angles of 35° - 47° near MMS8 and MMS9 from the estimated filament orientation of 0° (east of north). Re-reduction and direct fitting of the filament spine yields a new estimate of 86° as the difference between the position angles of the vectors and the orientation of the filament in this region (see § 4.3.1). The fact that this misalignment occurs within the boundaries of a single SCUBA field of view raises concern that a systematic effect in observing technique could be producing these vectors. In Appendix 4A, it is shown that flux in the reference position can have detrimental effects on the measured polarization percentage and position angle. However, even in extreme cases of significant polarized flux in the reference position, errors of 90° in position angle can only be produced for observed intensities close to zero and are extremely unlikely unless the polarization percentage in the reference position exceeds that of the source. Thus, it is unlikely that this source of systematic error is responsible for the polarization angles observed.

Fiege & Pudritz (2000c) consider both toroidally and poloidally dominated field geometries. In the northern part of OMC-3, the alignment of the polarization vectors along the filament agrees well with the predictions for a toroidally dominated field geometry. However, a poloidally dominated field is expected to produce a polarization pattern offset by 90° in position angle from the filament axis. The poloidally dominated pattern thus predicts the position angles observed in the southern part of OMC-3. However, there are several marked differences between the predicted poloidally-dominated pattern and the observed vectors. The predicted pattern has a local maximum in polarization percentage along the axis, with two symmetric depolarization holes on either side (c.f. Fig. 1 of Fiege & Pudritz 2000c). The polarization is then seen to rise again at larger radii from the axis. However, Figure 4.5b does not exhibit this behavior. The lowest values of polarization percentage measured are along the axis, just as in the rest of OMC-3. The cores to the east and west and the widening of the filament here makes this area difficult to model. Further study of this portion of the OMC-3 region with a larger spatial scale map should provide more insight into the possibility that this region is poloidally, rather than toroidally, dominated.

Models invoking a purely poloidal magnetic field geometry aligned with the axis cannot be reconciled with the polarization pattern along the northern part of OMC-3. Additionally, an r^{-4} profile is predicted by the classic unmagnetized, isothermal filament of Ostriker (1964). In fact, it can be shown that all isothermal models limited to poloidal field geometries and constant flux-to-mass loading along the field lines produce density gradients steeper than r^{-4}. In the Integral-shaped Filament, Johnstone & Bally (1999) measure a profile of r^{-2} as predicted for a helical field geometry.

When the vectors are overlain on the total intensity maps generated from the polarization data (the sum of the maps obtained for each waveplate position), the extent of the maps is limited to the SCUBA fields observed with the polarimeter (c.f. Fig. 1 in Paper I). However, larger scale 850 μm scan maps of this region (Johnstone & Bally 1999) allow us to place the polarization data in a broader context since they can be compared to larger scale dust features of the region. Close examination of the greyscale intensity of Figure 4.2 suggests two possible explanations for the observed 90° offset of the polarization vectors from the filament in the southern region of OMC-3. The dust emission becomes very extended and diffuse around MMS8-9. The continuum source MMS10 also lies to the east of the Integral-shaped Filament. A second (un-named) peak could lie to the west of MMS8. These bright sources, coupled with the extended low intensity emission, suggest that a second filamentary structure, nearly orthogonal to the main filament, could be present. In this case, the polarization vectors are in fact aligned with a filament axis, but not that of the Integral-shaped Filament. Figure 4.6 shows a qualitative illustration of the effect of crossed filaments, both of which are threaded by helical fields. The second filament has half the central density of the main filament, which runs roughly north to south. The filaments intersect only in projection in this model; at the projected overlap, the vectors align with the second (east-west) filament. The Fiege & Pudritz (2000c) model defines three free parameters. The first is a concentration parameter, C, given by $C = log(r/r_0)$ where r is the radius and r_0 is the core radius within which the density profile is flat. The core radius is given by $r_0 = \sigma(4\pi G\rho_c)^{-0.5}$ where σ is the one-dimensional line width, G is the gravitational constant and ρ_c is the central density. Both filaments have a concentration parameter, C, of 1.2, and dimensionless flux-to-mass loading parameters of $\Gamma_z = 13$ and $\Gamma_\phi = 18$ (as defined in Fiege & Pudritz (2000c)).

If a second filament is present, its effects on the polarization pattern should

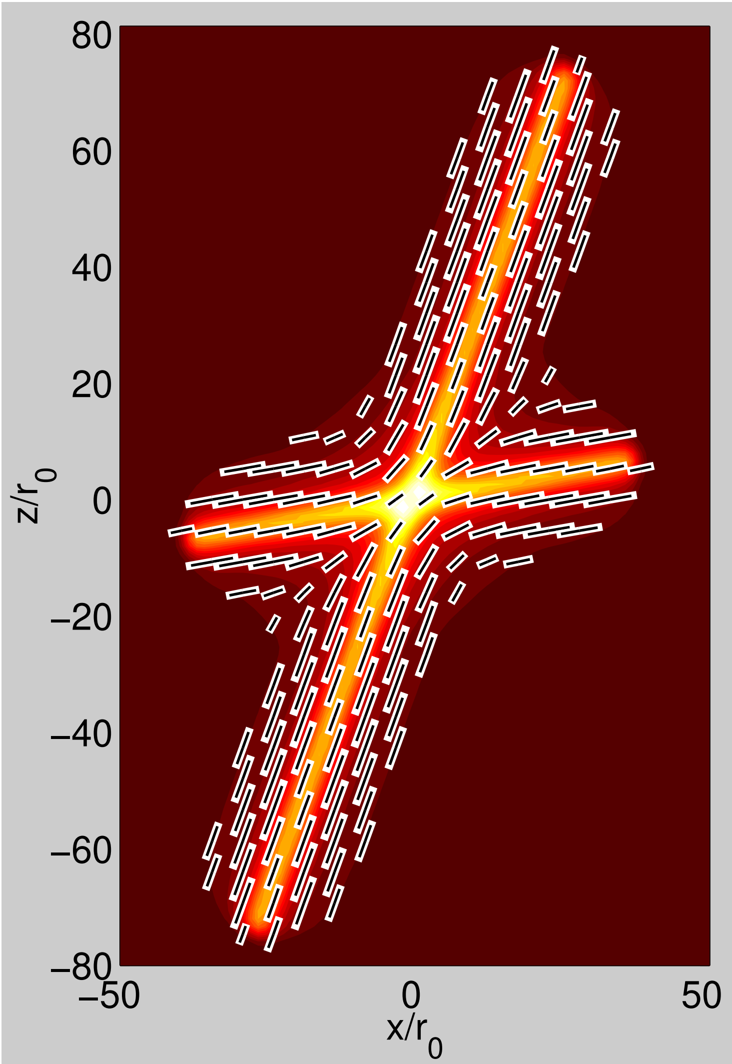

Figure 4.6: Model of Crossed Filaments
A qualitative model of the polarization pattern produced by a crossing of two filaments threaded by helical magnetic fields. The second (roughly east-west) filament has only half the central density of the main filament, which is meant to represent the Integral-shaped Filament. Both filaments lie in the plane of the sky. The model has been convolved with a Gaussian where the beamsize is one fifth the filament diameter. Vectors shown have $p > 0.05p_{max}$ and $I > 0.05I_{max}$ where $p_{max} = 10\%$.

obviously be limited to its width. This means that more extensive polarization observations south into OMC-2 should show re-alignment with the Integral-shaped Filament. The second filament also appears to extend in total intensity beyond the polarization data of Figure 4.2 to the northwest and southeast. Extended polarization data in these regions should reveal polarization data well-aligned with this faint dust emission, if two crossed filaments are present. Continued alignment with the dust structures will provide further evidence that the field orientation is related to the dense gaseous structures, either because the magnetic field has guided the condensation of gas, or because the gas has dragged in the magnetic field as the filament formed.

A second possibility is that the Integral-shaped Filament is the only filament present, but that it is bent (and thus changes inclination) south of MMS7. As discussed above, the northern region agrees well with the Type 1 models of Fiege & Pudritz (2000c) for a filament in the plane of the sky. However, even inclination of such models out of the plane of the sky is not expected to produce position angles other than 0° or 90° on the sky. If the filament were bent, however, then the cylindrical symmetry would be broken, and different position angles can result. This effect is easily considered qualitatively in terms of a wrapping cylindrical shape, such as a slinky, where the slinky represents magnetic field lines at a particular radius where the field is toroidally dominated. Consider what happens to the B_ϕ loops when you bend the slinky: they are compressed on the inside of the bend and pulled apart on the outside. Due to concentration of the magnetic field, the inside part dominates, breaking the front-back symmetry in the straight filament models and causing the vectors to turn in the direction orthogonal to the field in the inner part of the bend. One can thus consider the effect on an observed polarization pattern in projection. As long as there is cylindrical symmetry, vectors in front of and behind the axis can be paired and will sum to either 0° or 90°. However, once bends are introduced, then the components of the vectors in the plane of the sky can be very different on either side of the filament axis, and the projected vectors cannot be paired. In this scenario, vector sums through the cloud may take on any value. Figure 4.7 shows an example of such a model, where we self-consistently bend both the filament and the helical field using a Lagrangian formulation of the induction equation in the limit of perfect MHD. A full description of our technique will be presented in a forthcoming publication. As for the crossed filament model discussed above, this model filament has a concentration parameter, C, of 1.2, and dimensionless flux-to-mass loading parameters of $\Gamma_z = 13$ and $\Gamma_\phi = 18$ (see Fiege & Pudritz (2000c)).

4.5 Discussion

We have re-reduced the Matthews & Wilson (2000) 850 μm polarization data of the OMC-3 filament in Orion A, a region exhibiting strong filamentary structure and undergoing active star formation. Polarization observations are the key to revealing the presence of ordered magnetic fields in star-forming regions and determining whether their geometry is correlated with regions of high gas densities, as traced by dust. In OMC-3, we observe strong alignment between the polarization data and the orientation of the filamentary dense gas in the north, regardless of where embedded cores are located. Near the edges of our polarization data set, vectors appear to rotate to coincide with the orientations of faint structures of lower densities as illustrated in a larger scale intensity map of Johnstone & Bally (1999). Near the southern part of OMC-3, the vectors rapidly shift orientation, becoming almost orthogonal to the orientation of the bright Integral-shaped Filament, which could indicate the presence of a poloidally dominated field there.

Optical absorption polarization data on the periphery of the Lynds 1641 cloud (Vrba, Strom, & Strom 1988) and in M42 (Breger 1976) reveal a net polarization direction of 120°. In the case of a uniform field, we would thus have expected emission

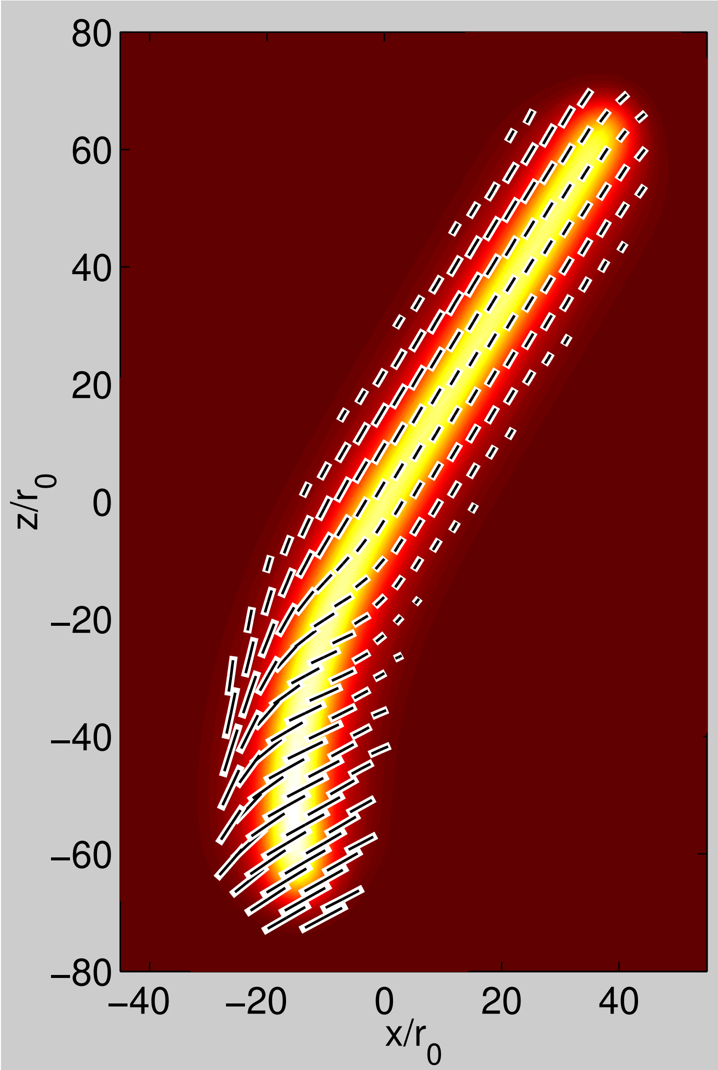

Figure 4.7: Model of a Bent Filament

A qualitative model of the polarization pattern produced by a magnetized filamentary cloud where the southern half of the filament has been bent into an arc with a radius of curvature of 6.4 times the filament's diameter. The whole filament is inclined to the plane of the sky at an angle of 20° and then rotated in the plane of the sky by 225°. The model is convolved with the same Gaussian beam as Figure 4.6, and the constraints on the vectors displayed are identical. The bending of the filament breaks the symmetry of the models presented in Fiege & Pudritz (2000c) causing the polarization pattern from the inner region of the bend to dominate, as discussed in the text.

polarization data to present vectors oriented at a position angle of $\sim 30°$ (since absorption and emission polarimetry should be orthogonal if they trace the same field geometry). The 100 and 350 μm data of OMC-1, located $20'$ further south along the Integral-shaped Filament from OMC-3, exhibit a polarization pattern with a mean direction of approximately 30° east of north (Schleuning 1998). These data were interpreted as support for a uniform field with position angle 120° (east of north) throughout the whole Orion A cloud. However, none of the vectors in OMC-3 suggest such a field geometry. Although the polarization data in the northern part of OMC-3 vary smoothly, they are not aligned with the data of OMC-1 nor the large scale optical data. In fact, the polarization orientations differ by $70 - 80°$. Furthermore, the southern part of OMC-3 shows an abrupt change in polarization orientation, which is not easily explained by a uniform field. Changing vector orientations (i.e. south of MMS7) could indicate a bend in the field lines. This is why the polarization pattern from the OMC-1 core was interpreted as being pinched in due to collapsing gas (Schleuning 1998). The mean position angle near MMS8-9 is not consistent with that of either OMC-1 or northern OMC-3. If the magnetic field is uniform (i.e. of identical strength and direction throughout the depth of the cloud), all the vectors should line up in the same direction, regardless of the behavior of the gas.

Thus, taken as a whole, the data in OMC-3 alone are not consistent with a uniform field. Including the OMC-1 core data as well brings the number of "mean field directions" in these two data sets up to at least three. Under the picture of a uniform field, this should not be the case. Interestingly, the orientation of the filament in OMC-1 can be estimated using the alignment of the two brightest cores. The angle between them is $\sim 30°$ east of north, with is consistent with the polarization position angle measured by Schleuning (1998) on large scales, but not with the interferometric position angles measured at 1.3 and 3.3 mm with the Berkeley Illinois Maryland Association (BIMA) interferometer (Rao et al. 1998).

An indirect method of estimating the magnetic field strength from polarimetry utilizes the assumption that the dispersion in the position angles of vectors is related to the magnetic field strength (Chandrasekhar & Fermi 1953). Inherent in this method is the assumption that there is a mean field orientation which can be identified (such as in the case of the spiral arms of the Galaxy in the original work of Chandrasekhar and Fermi). For complex field geometries in which the field reverses, there is no mean field to define; hence, we do not utilize this method to estimate a field strength toward OMC-3.

Our basic interpretations of the polarization pattern in Paper I remain unchanged. A comparison of filament to polarization position angles shows distributions centred on zero from MMS1 to MMS7, below which the vectors slowly rotate until they are misaligned from the filament (with a mean offset of $86° \pm 19°$). Additionally, the vector orientations are inconsistent with those predicted for poloidal fields where vectors would align perpendicular to the filament (Fiege & Pudritz 2000c). The northern data could suggest the presence of a transverse field. However, this interpretation would require either poorly aligned or poorly polarizing grains near the central axis of the filament. From a dynamical perspective, one might also expect a flattened sheet rather than a filament for this field geometry, since the magnetic support would be in a plane orthogonal to the field direction. Heiles (1987) observed Zeeman splitting of HI in the atomic envelope of Orion A and found evidence which supports the presence of a helical field geometry, although it was later interpreted in terms of the expanding Eridanus loop (Heiles 1997). The HI data sample a different gas component of the ISM than that probed by our polarimetry. Therefore, in order to interpret the three-dimensional field geometry local to the Integral-shaped Filament, it is vital that Zeeman splitting measurements of molecular gas within the filament be obtained.

In Paper I, we showed only a single radial cut across the MMS4 core to illustrate the depolarization across one of the filament's bright cores. A logarithmic plot of

p vs. I for our entire data set shows that depolarization is a *global* feature in this filament. Furthermore, the distribution of the polarization percentage as a function of the distance from the filament spine reveals that depolarization exists along the entire length of OMC-3, most importantly across the coreless region between MMS6 and MMS7. This result implies that depolarization is a feature of this filament even in the absence of condensed cores. Therefore, any model of filamentary clouds must be able to explain this feature.

The existing polarization data toward OMC-3 are insufficient in spatial extent to discriminate between two of our proposed explanations of a second filamentary structure or a bending in the Integral-shaped Filament. The behavior of the polarization south of MMS9 (into the region of OMC-2) is of particular interest. If the vectors in OMC-2 behave as the northern pattern of OMC-3, this could indicate support for a second filament, since only the region of juxtaposition is affected. (Observations of this region in CO with high velocity resolution will help to resolve the question of whether two filaments are juxtaposed on the sky.) On the other hand, if the vectors are asymmetric or misaligned from the parallel or perpendicular orientations in OMC-2, then this could indicate the model of a single bent filament better represents the physical properties of the Integral-shaped Filament. Extending the map to the east and west will reveal if strong polarization continues along the faint emission around MMS8 and MMS9. If neither hypothesis is supported by extending the data set, the filament may truly be poloidally dominated near the MMS8 and MMS9 cores.

In Paper I, we speculated that the effects of outflow from the powerful class 0 source MMS9 could have affected the magnetic field geometry to the east and west of that source, producing the polarization pattern observed. This is a particular concern for 850 μm SCUBA polarimetry because the ^{12}CO $J = 3 - 2$ line lies at the centre of the 850 μm filter bandwidth. The CO line may also be polarized and, if the CO emission is significant, it can dominate the polarization of the continuum.

However, the only part of OMC-3 where the CO has been shown to dominate the 850 μm continuum is in a Herbig-Haro knot west of the filament (Johnstone 2001).

Even if the field of an outflow is aligned with that of the young stellar object, it does not follow that the polarization directions would be the same. For example, Girart et al. (1999) found orthogonal polarization directions from 1.3 mm continuum dust in NGC 1333 IRAS 4A and ^{12}CO $J = 2 - 1$ line in its outflow. Finally, the outflow of MMS9 does not extend as far north as MMS7, where the direction of the polarization vectors begins to change. New data on outflows in the OMC-2/3 region identify MMS9 as the primary driving source in the southern part of OMC-3, while MMS8 is not associated with outflow in either H_2 shocks or CO emission (Aso et al. 2000; Yu et al. 2000). The outflow from MMS9 is aligned in a northwest to southeast orientation, contrary to the northeast to southwest orientation of the continuum emission. Based on CO emission, Yu et al. (2000) claim that MMS10 as identified by Chini et al. (1997) has no submillimetre counterpart. However, in the 850 μm map of Johnstone & Bally (1999) shown in Figure 1, there is a peak coincident with the 1.3 mm dust condensation observed previously. Aso et al. (2000) identify MMS10 as driving an east-west outflow. Disentangling the magnetic signatures of the cores and outflows in this region will require direct measurement of the polarization of the ^{12}CO $J = 3 - 2$ or the ^{12}CO $J = 2 - 1$ line.

We conclude that the helical field model of Fiege & Pudritz (2000a, Fiege & Pudritz (2000c) is consistent with our observations. This model predicts the depolarization along the axis of filaments and the position angle patterns, as well as explaining the r^{-2} density profile observed by Johnstone & Bally (1999). Although a quantitative model of OMC-3 as a bent filament is not yet complete, we are actively pursuing this possibility as a promising explanation for our data. There is no reason to suppose that a filament extending over a parsec should maintain a single inclination relative to the plane of the sky. Conversely, the misalignment of vectors toward MMS8 and MMS9 may not be a misalignment at all if a second filament is juxtaposed on the Integral-shaped Filament at their positions. The current data set is not extensive enough to distinguish between these two possible filament-field geometries. Polarization mapping to the east, west and south of the current mapped area would provide more insight into the magnetic field geometry in this region. High resolution data are also needed to further investigate other sources of the depolarization effect along the axis of the filament.

The authors would like to thank J. Greaves, T. Jenness, and G. Moriarty-Schieven at the JCMT for their assistance with problems both large and small during and especially after observing. Thanks to D. Johnstone for making the 850 μm scan map of the Integral-shaped Filament available to us and to J. Brown for access to the Faraday rotation data prior to its publication. We would also like to thank our referee for several suggestions which led to improvements in this manuscript. The research of BCM and CDW is supported through grants from the Natural Sciences and Engineering Research Council of Canada. BCM acknowledges funding from Ontario Graduate Scholarships. JDF acknowledges support from a postdoctoral fellowship, jointly funded by the Natural Sciences and Engineering Council and the Canadian Institute for Theoretical Astrophysics.

Appendix 4A – Effects of a Polarized Reference (or Sky) Position

The quality of submillimetre polarimetry data can be strongly affected by chopping on and off the source during observing and sky noise removal in data reduction. The former can affect the results if the difference in intensity of the source minus chop is not actually zero, or if the chop positions, commonly called the reference positions, are significantly polarized. Sky removal requires one to select one or more SCUBA bolometers which are devoid of significant flux to estimate sky variations on the timescale of 1 s. If the flux in these bolometers is in fact polarized or non-zero, then polarization data for the whole data set could be affected.

Typically, in reducing polarimetry data, the assumption is made that fluxes in the chop and sky bolometer positions are negligible and unpolarized. These assumptions are most likely valid in the case of point-like sources (such as protostars) in non-clustered environments (such as Taurus or Bok globules) where the background, even if non-zero, is flat enough that chopping reduces the background effectively to zero. More typically in star-forming regions, however, bright cores may be embedded within more extended structures, and even the largest chop throws of 150-180$''$ (at the JCMT) may be insufficient to reach "empty", unpolarized sky. If one were only interested in cores, one could use small chops, removing significant amounts of extended flux, but even in such cases, the difference between the on-source and chop positions may not be zero at the edges of the array given the rapid declines in surface intensities. For example, 850 μm data of the Integral-shaped Filament in which OMC-3 is located has been shown to exhibit a flux profile of r^{-1}, which implies a variation of flux across the filament on the scale of the chop throw (Johnstone & Bally 1999).

The effects of a polarized reference, or chop, position on the observed map are not necessarily intuitive. In order to illustrate the behavior of observed polarization percentage and position angle, we have used a simple model in which the polarization properties of the source and reference positions are known exactly. By subtracting the reference from the source polarization, the behavior of the observed polarization vectors can be compared to the input source values.

Linear polarization is defined by the Stokes parameters Q and U (and the total unpolarized intensity I),

$$Q = I_p \times \cos(2\theta) \quad U = I_p \times \sin(2\theta) \tag{4.3}$$

where I_p is the polarized intensity, the product of the polarization percentage, p, and the total intensity, I, and θ is the polarization position angle. Note that under these definitions, Q and U execute a period in 180° instead of 360°. This reflects the reality that 180° offsets are not detectable in linear polarization.

The percentage polarization is defined by

$$p = \frac{\sqrt{Q^2 + U^2}}{I} \times 100\% \tag{4.4}$$

while the position angle is given by

$$\theta = \frac{1}{2} \arctan\left(\frac{U}{Q}\right) \tag{4.5}$$

where $U/Q > 0$ for $-180° < 2\theta < -90°$ and $0° < 2\theta < 90°$. A ratio of $U/Q < 0$ can be found only where $-90 < 2\theta < 0°$ and $90° < 2\theta < 180°$. Finally, $U/Q = 0$ only where $2\theta = 0$ and $Q \neq 0$. Where both $Q = 0$ and $U = 0$ observationally, the source must be unpolarized.

If one defines I_s, p_s, and θ_s values for a source and I_r, p_r, and θ_r for a reference position, then one can deduce the quantities one would observe: I_{obs}, p_{obs}, and θ_{obs} by simple subtraction of I, Q, and U values at the two positions. In this exercise, we do not include an estimate of the rms noise, which serves primarily to truncate the useful data set observed at low I, Q and U values. Additionally, although chopping is typically done to reference positions on either side of the source field, we will consider only the source data and one reference position.

SCUBA and other bolometric arrays (SHARC, BOLOCAM) sample a wide area of sky compared to previous single bolometer instruments. Thus, many flux levels may be present across their fields of view. One might suspect that during SCUBA observations (which allow a maximum chop throw of $3'$), the reference position could be so close spatially to the source position that the same polarization properties could be present at both positions. Smoothly varying polarization patterns have been observed in many star-forming regions (e.g. see Dotson et al. 2000). Even in such cases, the observed polarization vector could be adversely affected; the magnitude of the effect depends on the relative polarized flux (i.e. $p \times I$) between the source and reference fields.

One can consider two straightforward cases which illustrate the effects of chopping on the observed polarization vectors. In the first case, consider a source polarized at $\theta_s = 0°$ and a reference polarization of $\theta_r = -90°$. Using equation (4.3), the values of Q_s, U_s, Q_r, and U_r can be calculated in terms of the polarized intensities at each position: $I_{p,s}$ and $I_{p,r}$. Subtraction of the reference values of Q and U show that the observed quantity, U_{obs}, remains zero, so by equation (4.5), the position angle measured will be the same as that of the source. However, application of equation (4.4) yields the result

$$p_{obs} = p_s \times \left[\frac{1 + (I_{p,r}/I_{p,s})}{1 - (I_r/I_s)}\right]$$

where I_{obs} has been replaced by $I_s - I_r$. Therefore, the true p_s is recovered only if both $I_{p,r}/I_{p,s}$ and I_r/I_s approach zero.

In the second case, consider a source polarized at $\theta_s = 0°$ and a reference polarization with position angle $\theta_r = 45°$. A similar calculation of respective Q and U values, subtraction and application of equations (4.5) and (4.4) reveals that since

$U_{obs} \neq 0$, both the position angle and the percentage polarization will in this case differ from those of the source. The observed position angle is a function of $I_{p,r}/I_{p,s}$:

$$\theta_{obs} = \frac{1}{2}\arctan\left(\frac{-I_{p,r}}{I_{p,s}}\right)$$

while the percentage polarization is again a function of $I_{p,r}/I_{p,s}$ and I_r/I_s:

$$p_{obs} = p_s \times \left[\frac{\sqrt{1+(I_{p,r}/I_{p,s})^2}}{1-(I_r/I_s)}\right].$$

In order to quantify this effect over many conditions, we subtracted a reference polarization from a source polarization under several different cases outlined in Table 4.2. In all cases, a source polarization of 10% and a position angle of 0° were used, with varying ranges of source intensity.[2] The reference polarization angle is assigned an offset from this value. The source total intensity is assigned a range of values from 1 to 20, and the reference flux is assumed to have a uniform polarized intensity equal to some fraction that of the source peak.

			Slope of log p_{obs} vs. log I_{obs} at $\theta_s - \theta_r = 90°$	
Case	I_r	p_r	minimum (high I_{obs})	maximum (low I_{obs})
A	0.4 (2% source peak)	10%	−0.085	−0.39
B	2 (10% source peak)	10%	−0.28	−0.65
C	5 (25% source peak)	10%	−0.50	−0.81
D	0.4 (2% source peak)	20%	−0.085	−0.49
E	2 (10% source peak)	20%	−0.34	−0.76
F	5 (25% source peak)	20%	−0.56	−0.88

Table 4.2: Systematic Depolarization Created by Chopping onto Polarized Sky

Figure 4.8 plots p_{obs} as a function of I_{obs} for Cases A, B and F. Where the reference polarization is aligned with the source polarization, the correct p_s is measured

[2]Calculations can be done with different θ_s values, but the results are completely identical to those presented here. What is relevant is the difference between θ_s and θ_r not the absolute value of either.

for all $I_{obs}> 0$ in Cases A and B. However, in Case F, the p_{obs} is underestimated, since $p_r > p_s$. For large offsets between θ_s and θ_r, the polarization percentage could be overestimated, particularly for low I_{obs} values. Near the source peak, the polarization observed converges on the true source polarization value. The values of $p_{obs}/p_s > 10$ are, in the case of p_s= 10%, completely unphysical and would be disregarded in any data set. Positive or negative offsets in position angle between source and reference produce the same p_{obs}. For this reason, only the solutions for positive offsets have been plotted on Figure 4.8.

Figure 4.9 shows that θ_s is recovered in all three cases when the source and reference polarizations are aligned. When the source and reference polarizations are not aligned, more interesting results are obtained. The largest discrepencies in θ_{obs} occur when the differences between θ_s and θ_r are small. Figure 4.9 illustrates that, for high values of I_{obs}, the largest errors in θ_{obs} from θ_s are observed for $\theta_s - \theta_r= 45°$, which corresponds to $2(\theta_s - \theta_r)$ of 90°. For very low I_{obs}, smaller offsets can produce an even larger error. As offsets increase toward 90°, a $2(\theta_s - \theta_r)$ value of 180° is approached. Since linear polarization measurements cannot discriminate between vectors 180° apart, the input θ_s is recovered. In Case A, which most closely parallels the MMS6 field of our data, at least in levels of intensity between the source and chop position (see § 4.2), the largest error which can be produced in position angle is $\pm 10°$, and that is only for the lowest values of I_{obs}. In Case B, which has a source peak flux to reference flux ratio similar to that of the MMS8-9 region in the OMC-3 data set (based on the Johnstone & Bally (1999) scan map data), the most extreme errors in position angle predicted range from $\pm(20 - 30)°$ even for very low intensities, as long as our assumption of similar polarization to the source holds. Even though we have noted that the largest errors in θ_{obs} occur for small angles, Figure 4.9 shows that in Case B, the small angle offsets do not dominate, and the θ_{obs} is within $\pm 20°$ of θ_s until fluxes are less than 10% of the peak I_{obs}. We have truncated our OMC-3 data set such that $I_{obs} > 0.0006$ (volts),

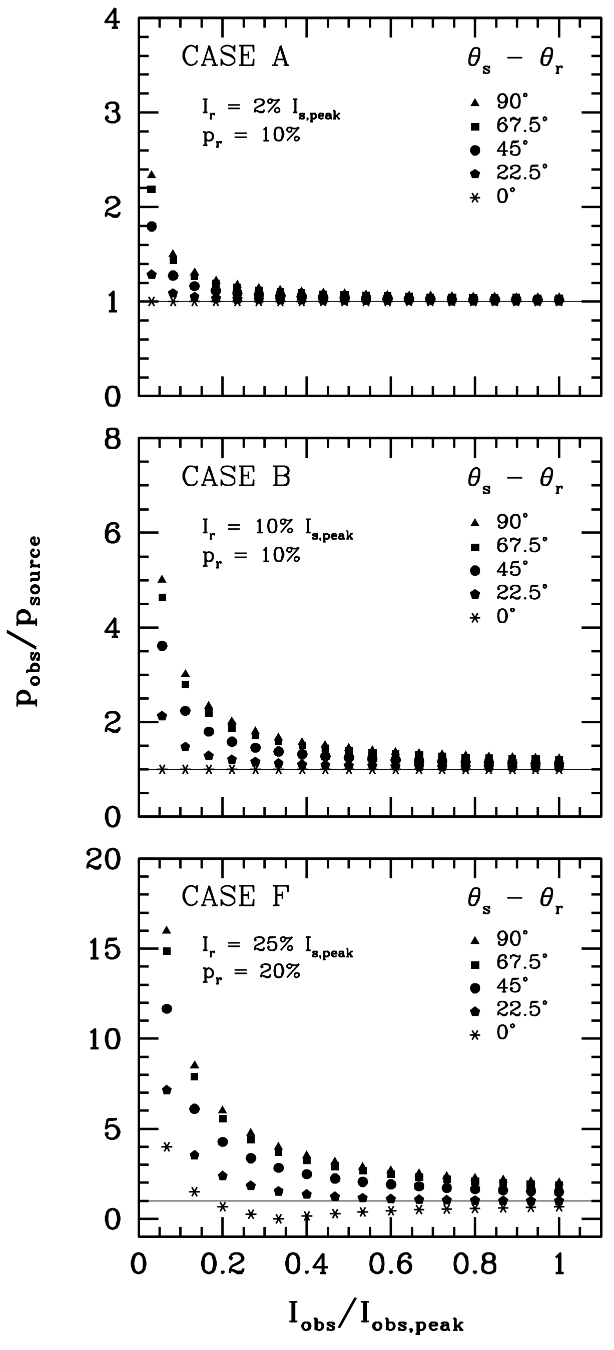

Figure 4.8: Error in polarization percentage induced by chopping
Ratio of observed to source polarization percentage versus observed intensity as a function of the observed peak intensity for three of the cases identified in Table 4.2. In each case, the source is polarized at a level of 10%. The ratios of input parameters of polarization percentage and intensity at the reference position compared to those at the source position are smallest for Case A and largest for Case F. The offset between source and reference angles, $\theta_s - \theta_r$, are labelled in each case. Clearly, the systematic effects due to chopping become more significant as the polarized flux in the reference beam grows relative to that of the source.

which is approximately 10% of the faintest peak in our map (MMS7) with a flux of 0.00554 ± 0.00002 (volts). For still lower intensities (where I_{obs} approaches 0), the largest discrepencies from the input θ_s are no greater than $\pm 40°$.

In comparison, Case F reveals potential errors of $\pm 90°$ for low $I_{obs} > 0$. If a true observation were done under these conditions, polarization vectors would be reliable only to a flux level about 50% of the observed peak. Near the peaks, errors are only on the order of $< \pm 20°$. Thus, even in this extreme case where the $p_r > p_s$ and the I_r is a significant fraction of I_s, it is unlikely that chopping alone could produce an alignment of θ_{obs} across a SCUBA field of view. In the idealized scenario we have discussed, the various fluxes across the SCUBA source field of view will be affected differently by the polarized flux in the reference position, creating vectors for which θ_{obs} varies systematically with I_{obs}. OMC-3's southern region contains vectors which are orthogonal to the filament orientation over the whole SCUBA field (a range of an order of magnitude in total flux). The vectors have a mean of $-70°$ with a range up to $\pm 30°$ from that value. There is no systematic variation in position angle with intensity. We thus conclude that the simple scenario discussed here (a constant polarized flux at the reference position) cannot be responsible for the misalignment between the filament and polarization vectors. We cannot rule out a variable polarized flux across the SCUBA footprint at the reference position, but our examination of the Johnstone & Bally (1999) data does not reveal large variations in intensity at those positions. If polarization percentage were varying, we have no means of detecting this variation with our data set.

However, polarization has been detected at 350 μm toward the northern part of OMC-3 using the Hertz polarimeter at the Caltech Submillimeter Observatory (Dowell 2001). These data show alignment along the filament as observed at 850 μm with SCUBA, although the 350 μm polarization percentages are $\sim 75\%$ those of the JCMT (Hildebrand et al. 2000). Since the CSO data were obtained with a chop throw of $6'$ (double that of the JCMT), and the behavior of the polarization

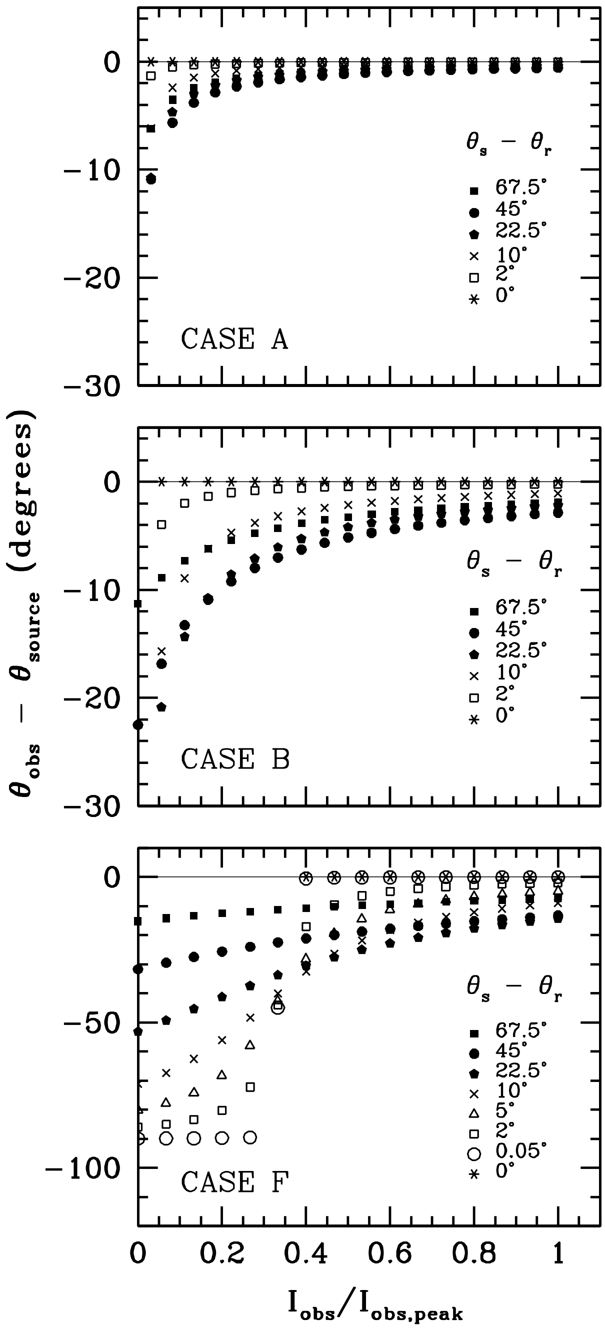

Figure 4.9: Error in position angle induced by chopping

Observed position angles at various observed intensities (as a function of the observed flux peak) for Cases A, B and F as described in Table 4.2. The assigned position angle of the source was 0°. Solutions for positive and negative offsets between source and reference position angles are symmetric about the source position angle; hence, we show only solutions for positive offsets here. The solution for an offset of 90° is discussed in the text and is identical to the solution for 0°. The offset angles, $\theta_s - \theta_r$, are labelled in each case. As for percentage polarization in Figure 4.8, the lower the ratio of total flux in the reference position to the source, the less impact chopping has on the observed values at the source position.

pattern is consistent between the two instruments, this provides some re-assurance that the SCUBA position angle data have not been grossly affected by a significant polarized flux at the reference position.

In practice, efforts should be made to select reference positions which are devoid of significant flux compared to the flux levels in the source field of view. Figures 4.8 and 4.9 show that even if the polarization percentage is comparable in both fields, the effects on the observable quantities recovered are minimized greatly if the total flux levels are low at the reference position.

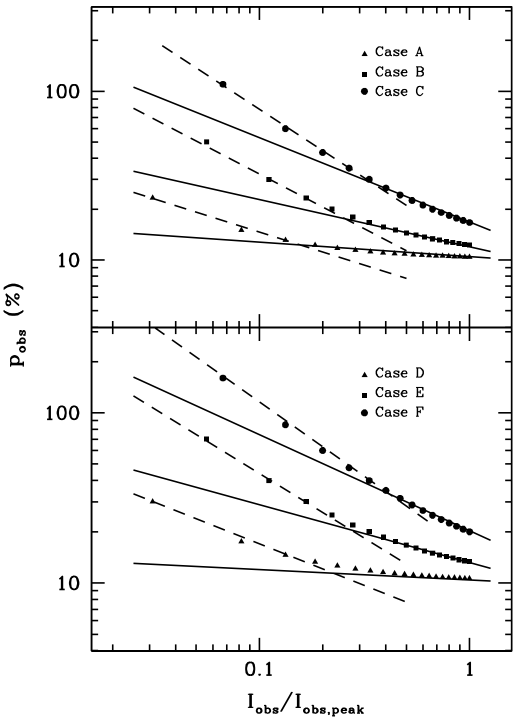

Figure 4.10: Depolarization induced by chopping
Depolarization effects expected for the cases described in Table 4.2. As Figure 4.4 shows, decreased polarization percentage with increased intensity is a global feature in OMC-3. Such an effect can clearly be produced by chopping onto a reference position with significant polarization, although the magnitude of the slope produced diminishes as the flux of the reference position (with respect to the source) decreases.

One of the key "observable" relationships in our data set of OMC-3 is the depolarization effect measured along the length of the filament. Systematically lower polarization percentages are measured toward regions of higher intensities. Figure 4.10 shows the log p_{obs} versus log $(I_{obs}/I_{obs,peak})$ plots for offsets of $\pm 90°$ between source and reference polarizations, which produces the largest error in polarization percentage. Unlike the OMC-3 data, for which the log-log plot of Figure 4.4 looks reasonably linear (given the noise and scatter), the depolarization effects of Figure 4.10 clearly are not linear. However, it is possible to sketch in a maximum and minimum slope. The minimum and maximum slopes encompass a range of slopes consistent with variation of percentage polarization with observed intensity for each of the six cases. Table 4.2 records the slopes; as one would expect, the depolarization produced is smallest for reference positions with low values of I_r and small values of p_r.

None of the slopes generated for data at high $I_{obs}/I_{obs,peak}$ reflect the slope of -0.65 derived for the OMC-3 data set. The closest effects are for reference fluxes 25% of the flux peak, which we believe does not represent the observed conditions in any part of OMC-3. The slopes at high $I_{obs}/I_{obs,peak}$ are the most likely to be observed in real data, since they are exhibited where signal-to-noise will be high. However, at lower $I_{obs}/I_{obs,peak}$, steeper slopes could be produced, and for completeness, we have included these as maximum depolarization effects produced by each case. For all but the lowest reference flux considered (2% of the source peak), a slope of -0.65 could be explained by polarized flux in the reference position. We note, however, that these slopes are produced only in regions of low flux, whereas our data continue to exhibit this slope even at the highest flux values.

These calculations reveal that the effective "depolarization" created by chopping onto a polarized reference position is dependent on the intensity and degree of polarization present as well as the offset between the source and reference position angle. We conclude that in the region of MMS8-9, it is possible that the depolarization observed could result from the scenarios described in Cases B, or possibly E. Cases C and F represent an extreme we do not believe exists in our data set. However, we note that the northern parts of OMC-3 have much lower reference fluxes compared to peak source positions (again, based on the Johnstone & Bally map). Near MMS6, for instance, the scenario is closer to Case A (or maybe Case D), for which the depolarization effect observed cannot be attributed to chopping effects.

Appendix 4B – Sky Subtraction

Bolometers must be carefully chosen for sky subtraction. Ideally, bolometers should be free of emission and, for polarimetry, unpolarized. SCUBA has a large field of view ($> 2.3'$) and when observing point sources, there are typically many "empty" bolometers to chose from for sky subtraction. Extended sources prove more difficult.

Figure 4.11 compares the data obtained in 6 sets of 3 consecutive observations each toward the MMS8 and MMS9 region. Taking 3 consecutive scans of the same source allows the resultant maps to be quickly combined for increased signal-to-noise at the telescope and minimizes sky rotation between them. Sets 1 and 2 were obtained on 5 September; Sets 3-5 on 6 September; and Set 6 on 7 September. Before sky subtraction is performed, the polarization position angles appear highly uniform, but are not oriented in the same direction in each data set (see the left panels of Figure 4.11). For example, Set 1 exhibits vectors which align closely to the filament, while Set 3 appears just the opposite. However, the sky subtracted versions of each data set reveal very similar polarization patterns, although these generally appear messier than the unsubtracted data. Generally, in the sky subtracted maps, the overall orientation of the vectors is approximately east to west, although there is some high scatter in the lower signal-to-noise regions.

The uniformity in the non-sky subtracted frames is easily understood since the dominant factor in the polarization detected is due to sky. If the opacity of the sky is changing during a single observation (which it is, necessitating the removal of the sky's effects), then one can expect a very uniform polarization map. For instance, if the sky becomes steadily more opaque during an observation, then maps made at each successive position of the waveplate will contain fainter fluxes. When the waveplate positions are paired up and subtracted to deduce Q and U, then the results must be positive. If the sky is dominant, than Q and U will produce approximately the same fluxes, both positive, which yield a position angle of 45° (east of north). The removal of sky effects removes this uniformity and leaves the more structured polarization of the source itself. The uniformity of each subset once the sky has been subtracted is a re-assurance that the subtraction routine is effectively removing sky variations.

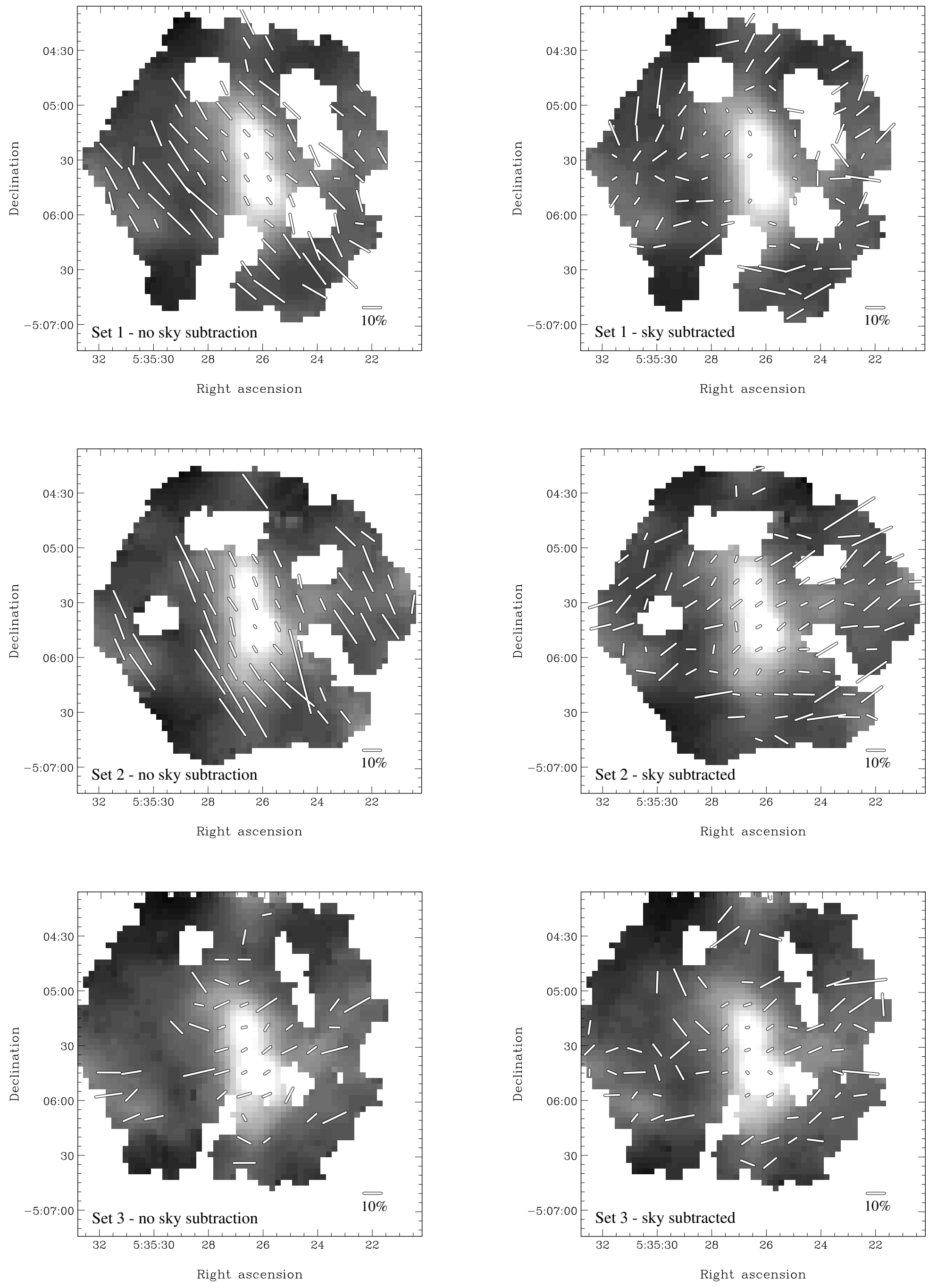

Figure 4.11: Effects of Sky Subtraction
Six data sets of the MMS8-MMS9 region are shown, each reduced with (right) and without (left) sky subtraction. These maps reveal that a high degree of uniformity in position angle can be observed before sky subtraction is performed. These patterns can be created by variations in sky conditions during the 12 minute polarization cycle and must be removed to reveal the true polarization vectors of the source.

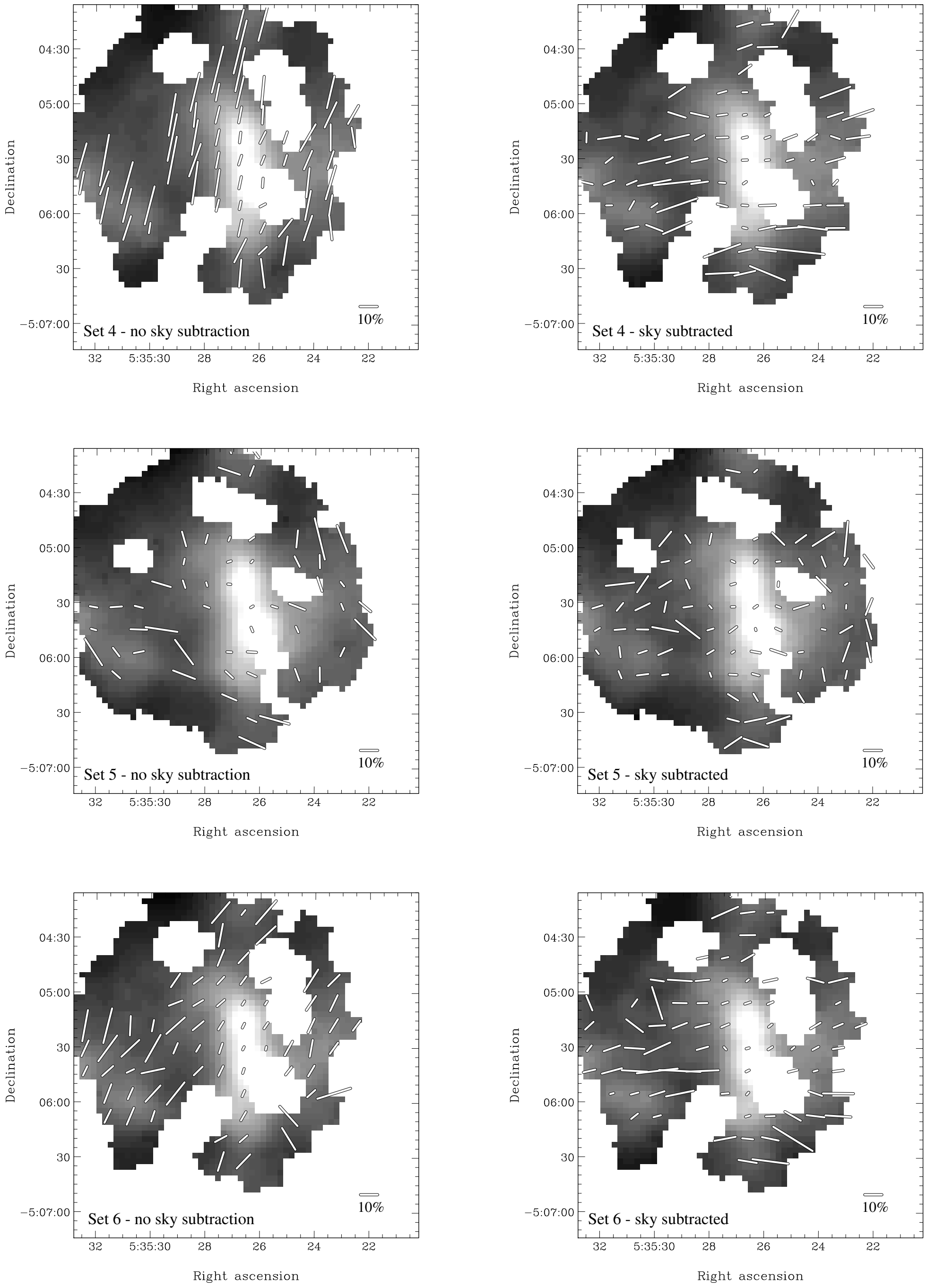

Figure 4.11 (continued)

Appendix 4C – Sub-dividing the OMC-3 data set

Figure 4.12 shows two subsets of the OMC-3 data. The constraints on the data plotted have been relaxed to reflect the fact that the noise is larger when only half the exposure time is used. Thus, instead of plotting values with the uncertainty in polarization percentage, $dp < 1\%$, we have plotted those vectors with $dp < 1.4\%$. Instead of selecting vectors with $p/dp = \sigma_p > 6$, we have plotted those with $\sigma_p > 4.2$.

The data reduction for each subset was performed in the same manner as for the entire data set as described in § 4.2. Despite the fact that some data are missing from each set due to the removal of noisy bolometers, the polarization patterns shown in Figure 4.12 are very consistent with each other and with that of Figure 4.2. The alignment between filament and vectors in the north and misalignment in the south is observed in both maps. Depolarization toward the filament spine is also observed. Seventy percent of the polarization percentages of the 190 vectors in common between these two sets of data are not significantly different from one another (i.e. $\frac{(p_1-p_2)}{(dp_1+dp_2)} < 3$). The upper limit on the quantity $p_1 - p_2$ is estimated to be $dp_1 + dp_2$ because we have reason to suppose these errors will be correlated.

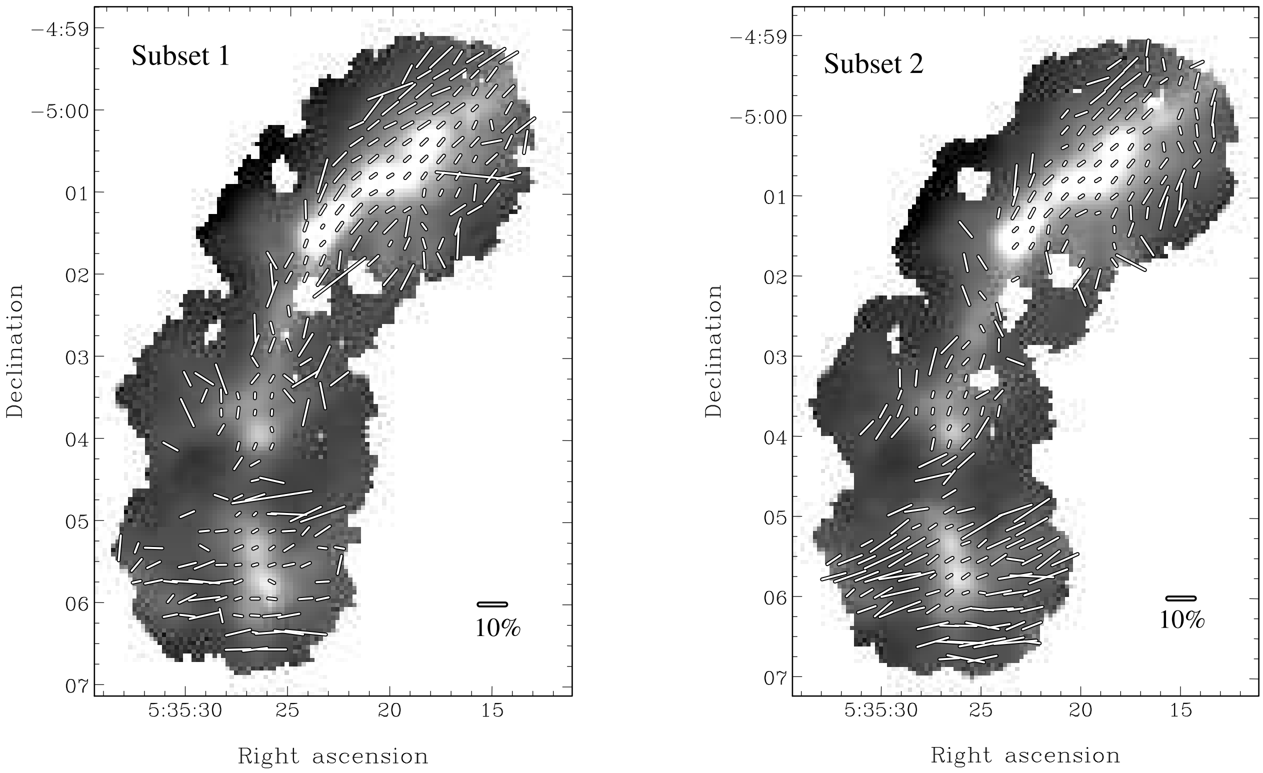

Figure 4.12: Two subsets of OMC-3 data

These two figures illustrate the consistency between two halves of the OMC-3 data set. Polarization vectors plotted have $p > 1\%$, an uncertainty in polarization percentage, dp, $< 1.4\%$ and $p/dp > 4.2$.

Appendix 4D – Polarization Percentages and Position Angles

Table 4.3 contains the percentage polarizations and position angles as plotted in Figure 4.2. The positions are given as arcsecond offsets from a position near the peak of MMS6, at J2000 coordinates $\alpha = 05^{\mathrm{h}}35^{\mathrm{m}}23\overset{\mathrm{s}}{.}5$ and $\delta = -05°01'\ 32\overset{''}{.}2$ ($\alpha = 05^{\mathrm{h}}32^{\mathrm{m}}55\overset{\mathrm{s}}{.}6$ and $\delta = -05°03'\ 25\overset{''}{.}0$ in B1950).

Table 4.3: OMC-3 850 μm Polarization Data

Δ R.A. ($''$)	Δ DEC. ($''$)	p (%)	dp (%)	σ_p	θ (°)	$d\theta$ (°)
48.0	−304.5	8.93	0.85	10.5	88.3	2.7
60.0	−292.5	13.03	0.78	16.6	−78.5	1.7
48.0	−292.5	10.83	0.47	23.0	−86.5	1.2
36.0	−292.5	13.92	0.61	22.7	89.7	1.3
60.0	−280.5	12.44	0.62	20.2	−75.5	1.4
48.0	−280.5	5.01	0.33	15.3	−89.0	1.9
36.0	−280.5	10.02	0.39	25.6	−87.7	1.1
24.0	−280.5	13.28	0.60	22.1	84.7	1.3
12.0	−280.5	12.53	0.77	16.2	−85.3	1.8
0.0	−280.5	8.18	0.69	11.9	−65.9	2.4
−12.0	−280.5	7.92	0.92	8.6	−70.2	3.3
108.0	−268.5	7.36	0.39	18.8	−73.6	1.5
96.0	−268.5	6.94	0.43	16.1	−65.5	1.8
84.0	−268.5	16.76	0.75	22.2	−71.3	1.3
72.0	−268.5	2.66	0.62	4.3	−68.4	6.7
60.0	−268.5	4.33	0.36	11.9	−66.9	2.4
48.0	−268.5	2.80	0.18	15.5	−79.3	1.8
36.0	−268.5	5.73	0.25	23.0	−79.2	1.2
24.0	−268.5	9.01	0.40	22.6	−85.2	1.3
12.0	−268.5	6.22	0.42	14.8	−87.3	1.9
0.0	−268.5	4.63	0.54	8.6	−79.7	3.3
−12.0	−268.5	9.46	0.70	13.5	−77.9	2.1
120.0	−256.5	2.61	0.37	7.0	−43.3	4.1
108.0	−256.5	4.93	0.29	16.8	−54.2	1.7
96.0	−256.5	8.87	0.41	21.8	−62.7	1.3
84.0	−256.5	15.87	0.77	20.7	−78.1	1.4
72.0	−256.5	4.84	0.63	7.7	−69.2	3.7
60.0	−256.5	4.49	0.25	18.3	−71.4	1.6
48.0	−256.5	2.60	0.15	17.5	−68.7	1.6

Table 4.3 (continued)

Δ R.A. ($''$)	Δ DEC. ($''$)	p (%)	dp (%)	σ_p	θ (°)	$d\theta$ (°)
36.0	−256.5	2.09	0.19	11.1	−71.8	2.6
24.0	−256.5	2.00	0.34	5.8	85.6	4.9
12.0	−256.5	8.01	0.36	22.3	−79.8	1.3
0.0	−256.5	7.70	0.43	17.9	−77.2	1.6
−12.0	−256.5	3.80	0.73	5.2	−67.6	5.5
132.0	−244.5	6.15	0.44	13.9	−74.3	2.1
120.0	−244.5	10.43	0.35	29.4	−72.6	1.0
108.0	−244.5	8.13	0.43	18.9	−73.9	1.5
96.0	−244.5	14.15	0.64	22.1	−81.4	1.3
84.0	−244.5	15.15	0.76	19.8	−85.5	1.4
72.0	−244.5	12.76	0.47	27.4	−77.0	1.0
60.0	−244.5	3.29	0.20	16.8	−63.2	1.7
48.0	−244.5	1.59	0.11	14.3	−60.3	2.0
36.0	−244.5	2.18	0.15	14.7	−59.6	2.0
24.0	−244.5	2.93	0.29	10.2	−70.9	2.8
12.0	−244.5	1.41	0.30	4.6	−62.5	6.2
0.0	−244.5	10.02	0.42	24.0	−80.8	1.2
−12.0	−244.5	11.51	0.79	14.6	−87.1	2.0
132.0	−232.5	7.02	0.43	16.5	−51.2	1.7
120.0	−232.5	8.95	0.43	20.8	−66.3	1.4
108.0	−232.5	6.29	0.57	11.1	−64.4	2.6
96.0	−232.5	13.09	0.67	19.5	−69.2	1.5
84.0	−232.5	10.59	0.57	18.6	−63.6	1.5
72.0	−232.5	6.77	0.35	19.1	−72.7	1.5
60.0	−232.5	3.71	0.18	20.6	−60.1	1.4
48.0	−232.5	2.58	0.10	26.3	−64.3	1.1
36.0	−232.5	3.02	0.13	22.4	−68.9	1.3
24.0	−232.5	4.41	0.24	18.1	−68.4	1.6
12.0	−232.5	5.78	0.29	20.1	−60.1	1.4
0.0	−232.5	4.01	0.42	9.7	−88.2	3.0
−12.0	−232.5	6.22	0.61	10.1	−48.0	2.8
−24.0	−232.5	10.85	0.83	13.0	−51.5	2.2
132.0	−220.5	6.35	0.77	8.2	−48.8	3.5
120.0	−220.5	6.95	0.80	8.7	−81.0	3.3
108.0	−220.5	4.97	0.71	7.0	−53.9	4.1
96.0	−220.5	9.44	0.72	13.0	−59.0	2.2
84.0	−220.5	4.64	0.46	10.0	−74.2	2.9
72.0	−220.5	4.90	0.30	16.4	−63.6	1.7
60.0	−220.5	4.47	0.17	26.4	−64.1	1.1
48.0	−220.5	1.50	0.09	16.2	−61.4	1.8
36.0	−220.5	2.82	0.15	18.7	−64.6	1.5
24.0	−220.5	4.44	0.39	11.4	−53.1	2.5
12.0	−220.5	5.70	0.55	10.4	−68.4	2.8
0.0	−220.5	4.87	0.40	12.1	−76.0	2.4

Table 4.3 (continued)

Δ R.A. (″)	Δ DEC. (″)	p (%)	dp (%)	σ_p	θ (°)	$d\theta$ (°)
−12.0	−220.5	7.13	0.48	14.9	−72.8	1.9
−24.0	−220.5	8.37	0.76	10.9	−59.8	2.6
96.0	−208.5	3.18	0.90	3.5	−55.8	8.1
84.0	−208.5	6.67	0.46	14.6	−62.7	2.0
72.0	−208.5	4.09	0.25	16.1	−75.2	1.8
60.0	−208.5	2.61	0.15	17.3	−63.5	1.7
48.0	−208.5	2.42	0.12	20.3	−64.2	1.4
36.0	−208.5	4.46	0.22	20.3	−68.5	1.4
24.0	−208.5	10.29	0.57	18.2	−66.8	1.6
12.0	−208.5	5.06	0.82	6.2	−73.2	4.6
0.0	−208.5	8.26	0.44	18.6	−61.5	1.5
−12.0	−208.5	10.23	0.55	18.6	−61.2	1.5
96.0	−196.5	8.72	0.79	11.1	−52.5	2.6
84.0	−196.5	4.97	0.62	8.0	−72.9	3.6
72.0	−196.5	3.25	0.33	9.7	−72.5	2.9
60.0	−196.5	2.53	0.22	11.5	−57.6	2.5
48.0	−196.5	2.88	0.23	12.4	−59.8	2.3
36.0	−196.5	5.01	0.46	10.9	−81.3	2.6
0.0	−196.5	16.91	0.68	24.8	−70.5	1.2
−12.0	−196.5	15.73	0.73	21.6	−57.5	1.3
72.0	−184.5	8.80	0.92	9.6	−79.4	3.0
60.0	−184.5	3.46	0.43	8.0	−71.8	3.6
48.0	−184.5	6.78	0.47	14.4	−66.6	2.0
36.0	−184.5	14.11	0.92	15.3	−79.6	1.9
60.0	−172.5	8.09	0.55	14.8	−71.8	1.9
48.0	−172.5	4.89	0.43	11.4	−50.7	2.5
60.0	−160.5	8.68	0.47	18.4	−56.6	1.6
48.0	−160.5	5.51	0.29	19.3	−60.4	1.5
36.0	−160.5	4.77	0.41	11.7	−53.5	2.4
108.0	−148.5	5.74	0.92	6.2	22.3	4.6
60.0	−148.5	3.21	0.36	9.0	−16.2	3.2
48.0	−148.5	2.03	0.17	11.8	−21.4	2.4
36.0	−148.5	2.94	0.25	11.6	−38.5	2.5
24.0	−148.5	2.32	0.76	3.1	−41.5	9.4
108.0	−136.5	2.33	0.78	3.0	−55.8	9.6
96.0	−136.5	5.13	0.69	7.5	−37.7	3.8
84.0	−136.5	5.02	0.65	7.8	−44.2	3.7
72.0	−136.5	2.24	0.40	5.5	−25.6	5.2
24.0	−136.5	3.18	0.46	7.0	−37.7	4.1
96.0	−124.5	4.55	0.87	5.2	−5.7	5.5
84.0	−124.5	1.88	0.53	3.5	−25.3	8.1
72.0	−124.5	2.16	0.27	8.0	0.2	3.6
60.0	−124.5	2.85	0.17	16.5	−6.4	1.7
48.0	−124.5	2.01	0.14	14.0	−14.8	2.0

Table 4.3 (continued)

Δ R.A. ($''$)	Δ DEC. ($''$)	p (%)	dp (%)	σ_p	θ (°)	$d\theta$ (°)
36.0	−124.5	1.69	0.19	8.8	−17.9	3.3
12.0	−124.5	7.35	0.56	13.2	−9.2	2.2
96.0	−112.5	4.39	0.92	4.8	−49.0	6.0
84.0	−112.5	4.15	0.58	7.2	−25.6	4.0
72.0	−112.5	2.75	0.31	8.9	−6.3	3.2
60.0	−112.5	1.81	0.24	7.5	−2.8	3.8
48.0	−112.5	1.77	0.20	9.0	−17.4	3.2
36.0	−112.5	1.77	0.25	7.1	−19.9	4.1
24.0	−112.5	1.49	0.50	3.0	−76.6	9.6
12.0	−112.5	2.53	0.49	5.1	−35.8	5.6
0.0	−112.5	4.34	0.74	5.9	20.1	4.9
96.0	−100.5	3.31	0.85	3.9	50.8	7.4
84.0	−100.5	4.19	0.70	6.0	16.8	4.8
72.0	−100.5	8.22	0.63	13.1	12.9	2.2
48.0	−100.5	3.23	0.30	10.8	−34.7	2.7
36.0	−100.5	1.95	0.32	6.1	−26.8	4.7
24.0	−100.5	3.65	0.79	4.6	58.0	6.2
12.0	−100.5	11.23	0.95	11.9	−71.7	2.4
48.0	−88.5	2.14	0.49	4.3	−15.7	6.6
36.0	−88.5	1.98	0.32	6.2	−45.7	4.6
24.0	−88.5	3.78	0.45	8.4	−16.5	3.4
12.0	−88.5	3.22	0.75	4.3	−53.0	6.6
48.0	−76.5	7.98	0.64	12.4	−31.6	2.3
36.0	−76.5	4.00	0.34	11.9	−35.2	2.4
12.0	−76.5	5.99	0.76	7.9	−13.5	3.6
48.0	−64.5	7.59	0.86	8.9	−2.7	3.2
36.0	−64.5	2.00	0.33	6.1	23.3	4.7
24.0	−64.5	2.35	0.33	7.1	30.1	4.0
12.0	−64.5	4.88	0.65	7.5	−0.5	3.8
12.0	−52.5	5.53	0.52	10.6	4.2	2.7
36.0	−40.5	7.18	0.69	10.4	0.5	2.8
24.0	−40.5	2.86	0.48	6.0	39.3	4.8
36.0	−28.5	5.59	0.81	6.9	3.1	4.1
24.0	−28.5	2.23	0.52	4.3	−40.8	6.7
12.0	−28.5	1.00	0.32	3.1	−32.1	9.2
0.0	−28.5	3.46	0.37	9.3	−41.3	3.1
−12.0	−28.5	9.02	0.73	12.3	−44.9	2.3
−48.0	−28.5	8.33	0.62	13.4	−37.0	2.1
−60.0	−28.5	8.43	0.68	12.3	−20.9	2.3
36.0	−16.5	6.90	0.66	10.5	24.7	2.7
24.0	−16.5	2.43	0.50	4.8	9.2	5.9
0.0	−16.5	1.71	0.23	7.5	−26.5	3.8
−12.0	−16.5	4.08	0.37	10.9	3.5	2.6
−24.0	−16.5	4.40	0.88	5.0	−0.4	5.7

Table 4.3 (continued)

Δ R.A. ($''$)	Δ DEC. ($''$)	p (%)	dp (%)	σ_p	θ (°)	$d\theta$ (°)
−36.0	−16.5	3.93	0.71	5.5	−41.2	5.2
−48.0	−16.5	1.48	0.36	4.2	−33.0	6.9
−72.0	−16.5	5.11	0.48	10.7	14.1	2.7
−84.0	−16.5	8.94	0.81	11.0	39.5	2.6
12.0	−4.5	1.72	0.27	6.3	−33.8	4.5
0.0	−4.5	1.81	0.16	11.4	−41.8	2.5
−12.0	−4.5	1.57	0.28	5.5	−10.1	5.2
−24.0	−4.5	4.00	0.32	12.5	−19.9	2.3
−36.0	−4.5	2.77	0.33	8.5	−26.7	3.4
−48.0	−4.5	1.23	0.25	5.0	−19.0	5.7
−60.0	−4.5	1.42	0.32	4.4	−5.3	6.5
−72.0	−4.5	3.13	0.28	11.4	14.4	2.5
−84.0	−4.5	2.23	0.39	5.8	−17.2	5.0
−96.0	−4.5	11.17	0.77	14.5	13.8	2.0
36.0	7.5	5.73	0.98	5.9	33.0	4.9
24.0	7.5	2.46	0.62	4.0	41.0	7.2
12.0	7.5	2.67	0.32	8.3	−24.1	3.5
0.0	7.5	1.11	0.12	9.0	−35.6	3.2
−12.0	7.5	2.75	0.12	23.1	−31.3	1.2
−24.0	7.5	3.75	0.19	19.7	−28.5	1.5
−36.0	7.5	3.12	0.22	13.9	−30.9	2.1
−48.0	7.5	2.59	0.23	11.3	−45.8	2.5
−60.0	7.5	3.41	0.29	11.7	−3.7	2.4
−72.0	7.5	2.28	0.28	8.1	16.8	3.5
−84.0	7.5	3.50	0.38	9.3	−21.0	3.1
−96.0	7.5	3.96	0.53	7.5	−1.7	3.8
12.0	19.5	5.13	0.39	13.3	0.8	2.2
0.0	19.5	4.05	0.17	23.5	−29.3	1.2
−12.0	19.5	3.63	0.10	37.1	−32.7	0.8
−24.0	19.5	4.14	0.11	39.1	−42.1	0.7
−36.0	19.5	3.72	0.17	21.6	−45.1	1.3
−48.0	19.5	3.40	0.18	18.9	−60.3	1.5
−60.0	19.5	1.45	0.21	6.8	−64.8	4.2
−72.0	19.5	2.34	0.25	9.3	−17.7	3.1
−84.0	19.5	3.68	0.38	9.6	−0.3	3.0
−96.0	19.5	3.17	0.43	7.3	−23.5	3.9
−108.0	19.5	6.48	0.63	10.3	−14.7	2.8
12.0	31.5	6.73	0.85	8.0	4.5	3.6
0.0	31.5	7.10	0.30	23.3	−18.0	1.2
−12.0	31.5	5.05	0.13	39.8	−31.0	0.7
−24.0	31.5	2.72	0.10	27.0	−40.7	1.1
−36.0	31.5	2.01	0.08	23.7	−50.6	1.2
−48.0	31.5	1.58	0.09	18.1	−51.7	1.6
−72.0	31.5	1.83	0.17	10.8	−24.8	2.6

Table 4.3 (continued)

Δ R.A. ($''$)	Δ DEC. ($''$)	p (%)	dp (%)	σ_p	θ (°)	$d\theta$ (°)
−84.0	31.5	2.39	0.25	9.5	−25.3	3.0
−96.0	31.5	5.13	0.35	14.8	−28.6	1.9
−108.0	31.5	7.79	0.52	14.9	−18.6	1.9
−120.0	31.5	8.56	0.72	11.9	−12.9	2.4
0.0	43.5	12.83	0.57	22.6	−8.7	1.3
−12.0	43.5	5.16	0.23	22.4	−29.7	1.3
−24.0	43.5	3.39	0.15	22.1	−46.3	1.3
−36.0	43.5	2.04	0.09	23.3	−51.8	1.2
−48.0	43.5	1.82	0.07	27.5	−54.1	1.0
−60.0	43.5	1.88	0.07	28.4	−45.8	1.0
−72.0	43.5	2.16	0.09	24.0	−33.0	1.2
−84.0	43.5	3.05	0.13	23.0	−34.4	1.2
−96.0	43.5	2.05	0.24	8.5	−32.6	3.4
−108.0	43.5	4.89	0.38	12.8	−85.7	2.2
−120.0	43.5	6.92	0.47	14.9	−24.1	1.9
−132.0	43.5	2.88	0.66	4.4	−43.2	6.5
−12.0	55.5	5.51	0.43	12.9	−21.2	2.2
−24.0	55.5	2.54	0.21	12.0	−54.6	2.4
−36.0	55.5	2.45	0.13	18.5	−44.0	1.5
−48.0	55.5	2.12	0.09	23.5	−48.4	1.2
−60.0	55.5	2.15	0.07	29.0	−46.5	1.0
−72.0	55.5	2.32	0.07	33.7	−43.9	0.8
−84.0	55.5	3.06	0.10	31.2	−38.8	0.9
−96.0	55.5	2.12	0.15	14.5	−25.0	2.0
−108.0	55.5	2.66	0.30	8.8	−27.9	3.3
−120.0	55.5	3.34	0.34	9.7	−38.8	2.9
−132.0	55.5	2.75	0.52	5.3	−17.8	5.4
−24.0	67.5	2.75	0.38	7.2	−52.8	4.0
−36.0	67.5	2.52	0.23	11.1	−57.2	2.6
−48.0	67.5	2.75	0.14	19.2	−44.6	1.5
−60.0	67.5	2.85	0.10	28.3	−51.0	1.0
−72.0	67.5	2.60	0.06	40.9	−46.3	0.7
−84.0	67.5	2.32	0.08	29.2	−34.5	1.0
−96.0	67.5	2.72	0.13	20.5	−45.7	1.4
−108.0	67.5	2.36	0.24	9.9	−18.2	2.9
−120.0	67.5	2.45	0.37	6.7	−89.1	4.3
−132.0	67.5	3.01	0.44	6.9	4.1	4.2
−144.0	67.5	4.33	0.56	7.8	−15.2	3.7
−36.0	79.5	3.78	0.30	12.6	−43.4	2.3
−48.0	79.5	3.23	0.20	16.3	−49.9	1.8
−60.0	79.5	3.70	0.15	24.5	−54.7	1.2
−72.0	79.5	3.54	0.10	35.2	−52.4	0.8
−84.0	79.5	2.31	0.11	21.8	−55.3	1.3
−96.0	79.5	2.50	0.14	17.8	−50.9	1.6

Table 4.3 (continued)

Δ R.A. (″)	Δ DEC. (″)	p (%)	dp (%)	σ_p	θ (°)	$d\theta$ (°)
−108.0	79.5	1.48	0.22	6.6	−27.8	4.3
−120.0	79.5	3.18	0.33	9.6	13.9	3.0
−132.0	79.5	3.52	0.36	9.7	−19.5	2.9
−144.0	79.5	4.01	0.59	6.8	−17.6	4.2
−36.0	91.5	7.85	0.55	14.3	−33.9	2.0
−48.0	91.5	5.37	0.35	15.5	−53.0	1.8
−60.0	91.5	5.59	0.21	26.4	−52.3	1.1
−72.0	91.5	5.22	0.20	26.6	−51.5	1.1
−84.0	91.5	5.14	0.17	30.8	−47.1	0.9
−96.0	91.5	4.52	0.23	19.8	−49.6	1.4
−108.0	91.5	1.87	0.25	7.3	−38.3	3.9
−120.0	91.5	2.93	0.25	11.9	−23.9	2.4
−132.0	91.5	3.30	0.26	12.6	−6.4	2.3
−144.0	91.5	7.69	0.60	12.9	−10.0	2.2
−48.0	103.5	12.31	0.98	12.5	−68.5	2.3
−60.0	103.5	6.95	0.45	15.4	−46.7	1.9
−72.0	103.5	6.64	0.29	22.8	−45.1	1.3
−84.0	103.5	5.15	0.27	19.1	−62.3	1.5
−96.0	103.5	3.50	0.38	9.3	−36.7	3.1
−108.0	103.5	2.50	0.33	7.6	−18.5	3.8
−120.0	103.5	1.97	0.22	9.1	−38.6	3.2
−132.0	103.5	3.55	0.21	16.8	−24.7	1.7
−144.0	103.5	5.90	0.59	10.0	−16.9	2.9
−60.0	115.5	4.20	0.77	5.5	−42.0	5.3
−72.0	115.5	6.35	0.44	14.5	−48.1	2.0
−84.0	115.5	6.91	0.39	17.9	−52.8	1.6
−96.0	115.5	4.45	0.55	8.0	−38.5	3.6
−108.0	115.5	2.98	0.47	6.4	−50.6	4.5
−120.0	115.5	3.90	0.22	17.8	−27.3	1.6
−132.0	115.5	4.37	0.28	15.4	−9.0	1.9
−72.0	127.5	6.26	0.72	8.6	−45.4	3.3
−84.0	127.5	8.35	0.55	15.3	−43.4	1.9
−96.0	127.5	4.39	0.53	8.3	−10.6	3.5
−108.0	127.5	1.85	0.50	3.7	−19.9	7.8
−120.0	127.5	5.48	0.42	13.0	−46.6	2.2
−132.0	127.5	5.77	0.80	7.2	−61.8	4.0
−96.0	139.5	3.82	0.89	4.3	3.6	6.7

Bibliography

Aitken, D. K., Greaves, J., Chrysostomou, A., Jenness, T., Holland, W., Hough, J. H., Pierce-Price, D., & Richer, J., 2000. *ApJ Letters* **534**, L173.

Alves, J. ., Lada, C. J., & Lada, E. A., 1999. *ApJ* **515**, 265.

Aso, Y., Tatematsu, K., Sekimoto, Y., Nakano, T., Umemoto, T., Koyama, K., & Yamamoto, S., 2000. *ApJS* **131**, 465.

Breger, M., 1976. *ApJ* **204**, 789.

Brown, J. C., 2001. *The Magnetic Field in the Outer Galaxy*. Ph. D. thesis, Dept. of Physics and Astronomy; University of Calgary, Calgary.

Carlqvist, P. & Kristen, H., 1997. *A&A* **324**, 1115.

Chandrasekhar, S. & Fermi, E., 1953. *ApJ* **118**, 113.

Chini, R., Reipurth, B., Ward-Thompson, D., Bally, J., Nyman, L. ., Sievers, A., & Billawala, Y., 1997. *ApJ Letters* **474**, L135.

Coppin, K. E. K., Greaves, J. S., Jenness, T., & Holland, W. S., 2000. *A&A* **356**, 1031.

Crutcher, R. M., 1999. *ApJ* **520**, 706.

Crutcher, R. M., Troland, T. H., Lazareff, B., Paubert, G., & Kazès, I., 1999. *ApJ Letters* **514**, L121.

Dotson, J. L., Davidson, J., Dowell, C. D., Schleuning, D. A., & Hildebrand, R. H., 2000. *ApJS* **128**, 335.

Dowell, C. D., 2001. *ApJ in preparation*.

Dowell, C. D., Hildebrand, R. H., Schleuning, D. A., Vaillancourt, J. E., Dotson, J. L., Novak, G., Renbarger, T., & Houde, M., 1998. *ApJ* **504**, 588.

Draine, B. T. & Weingartner, J. C., 1996. *ApJ* **470**, 551.

Fiege, J. D. & Henriksen, R. N., 1996. *MNRAS* **281**, 1038.

Fiege, J. D. & Pudritz, R. E., 2000a. *MNRAS* **311**, 85.

Fiege, J. D. & Pudritz, R. E., 2000b. *MNRAS* **311**, 105.

Fiege, J. D. & Pudritz, R. E., 2000c. *ApJ* **544**, 830.

Girart, J., Crutcher, R. M., & Rao, R., 1999. *ApJ Letters* **525**, L109.

Greaves, J., Holland, W., Chrysostomou, A., & Jenness, T., 2000. Imaging the polarized interstellar medium. In *Imaging at Radio through Submillimeter Wavelengths. Edited by Jeff Mangum. Publisher: The Astronomical Society of the Pacific, Conference Series, 2000. The conference was held June 6-8, 1999, in Tucson, Arizona.*, pp. E18.

Greaves, J., Holland, W., Jenness, T., Moriarty-Schieven, G., Chrysostomou, A., Berry, D., Murray, A., Nartallo, R., Ade, P., Gannaway, F., Haynes, C., Tamura, M., Momose, M., & Morino, J., 2001. *MNRAS in preparation.*

Greaves, J. S., Holland, W. S., & Ward-Thompson, D., 2001. *ApJ Letters* **546**, L53.

Heiles, C., 1987. Interstellar magnetic fields. In *ASSL Vol. 134: Interstellar Processes*, pp. 171.

Heiles, C., 1997. *ApJS* **111**, 245.

Hildebrand, R. H., 1988. *QJRAS* **29**, 327.

Hildebrand, R. H., Davidson, J. A., Dotson, J. L., Dowell, C. D., Novak, G., & Vaillancourt, J. E., 2000. *PASP* **112**, 1215.

Hildebrand, R. H., Dotson, J. L., Dowell, C. D., Schleuning, D. A., & Vaillancourt, J. E., 1999. *ApJ* **516**, 834.

Holland, W. S., Greaves, J. S., Ward-Thompson, D., & Andre, P., 1996. *A&A* **309**, 267.

Jenness, T., Lightfoot, J. F., & Holland, W. S., 1998. *Proc. SPIE* **3357**, 548.

Johnstone, D., 2001. *private communication.*

Johnstone, D. & Bally, J., 1999. *ApJ Letters* **510**, L49.

Kraus, J. D., 1986. *Radio astronomy.* Powell, Ohio: Cygnus-Quasar Books, 1986.

Lada, C. J., Alves, J., & Lada, E. A., 1999. *ApJ* **512**, 250.

Matthews, B., Fiege, J., & Moriarty-Schieven, G., 2001. *ApJ in preparation.*

Matthews, B. C. & Wilson, C. D., 2000. *ApJ* **531**, 868.

Nakamura, F., Hanawa, T., & Nakano, T., 1993. *PASJ* **45**, 551.

Ostriker, J., 1964. *ApJ* **140**, 1056.

Pudritz, R. E., 1985. *ApJ* **293**, 216.

Purcell, E. M., 1979. *ApJ* **231**, 404.

Rao, R., Crutcher, R. M., Plambeck, R. L., & Wright, M. C. H., 1998. *ApJ Letters* **502**, L75.

Schleuning, D. A., 1998. *ApJ* **493**, 811.

Schleuning, D. A., Dowell, C. D., Hildebrand, R. H., Platt, S. R., & Novak, G., 1997. *PASP* **109**, 307.

Shu, F., Najita, J., Ostriker, E., Wilkin, F., Ruden, S., & Lizano, S., 1994. *ApJ* **429**, 781.

Shu, F. H., Adams, F. C., & Lizano, S., 1987. *ARA&A* **25**, 23.

Uchida, Y. & Shibata, K., 1985. *PASJ* **37**, 515.

Ungerechts, H., Bergin, E. A., Goldsmith, P. F., Irvine, W. M., Schloerb, F. P., & Snell, R. L., 1997. *ApJ* **482**, 245.

Vrba, F. J., Strom, S. E., & Strom, K. M., 1988. *AJ* **96**, 680.

Ward-Thompson, D., Kirk, J. M., Crutcher, R. M., Greaves, J. S., Holland, W. S., & André, P., 2000. *ApJ Letters* **537**, L135.

Yu, K., Billawala, Y., Smith, M. D., Bally, J., & Butner, H. M., 2000. *AJ* **120**, 1974.

Chapter 5

Submillimetre Polarimetry of Intermediate Mass Cores and Filaments in Orion B

This chapter is a draft of the article "Magnetic Fields in Star-Forming Molecular Clouds III. Submillimetre Polarimetry of Intermediate Mass Cores and Filaments in Orion B" by B.C. Matthews, J.D. Fiege and G.H. Moriarty-Schieven, which has been submitted for publication to The Astrophysical Journal.

The breakdown of writing for this article was as follows. §5.1 was written jointly by GMS and BCM. BCM wrote the entirety of §5.2, but the map of Saturn used for the analysis of §5.2.1 was obtained by GMS. All the reduction and analysis of the data was done by BCM. The opening remarks in §5.3 are by JDF, with the sections on the individual objects written by BCM and GMS. BCM wrote §5.3.2. All data maps, plots and schematic illustrations are by BCM, with the exception of the two models presented in §5.4. The opening remarks of §5.4 and parts of §5.4.1 were written by JDF. BCM contributed some text to §5.4.1 and wrote §5.4.2 and 5.4.3. The sections on the models of NGC 2024, §5.4.3.1 and 5.4.3.2, were written primarily by JDF with some contributions by BCM on the geometry of the region. The summary, §5.5, was written by BCM, and Appendix 5A was compiled by BCM.

Abstract

Using the imaging polarimeter for the Submillimetre Common User Bolometric Array at the James Clerk Maxwell Telescope, we have detected polarized thermal emission at 850 μm from dust toward three star-forming core systems in the Orion B molecular cloud: NGC 2071, NGC 2024 and LBS 23N (HH 24). The polarization patterns are not indicative of those expected for unidirectional magnetic fields, and all exhibit diminished polarization percentages toward the highest intensity peaks. NGC 2024 has the most organized polarization pattern which is centred consistently along the length of a chain of 7 far-infrared sources. We have modelled NGC 2024 using a helical field geometry threading a curved filament and also as a magnetic field swept up by the ionization front of the expanding HII region. In the latter case, the field is bent by the dense ridge, which accounts for both the polarization pattern and existing measurements of the line-of-sight field strength toward the northern cores FIR 1 to FIR 4. The direction of the net magnetic field direction within NGC 2071 is perpendicular to the dominant outflow in that region, and the polarization emission may in fact be dominated by the CO $J = 3 - 2$ line.

5.1 Introduction

The Orion B (L1630) molecular cloud, at a distance of 415 pc (Anthony-Twarog 1982), is one of the nearest giant molecular clouds and is an active site of low- to high-mass star formation. It was one of the first clouds to be systematically studied for dense cores by Lada, Bally, & Stark (1991), who found that massive star formation takes place only in the five largest clumps, which together make up more than 50% of the mass of dense gas. We have chosen three of these five clumps, NGC 2071IR (LBS 8), NGC 2024 (LBS 33), and HH24 (LBS 23), for the current study. A fourth region, NGC 2068, contains a string of substantially smaller, fainter cores connected by weak dusty filaments (Mitchell et al. 2001). Polarimetry of this region will be presented in a forthcoming paper (Matthews & Wilson 2001).

Although the three regions have comparable gas masses, ranging from 230-460 $M_\odot$ (Lada, Bally, & Stark 1991), they have very different star formation properties. NGC 2024 is an HII region and the most prominent star formation region in Orion B, associated with a massive cluster, ionizing B stars, and stars at all phases of evolution (Mezger et al. 1988; Lada et al. 1991; Chandler & Carlstrom 1996). The submillimetre continuum emission was discovered by Mezger et al. (1988). The emission arises from a dense ridge of gas and dust behind the HII region, determined from the velocity of associated gas (Crutcher et al. 1986; Barnes et al. 1989), and consists of at least seven sources aligned along a ridge, similar to OMC-3 in Orion A (Johnstone & Bally 1999; Matthews & Wilson 2000; Matthews, Wilson, & Fiege 2001) although in the latter region significantly more mass exists in the filamentary gas. Two of these cores (FIR 4 and FIR 5) are the origins of unipolar molecular outflows, one of which is very highly collimated and very extended (Sanders & Willner 1985; Richer et al. 1992; Chandler & Carlstrom 1996), while the FIR 6 core exhibits a compact outflow (Chandler & Carlstrom 1996) and contains a water maser (Genzel & Downes 1977), a signature of intermediate-mass protostars. The rest of the cores show no sign of star formation activity (Visser et al. 1998).

NGC 2071IR lies four arcminutes north of the reflection nebula NGC 2071. This extended submillimetre source consists of a cluster of at least nine embedded infrared stars (Walther et al. 1993) with a combined infrared luminosity of 520 $L_{\odot}$ (Butner et al. 1990). The source IRS3 is thought to be the driving source of a massive bipolar molecular outflow (Bally 1982; Snell et al. 1984; Moriarty-Schieven et al. 1989; Eislöffel 2000). Houde et al. (2001) infer alignment between the outflow and its magnetic field by comparison of spectral lines of neutral and ionic species. Shocked molecular hydrogen (Bally & Lane 1982) and H_2O masers (Genzel & Downes 1979) are also seen towards this region, which is in a later evolutionary stage than NGC 2024 (Launhardt et al. 1996). Eislöffel (2000) has also documented several other outflows in the region. Based on a comparison between submillimetre continuum and CO(3-2) and HCO^+ line data, Motte et al. (2001) suggest that 20-100% of the 850 μm emission in the outflow region could originate from the line contamination.

By contrast with the other two regions, the HH 24-26 (LBS 23) cores have relatively little extended submillimetre emission and are mostly compact (Launhardt et al. 1996; Lis et al. 1999) and cold (<10K, Chini et al. 1993). Of the twelve condensations identified by Lis et al. (1999), our polarimetric image covers LMZ 2, 3, and 4. All three of these cores have 3.6 cm continuum sources (Bontemps, Andre, & Ward-Thompson 1995; Gibb 1999). LMZ 3 (also known as HH24MMS, Chini et al. 1993) is a class 0 protostar (Bontemps et al. 1995), while LMZ 4 is a T Tauri star with a known CO outflow (Snell & Edwards 1982; Gibb & Heaton 1993). These are all indicators of purely low-mass star formation.

Magnetic fields play a significant, even crucial role in the process of star formation, through magnetic support of molecular clouds, dissipation of angular momentum in accretion disks, and the generation of jets and outflows (see Heiles et al. (1993), and references therein). Polarized thermal emission at submillimetre wavelengths from aligned dust grains directly traces the direction of the magnetic field structure projected onto the plane of the sky (Hildebrand 1988), unlike absorption polarimetry which can be contaminated by scattering at short wavelengths. With the recent development of focal plane bolometer arrays equipped with polarimeters, sensitive imaging polarimetry in the submillimetre is now possible.

Imaging polarimeters functioning at 100 μm (aboard the Kuiper Airborne Observatory), 350 μm (at the Caltech Submillimeter Observatory), and 850 μm (at the James Clerk Maxwell Telescope) have detected polarized emission from dust toward many Galactic molecular clouds. These include the well-studied OMC-1 core in Orion (Schleuning 1998; Schleuning et al. 1997; Coppin et al. 2000; Dotson et al. 2000); Sagittarius A (Aitken et al. 2000); Sagittarius B2 (Dowell et al. 1998) and recently OMC-3 in Orion (Matthews & Wilson 2000; Matthews, Wilson, & Fiege 2001; Dowell 2001). Numerous protostellar and starless cores have also been mapped (i.e. Holland et al. 1996; Ward-Thompson et al. 2000).

Polarimetry provides information only on the plane-of-sky magnetic field orientation, but no information about the magnetic field strength, since the degree of alignment is also dependent on other factors such as grain shape, degree of alignment, and composition. To garner information about the magnetic field strength requires observation of Zeeman splitting of molecular or atomic spectral lines, which additionally provides information about the direction of the field along the line of sight.

In this paper, we present the first submillimetre polarimetry of the NGC 2071 core and the LBS 23N region. Zeeman observations do not exist toward either of these two clouds. Far-infrared polarimetry at 100 μm (Dotson et al. 2000) and Zeeman splitting observations of OH (Crutcher & Kazes 1983; Kazes & Crutcher 1986; Crutcher et al. 1999) exist for the NGC 2024 ridge of cores. In § 5.2, we describe the 850 μm observations and the data reduction. The data are presented in § 5.3 and the polarization patterns are interpreted in § 5.4. We summarize our results in § 5.5.

5.2 Observations and Data Reduction

The observations presented here were obtained on 1998 September 7 and 8 using SCUBA (Submillimetre Common User Bolometer Array) (Holland et al. 1999) at the James Clerk Maxwell Telescope[1] combined with the SCUBA polarimeter (Greaves et al. 2000; Greaves et al. 2001). The nights were very stable, with τ(225GHz) ranging from 0.05 to 0.07 during the period of observations. Calibration of the polarizer was performed on 1998 September 5 using the Crab Nebula, for which a percentage polarization $p = 19.3 \pm 4\%$ and position angle $\theta = 155 \pm 5°$ were measured.

Observations were made of two overlapping fields toward NGC 2024, and one field each toward NGC 2071 and LBS 23N. Each polarization cycle consists of 16 integrations at 22.5° rotation intervals in 8 minutes integration time. Six observations (48 minutes integration time) were made toward NGC 2071 and each position toward NGC 2024, and 27 observations (3.6 hours integration time) were made toward LBS 23N.

For each polarization cycle map, the raw SCUBA data were reduced using standard SCUBA software (Holland et al. 1999) to perform nod compensation, flatfielding and extinction corrections. More information on the polarimeter and its data cycle can be found in Greaves et al. (2000). For polarimetry data, extinction is estimated by extrapolation from the current CSO tau value at 225 GHz. Bolometers with anomalously high noise were then flagged, and the data were clipped at the 10 σ level. Sky noise and instrumental polarization (IP) removal was then performed. The removal of sky noise is, even for basic SCUBA data, a task fraught with danger, but is even more so for polarimetry. The techniques of sky removal are discussed in detail in Matthews, Wilson, & Fiege (2001); we have taken care to select empty

[1]The JCMT is operated by the Royal Observatory Edinburgh on behalf of the Particle Physics and Astronomy Research Council of the United Kingdom, the Netherlands Organization for Scientific Research, and the National Research Council of Canada.

bolometers for sky subtraction.

To first order, the removal of sky effects is achieved by chopping the JCMT secondary during SCUBA observations. Systematic errors can be introduced if significant polarized flux exists at the chop, or reference, positions. Large chop throws of 150″ were used for these observations (180″ is the maximum for the JCMT) to try to chop as far off the bright emission as possible. The possible effects of polarized flux in the reference beams (or bolometers used for sky removal) are discussed by Matthews, Wilson, & Fiege (2001).

Since we have access to large-scale 850 μm scan maps of Orion B north (Mitchell et al. 2001) and south obtained by the Canadian Consortium for Star Formation Studies at the JCMT, comparisons can be made between intensities of candidate bolometers for sky noise subtraction in the on-source position and the fluxes in the corresponding chop positions. For two of our regions, NGC 2024 and NGC 2071, comparison reveals that the differences between these two positions are significant, and that no bolometers on-source were "empty". The region around LBS 23N, on the other hand, reveals the same flux levels at the chop positions as at the edges of the on-source pointing. Thus, some bolometers at the edges of that map had average intensities of zero. To deal with sky bolometers which do not contain zero flux, the mean value per bolometer removed during sky noise subtraction is added back into the maps of NGC 2024 and NGC 2071, increasing the intensity in each bolometer. The main consequence of this addition is to reduce the polarization percentage, which is inversely proportional to I.

After correcting for source rotation across the array, the Stokes' parameters were calculated by comparing measurements offset by 45° in waveplate rotation (90° on the sky). The I, Q, and U maps for each pointing centre were averaged, and standard deviations were derived by comparing the individual data sets. The two overlapping fields toward NGC 2024 were then combined into a mosaic; polarization data are uncalibrated, so the data were combined simply by averaging. Since no absolute flux calibrations are done on polarimetry data, the zero points are unknown. This presents problems for creating maps requiring more than one SCUBA field, since one does not know which field contains the best base level to use as reference. We want to obtain the best estimates of uncalibrated flux without giving undue weight to either of our mapped fields. This was done by averaging the baseline levels in the two maps.

The maps were then binned spatially by a factor of 3 (NGC 2071) or 4 (NGC 2024 and LBS 23N) in both RA and DEC to yield 9 or 12″ sampling. Selection of "good" polarization vectors is done by filtering out all vectors for which $p < 1\%$ (since the IP values are accurate to just $\pm 0.5\%$) and then filtering by signal-to-noise of polarization percentage, uncertainty of polarization percentage, and the intensity level as appropriate to each field. The thresholding of p ensures that the effects of sidelobe polarization are low (see § 5.2.1). As further confirmation of the observed polarization patterns, we divided the data sets for each source into two subsets and performed complete reduction on each. The polarization patterns were qualitatively consistent with one another in all cases.

We have truncated our selection of vectors at levels of 2% of the NGC 2071IR peak intensity, 2.5% of the NGC 2024 source peak and 4% of the LBS 23N peak. Matthews, Wilson, & Fiege (2001) illustrate that percentage polarizations and position angles are reliable down to these levels in cases where the reference position's intensity is approximately 2% of the source peak intensity and the polarization percentage in the reference position is no greater than that of the source field. Thus, in the lowest flux regions, the polarization percentage could be overestimated by up to a factor of two while the polarization position angle is incorrect by $< \pm 10°$. Since JCMT data obtained by chopping off the source record only the difference between these two positions, our data provide no information about the polarized emission at the reference position. However, based on more extensive intensity maps produced by the scan-mapping technique, the chop positions are approximately 1%, 2% and $< 1\%$ of the on-source peaks for NGC 2071IR, NGC 2024, and LBS 23N respectively. These are effectively lower limits to the fractional fluxes relative to the peaks, since scan mapping data may remove the fluxes of very extended features. If there is a uniform background chopped out of the scan maps as well, then the reference position could in fact contain a more significant fraction of the source peak flux.

5.2.1 Sidelobe Polarization

Even though the sidelobes of the JCMT beam contain less than 1% of the main beam power at 850 μm, significant polarization can be measured there because the two incoming planes of polarization experience different optical effects. This can produce significant *sidelobe polarization*, that can become a source of systematic error especially when mapping extended fields in which the source located in the main beam is fainter than sources elsewhere in the SCUBA field. One can estimate the minimum believable source polarization percentage from the expression:

$$p_{crit} \geq 2 \times p_{sl} \left(\frac{P_{sl}}{P_{mb}}\right) \left(\frac{F_{sl}}{F}\right) \tag{5.1}$$

where p_{sl} is the IP in the relevant part of the sidelobe, P_{sl}/P_{mb} is the ratio of the sidelobe power to that in the main beam, and F_{sl}/F is the ratio of the mapped source flux in the sidelobe to that in the main beam (Greaves et al. 2001). Basically, p_{crit} is an estimate of the polarization percentage produced by the sidelobe source alone; hence only polarizations in excess of that value are believable.

For the regions of NGC 2071 and LBS 23N, sidelobe polarization will be minimal, since in both those fields, the field centres were located at the submillimetre peaks. However, in NGC 2024, our northern mapping field was centred roughly on FIR 3, but FIR 5 was at the edge of the SCUBA map, approximately 70″ from the centre. The ratio of the FIR 5 flux to the central flux is ~ 3.4. Using a map of Saturn from 31 August 1998, the average power at $70''$ from the field centre is approximately 0.3% of the main beam. The average instrumental polarization is 5.5%. Substitution in equation (5.1) yields $p_{crit} \geq 0.11\%$. The planetary map was generated with a chop throw of $120''$, somewhat less than the $150''$ chop used in NGC 2024. However, using planetary data on Saturn from 11 October 1999 with a $150''$ chop, we obtain an estimate of $p_{crit} \geq 0.2\%$. Hence, we are confident that our thresholding of polarization percentage at 1% removes all effects of sidelobe polarization in our maps.

5.3 The Polarization Data

The polarized emission in the submillimetre is thermal emission originating from rapidly spinning non-spherical grains, which are expected to be aligned, on average, perpendicular to the magnetic field. The precise details of the alignment processes are not entirely understood. However, it is well understood that supra-thermally rotating grains align perpendicular to the magnetic field on very short time-scales (e.g. Purcell 1979). Thus, grain alignment depends critically on the mechanisms by which grains are accelerated to supra-thermal rotational velocities. Radiative torques from short wavelength radiation (Draine & Weingartner 1996) and the well-known Purcell "rocket" mechanism (Purcell 1979) have both been proposed as candidate mechanisms. At present, however, these mechanisms appear insufficient to accelerate grains to the required rotational speeds in dark regions of molecular clouds (Lazarian et al. 1997). However, the data presented in this paper, as well as recent papers by other authors (Dotson et al. 2000; Matthews & Wilson 2000; Schleuning 1998), provide clear evidence that the grains *are* aligned and that the underlying field structure is well-ordered, as evidenced by the highly structured polarized emission seen in our maps. This result poses an important challenge for grain alignment models.

The shapes of grains, their size distribution, their composition, and the details of their alignment mechanisms all strongly affect the ability of grains to produce polarized thermal radiation, and hence influence the resulting polarization patterns. Unfortunately, none of these factors are well-constrained, either theoretically or observationally. However, Fiege & Pudritz (2000c) developed a pragmatic approach which combines *all* of the grain and alignment properties for a distribution of grain species into a single parameter $\langle\alpha\rangle$, which can be obtained observationally. It is this parameter which permits modeling of polarization patterns without detailed knowledge of grain and alignment physics. It was assumed in Fiege & Pudritz (2000c) that all grain species are uniformly mixed with the gas and aligned to the same extent everywhere within the cloud, which implies that $\langle\alpha\rangle$ is constant within any given cloud. However, their model is easily extended to allow systematic variations in grain and alignment properties throughout the cloud, by simply allowing $\langle\alpha\rangle$ to be a function of either the density, or equivalently, the distance from the centre of the cloud. Fortunately, allowing $\langle\alpha\rangle$ to vary within a cloud does not usually have enormous consequences in terms of the predicted polarization patterns (Fiege, Matthews, & Moriarty-Schieven 2001). Thus, our models are quite robust to different models of the grain alignment and composition.

If we assume, for now, that $\langle\alpha\rangle$ is constant, then the maximum possible polarization percentage, for the most favourable geometry with a constant field parallel to the plane of the sky, is given by the formula

$$p_{max} = \frac{\langle\alpha\rangle}{1 - \langle\alpha\rangle/6} \tag{5.2}$$

(Fiege & Pudritz 2000c). Since the maximum polarization percentage observed in submillimetre polarization maps is rarely greater than 10%, Fiege & Pudritz (2000c) estimated that $\langle\alpha\rangle$ should be on the order of 0.1. Our maps provide us with an opportunity to verify this estimate. The maximum polarization percentages for the three regions that we have mapped are 15% for NGC 2071, 13% for NGC 2024, and 22% for LBS 23N. The value for LBS 23N may be anomalously high; the next highest percentage measured is 12.6%. Therefore, 15% is a reasonable maximum value for NGC 2071, with 13% an upper limit for NGC 2024 and LBS 23N. Using 10% as a reasonable limit to the order of polarization percentages in these regions, and assuming this is close to the theoretical maximum for a line of sight passing through a magnetic field with ideal geometry, then we find that $\langle\alpha\rangle \approx 0.1$ for all three regions. These estimates are really lower bounds for $\langle\alpha\rangle$ because the observed polarization percentage will be reduced by any component of the field not parallel to the plane of the sky along the line of sight giving the highest polarization percentage. Nevertheless, we are encouraged that our estimates of $\langle\alpha\rangle$ do not vary wildly between the three regions, and conclude that $\alpha = 0.1$ is a reasonable global estimate for $\langle\alpha\rangle$.

In the absence of a complete theoretical model for the grain alignment process, we will take a pragmatic approach by assuming that grains are preferentially aligned perpendicular to the magnetic field without singling out any particular grain alignment theory as the cause.

5.3.1 Polarization Patterns

5.3.1.1 NGC 2071

In Figure 5.1 we present the 850 μm polarization vectors of NGC 2071 IR, superposed on a false colour image of the 850 μm dust emission (from Mitchell et al. 2001). The inset shows a "blow-up" of the central region in order to show the weak polarization features better.

Toward the region of strongest emission (the IR cluster), the percentage polarization is quite weak, typically less than 2%. However, polarization as strong as 15%

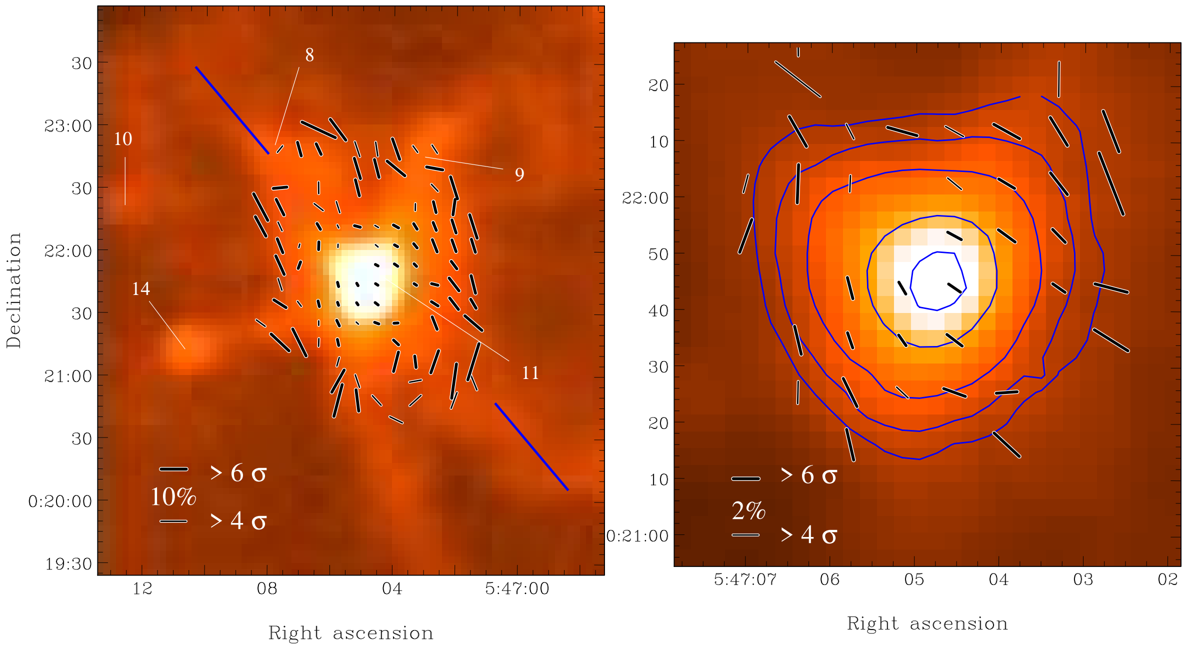

Figure 5.1: 850 μm polarization of NGC 2071.
Left: NGC 2071IR greyscale from (Mitchell et al. 2001) overlain with polarization vectors. The vectors are binned to 3 pixels (9″) so each vector represents just over half the 850 μm beamwidth (14″ at the JCMT). Vectors are only plotted where uncalibrated $I > 2\%$ of the source peak, polarization percentage exceeds 1% and the absolute uncertainty in polarization percentage is no greater than 1.5%. All vectors plotted have signal-to-noise in polarization percentage, $\sigma_p > 4$ (and therefore an uncertainty in position angle, $d\theta < 7.2°$), but bold vectors have $\sigma_p > 6$ ($d\theta < 4.8°$). Over the entire region, the mean position angle is 22° while the standard deviation is 32°. The mean polarization percentage is 5.1% with a standard deviation of 3.3%. Cores are labelled as in Mitchell et al. (2001), and blue lines mark the mean direction of the outflow from IRS 1. *Right:* Details of the central core (# 11 of Mitchell et al. 2001) with the same vector cutoffs except $I > 12\%$ of the peak flux. Blue contours trace the surface density in unpolarized 850 μm intensity. All coordinates are J2000.

is measured toward fainter parts of this region. The polarization pattern is highly symmetric, including the curvature of the vector orientation around the peak to the northeast and southwest. Over the entire core region, the vectors exhibit a mean orientation of 20° east of north. Closer to the peak, the dominant position angle is $\sim 30°$, which is within 10° of the orientation of the strongest outflow in the region (see Figure 5.1), which originates from the source IRS 1.

Motte et al. (2001) have compared the SCUBA 850 μm emission from NGC 2071 to pre-existing maps of CO $3-2$ and HCO^+ $4-3$ (Chernin & Masson 1992) and find that up to half the emission in the 850 μm bandpass could be originating in the outflow's line emission. Based on low-flow velocities of HCO^+ maps of the outflow, Girart et al. (1999) estimate the overall position angle to be $\approx 40°$ (east of north). Figure 5.1 shows this outflow orientation schematically. The outflow is well-aligned with the polarization vectors. If the polarization data are dominated by line emission, then the inferred field direction would align to within 10° of the CO outflow shown here, since in the case where lines are optically thick, the magnetic field will lie parallel to the observed polarization direction (Kylafis 1983).

Qualitatively, the polarization pattern is similar to that of OMC-1, which was interpreted as evidence for an hourglass magnetic field geometry in that region (Schleuning 1998). In this picture, the magnetic field is pinched toward the central source due to flux freezing with the infalling gas. However, we do not observe the flattening of the flux density profile toward NGC 2071 that is evident in the 350 μm flux map of OMC-1 (Schleuning 1998). The contours of the NGC 2071 as shown on Figure 5.1 are not oblate; even far from the peak, the core maintains a circular shape. There is no suggestion of oblateness or prolateness in this source.

5.3.1.2 LBS 23N

Figure 5.2 shows the dust polarization of the LBS 23N source and its surround-

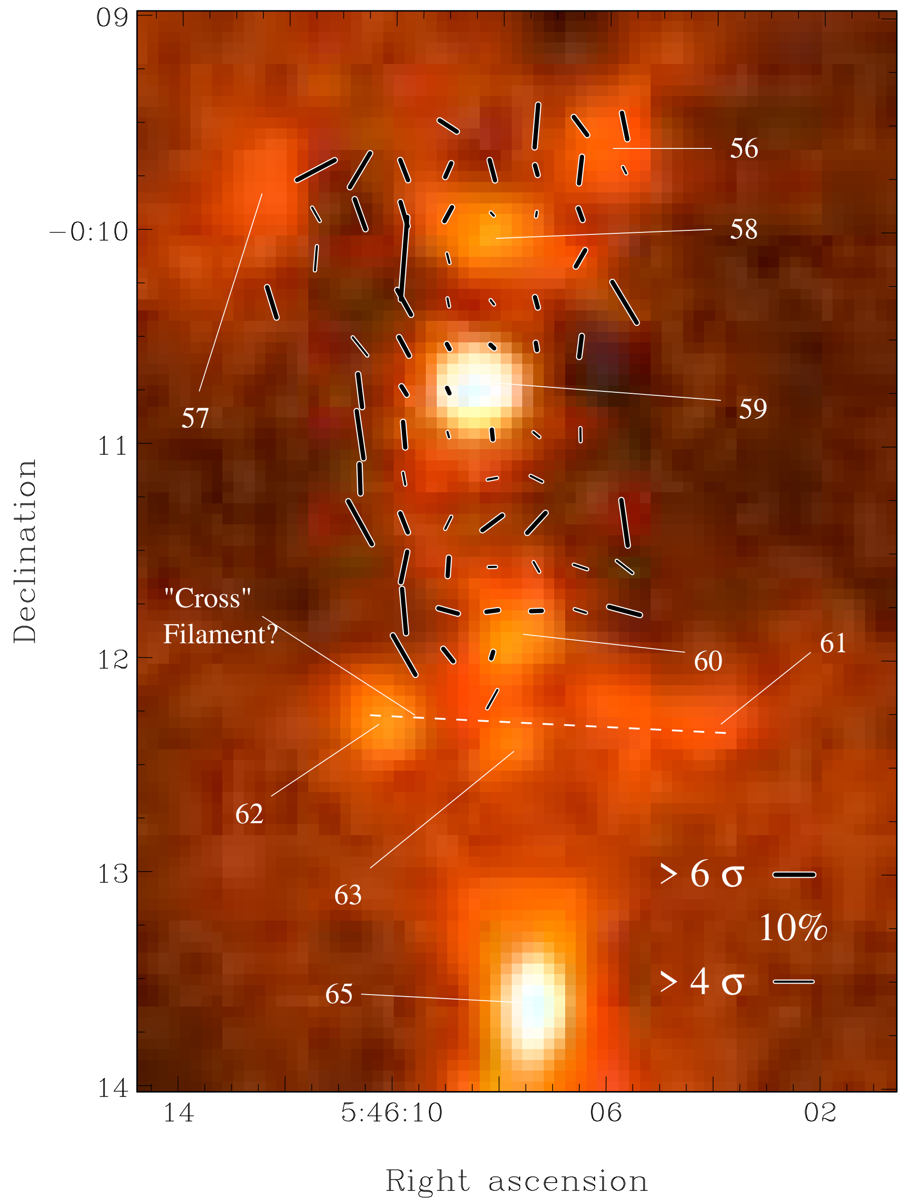

Figure 5.2: 850 μm polarization of LBS 23N.
LBS 23 greyscale is taken from Mitchell et al. (2001). The polarization vectors overlain have been binned to 12″. Vectors are plotted where $I > 4\%$ of the peak of core 59, $p > 1\%$, $dp < 1.5\%$ and $p/dp > 4$ ($d\theta < 7.2°$). Bold vectors show those where $p/dp > 6$ ($d\theta < 4.8°$). The core identifications are taken from Mitchell et al. (2001). The mean polarization percentage measured is 5.6% with a standard deviation of 3.8%. A potential "cross" filament could be oriented east-west and has been indicated by the presence of a dashed line. Coordinates are J2000.

ing region. A string of cores is overlain on a faint filamentary background of dust emission. The dominant orientation of the polarization pattern is north-south, except at the southern boundary, where the vectors lie almost east-west. The strongest polarization (22%) is seen in the east and west limbs of the "filament".

It is intriguing that at the southern-most boundary of our polarization map, the vectors are strongly aligned east-west. The 850 μm continuum map of Mitchell et al. (2001) shows that the underlying dust structure widens south of our polarization map to a filamentary segment oriented roughly east-west (see Figure 5.2). A similar shift of polarization orientation has been observed in the OMC-3 filament in Orion A where the filament's projected width on the plane of the sky appears to increase (Matthews & Wilson 2000; Matthews, Wilson, & Fiege 2001). As in the case of OMC-3, polarimetry in the southern region of LBS 23 will reveal whether the shift in vector orientation is related to changing inclination of the cloud to the plane of the sky, or perhaps the presence of a second filament oriented at 90° to the north-south line of cores. The faintness of the filamentary structure in LBS 23 will make it much more difficult to determine which interpretation is correct.

5.3.1.3 NGC 2024

The polarization pattern of the molecular ridge of NGC 2024 is shown in Figure 5.3, superimposed on a false colour image of the 850 μm dust emission.[2] Seven continuum sources (FIR 1-7) have been identified along the ridge (Mezger et al. 1988; Mezger et al. 1992). In the north (FIR 1-4), the vectors along the peaks are weak and parallel to the ridge. The southern sources (FIR 5-7) have very weak polarization toward the brightest cores and are significantly depolarized. To the east and west, the polarization becomes quite intense (up to 10%), and a change in

[2]JCMT data taken by Canadian Consortium for Star-Formation Studies, as yet unpublished.

vector orientation of approximately 90° is observed from west to east.

Linear polarization at 100 μm has been observed previously toward this region with the Kuiper Airborne Observatory (Hildebrand et al. 1995; Dotson et al. 2000). These data are centred on the FIR 5 core and cover the same area as our map. Figure 5.4 shows our polarization data and those of Dotson et al. (2000) at 100 μm plotted over contours of the 850 μm total emission. The 100 μm data are more sparsely sampled than the SCUBA data (owing to the 35″ beam), but the two patterns are remarkably consistent. The vectors trace the same V-shaped pattern seen at 850 μm, although the finer sampling by SCUBA makes the pattern much easier to see. The chop throw of the KAO observations was 10.5′, over four times greater than that used for our data set. The fact that the polarization patterns are very consistent suggests that the position angle at least has not been strongly affected by any systematic effects due to chopping. The maximum polarization percentage measured at 100 μm is $5.86^{+0.01}_{-1.00}$%, while the minimum vector has a polarization percentage of $0.36^{+0.06}_{-0.07}$% and a position angle of $164.9 \pm 5.2°$ (east of north), where the uncertainties are absolute upper limits. At roughly the same position, the 850 μm polarization is 1.63±0.15% at an angle of −20.7±2.7° (equivalent to 159.3±2.7°). This is a relatively low polarization percentage at 850 μm, and the position angles of the vectors agree within measurement uncertainties. At 850 μm, the maximum and minimum polarization percentages are 13.41 ± 1.13% and 1.02 ± 0.09%. Where the northern and southern parts of the filaments meet (i.e. between FIR 4 and 5), there is significant depolarization regardless of the low flux level. Depolarization in the filamentary material away from the cores is also observed between cores in OMC-3 in Orion A (see Matthews, Wilson, & Fiege 2001).

There is no obvious correspondence between the polarization position angles and the directions of outflows in the region. The strongest outflow is unipolar and extends from FIR 5 to the southeast (Richer, Hills & Padman 1992). Greaves, Holland & Ward-Thompson (2001) have measured polarized spectral line emission

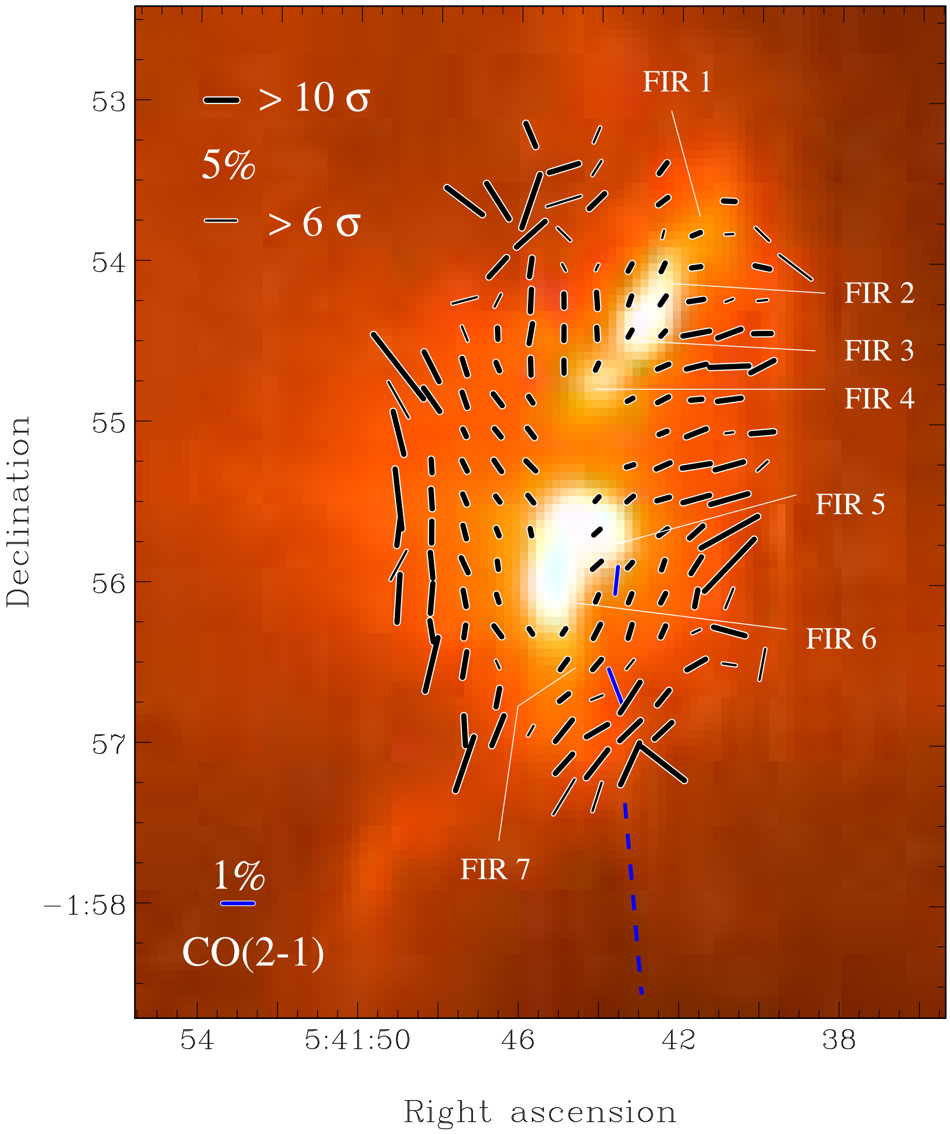

Figure 5.3: NGC 2024 850 μm polarization.
NGC 2024 greyscale overlain with polarization 12″ binned polarization vectors, almost the JCMT beamwidth of 14″ at 850 μm. Vectors are plotted where $I > 2.5\%$ of the FIR 5 peak, $p > 1\%$, $dp < 1\%$ and $p/dp > 6$ ($d\theta < 4.8°$). Bold vectors show those where $p/dp > 10$ ($d\theta < 2.9°$). Overall, these data represent the highest signal to noise polarization detections in our data set. The mean percentage polarization is 3.4% with a standard deviation of 2.3% in 159 vectors. The submillimetre cores are labelled as in Mezger et al. (1988). We have indicated the orientation of the FIR 5 unipolar outflow by a blue dashed line, and the CO $2-1$ line polarization vectors have been plotted (in blue) as measured by Greaves, Holland, & Ward-Thompson (2001). Coordinates are J2000.

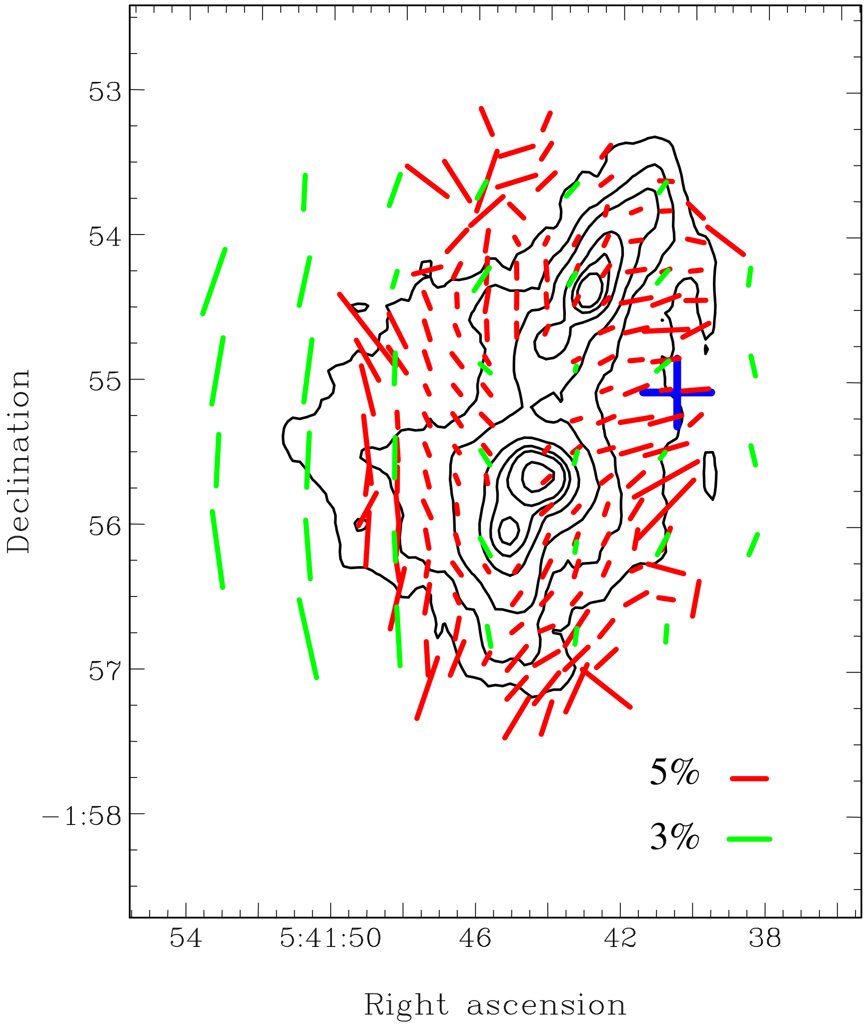

Figure 5.4: Comparison of Polarizations at 100 μm and 850 μm
Comparison of the polarization patterns at 850 μm (red) and 100 μm (green) reveals a strong consistency in position angle. The polarization percentages are considerably lower for 100 μm, possibly indicating that fewer dust grains are sampled within hotter dust or, more probably, that the dust grain alignment is lessened at higher temperatures. The 850 μm contours are plotted at 80, 90, 95, 98, 99, 99.5 and 99.9 percentiles. A blue cross marks the location of the maximum line of sight magnetic field as measured by Crutcher et al. (1999).

from the CO 2-1 line utilizing the Goldreich-Kylafis effect (Goldreich & Kylafis 1981) in the outflow of FIR 5. The polarization vectors measured in the outflow are plotted on Figure 5.3, along with the orientation of the outflow itself. For large CO optical depths, line polarization will be parallel to the field, unless the field is at a large angle to the velocity gradient (Kylafis 1983). Therefore, Greaves, Holland, & Ward-Thompson (2001) conclude that the magnetic field associated with the outflowing gas is aligned with the outflow itself. If the large scale field in the region maintains the same orientations, we would expect the continuum polarization vectors to lie perpendicular to the outflow. But the continuum vectors do not exhibit this behavior, nor is their orientation changed by their proximity to the outflow. Thus, we conclude that, with respect to the continuum polarization, a more complex field geometry may thread this region.

5.3.2 Depolarization toward High Intensities

As observed in many other regions, a declining polarization percentage is detected toward high intensity regions in each of our fields. This so-called "depolarization effect" is interesting because it implies that in regions of high density, the dust grains are less effectively aligned than in regions of low density. Figure 5.5 shows the percentage polarization as a function of unpolarized I for each region. The depolarization effect is clearly a global feature in our maps and is not limited to a single region or core. The slopes of Figure 5.5 range from -0.5 to -0.9, but the trend of declining polarization is clear. The same trend was measured in the OMC-3 region of Orion A (Matthews, Wilson, & Fiege 2001). This "depolarization effect" can be systematically produced by chopping to remove background sky during observing. However, Matthews, Wilson, & Fiege (2001) show that the depolarizations measured in Orion B cannot be produced by the effects of chopping alone. Therefore, there must be a physical reason why the depolarization is occurring.

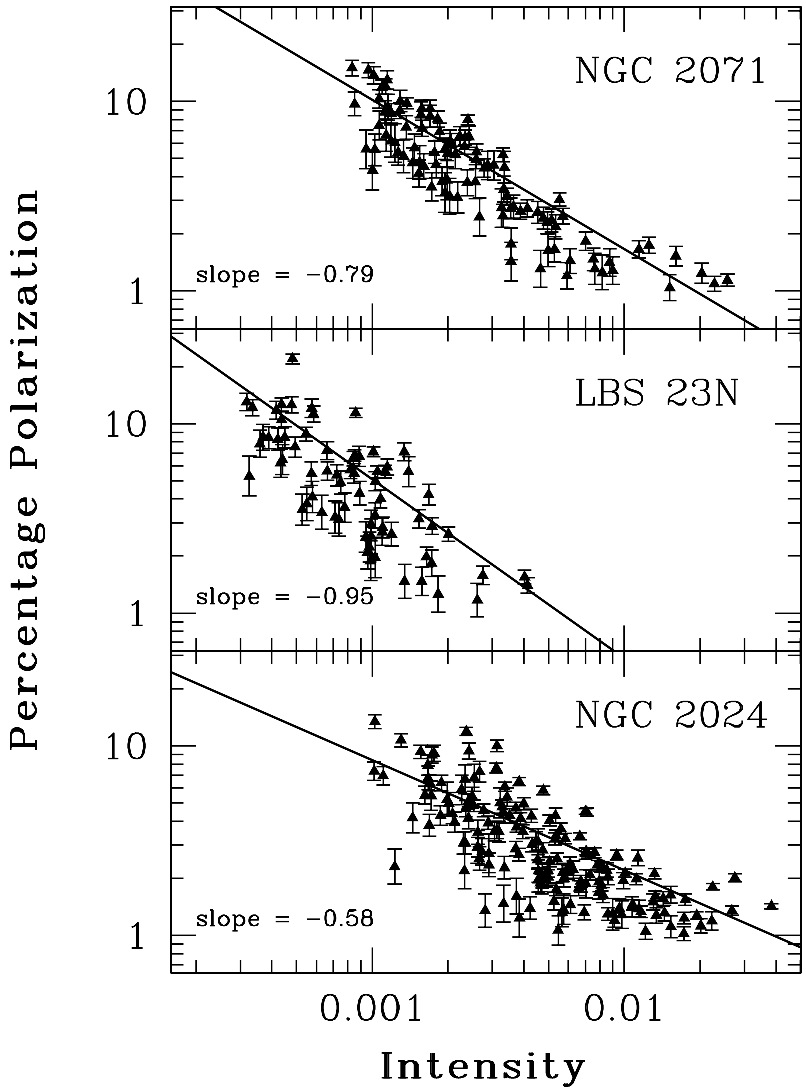

Figure 5.5: The Depolarization Effect in Orion B.
The depolarization effect typically seen in protostars and extended regions (such as OMC-3 in Orion A) is also observed in NGC 2071, NGC 2024 and LBS 23N. For all three regions, the brightest positions have the smallest polarizations, exhibiting $< 2\%$ whereas the faintest regions show polarizations approaching and exceeding 10%. Decreased polarization percentage is observed for a large range of I values in NGC 2024. This region's cores also contain the largest areas where depolarization is total, or the levels of polarization are so low (i.e. $< 1\%$) as to be consistent with zero. Extremely high volume densities (on the order of 10^8 cm^{-3}) have been estimated in NGC 2024 (Mezger et al. 1988).

The issue of depolarization in dense regions is particularly interesting as a test of alignment mechanisms. Grain alignment theories at present cannot explain why grains appear so well aligned in regions of intermediate density within molecular clouds. For example, the Purcell mechanism (Purcell 1979) and its variations are not likely to work in these dense regions, where atomic hydrogen is almost completely absent (Lazarian, Goodman, & Myers 1997). The radiative alignment mechanism (Draine & Weingartner 1996), which aligns grains efficiently in the ISM, is unlikely to work in dense molecular regions, where short wavelength starlight (needed to spin up and align grains) is blocked. Appealing to embedded sources to provide the necessary radiation is not likely to help, since this would predict the best alignment to be associated with the dense regions around evolved protostars, while the opposite is observed. Thus, our observations pose an interesting and extremely important challenge for grain alignment theory.

We consider 3 possible explanations for this "polarization hole" effect. First of all, it is possible that the polarization holes in our maps are the result of grains in the central regions of highest density that are either poorly aligned, or intrinsically poor polarizers (Weintraub et al. 2000; Goodman et al. 1995). In such a case, all dust grains through the cloud contribute to the continuum intensity, but only the fraction which are aligned can contribute to the polarized intensities of the Stokes' vectors Q and U. Therefore, toward regions of high intensity, the ratio of polarized to total intensities is systematically reduced. Alternatively, Fiege & Pudritz (2000c) proposed that the depolarization could be the result of the field structure itself, since helically twisted fields result in axial depolarization as a result of oppositely signed contributions to the Stokes' vectors from the poloidal and toroidal field components. This field geometry has been used to model the OMC-3 part of Orion A's Integral-shaped Filament (Matthews, Wilson, & Fiege 2001). A third possibility is that an unordered, or tangled, field exists on spatial scales smaller than our beam, and the field averages to zero in the JCMT's $14''$ beam. It is entirely possible that more than one of these effects could be contributing to the depolarization observed in our maps.

Interestingly, NGC 2071 does not exhibit a polarization hole coincident with the peak of the dust emission; instead, two polarization holes are detected, offset to the northeast and southwest of the dust emission peak. These polarization holes are not due to bad bolometers or low signal-to-noise. The degree of polarization in those locations is less than 1% and hence polarization can be considered insignificant at these positions. In NGC 2024, depolarization is so significant in the case of FIR 5-7 that polarization is negligible across those cores. In LBS 23N, depolarization can be seen in Figure 5.2 toward the brightest core, OriBN 59 (see Mitchell et al. 2001). It is difficult to sample the depolarization in the fainter sources of Figure 5.2 because they are unresolved, but OriBN 58 does show significant depolarization. Our mapping does not extend to the OriBN 60 core, and further data toward LBS 23 (south) will be needed to determine whether or not the observed depolarization extends to this region.

5.4 Interpreting Polarization Patterns

Polarization vectors in the submillimetre are perpendicular to the direction of the net magnetic field projected onto the plane of the sky. However, this interpretation should be used as a rough guide only. It is generally insufficient to infer the field structure by simply rotating the polarization vectors by 90°, since this procedure inherently assumes that the dominant component of magnetic field is 2-dimensional and parallel to the plane of the sky, and that the magnetic field orientation is constant through the depth of the cloud. Magnetic fields in star-forming gas are almost certainly complex and inherently three dimensional. A simple example serves to illustrate the difficulty. Fiege & Pudritz (2000c) recently calculated the polarized emission from their models of filamentary clouds threaded by helical magnetic fields

(Fiege & Pudritz 2000a). They demonstrated that the polarization is always parallel or perpendicular to the symmetry axis of the filaments in the plane of the sky, (sometimes with sudden 90° flips in orientation at some radial distance). Therefore, a complex underlying field geometry can produce highly aligned polarization data. *Simply rotating the polarization vectors derived from their models does not recover the input field geometries.* This cautionary result is quite general and is probably of even greater importance for interpreting the more complex polarization patterns observed in cores.

It is important to note that there is a degeneracy associated with polarization data. Variations in the field geometry, grain physics and degree of alignment can be made which can generate different field models which can produce the same polarization signature. The situation is not hopeless, however. There are many competing models of magnetized filaments and cores, which are reasonable on theoretical grounds and can be tested using the polarimetry data that are now becoming available. Most existing models of filaments make the reasonable simplifying assumption that such apparently axisymmetric objects are threaded by axisymmetric fields (thus, they implicitly assume that the ordered field component dominated over any random, or turbulent, component). The magnetic field might be purely poloidal (Chandrasekhar & Fermi 1953; Stodólkiewicz 1963; Nagasawa 1987; Gehman, Adams, & Watkins 1996), or it might be twisted into a helix (Nakamura, Hanawa, & Nakano 1993; Fiege & Pudritz 2000a). Cores have generally been modeled as axisymmetric objects that are threaded by purely poloidal fields and flattened into an oblate shape as a result of magnetic stresses (i.e. Mouschovias 1976; Tomisaka et al. 1988). More recently, Fiege & Pudritz (2000d) proposed that cores might inherit a magnetic field with a toroidal component from a parent filament threaded by a helical field. The magnetic stresses in these models work primarily in the opposite sense, squeezing them into a prolate shape. Basu (2000) suggests that cores are in fact neither oblate nor prolate but triaxial and under this model relates the field geometry to the projected minor axes of cores.

A viable model should simultaneously account for the orientation of the polarization vectors, the variation of the polarization percentage across the map, the projected surface density structure (as inferred from the submillimetre flux), and the orientation of the inferred magnetic field relative to the dense structures in the gas. Since magnetic fields play an important role in shaping the underlying structures (see Mouschovias 1976; Tomisaka et al. 1988; Fiege & Pudritz 2000a; Fiege & Pudritz 2000c for example), this combination of information can help to constrain models much better than considering the polarization data in isolation. Certainly, our procedure is adequate to reject models that are qualitatively inconsistent with the data. Moreover, we find that certain field structures produce identifiable, although sometimes surprising, "signatures" in the polarization data, which can be used as a guide toward developing detailed models.

Alternatively, one could compare the data with polarization maps predicted from simulations. The resulting field structures will not generally be axisymmetric, and the polarization patterns may be quite complex. The main drawback of this technique is that it cannot be used to model the field structure in individual objects. However, some insight might be obtained for the general statistical behavior of polarization maps for ensembles of objects.

5.4.1 NGC 2071

Since NGC 2071 exhibits virtually no filamentary structure, it must be assessed in terms of core models. The massive nature of this core also lends itself easily to comparison with the OMC-1 core of Orion A. There are no Zeeman data toward this region, so only the polarization data constrain the field geometry. The polarization map is similar to the 100 μm polarization map of the KL core in Orion A made by Schleuning (1998). In that region, the field configuration deduced was an "hourglass" magnetic field, created as the core contracted perpendicular to field lines. However, there is an important difference between Figure 5.1 and Schleuning's 100 and 350 μm maps. The KL core is a flattened structure, whose long axis (in projection) is parallel to the mean direction of the polarization vectors. This is precisely what one would expect for an oblate core threaded by an hourglass field (Mouschovias 1976; Tomisaka et al. 1988). The NGC 2071 core, however, is not flattened at all. There is no evidence of elongation either parallel or perpendicular to the outflow, either in our data (see Figure 5.1) or the 50 and 100 μm observations of Butner et al. (1990).

A recent comparison of line profiles of the coexisting neutral (HCN) and ionic (HCO^+) species by Houde et al. (2001) shows that there is alignment of a magnetic field with the highly collimated outflow from the NGC 2071, for which IRS 1 is thought to be the source. This is strong evidence for magnetization in the outflow, which is predicted by theory, but does not suggest that the larger scale field structure of the core sampled by Figure 5.1 must be correlated to the outflow field direction. Motte et al. (2001) estimate that 20-100% of the continuum emission at 850 μm could arise from the CO $J = 3 - 2$ line. Since SCUBA polarimetry is sensitive to both the continuum and line polarizations, both could be detected simultaneously. Even if the fields of the core and outflow are aligned, however, their polarization patterns can be very different. Using BIMA, Girart, Crutcher, & Rao (1999) mapped the 1.3 mm continuum polarization of the protostellar core NGC 1333 IRAS 4A and the polarized line emission from CO $J = 2 - 1$ in its protostellar outflow. Although these data reveal a similar magnetic field orientation in the source and the outflow near the source, the polarization directions are orthogonal to one another, as predicted by theory (Kylafis 1983). Thus, in regions where the CO emission is so strong that it produces a significant amount of flux in a continuum bandpass, the net polarization measured with a bolometer could take on any value depending on the relative strengths of the two polarization components. Telescopes using spectroscopic methods, such as BIMA, are not sensitive to polarized thermal emission from dust.

The direction of the most powerful outflow of NGC 2071 is shown in Figure 5.1. It is aligned at a position angle of 40° (east of north). The mean polarization position angle in our data set is $\sim 22°$, with a dispersion about the mean of 32°. In the subset of vectors toward the peak, the mean position angle is 34° with a standard deviation about the mean of 33°. This means that the vectors are, in general, well aligned with the direction of the outflow. Note that if the magnetic field direction is inferred by rotating the vectors by 90°, then this would imply that *the field of the core is perpendicular to the primary outflow.* This would be problematic for models of protostellar formation which favor collapse along field lines, resulting in outflows aligned with the field of the core.

We note that this 90° offset between the core's magnetic field as traced by emission from dust and the orientation of the outflow may actually be unremarkable. NGC 2071 is a massive core forming many stars; this is very different from the case of an isolated protostellar core which forms a single star system. Within several star-forming regions, outflows of various orientations are observed, i.e. OMC-2/3 in Orion A (Aso et al. 2000; Yu et al. 2000). If a mean field really threaded such cores and was able to dominate collapse, one should naively expect all outflows within a massive core to be aligned. Since this is not observed (Eislöffel 2000), it is clear that even if a mean field threads a core, it is likely not the sole determining factor in the orientation of the core which forms or the orientation of collapse and outflow.

However, there is another potential explanation for why the polarization pattern is aligned with the outflow. According to theory, in the case of high density gas, the linear polarization produced by spectral lines should be parallel to the magnetic field. Polarization of spectral lines in the outflow of NGC 2071 has not yet been measured, but Greaves, Holland, & Ward-Thompson (2001) have measured polarization from the CO $2-1$ line in the outflow of FIR 5 in NGC 2024 and found the vectors to be aligned with the outflow. Based on theory, a magnetic field aligned with the outflow is inferred. The CO $3-2$ line lies within the 850 μm bandpass and has been shown in some cases to dominate the continuum. If the line emission is detected by SCUBA and is significant compared to the continuum, then 850 μm polarization data parallel to the outflow can imply a field aligned with the outflow. Therefore, either our data do not sample the thermal dust emission from the core due to contamination from the CO $3-2$ line, or the field of the core is misaligned with the outflow.

5.4.2 LBS 23N

The polarization structure of the LBS 23N region is somewhat less orderly than that of either NGC 2071 or NGC 2024, and there are no Zeeman data toward this region. However, there remains sufficient structure in the polarization map to warrant some comparison to filamentary models.

The LBS 23N region is a linear string of roughly equally spaced condensations, which might be the result of fragmentation due to gravitational instabilities (see Chandrasekhar & Fermi (1953), Nakamura et al. (1993) and Fiege & Pudritz (2000b) for a discussion of gravitational instabilities in magnetized filaments). The overall orientation of the polarization vectors is along the filament, with some degree of scatter in position angle. The mean position angle in the 70 vectors is 8.7° with a standard deviation of 5.0°.

We offer three possible explanations for such a pattern. The first possibility is that the original filament is threaded by a magnetic field transverse to the symmetry axis. This magnetic field geometry would certainly reproduce the orientation of the majority of the polarization vectors. However, it is not easy to understand how such a field geometry could be associated with a filament or linear string of cores collapsed in three dimensions, since a transverse field would more likely be associated with a sheet-like distribution of material.

Alternatively, Fiege & Pudritz (2000c) proposed that such a pattern could be explained as the result of a helical field dominated by the toroidal field component (Type 1, according to their classification) as observed in the OMC-3 filament of Orion A. Helical field geometry can create polarization patterns where vectors flip by 90° at the interface between poloidally and toroidally dominated regions, which could occur if the field threading the southern part of the filament is less tightly wound than in the north. Such a flip is suggested by our data at the southern end of the polarimetry map. However, we note that these data provide only sparse coverage of this region and are the lowest signal-to-noise data of all three regions. Modelling of this region will require observations of the southern part of the filament.

Finally, Matthews, Wilson, & Fiege (2001) present a model for two crossed filaments, unconnected but overlapping on the plane of the sky. In such a case, the vectors in the overlap region can be dominated by one of the two filaments. The east-west filamentary structure is identified in Figure 5.2. As for the previous case, this scenario can be tested by more extensive mapping into LBS 23S.

5.4.3 NGC 2024

The overall appearance of NGC 2024's submillimetre emission is that of a short filament which is broken into three main condensations. The polarization vectors show a complicated but extremely well-ordered pattern throughout the region. An interesting feature of the map is a rather abrupt change in orientation across the central ridge of the filament. This feature cannot be reconciled easily with a purely poloidal field along the filament axis, since that geometry would produce polarization vectors perpendicular to the axis, *irrespective of the inclination of the filament.* Fiege & Pudritz (2000c) found that polarization vectors can flip by 90° across the central axis of a filament threaded by a helical field, when the filament is inclined at an angle relative to the plane of the sky. However, the polarization vectors in their model are always aligned either parallel or perpendicular to the filament. Clearly, this is not the case in our map, where the vectors form a "V" like pattern, with the apex located on the central ridge of the filament. However, we show below that a simple extension to their model can readily account for the qualitative features of this map.

The interpretation of the polarization pattern is constrained by measurements of the line of sight magnetic field component, B_{los} (also denoted $B_{||}$). Crutcher et al. (1999), using Zeeman splitting of OH absorption lines, detected a peak in B_{los} of almost 100 μG at a position west of FIR 4. The field strength declines smoothly from this southwestern position in their map to the northeast, where it drops to zero (cf. their figure 3). OH samples gas densities of approximately 10^4 cm^{-3}, which are substantially lower than the volume densities estimated along the NGC 2024 molecular ridge. The extended filamentary structure in which the cores are embedded have $< n_H > \approx 5 \times 10^6$ cm^{-3}, while the cores themselves have $< n_H > \approx 2 \times 10^8$ cm^{-3} (Mezger et al. 1992). Thus, it is not certain that the field being traced by the Zeeman data threads the same dense gas whose magnetic field is traced by our polarization measurements. However, the fact that the positions of low polarization percentage in both 100 μm and 850 μm correspond closely with the maximum in line-of-sight field could support a correlation in the fields traced by the two techniques. With this in mind, we offer two theoretical models for this pattern.

Schulz et al. (1991) measured NH_3 and CS gas toward NGC 2024 and found distributions of dense gas which closely mirrored the pattern of dust condensations. This supported previous conclusions that the dense ridge is in fact located on the far-side of the HII region (Chandler & Carlstrom 1996; Crutcher et al. 1999), as originally schematically illustrated by Barnes et al. (1989). We illustrate the likely configuration in Figure 5.6. In order for OH to be observed in absorption, there

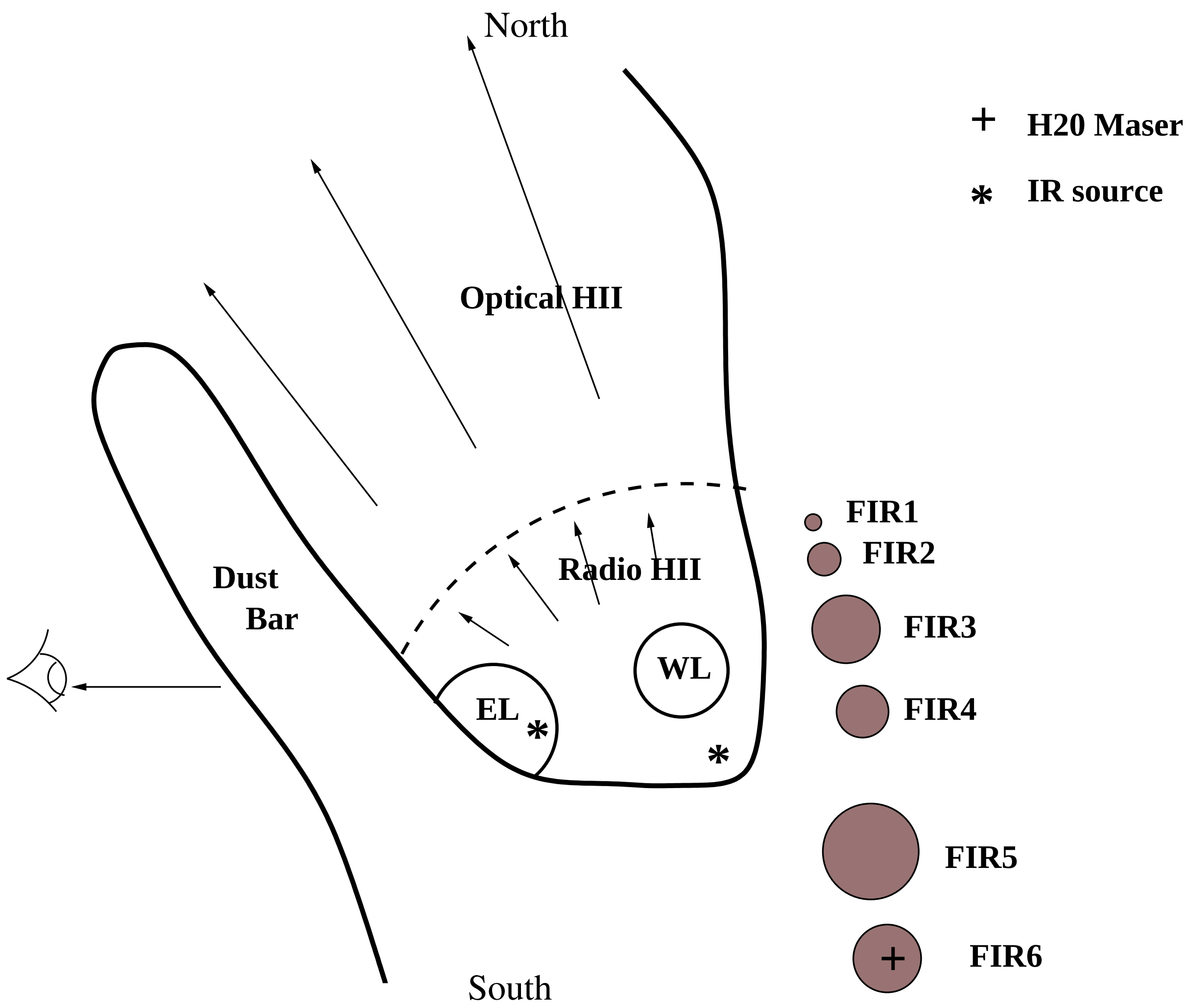

Figure 5.6: Schematic Geometry of the NGC 2024 region.
The geometry of the NGC 2024 HII dense cores and foreground dark dust lane, as seen from the western edge of the cloud. From the Earth's perspective, the dark lane (unassociated with the dense cores) is seen in the foreground of the HII region. The HII region has blistered out of the molecular cloud to the north, west and east but is hindered to the south by dense molecular material as indicated by radio maps of the ionized emission (Barnes et al. 1989). The IR sources marked include IRS 2 (within the Eastern Loop) and IRS 3, near the southern boundary of the HII region.

must be a source of background continuum emission. Thus, either the OH Zeeman data trace the field in the foreground dust lanes (with the observable HII region as the continuum source) or the OH absorption is occuring in the denser molecular cloud, thus requiring a second source of continuum emission behind the ridge. For instance, the HII region could have penetrated to different depths of the cloud due to density variations. The latter scenario is favored by Crutcher et al. (1999) with the ridge located on the far side of the HII region.

In the first case, the Zeeman splitting OH absorption data may be sampling an envelope of gas either in the foreground of the HII region itself, or simply at the boundary between the HII region and the very dense molecular cloud behind it, regardless of the location of the dense ridge. In this case, the Zeeman data may be unrelated to the polarization data and would not provide a constraint. In the second case, we assume that although the OH data sample a less dense region of gas, the measurements are sampling the same field geometry in both regions.

5.4.3.1 A Helical Field Model

In this model, the basic idea is that straight, infinite filaments are an idealization, which needs to be relaxed when comparing models with real data. Figure 5.7 shows a finite segment of a filament model from Fiege & Pudritz (2000a), which we have "bent" into a circular arc using a simple mathematical transformation that maps planes parallel to the axis of the filament into concentric cylinders of some specified mean radius of curvature. The density and magnetic field are transformed self-consistently, using the Lagrangian formulation of the MHD induction equations (see Parker for example). We will thoroughly discuss the details of our modeling technique in a future paper.

The polarization structure of the theoretical map reproduces most of the qualitative features of Figure 5.3. On the other hand, models that are threaded by

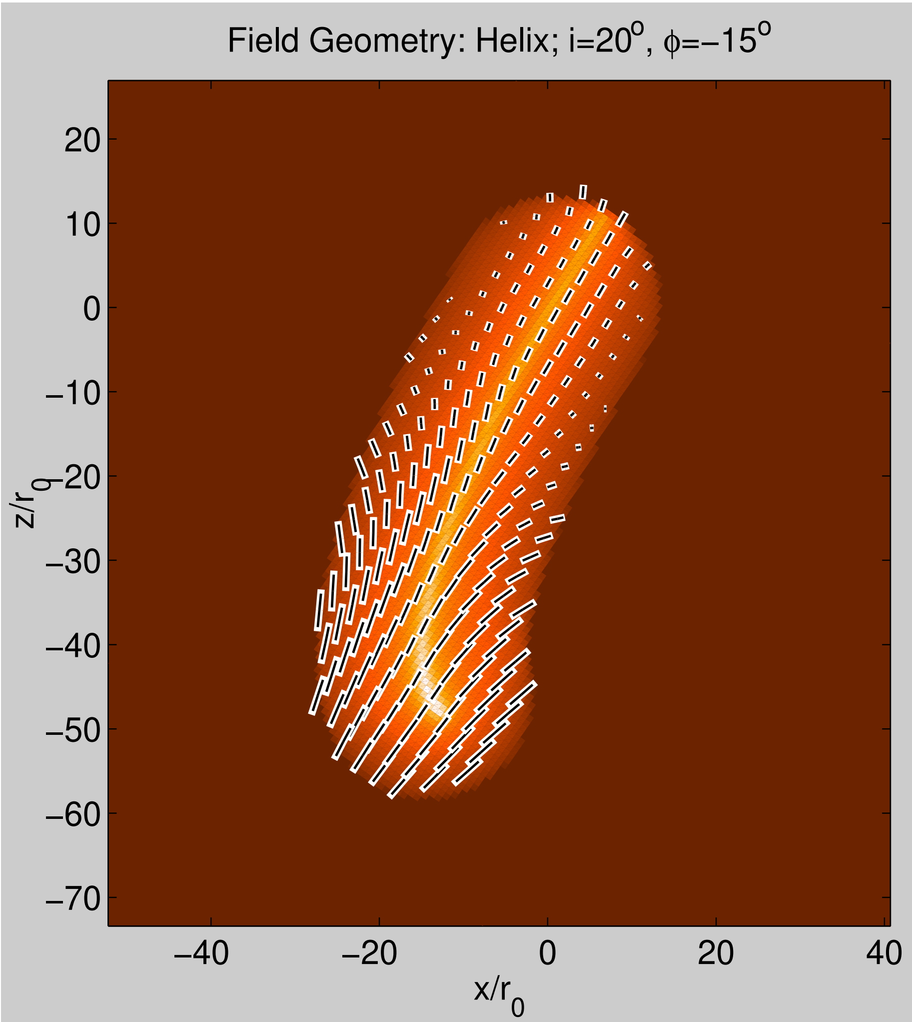

Figure 5.7: A Helical Field Model for NGC 2024.
We show an example of a "bent filament" model (discussed in Section 5.4.3) for comparison with NGC 2024. The model is a Fiege & Pudritz (2000a) filament model constructed with the following parameters: $C = 1.1$, $\Gamma_z = 8$, $\Gamma_\phi = 15$. The length of the filament is 6×10^C and the ends have been rounded. We have bent the entire filament into a circular arc perpendicular to the plane of the sky and toward the observer, keeping the top of the filament parallel to the original orientation. The same pattern would be produced for a filament bent away from the observer. The radius of the arc is $3/\pi$ times the filament length. We then rotated the entire structure by $20°$ and inclined it relative to the plane of the sky by $-15°$.

purely poloidal fields do not agree with the data. Note that the model shown is a preliminary result and should not be regarded as our final, best fit to the data. Nevertheless, we have provided the exact parameters of this model in the caption of Figure 5.7.

It is interesting that a bend in the filament is required to reproduce the polarization pattern shown in Figure 5.3. If the filament is bent so that the source FIR 5 is closest to the expanding ionization front of the HII region, then this could explain why it is the most evolved source along the ridge. The outflow from this source is the most powerful in the region (Richer et al. 1992), while evidence for less evolved outflows can be found in the sources FIR 4 and FIR 6. Fukuda & Hanawa (2000) present a numerical simulation of triggered star formation along a filament by the expansion of an HII region. In their picture, compression triggers two cores (i.e. FIR 4 and FIR 5) to collapse, and then at a later time, further collapse is triggered further up and down the filament. This sequence was observed by Chandler & Carlstrom (1996) in their study of outflows from NGC 2024, where the dynamical ages of outflows from FIR 5, FIR 4 and FIR 6 are 1.4×10^4 yr, 2.6×10^3 yr, and 400-3300 yr.

5.4.3.2 Expansion of the HII Region around A Dense Ridge

The expected Zeeman pattern from a helical field is a change in orientation of B_{los} across the ridge. This is not consistent with the observations of Crutcher et al. (1999) toward the northern portion of the NGC 2024 dense ridge. In order to reconcile the Zeeman and polarization data, we suggest that the magnetic field throughout the cloud has been distorted from its original structure by the expansion of the HII region, as shown in the cartoon of Figure 5.8. The field may be pushed out on the surface of the ionization front, but will bend around any very dense structures embedded in the molecular cloud.

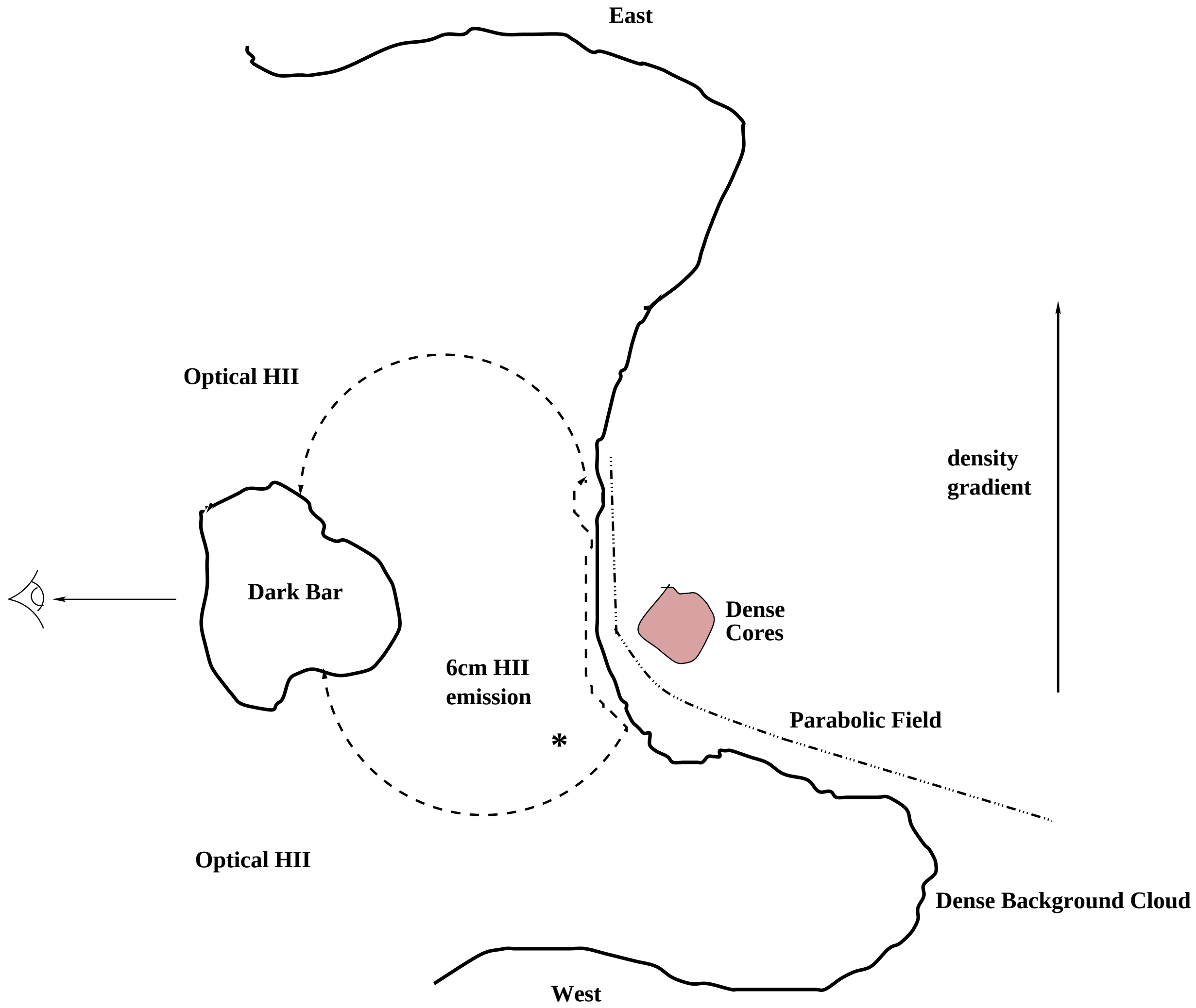

Figure 5.8: Geometry of the NGC 2024 region, viewed from the north. The geometry of the NGC 2024 region as viewed from the north, looking down on the ridge of dense cores. A proposed orientation of the field line is shown as a hatched line. We speculate that the field has been compressed into a smooth layer on the edge of the expanding HII region. The ionization front has penetrated the molecular material more deeply to the west where the cloud is less dense, but is hindered by the dense ridge. This accounts for the field lying predominantly in the plane of the sky to the east of the ridge, but significantly in the line of sight to the west.

The asymmetric Zeeman data require either the ionizing source to be to the west of the dense ridge, or an asymmetry in the density of the molecular cloud whereby the cloud density rises to the east, inhibiting the extension of the HII region on that side (Barnes et al. 1989). The contours of Figure 5.4 show that the dust extends further to the east the ridge than to the west. If the source of the ionization front is to the west of the molecular ridge, then the vectors seen from our line of sight will stretch across the front of the ridge and to the east entirely in the plane of the sky (i.e. the B_{los} component is zero). To the west of the molecular ridge, such a source would produce an ionization front which would be bending around the ridge, with components B_{los} and $B_{\perp}$ both non-zero. In this scenario, it does not matter (for the model) whether the dust condensations and OH are in front or behind the HII region. Since dust is optically thin, the same pattern can be produced by bending of field lines around a dense ridge.

However, a preponderance of evidence (Barnes et al. 1989) now exists which establishes a strong case for the location of the dense cores and high density gas behind the HII region, as shown in Figure 5.6. Although Barnes et al. (1989) calculated the ionizing radiation detected in the nebula to require the IRS 3 source to be an O9 (or earlier) star, they conclude this to be unlikely unless the extinction toward IRS 3 is 4.1 mag in K, a factor of 2 greater than the average extinction derived toward that star. Instead, they suggest that an ensemble of B stars must have formed the HII region. If each star has formed a bubble of ionized radiation around it, as IRS 2 has produced the Eastern Loop (see Figure 5.6), then the cumulative effect could produce the HII region.

In order for this picture to be physically reasonable, the ionization front must be interacting with the molecular ridge. Gaume, Johnston, & Wilson (1992) detected 1.3 cm emission at $3''$ resolution located south of FIR 4 (their NH_3 4) and north of FIR 5 (their NH_3 5). North of the FIR 5 source, the 1.3 cm emission arises from a dense, ionized interface between the molecular cloud (and ridge of cores) and the HII region. The ionized emission near FIR 4 has diffuse and compact components. The compact component is located on the far side of the HII region near the molecular ridge. Additionally, higher NH_3 temperatures, larger line widths and smaller abundances suggest that the FIR 4 and FIR 5 sources are nearest the ionization front of the HII region. Schulz et al. (1991) show that ionized gas in fact fills the bay in the molecular bar surrounding IRS 3 (see their figure 7), and that the ridge is effectively separated into two subregions by the ionization front of the HII region. We proceed on the basis that the ridge existed prior to the formation of the HII region. This does not preclude the triggering of star formation in the ridge by the HII region expansion.

The polarization model shown in Figure 5.9 is based on the idea that the magnetic field has been swept up in a shell during the expansion of the HII region and stretched over the surface of the dense filamentary system of cores embedded in the wall of the molecular cloud. The stretching of the field in this scenario would tend to make the field quite uniform by the time the shell reached the system of cores. The structure of the magnetic field is idealized as follows. We assume that the field is swept into a band with a Gaussian planar distribution of the form

$$B_0 = \left[B_{x0} * exp^{-\frac{(y_0 - y_c)^2}{(\delta y^2)}}, 0, B_{z0} * exp^{-\frac{(y_0 - y_c)^2}{(\delta y^2)}} \right] \tag{5.3}$$

when it first encounters the embedded filament, where $\hat{y}$ is along the line of sight, y_c is the offset of the field's centre from the filament axis, δy is the width of the field region and $B_{x,0}$ and $B_{z,0}$ are respectively the maximum, central values of the $\hat{x}$ and $\hat{z}$ field components. The field is therefore at angles with respect to the filament generally, which is oriented in the $\hat{z}$ direction and is assumed to be an unmagnetized, Ostriker (1964) type filament. We model the wrapping of the field around the filament by applying a coordinate trasformation of the form

$$x_0 = x, y_0 = y - (x/w)^2, z_0 = z \tag{5.4}$$

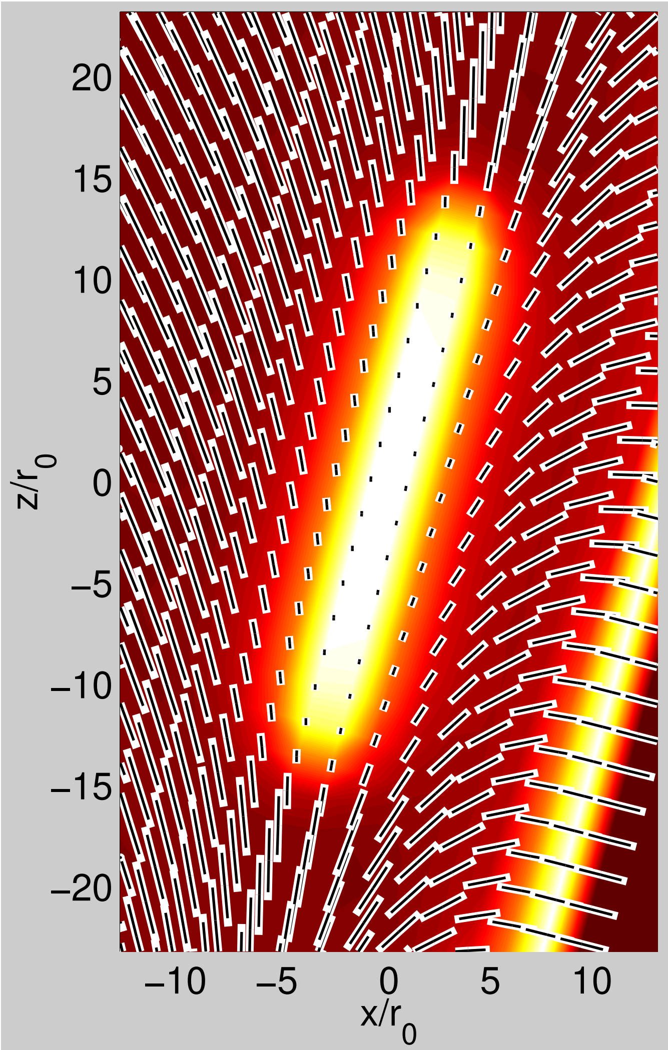

Figure 5.9: Polarization Pattern Produced by a Parabolic Field.
Model showing the polarization pattern from a parabolic field bent around a dense ridge of gas, under the scenario depicted in Figure 5.8 and described in the text. The filament is unmagnetized and the field is contained entirely in the shell of gas. The density of the shell containing the field must be $\sim 10\%$ that of the central axis of the filament. The parabolic shell is originally symmetric along the line of sight, but is rotated by $20°$ to produce the correct behavior in the polarization and B_{los}. The inclination is $60°$ and the whole filament is rotated by on the plane of the sky $-15°$.

to the planar field giving by equation (5.3). $y_0 = -10^C$ for the front of the shell, so that it just touches the filament. The field is distorted using the Lagrangian forms of the MHD induction equation and the equation of mass conservation:

$$\frac{\mathbf{B}}{\rho} = \mathbf{J} \tag{5.5}$$

$$\frac{\mathbf{B_0}}{\rho_0} = \mathbf{J} \tag{5.6}$$

$$\rho = \frac{\rho_0}{|\mathbf{J}|}, \tag{5.7}$$

where the $\mathbf{J}$ is the Jacobian of the coordinate transformation given by equation (5.4) and $|\mathbf{J}|$ is its determinant. The determinant is unity, so that the density is unchanged. It is a simple matter to demonstrate that this transformation bends the field into a parabolic shape. The Zeeman data of Crutcher et al. (1999) suggest that the magnetic field is approximately parallel to the surface of the molecular cloud east of the filament, and strongly bent into the line of sight on the West. This is also supported by Barnes et al. (1989), who suggest that the molecular cloud may be denser east of the ridge than to the west, since the field would be swept further back on the side of lower density. Thus we rotate our field configuration by $20°$ counter-clockwise (looking toward the origin from the $\hat{z}$ axis) to mimic this asymmetry. The inclination angle that best reproduces the observed polarization map is $60°$ into the plane of the sky with a further rotation of the filament and the field of $-15°$ to better represent the data. The resultant polarization pattern is shown in Figure 5.9.

Taking into account both the polarization and the Zeeman data, the field geometry bent around a dense ridge more effectively reproduces the observed data toward this region. However, this model alone does not account for any field which could exist in the gas of the filament itself. The dense ridge is unlikely to be devoid of field, given the fact that polarization has been measured toward both other regions of dense gas in Orion B as well as regions in other clouds (e.g. the Integral-shaped

Filament, Matthews, Wilson, & Fiege 2001). Therefore, we may simply be sampling the dominant field of foreground dense gas, perhaps due to enhanced field strength, degree of alignment or both.

The possibility that fields of the filament and surrounding gas could both contribute to the observed polarization and Zeeman data prevents us from dismissing the helical field geometry for the filament itself. In order to explain the observations using a parabolic field, we have required a substantial amount of mass in the foreground gas. If the field in this gas were smoothly distributed, then the sum of this field and a helical field (which reverses direction across the axis) could result in Zeeman data which show a high field strength on one side of the filamentary gas (where the fields add) and zero on the other side (where they effectively cancel). Cancellation would not occur in polarization data since these data are weighted by the abundance of dust, which must be present in the filament (since we see the dust in emission defining the same ridge as is observed in dense gas tracers), but be substantially less abundant in the ionization front of the HII region.

5.5 Summary

The polarization patterns observed in Orion B are dominated by orderly structure on scales at least as large as the areas mapped (with the possible exception of the LBS 23N region). This result can only be consistent with magnetic fields that are ordered on similar scales or larger. The filamentary clouds, NGC 2024 and LBS 23N, exhibit polarization patterns which appear inconsistent with purely poloidal magnetic fields threading the filaments. The NGC 2024 polarization pattern in particular necessitates the use of curved magnetic field lines to effectively model the data. The fact that the polarization pattern is symmetric about the dense ridge of cores suggests that there is a correlation between the presence of dense gas and the exhibited polarization pattern.

The polarization systematically decreases with intensity for all three regions mapped. This result is in agreement with Matthews, Wilson, & Fiege (2001), who note depolarization toward the axis of the Integral-shaped Filament in OMC-3, as well as most submillimetre and millimetre observations of star-forming regions (see Weintraub, Goodman, & Akeson (2000) for a review). This "polarization hole" effect is a *global* property of our maps, and not just a local phenomenon that occurs for a few pixels near the very brightest emission.

NGC 2071 is a massive core forming multiple protostars within its bounds. Its polarization pattern is ordered and exhibits similar behavior to that of OMC-1, a much more massive core in Orion A. In OMC-1, rotation of the polarization vectors to yield the net $B_\perp$ direction led to the conclusion that the magnetic field geometry was shaped as an hourglass, with pinching of the field lines due to the collapse of the core where the field is drawn in with the gas (Schleuning 1998). In NGC 2071, the core does not show the flattening of OMC-1 as expected if the core were collapsing. We note that if the vectors of NGC 2071 were rotated to infer a net field direction, this direction would be *perpendicular* to the most powerful outflow in the region. However, if our 850 μm emission is dominated by the CO $3-2$ line emission, then the polarization vectors can be parallel to the direction of the mean field; in this scenario, the inferred field from our data would be parallel to the IRS 3 outflow. However, even in this case, the fact that the core is not flattened means that this core is quite different from that of OMC-1, where the hourglass field model is more convincing.

LBS 23N exhibits the least orderly polarization patterns of the three regions studied. Most of the polarization vectors are aligned in a north-south orientation, particularly to the east of the cores. The cores themselves are significantly depolarized. Near the southern boundary of the data set, the vectors rotate to an east-west orientation. An augmentation of the data set to include the southern cores of LBS 23 is required to model these data properly.

The NGC 2024 ridge of cores presents the most interesting polarization data. The polarization is strong everywhere but the cores, which are significantly depolarized. The data agree very well with the 100 μm polarization data obtained with the KAO Stokes polarimeter (Dotson et al. 2000), even though these wavelengths likely probe different dust temperatures. Interestingly, the region between FIR 4 and FIR 5 exhibits diminished intensity but no polarization is detected there. We are able to model the polarization pattern well using a helical field geometry threading a curved filament. However, given the overall geometry of the region – an HII region expanding into the molecular cloud in which the cores are embedded – we prefer a model in which the ionization front has swept up the magnetic field and is now stretching it around the ridge of dense cores. A third possibility is that a helical field, treading the filament, is observed in the polarization data, while the Zeeman data sample a net field of the filament and a smooth field of comparable strength associated with the ionization front.

The depolarization between the cores could be produced where the line of sight field is strong. The data set of Crutcher et al. (1999) does not cover our entire map area. Evidence for ionized gas to the south of FIR 4 and north of FIR 5 shows that the ionization front of the HII region has reached the molecular ridge and is penetrating into the dense gas (Gaume et al. 1992). In this case (and assuming a density gradient), the line of sight field strength should be strongest to the south-west of FIR 4 and north-east of FIR 5 as the field curves into the line of sight. In fact, there is a hint of a second peak in the line of sight field at the edge of the Crutcher et al. (1999) map, just to the north-east of FIR 5.

We note that our analysis of the NGC 2024 polarization data have been aided immensely by the existence of Zeeman maps of the line of sight field strength toward part of this region. Unfortunately, very few regions have been successfully mapped using Zeeman splitting (Crutcher 1999). This is an area where future technological advances in instrumentation would greatly improve our understanding of magnetic fields in molecular clouds.

The authors would like to thank J. Greaves and T. Jenness for assistance during observing and data reduction. We also extend thanks to our fellow consortium members: C. Wilson and R. Pudritz for feedback on this manuscript. The research of BCM is supported through grants from the Natural Sciences and Engineering Research Council of Canada. BCM acknowledges funding from Ontario Graduate Scholarships. JDF acknowledges support from a postdoctoral fellowship, jointly funded by the Natural Sciences and Engineering Council and the Canadian Institute for Theoretical Astrophysics.

Appendix 5A – Polarization Data

Tables 5.1, 5.2, and 5.3 present the polarization data for the regions NGC 2024, LBS 23N, and NGC 2071 respectively. Each table contains only those vectors plotted on Figures 5.1, 5.2, and 5.3. Positional offsets for NGC 2071 are from $\alpha_{J2000} = 05^{\mathrm{h}}47^{\mathrm{m}}5\overset{\mathrm{s}}{.}16$ ($05^{\mathrm{h}}44^{\mathrm{m}}31\overset{\mathrm{s}}{.}0$ in B1950) and $\delta_{J2000} = +00^\circ\ 21'\ 47\overset{''}{.}1$ ($+00^\circ\ 20'\ 45\overset{''}{.}0$ in B1950). The reference position for LBS 23N is $\alpha_{J2000} = 05^{\mathrm{h}}46^{\mathrm{m}}11\overset{\mathrm{s}}{.}16$ ($05^{\mathrm{h}}43^{\mathrm{m}}37\overset{\mathrm{s}}{.}0$ in B1950) and $\delta_{J2000} = -00^\circ\ 09'\ 13\overset{''}{.}0$ ($-00^\circ\ 10'\ 15\overset{''}{.}2$ in B1950). Finally the reference position for NGC 2024 is $\alpha_{J2000} = 05^{\mathrm{h}}41^{\mathrm{m}}44\overset{\mathrm{s}}{.}1$ ($05^{\mathrm{h}}39^{\mathrm{m}}12\overset{\mathrm{s}}{.}6$ in B1950) and $\delta_{J2000} = -01^\circ\ 54'\ 49\overset{''}{.}7$ ($-01^\circ\ 56'\ 15\overset{''}{.}0$ in B1950).

The columns in each table are: (1) the R.A. offset in arcseconds; (2) the DEC. offset in arcseconds; (3) the polarization percentage at that position; (4) the uncertainty in the polarization percentage; (5) the signal-to-noise ratio of the polarization percentage; (6) the polarization position angle; and (7) the uncertainty in the polarization position angle.

Table 5.1: NGC 2071 850 μm Polarization Data

Δ R.A. ($''$)	Δ DEC. ($''$)	p (%)	dp (%)	σ_p	θ ($^\circ$)	$d\theta$ ($^\circ$)
−16.5	−67.5	5.56	1.07	5.2	63.8	5.5
10.5	−58.5	12.99	1.41	9.2	−14.7	3.1
1.5	−58.5	8.51	1.33	6.4	7.0	4.5
−7.5	−58.5	5.14	1.04	4.9	42.8	5.8
−25.5	−58.5	6.04	1.40	4.3	−47.7	6.7
−43.5	−58.5	6.64	1.31	5.1	−20.4	5.7
10.5	−49.5	10.04	1.31	7.7	−29.3	3.7
1.5	−49.5	5.25	0.90	5.8	18.8	4.9
−25.5	−49.5	4.73	0.87	5.4	−80.1	5.3
−43.5	−49.5	13.76	1.48	9.3	−8.0	3.1
−52.5	−49.5	7.48	1.29	5.8	22.0	5.0
10.5	−40.5	3.54	0.61	5.9	−16.1	4.9
−16.5	−40.5	8.00	0.48	16.6	−14.2	1.7
−25.5	−40.5	4.56	0.68	6.7	6.9	4.3
−34.5	−40.5	9.33	1.46	6.4	−19.2	4.5
−52.5	−40.5	15.03	1.40	10.7	−17.2	2.7

Table 5.1 (continued)

Δ R.A. ($''$)	Δ DEC. ($''$)	p (%)	dp (%)	σ_p	θ (°)	$d\theta$ (°)
37.5	−31.5	9.70	1.41	6.9	46.9	4.2
28.5	−31.5	11.90	1.02	11.6	26.4	2.5
19.5	−31.5	3.11	0.59	5.2	−2.2	5.5
10.5	−31.5	2.49	0.35	7.1	13.0	4.1
−16.5	−31.5	2.73	0.35	7.9	47.0	3.6
46.5	−22.5	4.34	1.06	4.1	54.2	7.0
19.5	−22.5	1.77	0.34	5.2	−1.2	5.5
10.5	−22.5	2.48	0.23	10.7	26.1	2.7
1.5	−22.5	1.25	0.26	4.8	47.0	6.0
−7.5	−22.5	1.83	0.21	8.8	70.0	3.2
−16.5	−22.5	1.66	0.25	6.6	−85.7	4.4
−34.5	−22.5	5.31	0.88	6.0	21.6	4.7
−52.5	−22.5	8.94	0.83	10.8	49.6	2.7
37.5	−13.5	5.70	0.93	6.1	57.6	4.7
28.5	−13.5	2.46	0.57	4.3	37.1	6.6
19.5	−13.5	2.29	0.30	7.6	13.5	3.8
10.5	−13.5	1.28	0.21	6.0	18.6	4.7
1.5	−13.5	1.04	0.17	6.3	35.0	4.5
−7.5	−13.5	1.53	0.18	8.4	53.0	3.4
−34.5	−13.5	3.15	0.31	10.1	57.8	2.8
−43.5	−13.5	5.76	0.50	11.6	37.1	2.5
−52.5	−13.5	4.17	0.68	6.1	30.2	4.7
37.5	−4.5	4.77	0.97	4.9	18.0	5.8
10.5	−4.5	1.74	0.17	10.3	14.1	2.8
1.5	−4.5	1.09	0.10	11.2	29.7	2.5
−7.5	−4.5	1.14	0.09	13.3	55.8	2.2
−25.5	−4.5	1.20	0.19	6.2	55.5	4.6
−34.5	−4.5	2.64	0.26	10.2	75.3	2.8
−43.5	−4.5	6.45	0.60	10.7	37.7	2.7
−52.5	−4.5	7.21	0.69	10.4	13.9	2.8
37.5	4.5	8.08	0.81	10.0	24.3	2.9
28.5	4.5	2.78	0.39	7.2	−20.5	4.0
−7.5	4.5	1.24	0.15	8.3	61.8	3.4
−16.5	4.5	1.66	0.17	9.5	54.2	3.0
−25.5	4.5	1.44	0.22	6.7	44.0	4.3
−43.5	4.5	3.73	0.59	6.3	37.1	4.5
37.5	13.5	5.95	0.76	7.8	21.6	3.7
28.5	13.5	1.43	0.33	4.3	−15.0	6.7
19.5	13.5	3.03	0.25	12.4	−2.0	2.3
10.5	13.5	1.31	0.25	5.3	−2.7	5.4
−7.5	13.5	1.41	0.24	5.9	50.4	4.9

Table 5.1 (continued)

Δ R.A. (″)	Δ DEC. (″)	p (%)	dp (%)	σ_p	θ (°)	$d\theta$ (°)
−16.5	13.5	1.47	0.20	7.3	58.9	3.9
−25.5	13.5	2.18	0.32	6.8	38.0	4.2
−34.5	13.5	5.23	0.44	12.0	21.3	2.4
−43.5	13.5	4.95	0.57	8.6	19.3	3.3
−52.5	13.5	5.38	0.84	6.4	16.8	4.5
46.5	22.5	8.81	1.23	7.2	28.4	4.0
37.5	22.5	3.78	0.65	5.8	25.3	4.9
19.5	22.5	2.73	0.29	9.3	29.7	3.1
10.5	22.5	1.31	0.29	4.5	26.9	6.4
1.5	22.5	2.42	0.32	7.4	74.1	3.8
−7.5	22.5	1.64	0.32	5.0	60.2	5.7
−16.5	22.5	2.35	0.33	7.1	61.0	4.0
−25.5	22.5	2.60	0.34	7.6	31.4	3.8
−34.5	22.5	3.45	0.55	6.3	21.2	4.5
−43.5	22.5	5.42	0.54	10.0	17.7	2.9
−52.5	22.5	9.78	0.68	14.4	17.8	2.0
46.5	31.5	11.95	1.13	10.6	27.9	2.7
37.5	31.5	6.91	0.72	9.6	26.4	3.0
19.5	31.5	4.49	0.86	5.2	52.1	5.5
10.5	31.5	4.60	0.80	5.8	17.6	5.0
−25.5	31.5	2.74	0.64	4.3	−0.8	6.7
−34.5	31.5	4.45	0.51	8.8	13.6	3.3
−43.5	31.5	6.17	0.83	7.5	−7.8	3.8
37.5	40.5	5.39	0.73	7.4	−84.2	3.9
19.5	40.5	4.60	0.83	5.5	0.8	5.2
1.5	40.5	6.54	0.79	8.2	14.3	3.5
−34.5	40.5	3.77	0.78	4.8	43.7	5.9
−43.5	40.5	9.15	0.97	9.4	17.7	3.0
1.5	49.5	8.38	1.12	7.5	17.0	3.8
−7.5	49.5	7.30	1.04	7.0	14.0	4.1
−16.5	49.5	9.14	0.96	9.5	50.5	3.0
−34.5	49.5	6.52	0.84	7.8	80.0	3.7
37.5	58.5	3.30	0.80	4.1	−38.6	7.0
28.5	58.5	5.63	0.71	7.9	15.2	3.6
19.5	58.5	4.63	0.73	6.3	25.0	4.5
1.5	58.5	6.19	1.22	5.1	18.3	5.7
−7.5	58.5	5.60	1.31	4.3	8.9	6.7
−16.5	58.5	8.65	1.01	8.5	19.5	3.4
−25.5	58.5	3.16	0.69	4.5	35.9	6.3
−34.5	58.5	3.84	0.91	4.2	33.1	6.8
19.5	67.5	14.62	1.33	11.0	64.9	2.6
10.5	67.5	10.32	1.19	8.7	36.5	3.3

Table 5.2: LBS 23N 850 μm Polarization Data

Δ R.A. ($''$)	Δ DEC. ($''$)	p (%)	dp (%)	σ_p	θ ($^\circ$)	$d\theta$ ($^\circ$)
−9.0	−124.5	5.58	1.03	5.4	−29.1	5.3
15.0	−112.5	12.03	1.37	8.8	29.9	3.3
3.0	−112.5	4.29	0.60	7.1	38.4	4.0
−9.0	−112.5	1.83	0.30	6.1	−16.7	4.7
15.0	−100.5	11.75	1.25	9.4	5.1	3.1
3.0	−100.5	5.34	0.68	7.8	74.4	3.7
−9.0	−100.5	3.14	0.34	9.1	−82.0	3.1
−21.0	−100.5	2.88	0.30	9.7	−88.8	3.0
−33.0	−100.5	3.12	0.62	5.0	71.7	5.7
−45.0	−100.5	8.47	1.35	6.3	75.1	4.5
15.0	−88.5	8.27	1.12	7.4	−11.9	3.9
3.0	−88.5	4.88	0.68	7.1	−3.4	4.0
−9.0	−88.5	1.97	0.49	4.1	−88.2	7.1
−21.0	−88.5	2.94	0.50	5.9	29.4	4.9
−33.0	−88.5	3.77	0.76	5.0	71.7	5.7
−45.0	−88.5	5.28	1.28	4.1	51.7	6.9
27.0	−76.5	13.00	1.34	9.7	28.8	3.0
15.0	−76.5	5.45	0.80	6.9	21.6	4.2
3.0	−76.5	3.61	0.65	5.6	−26.6	5.1
−9.0	−76.5	6.55	0.57	11.5	−53.6	2.5
−21.0	−76.5	7.21	0.77	9.4	−42.3	3.1
−45.0	−76.5	12.16	1.20	10.2	7.8	2.8
27.0	−64.5	7.82	1.29	6.0	1.8	4.7
15.0	−64.5	3.21	0.63	5.1	10.3	5.6
−9.0	−64.5	2.52	0.47	5.4	−78.8	5.4
−21.0	−64.5	3.40	0.71	4.8	62.8	5.9
27.0	−52.5	12.61	1.01	12.5	8.1	2.3
15.0	−52.5	6.77	0.47	14.5	4.9	2.0
3.0	−52.5	1.47	0.26	5.7	16.3	5.0
−9.0	−52.5	2.61	0.23	11.5	5.2	2.5

Table 5.2 (continued)

Δ R.A. (″)	Δ DEC. (″)	p (%)	dp (%)	σ_p	θ (°)	$d\theta$ (°)
−21.0	−52.5	2.09	0.42	5.0	50.1	5.7
−33.0	−52.5	3.51	0.67	5.3	0.6	5.4
27.0	−40.5	8.82	0.74	11.9	6.9	2.4
15.0	−40.5	2.61	0.37	7.1	32.3	4.1
3.0	−40.5	1.55	0.13	11.6	23.5	2.5
27.0	−28.5	6.18	1.06	5.8	38.5	4.9
15.0	−28.5	5.57	0.41	13.5	28.3	2.1
3.0	−28.5	1.58	0.18	8.8	27.8	3.2
−9.0	−28.5	1.40	0.13	10.9	46.0	2.6
−21.0	−28.5	1.98	0.24	8.4	7.9	3.4
−33.0	−28.5	5.60	0.63	8.9	−6.9	3.2
51.0	−16.5	8.44	1.14	7.4	17.0	3.9
15.0	−16.5	7.53	0.92	8.2	29.0	3.5
3.0	−16.5	2.23	0.41	5.5	11.5	5.2
−9.0	−16.5	1.47	0.30	4.9	36.3	5.9
−21.0	−16.5	2.83	0.36	7.9	15.6	3.6
−45.0	−16.5	12.59	1.23	10.2	30.8	2.8
39.0	−4.5	6.46	1.17	5.5	−4.9	5.2
15.0	−4.5	21.96	1.30	16.8	−4.4	1.7
3.0	−4.5	2.54	0.54	4.7	15.1	6.1
−33.0	−4.5	4.97	0.58	8.6	−29.4	3.3
39.0	7.5	4.09	0.77	5.3	29.8	5.4
27.0	7.5	8.46	1.11	7.7	19.7	3.7
15.0	7.5	6.71	0.83	8.1	16.4	3.6
3.0	7.5	4.21	0.53	8.0	−28.8	3.6
−9.0	7.5	1.17	0.23	5.0	45.7	5.8
−21.0	7.5	1.26	0.28	4.5	−10.5	6.3
−33.0	7.5	3.28	0.50	6.5	20.0	4.4
39.0	19.5	11.24	1.09	10.3	−62.0	2.8
27.0	19.5	10.48	1.05	9.9	−30.8	2.9
15.0	19.5	5.70	0.58	9.8	21.4	2.9
3.0	19.5	4.01	0.44	9.2	−23.6	3.1
−9.0	19.5	5.57	0.43	12.9	14.6	2.2
−21.0	19.5	2.68	0.44	6.1	14.9	4.7
−33.0	19.5	7.10	0.43	16.4	−6.7	1.8
−45.0	19.5	1.89	0.46	4.1	26.3	7.0
3.0	31.5	5.46	0.66	8.2	57.2	3.5
−21.0	31.5	11.41	0.66	17.3	−4.8	1.7
−33.0	31.5	5.90	0.57	10.3	36.8	2.8
−45.0	31.5	7.10	0.78	9.1	11.6	3.2

Table 5.3: NGC 2024 850 μm Polarization Data

Δ R.A. ($''$)	Δ DEC. ($''$)	p (%)	dp (%)	σ_p	θ (°)	$d\theta$ (°)
13.5	−147.0	6.77	1.13	6.0	−31.0	4.8
1.5	−147.0	4.99	0.90	5.5	−17.9	5.2
49.5	−135.0	9.39	0.93	10.1	−18.8	2.8
13.5	−135.0	4.28	0.38	11.3	−41.6	2.5
1.5	−135.0	5.81	0.32	18.2	−38.1	1.6
−10.5	−135.0	7.63	0.44	17.2	−24.5	1.7
−22.5	−135.0	8.92	0.90	9.9	51.7	2.9
49.5	−123.0	4.96	0.64	7.7	3.3	3.7
37.5	−123.0	5.35	0.60	8.9	−22.2	3.2
25.5	−123.0	1.87	0.32	5.8	−29.2	4.9
13.5	−123.0	4.50	0.15	29.7	−39.0	1.0
1.5	−123.0	4.03	0.27	15.2	−59.8	1.9
−10.5	−123.0	4.76	0.39	12.2	−46.0	2.3
−22.5	−123.0	3.95	0.50	8.0	−47.0	3.6
37.5	−111.0	3.12	0.37	8.5	−11.0	3.4
13.5	−111.0	1.94	0.19	10.2	−50.5	2.8
1.5	−111.0	2.05	0.30	6.8	−67.8	4.2
−10.5	−111.0	6.07	0.35	17.1	−33.0	1.7
−22.5	−111.0	3.07	0.42	7.3	−38.7	3.9
61.5	−99.0	9.10	0.90	10.1	−13.4	2.8
49.5	−99.0	4.27	0.37	11.6	−9.6	2.5
37.5	−99.0	1.37	0.26	5.4	23.6	5.4
13.5	−99.0	2.11	0.13	16.0	−35.9	1.8
1.5	−99.0	2.22	0.23	9.7	−41.3	3.0
−10.5	−99.0	1.96	0.29	6.8	−39.4	4.2
−34.5	−99.0	3.57	0.35	10.1	−60.2	2.8
−46.5	−99.0	2.18	0.47	4.7	81.4	6.1
−58.5	−99.0	5.21	1.08	4.8	−10.8	5.9
61.5	−87.0	3.55	0.42	8.4	9.3	3.4
49.5	−87.0	2.14	0.25	8.7	−8.7	3.3
37.5	−87.0	2.21	0.20	11.3	35.7	2.5
25.5	−87.0	1.11	0.15	7.5	33.0	3.8
13.5	−87.0	1.12	0.10	11.2	−33.3	2.6
1.5	−87.0	2.65	0.17	15.9	−27.0	1.8
−10.5	−87.0	2.38	0.19	12.3	−16.2	2.3
−22.5	−87.0	2.02	0.19	10.7	−24.0	2.7
−34.5	−87.0	1.47	0.33	4.5	−65.9	6.4
−46.5	−87.0	5.39	0.60	9.0	74.8	3.2
73.5	−75.0	7.90	0.98	8.0	−3.6	3.6
61.5	−75.0	4.94	0.35	13.9	−4.9	2.1

Table 5.3 (continued)

Δ R.A. (″)	Δ DEC. (″)	p (%)	dp (%)	σ_p	θ (°)	$d\theta$ (°)
49.5	−75.0	2.70	0.19	14.4	10.1	2.0
37.5	−75.0	1.41	0.17	8.2	17.2	3.5
1.5	−75.0	1.31	0.12	10.5	−23.7	2.7
−10.5	−75.0	1.63	0.15	10.7	−20.7	2.7
−22.5	−75.0	1.77	0.16	10.8	−26.4	2.7
−34.5	−75.0	2.81	0.25	11.3	−10.2	2.5
−46.5	−75.0	3.50	0.52	6.8	−22.0	4.2
73.5	−63.0	5.45	0.99	5.5	−28.7	5.2
61.5	−63.0	4.26	0.35	12.3	5.7	2.3
49.5	−63.0	2.73	0.16	16.9	24.9	1.7
37.5	−63.0	1.38	0.14	10.0	7.6	2.9
1.5	−63.0	2.01	0.09	21.9	−48.0	1.3
−10.5	−63.0	1.27	0.12	10.6	−41.8	2.7
−22.5	−63.0	1.67	0.13	13.0	−19.0	2.2
−34.5	−63.0	3.24	0.21	15.7	−32.1	1.8
−46.5	−63.0	11.87	0.57	20.8	−43.6	1.4
73.5	−51.0	4.43	0.55	8.1	−7.3	3.5
61.5	−51.0	3.65	0.25	14.7	−0.6	2.0
49.5	−51.0	2.30	0.14	16.3	14.6	1.8
37.5	−51.0	1.33	0.09	14.0	20.9	2.0
25.5	−51.0	1.23	0.09	14.0	11.9	2.0
1.5	−51.0	1.42	0.04	32.4	−48.3	0.9
−22.5	−51.0	1.84	0.13	14.0	−52.1	2.0
−34.5	−51.0	3.01	0.27	11.2	−47.6	2.6
−46.5	−51.0	10.69	0.86	12.4	−60.8	2.3
73.5	−39.0	9.98	0.69	14.4	6.6	2.0
61.5	−39.0	3.22	0.24	13.3	3.7	2.2
49.5	−39.0	1.81	0.13	14.2	21.7	2.0
37.5	−39.0	1.20	0.10	11.5	34.7	2.5
25.5	−39.0	1.61	0.10	16.5	37.9	1.7
1.5	−39.0	1.02	0.09	11.8	−39.7	2.4
−10.5	−39.0	1.45	0.09	16.0	−50.1	1.8
−22.5	−39.0	2.14	0.19	11.6	−74.0	2.5
−34.5	−39.0	4.56	0.36	12.8	−74.1	2.2
−46.5	−39.0	6.39	0.63	10.2	−74.0	2.8
61.5	−27.0	2.27	0.30	7.5	3.5	3.8
49.5	−27.0	1.95	0.16	12.1	25.7	2.4
37.5	−27.0	2.24	0.14	16.5	34.0	1.7
25.5	−27.0	2.34	0.13	17.4	44.3	1.6
−10.5	−27.0	1.29	0.10	12.8	−72.7	2.2
−22.5	−27.0	2.53	0.18	13.9	−66.6	2.1
−34.5	−27.0	4.69	0.31	15.1	−80.7	1.9
−46.5	−27.0	4.83	0.35	13.9	−74.6	2.1

Table 5.3 (continued)

Δ R.A. (″)	Δ DEC. (″)	p (%)	dp (%)	σ_p	θ (°)	$d\theta$ (°)
−58.5	−27.0	2.30	0.49	4.7	−47.5	6.1
73.5	−15.0	7.29	0.92	7.9	13.9	3.6
49.5	−15.0	1.39	0.19	7.3	25.1	3.9
37.5	−15.0	1.75	0.13	13.3	38.3	2.2
25.5	−15.0	1.93	0.14	14.1	36.9	2.0
−22.5	−15.0	1.45	0.16	9.1	−67.7	3.2
−34.5	−15.0	3.52	0.29	12.1	−67.8	2.4
−46.5	−15.0	1.35	0.28	4.9	−82.1	5.9
−58.5	−15.0	3.81	0.50	7.6	−85.3	3.8
73.5	−3.0	6.76	0.96	7.0	29.1	4.1
61.5	−3.0	4.65	0.47	10.0	34.9	2.9
49.5	−3.0	2.66	0.21	12.5	19.0	2.3
37.5	−3.0	2.44	0.15	16.8	37.7	1.7
25.5	−3.0	1.32	0.12	11.1	31.6	2.6
−10.5	−3.0	1.05	0.10	10.3	−61.8	2.8
−22.5	−3.0	2.08	0.13	16.5	−62.1	1.7
−34.5	−3.0	1.86	0.22	8.5	−84.5	3.4
−46.5	−3.0	3.92	0.33	12.1	−82.4	2.4
73.5	9.0	13.41	1.13	11.9	37.8	2.4
61.5	9.0	5.49	0.58	9.5	26.8	3.0
49.5	9.0	2.86	0.24	11.8	16.8	2.4
37.5	9.0	1.51	0.16	9.2	22.4	3.1
25.5	9.0	2.77	0.11	25.1	1.6	1.1
13.5	9.0	2.13	0.10	20.6	1.3	1.4
1.5	9.0	1.27	0.06	20.9	−23.8	1.4
−22.5	9.0	2.03	0.19	10.6	−67.1	2.7
−34.5	9.0	3.35	0.23	14.4	−76.1	2.0
−46.5	9.0	6.46	0.33	19.7	−87.7	1.5
−58.5	9.0	4.36	0.50	8.8	−62.4	3.3
49.5	21.0	2.54	0.36	7.0	22.0	4.1
37.5	21.0	1.89	0.21	9.2	2.2	3.1
25.5	21.0	3.32	0.14	24.5	−9.5	1.2
13.5	21.0	2.30	0.12	19.1	−1.0	1.5
1.5	21.0	1.98	0.13	15.1	3.2	1.9
−10.5	21.0	1.35	0.08	17.7	−28.7	1.6
−22.5	21.0	1.19	0.13	8.9	−43.9	3.2
−34.5	21.0	4.46	0.23	19.6	−79.7	1.5
−46.5	21.0	4.14	0.28	14.6	−69.5	2.0
−58.5	21.0	2.91	0.35	8.4	−89.4	3.4
49.5	33.0	4.16	0.77	5.4	−75.3	5.3
37.5	33.0	2.35	0.34	6.9	−26.5	4.2
25.5	33.0	3.73	0.25	15.1	−2.8	1.9

Table 5.3 (continued)

Δ R.A. (″)	Δ DEC. (″)	p (%)	dp (%)	σ_p	θ (°)	$d\theta$ (°)
13.5	33.0	2.21	0.20	11.1	1.1	2.6
1.5	33.0	2.69	0.15	18.1	4.1	1.6
−10.5	33.0	1.63	0.17	9.9	−19.7	2.9
−22.5	33.0	1.80	0.07	25.5	−35.0	1.1
−34.5	33.0	2.56	0.24	10.5	−81.5	2.7
−46.5	33.0	1.32	0.23	5.6	−68.4	5.1
−58.5	33.0	1.61	0.35	4.6	−84.0	6.2
37.5	45.0	4.28	0.51	8.3	−42.2	3.4
25.5	45.0	3.07	0.42	7.4	−8.3	3.9
13.5	45.0	1.23	0.29	4.3	29.2	6.7
1.5	45.0	1.06	0.19	5.6	−25.6	5.2
−10.5	45.0	1.39	0.15	9.0	−28.6	3.2
−22.5	45.0	1.54	0.11	14.3	−24.8	2.0
−34.5	45.0	1.56	0.14	11.4	−82.5	2.5
−58.5	45.0	2.50	0.29	8.6	77.7	3.3
−70.5	45.0	6.64	1.16	5.7	52.6	5.0
25.5	57.0	6.36	0.61	10.4	−48.2	2.7
13.5	57.0	2.92	0.59	5.0	45.8	5.8
−22.5	57.0	1.29	0.25	5.2	−15.0	5.5
−34.5	57.0	1.50	0.14	10.4	−68.0	2.8
−46.5	57.0	1.28	0.21	6.0	−86.9	4.8
−58.5	57.0	3.11	0.49	6.3	46.3	4.5
49.5	69.0	7.34	0.83	8.8	52.7	3.3
37.5	69.0	6.92	0.78	8.8	32.4	3.2
25.5	69.0	9.29	0.76	12.3	−18.8	2.3
13.5	69.0	5.85	1.05	5.6	−72.8	5.2
1.5	69.0	3.52	0.44	7.9	−45.8	3.6
−22.5	69.0	2.00	0.21	9.4	−52.7	3.1
−46.5	69.0	1.92	0.23	8.3	86.5	3.4
13.5	81.0	5.06	0.45	11.3	−73.1	2.5
1.5	81.0	2.75	0.44	6.2	−32.5	4.6
−22.5	81.0	2.18	0.30	7.3	−36.2	3.9
25.5	93.0	4.15	0.55	7.5	23.1	3.8
1.5	93.0	2.70	0.63	4.3	−22.7	6.7

Bibliography

Aitken, D. K., Greaves, J., Chrysostomou, A., Jenness, T., Holland, W., Hough, J. H., Pierce-Price, D., & Richer, J., 2000. *ApJ Letters* **534**, L173.

Anthony-Twarog, B. J., 1982. *AJ* **87**, 1213.

Aso, Y., Tatematsu, K., Sekimoto, Y., Nakano, T., Umemoto, T., Koyama, K., & Yamamoto, S., 2000. *ApJS* **131**, 465.

Bally, J., 1982. *ApJ* **261**, 558.

Bally, J. & Lane, A. P., 1982. *ApJ* **257**, 612.

Barnes, P. J., Crutcher, R. M., Bieging, J. H., Storey, J. W. V., & Willner, S. P., 1989. *ApJ* **342**, 883.

Basu, S., 2000. *ApJ Letters* **540**, L103.

Bontemps, S., Andre, P., & Ward-Thompson, D., 1995. *A&A* **297**, 98.

Butner, H. M., Evans, N. J., Harvey, P. M., Mundy, L. G., Natta, A., & Randich, M. S., 1990. *ApJ* **364**, 164.

Chandler, C. J. & Carlstrom, J. E., 1996. *ApJ* **466**, 338.

Chandrasekhar, S. & Fermi, E., 1953. *ApJ* **118**, 116.

Chernin, L. M. & Masson, C. R., 1992. *ApJ Letters* **396**, L35.

Chini, R., Krugel, E., Haslam, C. G. T., Kreysa, E., Lemke, R., Reipurth, B., Sievers, A., & Ward-Thompson, D., 1993. *A&A* **272**, L5.

Coppin, K. E. K., Greaves, J. S., Jenness, T., & Holland, W. S., 2000. *A&A* **356**, 1031.

Crutcher, R. M., 1999. *ApJ* **520**, 706.

Crutcher, R. M., Henkel, C., Wilson, T. L., Johnston, K. J., & Bieging, J. H., 1986. *ApJ* **307**, 302.

Crutcher, R. M. & Kazes, I., 1983. *A&A* **125**, L23.

Crutcher, R. M., Roberts, D. A., Troland, T. H., & Goss, W. M., 1999. *ApJ* **515**, 275.

Dotson, J. L., Davidson, J., Dowell, C. D., Schleuning, D. A., & Hildebrand, R. H., 2000. *ApJS* **128**, 335.

Dowell, C. D., 2001. *ApJ in preparation.*

Dowell, C. D., Hildebrand, R. H., Schleuning, D. A., Vaillancourt, J. E., Dotson, J. L., Novak, G., Renbarger, T., & Houde, M., 1998. *ApJ* **504**, 588.

Draine, B. T. & Weingartner, J. C., 1996. *ApJ* **470**, 551.

Eislöffel, J., 2000. *A&A* **354**, 236.

Fiege, J. D., Matthews, B. C., & Moriarty-Schieven, G. H., 2001. *in preparation.*

Fiege, J. D. & Pudritz, R. E., 2000a. *MNRAS* **311**, 85.

Fiege, J. D. & Pudritz, R. E., 2000b. *MNRAS* **311**, 105.

Fiege, J. D. & Pudritz, R. E., 2000c. *ApJ* **544**, 830.

Fiege, J. D. & Pudritz, R. E., 2000d. *ApJ* **534**, 291.

Fukuda, N. & Hanawa, T., 2000. *ApJ* **533**, 911.

Gaume, R. A., Johnston, K. J., & Wilson, T. L., 1992. *ApJ* **388**, 489.

Gehman, C. S., Adams, F. C., & Watkins, R., 1996. *ApJ* **472**, 673.

Genzel, R. & Downes, D., 1977. *A&A Suppl.* **30**, 145.

Genzel, R. & Downes, D., 1979. *A&A* **72**, 234.

Gibb, A. G., 1999. *MNRAS* **304**, 1.

Gibb, A. G. & Heaton, B. D., 1993. *A&A* **276**, 511.

Girart, J. ., Crutcher, R. M., & Rao, R., 1999. *ApJ Letters* **525**, L109.

Girart, J., Ho, P. T. P., Rudolph, A. L., Estalella, R., Wilner, D. J., & Chernin, L. M., 1999. *ApJ* **522**, 921.

Goldreich, P. & Kylafis, N. D., 1981. *ApJ Letters* **243**, L75.

Goodman, A. A., Jones, T. J., Lada, E. A., & Myers, P. C., 1995. *ApJ* **448**, 748.

Greaves, J., Holland, W., Chrysostomou, A., & Jenness, T., 2000. Imaging the polarized interstellar medium. In *Imaging at Radio through Submillimeter Wavelengths. Edited by Jeff Mangum. Publisher: The Astronomical Society of the Pacific, Conference Series, 2000. The conference was held June 6-8, 1999, in Tucson, Arizona.*, pp. E18.

Greaves, J., Holland, W., Jenness, T., Moriarty-Schieven, G., Chrysostomou, A., Berry, D., Murray, A., Nartallo, R., Ade, P., Gannaway, F., Haynes, C., Tamura, M., Momose, M., & Morino, J., 2001. *MNRAS in preparation.*

Greaves, J. S., Holland, W. S., & Ward-Thompson, D., 2001. *ApJ Letters* **546**, L53.

Heiles, C., Goodman, A. A., McKee, C. F., & Zweibel, E. G., 1993. Magnetic fields in star-forming regions - observations. In *Protostars and Planets III*, pp. 279.

Hildebrand, R. H., 1988. *QJRAS* **29**, 327.

Hildebrand, R. H., Dotson, J. L., Dowell, C. D., Platt, S. R., Schleuning, D., Davidson, J. A., & Novak, G., 1995. Far-infrared polarimetry. In *ASP Conf. Ser. 73: From Gas to Stars to Dust*, pp. 97.

Holland, W. S., Greaves, J. S., Ward-Thompson, D., & Andre, P., 1996. *A&A* **309**, 267.

Holland, W. S., Robson, E. I., Gear, W. K., Cunningham, C. R., Lightfoot, J. F., Jenness, T., Ivison, R. J., Stevens, J. A., Ade, P. A. R., Griffin, M. J., Duncan, W. D., Murphy, J. A., & Naylor, D. A., 1999. *MNRAS* **303**, 659.

Houde, M., Phillips, T. G., Bastien, P., Peng, R., & Yoshida, H., 2001. *ApJ* **547**, 311.

Johnstone, D. & Bally, J., 1999. *ApJ Letters* **510**, L49.

Kazes, I. & Crutcher, R. M., 1986. *A&A* **164**, 328.

Kylafis, N. D., 1983. *ApJ* **267**, 137.

Lada, E. A., Bally, J., & Stark, A. A., 1991. *ApJ* **368**, 432.

Lada, E. A., Evans, N. J., Depoy, D. L., & Gatley, I., 1991. *ApJ* **371**, 171.

Launhardt, R., Mezger, P. G., Haslam, C. G. T., Kreysa, E., Lemke, R., Sievers, A., & Zylka, R., 1996. *A&A* **312**, 569.

Lazarian, A., Goodman, A. A., & Myers, P. C., 1997. *ApJ* **490**, 273.

Lis, D. C., Menten, K. M., & Zylka, R., 1999. *ApJ* **527**, 856.

Matthews, B. & Wilson, C., 2001. *ApJ in preparation.*

Matthews, B., Wilson, C., & Fiege, J., 2001. *ApJ accepted.*

Matthews, B. C. & Wilson, C. D., 2000. *ApJ* **531**, 868.

Mezger, P. G., Chini, R., Kreysa, E., Wink, J. E., & Salter, C. J., 1988. *A&A* **191**, 44.

Mezger, P. G., Sievers, A. W., Haslam, C. G. T., Kreysa, E., Lemke, R., Mauersberger, R., & Wilson, T. L., 1992. *A&A* **256**, 631.

Mitchell, G., Johnstone, D., Moriarty-Schieven, G., Fich, M., & Tothill, N., 2001. *ApJ* **556**, 215.

Moriarty-Schieven, G. H., Hughes, V. A., & Snell, R. L., 1989. *ApJ* **347**, 358.

Motte, F., André, P., Ward-Thompson, D., & Bontemps, S., 2001. *A&A* **372**, L41.

Mouschovias, T. C., 1976. *ApJ* **207**, 141.

Nagasawa, M., 1987. *Prog. Theor. Phys.* **77**, 635.

Nakamura, F., Hanawa, T., & Nakano, T., 1993. *PASJ* **45**, 551.

Ostriker, J., 1964. *ApJ* **140**, 1056.

Purcell, E. M., 1979. *ApJ* **231**, 404.

Richer, J. S., Hills, R. E., & Padman, R., 1992. *MNRAS* **254**, 525.

Sanders, D. B. & Willner, S. P., 1985. *ApJ Letters* **293**, L39.

Schleuning, D. A., 1998. *ApJ* **493**, 811.

Schleuning, D. A., Dowell, C. D., Hildebrand, R. H., Platt, S. R., & Novak, G., 1997. *PASP* **109**, 307.

Schulz, A., Guesten, R., Zylka, R., & Serabyn, E., 1991. *A&A* **246**, 570.

Snell, R. L. & Edwards, S., 1982. *ApJ* **259**, 668.

Snell, R. L., Scoville, N. Z., Sanders, D. B., & Erickson, N. R., 1984. *ApJ* **284**, 176.

Stodólkiewicz, J., 1963. *Acta Astron.* **13**, 30.

Tomisaka, K., Ikeuchi, S., & Nakamura, T., 1988. *ApJ* **326**, 208.

Visser, A. E., Richer, J. S., Chandler, C. J., & Padman, R., 1998. *MNRAS* **301**, 585.

Walther, D. M., Robson, E. I., Aspin, C., & Dent, W. R. F., 1993. *ApJ* **418**, 310.

Ward-Thompson, D., Kirk, J. M., Crutcher, R. M., Greaves, J. S., Holland, W. S., & André, P., 2000. *ApJ Letters* **537**, L135.

Weintraub, D. A., Goodman, A. A., & Akeson, R. L., 2000. Polarized light from star-forming regions. In *Protostars and Planets IV*, pp. 247.

Yu, K., Billawala, Y., Smith, M. D., Bally, J., & Butner, H. M., 2000. *AJ* **120**, 1974.

Chapter 6

Polarimetry of the Filamentary NGC 2068 Cloud in Orion B

This chapter is a draft of the article "Magnetic Fields in Star-Forming Molecular Clouds IV. Polarimetry of the Filamentary NGC 2068 Cloud in Orion B" by B.C. Matthews and C.D. Wilson, which has been submitted to The Astrophysical Journal.

Abstract

We present submillimetre polarimetry at 850 μm toward the filamentary star-forming region associated with the reflection nebulosity NGC 2068 in Orion B. These data were obtained using the James Clerk Maxwell Telescope's SCUBA polarimeter. The polarization pattern observed is not consistent with that expected for a unidirectional field geometry. There are three distinct distributions of polarization angle, which could represent regions of differing inclination and/or field geometry within the filamentary gas. In general, the polarization pattern does not correlate with the underlying total dust emission. The presence of varying inclinations against the plane of the sky is consistent with the comparison of the 850 μm continuum emission to the optical emission from the Palomar Optical Sky Survey, which shows that the western dust emission lies in the foreground of the optical nebula while the eastern dust emission is generated in the background. Percentage polarizations are high, particularly toward the north-east region of the cloud. The mean polarization percentage in the region is 5.0% with a standard deviation of 3.1%. Depolarization toward high intensities is identified in all parts of the filament.

6.1 Introduction

At a distance of $\sim$ 415 pc (Anthony-Twarog 1982), the Orion B cloud is the closest star-forming region which is actively forming massive stars. Within this giant molecular cloud, star formation is concentrated into five distinct regions: NGC 2071, NGC 2068, LBS 23 (HH 24), NGC 2024 and NGC 2023, as determined from unbiased surveys for young stellar objects (Lada, Bally, & Stark 1991) and dense CS gas (Lada et al. 1991). In order to probe the conditions within these regions, they have been observed in various line transitions of many molecules (e.g. CS $J = 5 - 4$, Lada et al. 1997; three transitions of HCO^+, Gibb et al. 1995; CO $J = 7 - 6$, Krugel et al. 1989; CO $J = 4 - 3$, Walker et al. 1988; CO $J = 3 - 2$, White et al. 1981; CO $J = 1 - 0$ and ^{13}CO $J = 1 - 0$, White & Phillips 1981). Continuum studies have searched the regions around the CS cores for dust emission (e.g. Launhardt et al. 1996). Larger scale maps of the dust emission have been produced using the sensitive SCUBA detector at the James Clerk Maxwell Telescope (Mitchell et al. 2001; Motte et al. 2001). Mitchell et al. (2001) observed 850 μm dust emission, as well as some ^{12}CO $J = 3 - 2$, ^{13}CO and C^{18}O $J = 2 - 1$ emission, from the NGC 2068 region. The submillimetre emission lies south of the reflection nebula which is seen optically and contains an infrared cluster (Lada, Bally, & Stark 1991). The overall structure is that of a "clumpy filament" in which 18 distinct compact sources are identified. Most of the submillimetre sources fall outside the boundary of the cluster identified in CS by Lada et al. (1991).

Prior to the Mitchell et al. (2001) study, evidence for outflow existed only from high velocity wings of ^{12}CO and ^{13}CO $J = 1 - 0$ emission (Edwards & Snell 1984; Gibb & Little 2000) toward the location of an H_2O maser (Haschick et al. 1983). This source is coincident (within $2''$) with the dust condensation designated OriBN 51 by Mitchell et al. (2001). Other searches for Herbig-Haro objects in the NGC 2068 region (i.e. Jones et al. 1987) concentrated on the region LBS 23. Zhao et al. (1999) find an HH object near the coordinates of the NGC 2068 dust emission (HH-

442). However, they do not identify the source of the H_2 emission. Mitchell et al. (2001) detect evidence for bipolar outflows around OriBN 51, as expected, and also around the OriBN 35 and OriBN 36 peaks (see their Fig. 1c or Figure 6.1 below), although the sources of these outflows are ambiguous due to the close proximity of OriBN 33 and OriBN 37 to the positions of high velocity gas. OriBN 39 has a 2MASS infrared source associated with it, and thus should be a source of outflow. Evidence for redshifted gas near OriBN 47 also suggests some outflow from this source. Thus, it is clear that intense star-formation is ongoing in this region.

The addition of a polarimeter to SCUBA also permits mapping of polarized emission from dust at 850 μm over fields of many arcminutes. The study of polarized emission is of great interest since at long wavelengths ($\lambda > 25$ μm), it effectively traces the orientation of magnetic fields local to star-forming regions (Hildebrand 1988). Magnetic fields have been shown to be energetically comparable to gravity and kinetic motions within molecular clouds (Myers & Goodman 1988; Crutcher 1999; Basu 2000) and are theorized to provide vital support to clouds, preventing global collapse (see Mouschovias 1987; McKee, Zweibel, Goodman, & Heiles 1993 and references therein). Such support is necessary to explain the low star-forming efficiencies observed in molecular clouds, including Orion B where the efficiency is ~ 1 % (Carpenter 2000). We have previously observed the polarized emission from the regions NGC 2071, LBS 23, and NGC 2024 (Matthews, Fiege, & Moriarty-Schieven 2001), as well from the OMC-3 part of the Integral-shaped Filament in Orion A (Matthews, Wilson, & Fiege 2001). In each region observed, strong degrees of polarization are detected ($\geq 10\%$), but the polarization percentage systematically decreases toward regions of high intensity. This trend, known as the "depolarization effect", has been observed in many other regions, including massive cores such as OMC-1 (Schleuning et al. 1997) and protostellar and starless cores (Girart et al. 1999; Ward-Thompson et al. 2000).

Polarization data probe only two directions of the magnetic field geometry –

those on the plane of the sky. Additionally, they provide no information about the strength of the magnetic field. This is because the degree of polarization measured is dependent not only on the strength of the field, but also on the degree of grain alignment, the effectiveness of the spin-up of the grains, and the dust grain composition. All of these are poorly known quantities, although comparisons of polarizations at different wavelengths are beginning to test models of grain composition and alignment (Hildebrand et al. 2000). In order to investigate the third dimension of the magnetic field which is aligned along the line of sight, B_{los}, measurements of the Zeeman splitting of atomic or, for dense gas, molecular lines must be used. These data provide both the direction and strength of B_{los}. To date, relatively few star-forming regions have estimates of B_{los}; the number toward which both polarimetry and Zeeman splitting observations have been observed is even smaller.

Where field geometries are simple and the direction of the plane-of-sky magnetic field does not vary through the cloud depth, the polarized emission detected is perpendicular to the mean magnetic field and the latter can be inferred simply by rotating the polarization vectors by 90°. If the field has a more complex, irregular geometry, then interpretation becomes more difficult. In such cases, it is best to compare directly the polarization maps with polarization patterns predicted from a physical model of a magnetized cloud. It is important to recognize that the polarizations measured are vector sums along a particular line of sight through the cloud observed, weighted by column density. Fiege & Pudritz (2000a) present a model for a filamentary cloud in which a helical magnetic field threads the filament and plays an important role in determining the radial density structure. This model predicts an r^{-2} density profile, which has been observed in several clouds, including the Integral-shaped Filament (Johnstone & Bally 1999) and several clouds in Cygnus (Lada, Alves & Lada 1999; Alves, Lada & Lada 1999). The helical field geometry also predicts depolarization toward the axis of a filament due to cancellation effects on either side of the axis. Fiege & Pudritz (2000b) present predicted polarization patterns for cases in which the field is either poloidally or toroidally dominated as well as for various filament inclinations.

Polarimeters aboard the Kuiper Airborne Observatory (KAO), at the Caltech Submillimeter Observatory (CSO), and the James Clerk Maxwell Telescope (JCMT) have detected far-infrared and submillimetre polarization toward many Galactic molecular clouds (Schleuning et al. 1997; Dowell et al. 1998; Schleuning 1998; Aitken et al. 2000; Coppin et al. 2000; Dotson et al. 2000; Matthews & Wilson 2000; Matthews, Wilson, & Fiege 2001; Matthews, Fiege, & Moriarty-Schieven 2001) although until recently, limitations on detector sensitivity restricted observations to bright and/or compact, usually massive, cores. Detections of polarized thermal emission from dust have now been made toward individual protostellar envelopes (Girart et al. 1999; Holland et al. 1996) and starless cores (Ward-Thompson et al. 2000). There are no prior observations of polarized emission from the NGC 2068 dust emitting region. However, Mannion & Scarrott (1984) measured linear polarization from scattering against the reflection nebula north of the molecular condensations. Based on the centrosymmetric pattern observed, Mannion and Scarrott ruled out the presence of aligned grains within the reflection nebula. They infer the presence of a foreground assembly of grains illuminated from behind solely by the star HD 38563N. The position of this star is $\sim 5'$ north-east of the dust emission on which we report in this work, concident with the near-IR cluster observed by Lada, Bally, & Stark (1991).

This paper is the fourth in a series which seeks to compare the polarization patterns (and inferred magnetic field geometries) in different star-forming regions. The observations and data reduction techniques are described in §6.2. The polarization data are presented and analyzed in §6.3. The implications of these data for the local magnetic field geometry and that of Orion B as a whole are discussed in § 6.4, and § 6.5 summarizes our results.

6.2 Observations and Data Reduction

Using the UK/Japan polarimeter with the SCUBA detector at the James Clerk Maxwell Telescope[1], we have mapped polarized thermal emission from dust at 850 μm toward a filamentary dust cloud associated with the star-forming region NGC 2068. The observations were taken from 11 to 16 October 1999, and additional data were added on 18 February 2000. The polarizer and general reduction techniques are described in Greaves et al. (2001) and Greaves et al. (2000). More information on data reduction and systematic errors can be found in Matthews, Wilson, & Fiege (2001).

Six different SCUBA fields were required to map the entire NGC 2068 filament. Initially, four fields were used, but then the number of fields was increased and the positions shifted; hence 10 independent field centres were used. The field centres and other observing parameters are summarized in Table 6.1. The data were obtained using a 16 point jiggle-map mode, in which the telescope is "jiggled" in order to completely sample the SCUBA field. Chopping to a reference position was done to remove sky effects. The maximum chop throw possible is $180''$. We typically used $150''$ to ensure we were not chopping onto polarized emission. The tau(225 GHz) ranged from 0.03 to 0.09 over the observations, but $> 85\%$ were taken when tau(225 GHz) was 0.06 or 0.07.

We have reduced the data using the Starlink software package POLPACK, designed to include polarization data obtained with bolometric arrays. The data have been corrected for an error in the SCUBA computer's clock which placed incorrect LST times in the data headers from July 1999 to May 2000. This error did not affect the telescope's acquisition or tracking but affects data reduction since the elevation and sky rotation are calculated from the LST times in the data files. The evolution

[1]The JCMT is operated by the Joint Astronomy Centre on behalf of the Particle Physics and Astronomy Research Council of the UK, the Netherlands Organization for Scientific Research, and the National Research Council of Canada.

Pointing Centre		Chop Position Angle	Number of
R.A. (J2000)	Dec. (J2000)	(east of north)	Times Observed
$05^h46^m26\overset{s}{.}5$	$+00°00'21\overset{''}{.}9$	40°	3
$05^h46^m30\overset{s}{.}5$	$-00°01'48\overset{''}{.}4$	90°	3
$05^h46^m37\overset{s}{.}6$	$+00°00'33\overset{''}{.}1$	155°	3
$05^h46^m47\overset{s}{.}9$	$+00°01'0\overset{''}{.}3$	155°	3
$05^h46^m25\overset{s}{.}7$	$+00°00'34\overset{''}{.}9$	40°	17
$05^h46^m28\overset{s}{.}7$	$-00°01'55\overset{''}{.}3$	90°	18
$05^h46^m31\overset{s}{.}2$	$-00°00'25\overset{''}{.}5$	165°	18
$05^h46^m39\overset{s}{.}2$	$+00°00'48\overset{''}{.}9$	155°	13
$05^h46^m44\overset{s}{.}7$	$+00°00'33\overset{''}{.}5$	155°	12
$05^h46^m50\overset{s}{.}3$	$+00°01'23\overset{''}{.}1$	155°	11

Table 6.1: Observing Parameters for Jiggle Mapping
The chop throw used for all observations was 150″, with the exception of the pointing centre $\alpha = 05^h46^m31\overset{s}{.}2$ and $\delta = -00°00'25\overset{''}{.}5$, for which the throw was 180″.

of the magnitude of this error over time has been tracked and can therefore be corrected retroactively by adjusting the times in the headers (see the JCMT website for details). The error in timing after this adjustment is ±10s.

After extinction correction, noisy bolometers were identified and removed from the data sets. The data were sky subtracted using bolometers with mean values close to zero, but not those which were significantly negative. At 850 μm, the sky is highly variable on timescales of seconds. This variability must be measured and removed from the data. Chopping removes the effects of slow sky variability; however, fast variations remain in the data, which require sky subtraction using array bolometers devoid of significant flux. We used between one and three bolometers to determine the sky variability, using the existing scan maps of total intensity at 850 μm (Mitchell et al. 2001) to help select empty bolometers. The methods of sky subtraction are discussed in detail in Jenness, Lightfoot, & Holland (1998). As part of our analyses of other regions, we determined that sky subtraction can be done effectively with a single bolometer (Matthews, Wilson, & Fiege 2001) and that the POLPACK reduction process is extremely robust with respect to the selection of sky bolometers

(Matthews, Fiege, & Moriarty-Schieven 2001). We have not added the mean flux removed by sky subtraction back into the NGC 2068 maps, since the flux in the sky positions was sufficiently close to zero (as determined from the large scale intensity map of Mitchell et al. 2001).

Once the instrumental polarizations (IPs) were removed from each bolometer, all the data sets were combined to produce a final map in three Stokes' parameters, I, Q and U, where I is the total, unpolarized intensity and Q and U are two orthogonal components of linearly polarized light. These three Stokes' parameters were then combined to yield the polarization percentage, p, and polarization position angle , θ, in the map according to the relations:

$$p = \frac{\sqrt{Q^2 + U^2}}{I}; \quad \theta = \frac{1}{2}\arctan(U/Q). \tag{6.1}$$

The uncertainties in each of these quantities are given by:

$$dp = p^{-1}\sqrt{[dQ^2Q^2 + dU^2U^2]}; \quad d\theta = 28.6^\circ/\sigma_p \tag{6.2}$$

where σ_p is the signal-to-noise in p, or p/dp.

A bias exists which tends to increase the p value, even when Q and U are consistent with $p = 0$ because p is forced to be positive. The polarization percentages were debiased according to the expression:

$$p_{db} = \sqrt{p^2 - dp^2}. \tag{6.3}$$

Future references to polarization percentage, or p, refer to the debiased value.

In order to improve the σ_p, and hence $d\theta$, the data were binned to $15''$ sampling. This improves σ_p by a factor of five over the unbinned $3''$ sampled data. Good vectors were selected to have $\sigma_p > 3$, $dp < 1\%$, $p > 1\%$ and be coincident with positions where the total unpolarized 850 μm flux exceeds 20% that of the faintest of the six compact peaks, OriBN 35. The filtering of polarizations less than 1% accounts for the uncertainties in the IP values, as well as for any contamination due to sidelobe polarization, as discussed in Greaves et al. (2001). Sidelobe contamination refers to a polarized signal measured within the main beam due to a source within a sidelobe. If there is enough polarized flux ($p \times I$) from a source in a sidelobe position, a signal can be produced in the main beam despite the fact that the power in the JCMT sidelobes at 850 μm is typically $\leq 1\%$ that of the main beam. Greaves et al. (2001) derive the minimum believable polarization percentage, p_{crit}, based on: the ratio of power in the sidelobe to the main beam, P_{sl}/P_{mb}; the ratio of unpolarized, total flux of the source in the sidelobe to that in the main beam, F_{sl}/F; and the IP estimate at the sidelobe, p_{sl}:

$$p_{crit} \geq 2 \times p_{sl} \left(\frac{P_{sl}}{P_{mb}}\right) \left(\frac{F_{sl}}{F}\right). \tag{6.4}$$

We can estimate the extreme value of p_{crit} for the entire NGC 2068 region by calculating the worst case scenario. This occurs for the field centred at α(J2000) = $05^{\mathrm{h}}46^{\mathrm{m}}31\overset{\mathrm{s}}{.}2$ and δ(J2000) = $-00°00'25\overset{''}{.}5$, in which the brightest source in our map, OriBN 51, was approximately 54$''$ from the centre of the array. The beam responses and IP values are obtained from maps of unpolarized planets. Using polarization maps of Saturn from 14 October 1999, 16 October 1999 and 18 February 2000, the ratios of power in the sidelobe versus main beam are deduced to be 0.009, 0.01, and 0.004 respectively. The corresponding mean IP values at this sidelobe position are 4.5%, 4.7%, and 4.3%. The ratio of the flux of Ori BN 51 to the centre of the field is ~ 7. Hence, using equation (6.4), the p_{crit} values are determined to be 0.57%, 0.66%, and 0.24%. Thus, by selecting only values of $p > 1\%$, the polarizations cannot be attributable to sidelobe polarization.

6.3 NGC 2068 Polarization Data

Figure 6.1 shows the polarization data toward the NGC 2068 filamentary cloud. These data are displayed over a portion of the Mitchell et al. (2001) map of Orion B North. The polarization data are binned to 15″, slightly greater than the 14″ beamwidth of the JCMT at 850 μm. Thus, each vector can be treated as an independent measurement of the local polarization at 850 μm. By eye, one can readily discern that three different populations of position angles exist within Figure 6.1. Separation of the data into three regions based on boundaries in RA can generally separate these populations. Figure 6.2 shows the distributions in position angle over the whole map, and for each of the three subsections. Region 1 encompasses the eastern part of the map, including all vectors east of the J2000 position of $05^{h}46^{m}39\overset{s}{.}8$. Region 2 is west of Region 1, to the RA $05^{h}46^{m}33\overset{s}{.}8$ (J2000). Region 3 covers the western section of the map, including all vectors west of $05^{h}46^{m}33\overset{s}{.}8$ (J2000).

NGC 2068 contains six compact dust condensations (Mitchell et al. 2001), as well as a dozen more amorphous, fainter condensations. In the OMC-3 filament of Orion A, the polarization pattern was no different in the presence of embedded cores than elsewhere along the filament (Matthews, Wilson, & Fiege 2001). However, in Figure 6.1, polarization vectors near cores are smaller and more variable in direction, particularly near the cores OriBN 35, 47 and especially 51. In the latter case, no polarization is detected toward the core. Toward each of these cores, there is evidence of outflow; they are not pre-protostellar in nature. We note however that across the outflow source OriBN 39 and the compact core OriBN 38, the polarization vectors are consistent with the patterns surrounding the cores. The effect of the cores on the polarization pattern indicates that the filament is not dominating the polarized emission as was the case in OMC-3 in Orion A (Matthews, Wilson, & Fiege 2001).

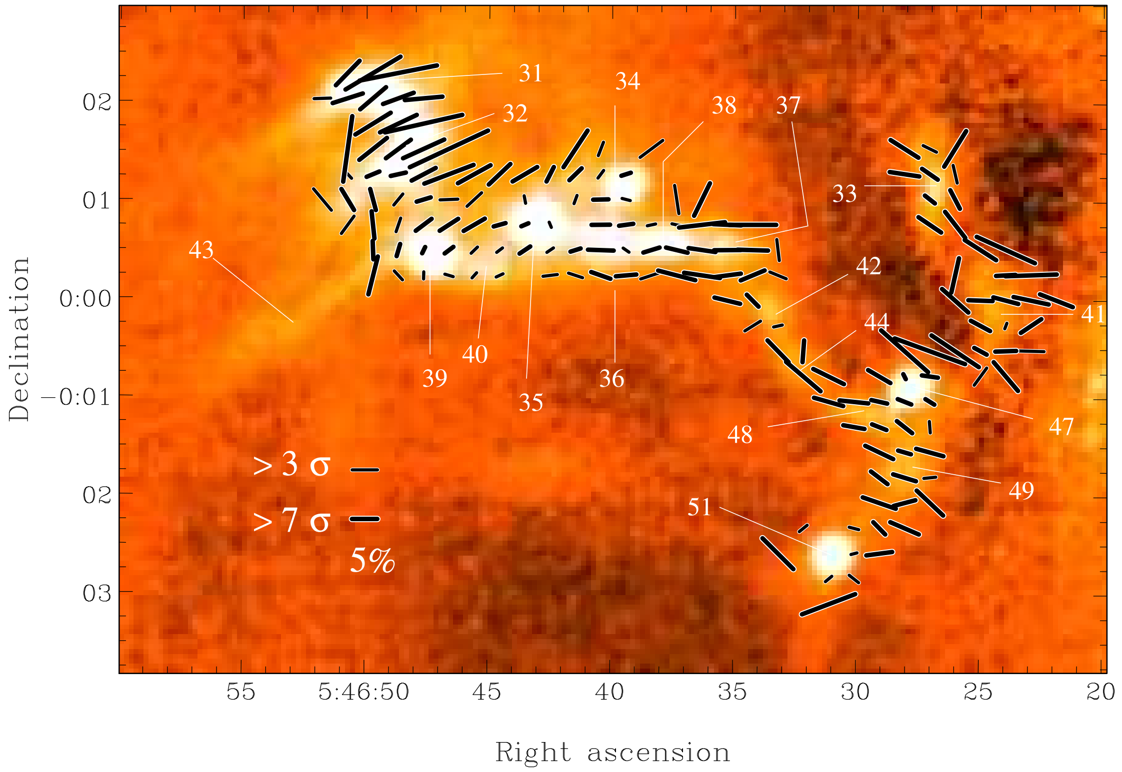

Figure 6.1: The 850 μm Polarization Pattern Across NGC 2068
The coloured greyscale is a larger-scale scan map provided by Mitchell et al. (2001). The greyscale range is -2σ to 3σ. Polarization data were sampled at $3''$ and have been binned to $15''$ (> the JCMT beamwidth). All vectors plotted are coincident with location where the total, unpolarized intensity > 20% that of OriBN 35 (10% that of OriBN 51). The thin vectors have signal-to-noise $\sigma_p > 3$, while the thick vectors have $\sigma_p > 7$. The thin vectors are accurate in position angle to better than 10°, while the thicker vectors are accurate to better than 4°. The coordinates of the map are J2000.

6.3.1 Polarization Position Angle and Filament Orientation

In Region 1, the mean polarization position angle is 109° east of north, which is equivalent to −71° in linear polarization (since vectors offset by 180° are indistinguishable). The amorphous cores near the north-east have the highest polarizations, and the vector orientations there are roughly perpendicular to the projected filamentary axis, aligned in a north-east to south-west orientation. Interestingly, the vectors along the three cores OriBN 34, 35 and 39 align well with those to the north-east, but now appear to lie parallel to the string of three cores. In Region 2, which includes the cores OriBN 37, 38 and part of 36, the vectors also follow the

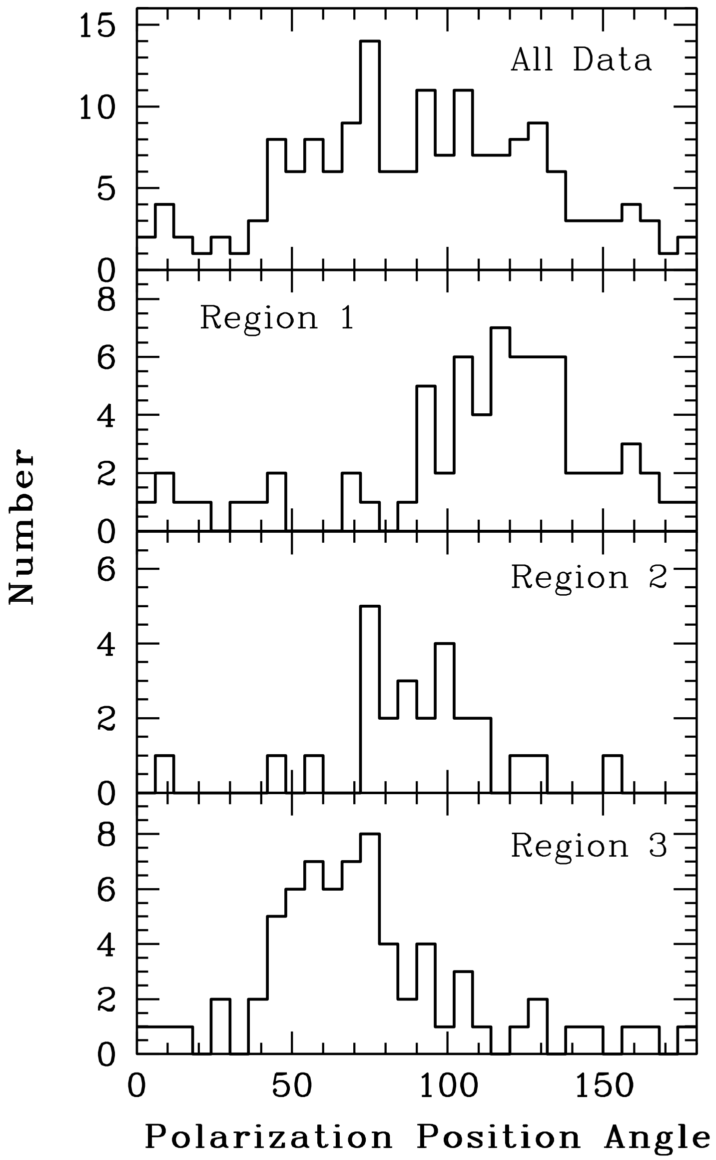

Figure 6.2: The Distribution of Polarization Position Angle in NGC 2068. The position angles of all vectors plotted on Figure 6.1 are presented in the top panel. The distribution of vectors has a mean of 91.4° and standard deviation about the mean of 40°. Additionally, the distribution of position angles in all three subsets of the data as defined in the text are shown.

string of cores. Finally, in Region 3, which includes all cores west of OriBN 42, the polarization vectors are distributed about a mean of 74°, although the projected filament direction varies considerably. The vectors thus tend to follow the filament near OriBN 42 to 48, and then lie perpendicular to the filamentary dust emission along the whole eastern edge. Overall, there is no strong correlation between the filament orientation and the vector position angles.

Table 6.2 summarizes the statistics of the three data subsets plus the whole data set for the NGC 2068 region, as well as the results of single Gaussian fits to each of the position angle distributions shown in Figure 6.2. The mean position angle is denoted μ, while the width of the distribution is $w(\theta)$. The reduced chi-squared value is also listed and in each case is < 1. The fit to Region 3 gives a mean of 66° with a width of 18°. Region 2 gives a mean of 93° with a width of 16°, and Region 1 yields mean and width of 123° and width 24°. The results of the fits are consistent with the statistical mean and standard deviation in the position angles.

Region	# Vectors	Statistics					Gaussian Fits		
		$< p >$ (%)	Median p (%)	s(p) (%)	$< \theta >$ (°)	s(θ) (°)	μ (°)	$w(\theta)$ (°)	χ^2_{red}
1	68	4.9	3.6	3.6	109.2	41	123	24	0.7
2	26	4.7	5.2	2.2	93.4	16	93	16	0.4
3	69	5.2	4.8	2.9	74.3	35	66	18	0.7
all	163	5.0	4.3	3.1	91.4	40	95	41	0.2

Table 6.2: Polarization Percentage and Position Angle within NGC 2068

6.3.2 Polarization Percentage

The results of a basic statistical analysis of the polarization percentage distributions in the NGC 2068 cloud and its subset of three regions are reported in Table 6.2. The mean polarization percentage in the whole filamentary cloud is 5.0% with a standard deviation of 3.1%. Similar values are found for each separate region within

NGC 2068. No systematic variation in polarization percentage is obvious from examination of Table 6.2. Interestingly, Region 2 has the highest median value of p, and it is the only region where the median exceeds the mean, which indicates that in this region, polarization is high. The mean is not biased by only a few vectors of particularly high polarization percentage.

One of the most interesting properties of dust emission polarimetry has been the measurement of declining polarization percentage with increasing unpolarized intensity. Figure 6.3 shows this same trend in the NGC 2068 region and its subregions that has been observed in other regions. Over the entire data set, the variation of p with total intensity follows a power law of the form: $p = A \times I^{\gamma}$, where $\gamma = -0.81 \pm 0.04$ and $A = (1.6 \pm 0.4) \times 10^{-2}$. No systematic variation in polarization percentage between regions is evident from examination of Figure 6.3. We do note, however, that the effect is strongest in Region 3. In Region 1, the vectors surrounding the cores OriBN 31 and 32 are shown as filled triangles, while the rest of the region's vectors are plotted as open triangles. It is clear that the highest polarizations are observed at the extreme north-east of the NGC 2068 region.

As discussed in Matthews, Wilson, & Fiege (2001), a depolarization effect can be produced systematically by chopping the telescope during observing. However, based on that analysis, the steep profiles shown in Figure 6.3 could not be explained by this effect unless there were *significant* polarized flux in the chop position. For example, if the reference, or chop, position had 25% of the peak flux in the source field and was polarized to twice the degree of the source field, then a slope of -0.88 could be produced on a $\log p$ versus $\log I$ plot *in regions of low total intensity.* Even under this extreme scenario, in regions of high flux, we would not expect such a sharp decline in polarization percentage with intensity. We thus conclude that the depolarization effect in this region is not produced by systematic effects of chopping.

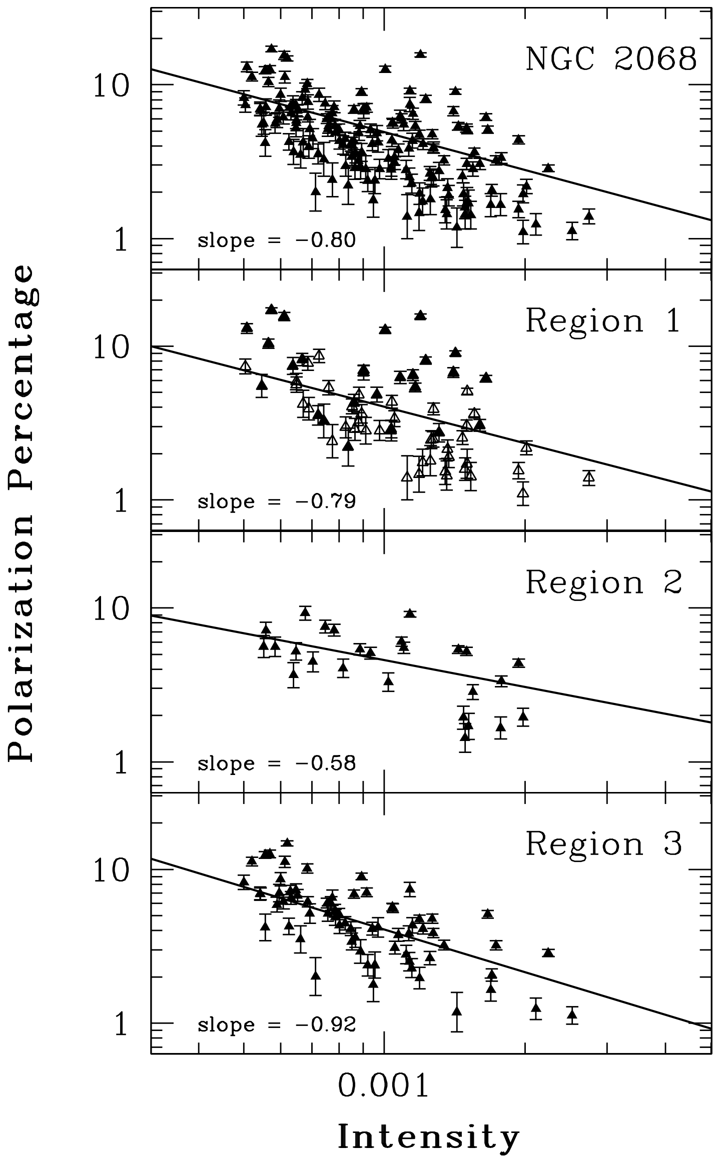

Figure 6.3: The depolarization effect in NGC 2068.
We have plotted p versus I in log space and included fits to the corresponding p versus I profiles. The fits are to the power law: $p = A \times I^{\gamma}$, where γ is shown as the slope of the log-log plot. Plots are shown for each of the subregions discussed in the text. The Region 1 panel illustrates positions at the extreme north-east (near OriBN 31 and 32) as filled triangles, while the rest of the vectors in the area are plotted as open triangles. The strongest polarizations are located in the north-east area.

6.4 Discussion

6.4.1 Polarization Percentage in Orion B

Figure 6.4 shows the distributions of polarization percentage in the regions of Orion B observed with the SCUBA polarimeter. These distributions have been normalized to the total number of vectors measured in each region, and the counts expressed as a fraction of the total. The error bars represent the $\sqrt{N}$ statistical uncertainty in the number of counts, also normalized to the total in each map. The distribution for NGC 2068 is comparable to those measured in the other star-forming regions of Orion B North – NGC 2071 and LBS23N – and with measurements toward the OMC-3 filament in Orion A (Matthews, Wilson, & Fiege 2001). The NGC 2024 region is dominated by low percentage polarizations, with the majority between 1-2%. This result could imply NGC 2024 has weaker magnetic fields, poorer grain rotation or alignment, a different grain composition, or some combination of these factors. The fact that NGC 2071, NGC 2068 and LBS 23N show distributions which are reasonably flat from 1-6% could indicate similar grain properties, field strengths, and degrees of grain aligment, but this cannot be proven with these data. The densities toward the NGC 2024 cores have been estimated to be abnormally high (10^8 cm^{-3} Mezger et al. 1988), but Schulz et al. (1991) suggest the values are more typical of cores (10^6 cm^{-3}). Polarization data at other wavelengths (such as 350 μm) could help constrain the dust properties according to models (see Hildebrand et al. 2000 and references therein), and observations of dense molecular tracers like OH for Zeeman splitting could provide more detailed information about the field geometries in these four regions.

Toward all four regions of Orion B observed in polarized emission, the depolarization effect is detected (see Fig. 5 of Matthews, Fiege, & Moriarty-Schieven (2001) and Figure 6.3). Matthews, Fiege, & Moriarty-Schieven (2001) show that

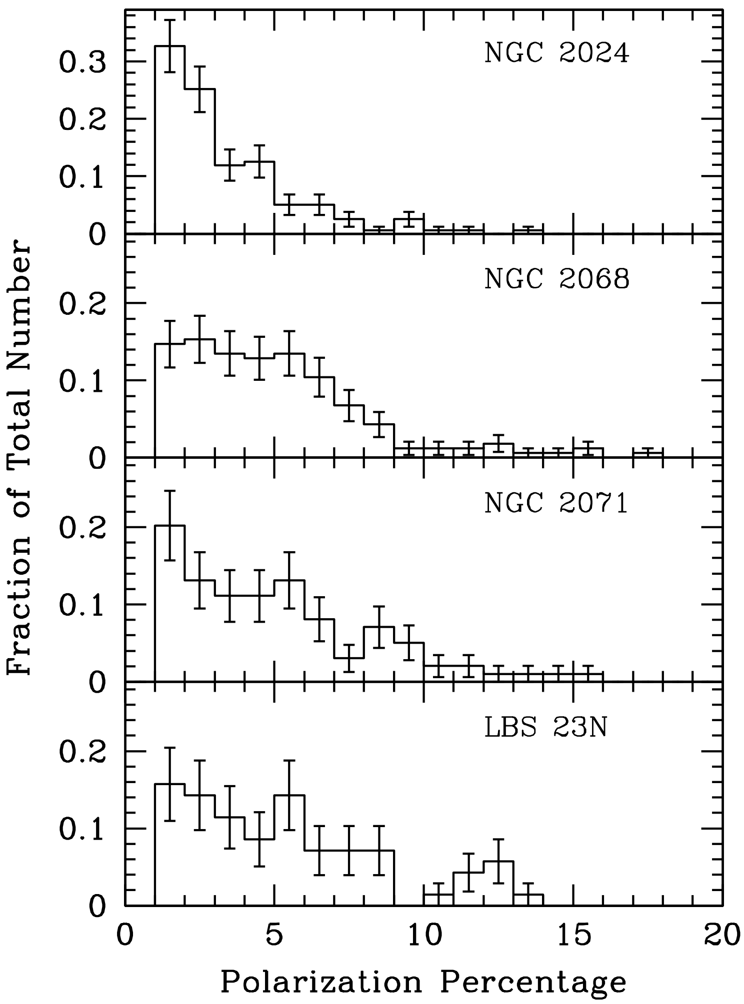

Figure 6.4: The Distribution of Polarization Percentage in Four Regions of Orion B.
The distributions for NGC 2024, NGC 2071 and LBS 23N are from data presented in Matthews, Fiege, & Moriarty-Schieven (2001). Clearly, the distribution of NGC 2024 is most heavily weighted to small values of p. In contrast, the regions of NGC 2068 and LBS 23N, and, to a lesser extent, NGC 2071, all show a flat distribution out to $\sim 6\%$, where they then decline.

NGC 2024 exhibits a similar depolarization signature to the northern core NGC 2071. However, LBS 23N (referred to as part of NGC 2068 in some papers) has a significantly steeper slope of -0.95, which is more consistent with that of Region 3 in our data set.

6.4.2 Evidence for Varying Inclinations in NGC 2068

The filamentary dust emission of NGC 2068 likely arises from dust at different depths in the Orion B cloud. The comparison between the Palomar Observatory Sky Survey optical data and the dust emission has been made by Mitchell et al. (2001). We produce a similar image in Figure 6.5, which shows that while the western dust emission lines up well with the optically dark dust lane, the eastern dust emission has no corresponding dark lane. (North of the HII region lies another dust condensation not yet observed with the polarimeter.) Hence, it is likely that the dust emission may lie on the outer edge of the reflection nebula with the western material in the foreground and the eastern material behind. Thus, it is clear that this filament does not lie in the plane of the sky, and that the inclination on the sky is likely variable.

An obvious question is whether or not all the dust emission arises from material which is spatially related. It is noteworthy that the core OriBN 34 does not appear to line up well with the filamentary material of Figure 6.1. In fact, our comparison of the optical and dust emission shows that the location of OriBN 34 is optically dark. This could be a coincidence, or OriBN 34 could be closer than the dust emission appearing next to it on the SCUBA image. OriBN 39 also appears dark and could be in the foreground. Mitchell et al. (2001) present ^{13}CO $J = 2-1$ toward NGC 2068 and a partial map of the north-eastern region in C^{18}O $J = 2-1$ (see their Figs. 6 and 7). The ^{13}CO contours are closely correlated to the 850 μm dust emission. The same is true for the C^{18}O emission where data exist. These maps are integrated

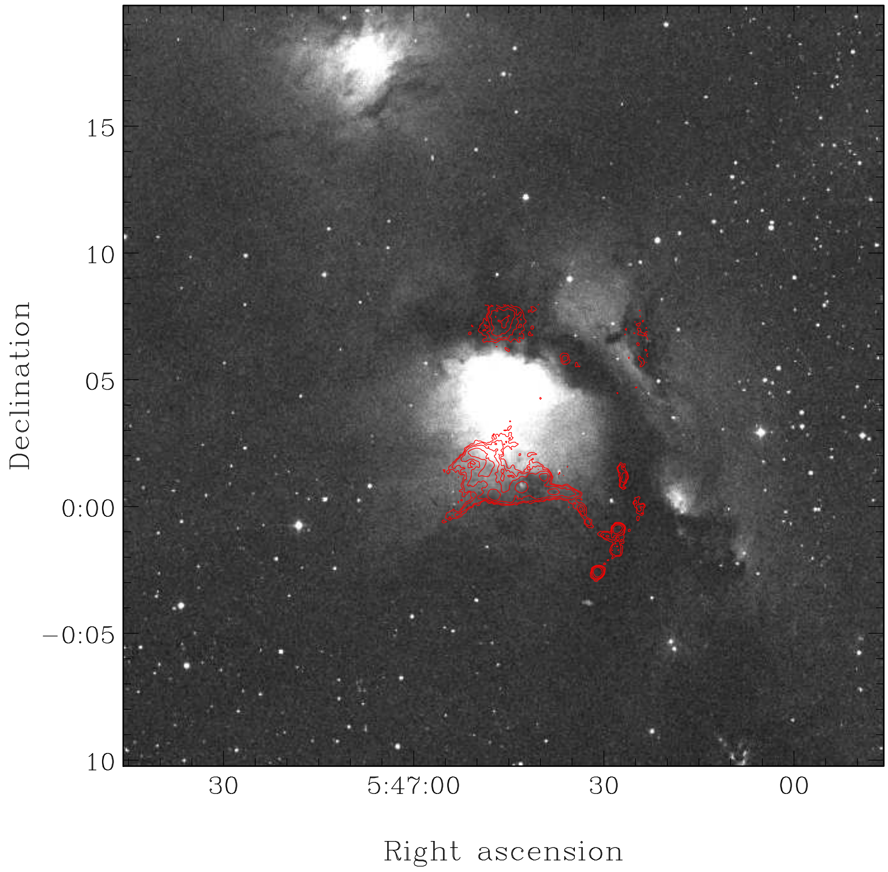

Figure 6.5: The optical and dust emission from NGC 2068.
The optical image from the Palomar Sky Survey is presented, covering an area of $30' \times 30'$. The NGC 2068 reflection nebula is central. The SCUBA total, unpolarized dust emission at 850 μm is shown in contours of 90, 93, 96 and 99 percentiles from Mitchell et al. (2001). The western edge of the dust emission appears to be coincident with the optical dust lane. At the east, however, the region of dust emission appears bright in the optical, and hence the dust must lie behind the nebula. A northern dust peak has not yet been observed with the polarimeter.

over velocity ranges from 5 km s^{-1} $< v_{LSR} <$ 15 km s^{-1} and 7 km s^{-1} $< v_{LSR} <$ 13 km s^{-1}, respectively. Thus, the emission is confined to the Orion B cloud. The fact that OriBN 34 and 39 show similar polarization position angles as the eastern area but may be in the foreground would argue against these regions being completely spatially distinct (unless the cores are not contributing as much polarized emission as the background diffuse material. If the material is spatially separated, then the similar orientations of the polarization position angles could infer that the field, if not unidirectional, could be organized on spatial scales at least as large as the separation between them.

The 2.4 μm emission from the NGC 2068 reflection nebula spans approximately $6'$ in spatial extent (Sellgren 1984). This is consistent with the physical size of the nebula in optical emission as shown in Figure 6.5, and at a distance of 415 pc corresponds to 0.7 pc. If the nebula is as deep as it is wide, then the source of dust emission at the north-east could be more than a parsec displaced spatially from the cores at the west (taking $7'$ as an estimate of their separation in projection).

6.4.3 Field Geometry

6.4.3.1 A Unidirectional Field

Although the vectors of NGC 2068 do not show the strong alignment of polarization position angle with the filament orientation observed in OMC-3, neither do they support a field of constant B_{pos} direction in NGC 2068. If one assumes that the magnetic field geometry throughout a cloud's depth is reasonably unidirectional, then the direction of the field can be obtained by rotating emission polarization data by 90°. Doing this in the NGC 2068 polarization map will clearly not produce aligned vectors, any more than the polarization data themselves are aligned. Therefore, we can rule out a unidirectional field across all of NGC 2068.

We can compare the polarization position angles across those regions observed thus far in Orion B. In the three regions of Orion B North, no evidence for similar polarization orientations exists. Toward NGC 2071, the polarization vectors align generally with the prominent outflow from the IRS 1 source at a position angle of 40° east of north. Within the LBS 23N string of cores to the south of NGC 2068, the vectors are generally aligned north-south (position angle 0°) although the scatter in this faint region is considerable. Neither of these orientations is dominant in NGC

2068. Thus, there is no support for a unidirectional field in NGC 2068 or across the star-forming regions of Orion B North.

The one region observed in Orion B South is NGC 2024, and the polarization pattern from that region has been modeled as arising either from a helical field geometry or from the expansion of the ionization front due to the associated HII region by Matthews, Fiege, & Moriarty-Schieven (2001). The latter geometry is favored since it is most compatible with the total physics and geometry of NGC 2024. It is clear that the polarization patterns across these star-forming regions can be strongly correlated with the dust and gas structures of a particular region, and that each region must be modeled separately.

6.4.3.2 More Complex Geometries

As discussed above, there is evidence that the dust arises from a connected gas structure. However, the spatial separation between the filament edges could be > 1 pc. The regions of different position angles could indicate regions of different field geometry or inclinations. We propose two model geometries which could potentially explain the variable position angles observed.

Since the cores are mainly aligned along a filamentary structure, a helical field geometry is appealing. It can explain the confinement of gas in the filament, the fragmentation to cores and the elongation of the asymmetric concentrations along the axis of the filament, which is certainly the case for OriBN 31, 32, 33, 41 and 49. Fiege & Pudritz (2000b) show possible polarization patterns for different helical field conditions (i.e. poloidally-dominated versus toroidally-dominated). These models are developed for straight filaments, and Fiege & Pudritz (2000b) find that for such filaments, the polarization vectors align either parallel or perpendicular to the projected filament axis regardless of the inclination of the filament. However, Matthews, Wilson, & Fiege (2001) present a model for a helical field threading a bent filament. In this case, the vectors may adopt any orientation relative to the filament due to the asymmetries in the filament. The relative alignment depends on the filament's inclination and rotation on the plane of the sky.

Thus, as inclination and angle in the plane of the sky vary, a helically-threaded filament should produce different polarization position angles relative to the projected filament orientation. For instance, if the polarization positions are aligned with the filament, a toroidally-dominated helical field could wrap the filament locally. Conversely, where the vectors appear perpendicular to the filament, a helical field would be poloidally-dominated, or the filament and field could be significantly bent. At the north-western edge near the cores OriBN 33 and 41, the vectors are neither parallel nor perpendicular to the filament. This could also indicate that the filament is bent along its length in this area. Modeling such a complex filamentary structure will be difficult, since more than one filament/field geometry can produce similar polarization pattern.

One additional test for the presence of a helical field geometry is the radial profile of the total, unpolarized emission. Using the 850 μm map of Mitchell et al. (2001), a radial profile can be built up by taking several slices across the filament. We have attempted to confine the cuts to the regions between cores along NGC 2068. Figure 6.6 shows the profiles through several such slices, taken between the OriBN 44 and 48, between 32 and 39 and between 35 and 36. For the second cut, both sides of the profile were used; for the other two, one side of the slice was discarded due to the presence of extended emission from the filament near OriBN 47 (for the cut between OriBN 44 and 48) and extended emission from core OriBN 34 (for the cut between OriBN35 and 36). The fluxes have been normalized to the maximum through the cuts (respectively 0.07 Jy beam^{-1}, 0.32 Jy beam^{-1}, and 0.28 Jy beam^{-1}); this position is assumed to be the axis of the filament. The NGC 2068 filament is so narrow and faint, it is difficult to interpret the profiles. However, the slopes corresponding to flux radial profile indices of -1 and -0.5 are shown on Figure

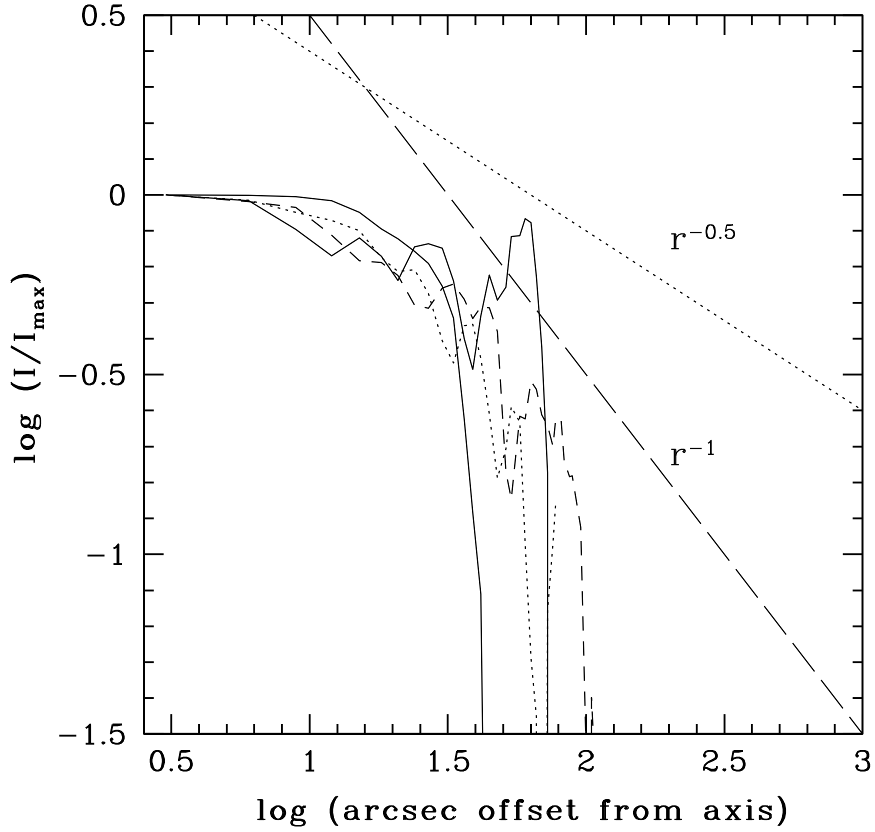

Figure 6.6: Radial Flux Profile of NGC 2068.
A series of crosscuts show the radial distribution of flux off the filament axis. The filament is very narrow so flux does not extend very far off the filament's axis (the intensity peak). Slices were taken between cores to avoid probing the profiles of very high density gas and dust. The positions of the cuts are discussed in the text. Assuming uncertainties of 10% in the intensities measurements, the uncertainty in each value of $\log(I/I_{max})$ is ~ 0.08. Slopes of r^{-1} and $r^{-0.5}$ flux profiles are shown.

6.6. Near the axis, the flux falls off with a distribution consistent with a power law index of -0.5. Toward lower fluxes, the index could be closer to -1; however, at these low flux levels, interpretation of the index becomes difficult. The flux profile of $r^{-0.5}$ corresponds to a density profile of $r^{-1.5}$ for an isothermal filament. The helical field geometry predicts a density profile with index -2 for an isothermal equation of state. For other equations of state (e.g. the logotrope, McLaughlin & Pudritz 1996), a shallower range of density profiles can be generated. Unmagnetized, isothermal filaments predict much steeper profiles, with indices of -4.

A second possible field geometry is suggested by the position of the molecular filament so near the periphery of the reflection nebula of NGC 2068. Matthews, Fiege, & Moriarty-Schieven (2001) present a model of the polarization data toward the NGC 2024 dense ridge of cores in which the field, compressed by the expansion of the NGC 2024 HII region, is then moulded around the dense ridge as the ionization front approaches the cores. This picture accounts for both the polarization pattern at 850 μm and the measurements of the line-of-sight field direction and strength measured by Crutcher et al. (1999). The expansion of the reflection nebula could produce a similar effect in NGC 2068, although the pattern produced is much more complex. In NGC 2024, the ridge is entirely located on the far-side of the HII region, whereas in NGC 2068 the comparison of optical and 850 μm dust emission in Figure 6.5 indicates that the dust emission arises from both the near and far-side of the nebula.

A recent publication on the formation of quiescent cores through turbulent flows (Padoan et al. 2001) provides a third possible interpretation of the polarization pattern. This work discusses the potential formation of cores due to the presence of super-sonic turbulent flows within molecular clouds. In this model, cores form by accretion along filamentary structures, with the brightest cores forming at the loci of intersecting shocks. The core OriBN 47 lies at the intersection of three filamentary segments. As predicted by Padoan et al. (2001), this core exhibits depolarization, although at the distance of Orion B, it is difficult to achieve a good sampling of polarization vectors across this core. Thus, we do not see the large changes in position angle predicted near cores (see their Fig. 3) and routinely observed in Bok globules and starless cores in closer regions of star formation (e.g. see Ward-Thompson et al. 2000). However, the polarization pattern along the larger scale filamentary structure is well sampled in our map. In the turbulent flows model, the polarization vectors along the filamentary structures are seen to align well with the filaments' axes. In NGC 2068, only the filament segment east of OriBN 48 exhibits this behavior. The segments to the north-west and south-west show vectors oriented roughly perpendicular to the filamentary structure, which does not agree well with the turbulent flows picture. A simulation of turbulent flows along filaments of higher density may agree more strongly with our observations in NGC 2068. If a threshold in extinction exists beyond which grains are not effectively aligned (Padoan et al. 2001), then denser turbulent flows could exhibit less correlation between the filamentary axis and the inferred polarization.

6.5 Summary

We have detected polarized emission from aligned dust grains at 850 μm with the SCUBA polarimeter. These data reveal strong degrees of polarization (up to 17%) toward the NGC 2068 region, with higher polarization percentages detected toward regions of fainter total intensity. This depolarization effect has been observed in most regions of polarized emission. Significant depolarization has been detected toward several compact cores along the filament. Within the cores of LBS 23N and some cores along the NGC 2024 dense ridge, significant depolarization was also measured (Matthews, Fiege, & Moriarty-Schieven 2001). We note that this was not the case in the OMC-3 filament of Orion A, where the polarization patterns behaved consistently in the presence or absence of embedded cores (Matthews, Wilson, & Fiege 2001). This was attributed to the fact that filamentary dust dominated the polarization pattern in Orion A, but that this is not the case in Orion B.

The polarization pattern is inconsistent with that expected for a unidirectional field geometry, for which unidirectional vectors should be seen across the entire region. The polarization position angles are roughly distributed in three distinct distributions which do not align with the orientations of the filamentary total intensity emission. This is also different from the pattern observed in the OMC-3 part of the Integral-shaped Filament by Matthews, Wilson, & Fiege (2001) where the vectors aligned with the filament orientation along 75% of the filament's length.

Taken in comparison with the polarization data for three other star-forming regions in Orion B (Matthews, Fiege, & Moriarty-Schieven 2001), there is also no evidence for a constant B_{pos} orientationcross the Orion B cloud as a whole.

Comparison of optical and 850 μm dust emission establishes that the dust filament is not lying in the plane of the sky, but must be twisted such that its western edge is in the foreground of the optical reflection nebula, while the eastern edge lies behind. These changes in inclination can help explain the polarization pattern observed. Matthews, Wilson, & Fiege (2001) show that a bent filament threaded by a helical field geometry can produce polarization vectors offset from the filament orientations by varying degrees. Material lying on the edge of an expanding relection nebula could also exhibit different magnetic field orientations at different locations depending on how effectively the field has been compressed by the expansion. The complexity of this filamentary structure will make modeling difficult, since there may be many degenerate choices of filament/field configurations which can produce the observed polarization pattern.

These are the first observations of polarized emission toward this filament. The strength of the polarization percentages detected suggests that polarized emission should be detectable at other wavelengths. For instance, observations at 350 μm with the Hertz polarimeter would provide some information on the polarization spectrum for this region. This could lead to constraints on the grain population along the filament. Additionally, Zeeman data on B_{los} field would provide significant constraint to the three-dimensional field structure.

The authors thank the members of the Canadian Consortium on Star Formation for the 850 μm scan map of the Orion B North cloud. Thanks to J. Greaves, T. Jenness, and G. Moriarty-Schieven at the JCMT for assistance during and after observing. The research of BCM and CDW has been supported through grants from the Natural Sciences and Engineering Research Council of Canada. BCM acknowledges funding from Ontario Graduate Scholarships.

Appendix 6A – The Polarization Data

Table 6.3 contains the polarization data plotted in Figure 6.1. Positional offsets are given from the J2000 coordinates $\alpha = 05^{\rm h}46^{\rm m}33\overset{s}{.}8$ and $\delta = 00°01'43\overset{''}{.}0$ ($\alpha = 05^{\rm h}44^{\rm m}00\overset{s}{.}0$ and $\delta = 00°00'00\overset{''}{.}0$ in B1950). Vectors are binned to 15″ sampling and all have $\sigma_p > 3$, $p > 1\%$, and an absolute uncertainty in polarization percentage, $dp < 1\%$. The total intensity at the vector position exceeds 20% of the faintest compact peak, OriBN 35. This minimizes the chances of systematic effects from chopping to a reference position, as discussed in Appendix A of Matthews, Wilson, & Fiege (2001).

Table 6.3: NGC 2068 850 μm Polarization Data

Δ R.A. (″)	Δ DEC. (″)	p (%)	dp (%)	σ_p	θ (°)	$d\theta$ (°)
−36.0	−244.5	11.22	0.96	11.7	−69.3	2.5
−36.0	−229.5	1.65	0.28	5.8	−48.9	4.9
−51.0	−229.5	2.39	0.47	5.1	51.9	5.6
−6.0	−214.5	8.62	0.85	10.1	45.0	2.8
−51.0	−214.5	1.24	0.20	6.2	−76.1	4.6
−66.0	−214.5	5.17	0.59	8.7	−82.6	3.3
−21.0	−199.5	2.01	0.57	3.5	−50.8	8.1
−51.0	−199.5	1.96	0.31	6.2	75.4	4.6
−66.0	−199.5	3.40	0.44	7.8	43.8	3.7
−81.0	−199.5	6.16	0.65	9.5	66.8	3.0
−66.0	−184.5	6.91	0.41	16.9	71.1	1.7
−81.0	−184.5	4.46	0.45	10.0	−75.7	2.9
−96.0	−184.5	7.21	0.62	11.6	46.5	2.5
−66.0	−169.5	4.11	0.43	9.5	52.5	3.0
−81.0	−169.5	4.75	0.30	15.7	73.1	1.8
−96.0	−169.5	2.38	0.39	6.1	−84.2	4.7
−66.0	−154.5	6.16	0.46	13.5	64.6	2.1
−81.0	−154.5	2.65	0.27	9.9	74.3	2.9
−96.0	−154.5	5.59	0.37	15.2	74.7	1.9
−51.0	−139.5	4.26	0.52	8.2	80.0	3.5
−66.0	−139.5	3.10	0.29	10.5	68.3	2.7
−81.0	−139.5	3.86	0.25	15.2	51.7	1.9
−96.0	−139.5	2.28	0.33	7.0	4.1	4.1
−36.0	−124.5	6.03	0.43	14.0	74.2	2.0

Table 6.3 (continued)

Δ R.A. ($''$)	Δ DEC. ($''$)	p (%)	dp (%)	σ_p	θ (°)	$d\theta$ (°)
−51.0	−124.5	5.70	0.32	17.6	84.0	1.6
−66.0	−124.5	3.22	0.23	14.1	77.2	2.0
−81.0	−124.5	2.86	0.15	19.6	68.1	1.5
−96.0	−124.5	2.06	0.19	10.9	58.6	2.6
−21.0	−109.5	8.99	0.46	19.5	49.5	1.5
−36.0	−109.5	6.78	0.59	11.4	63.6	2.5
−66.0	−109.5	5.12	0.42	12.2	59.9	2.4
−81.0	−109.5	1.12	0.15	7.7	27.8	3.7
−96.0	−109.5	3.22	0.22	14.5	81.6	2.0
−126.0	−109.5	4.21	0.62	6.8	−36.5	4.2
−141.0	−109.5	7.42	0.80	9.3	40.2	3.1
−6.0	−94.5	6.00	0.63	9.5	43.9	3.0
−21.0	−94.5	4.32	0.52	8.3	−4.2	3.5
−81.0	−94.5	12.43	0.63	19.7	48.2	1.5
−96.0	−94.5	14.80	0.56	26.5	69.9	1.1
−111.0	−94.5	11.26	0.74	15.3	56.0	1.9
−126.0	−94.5	2.80	0.39	7.2	61.0	4.0
−141.0	−94.5	4.12	0.34	12.3	−87.7	2.3
−156.0	−94.5	5.16	0.76	6.8	88.2	4.2
9.0	−79.5	3.66	0.69	5.3	−57.8	5.4
−6.0	−79.5	1.78	0.45	3.9	−77.3	7.3
−126.0	−79.5	4.33	0.49	8.9	61.8	3.2
−141.0	−79.5	1.18	0.35	3.4	−21.7	8.4
−156.0	−79.5	4.88	0.59	8.3	−56.1	3.5
24.0	−64.5	5.22	0.67	7.8	76.6	3.7
9.0	−64.5	3.30	0.45	7.4	44.5	3.9
−111.0	−64.5	6.96	0.71	9.8	47.9	2.9
−126.0	−64.5	4.77	0.33	14.3	88.1	2.0
−141.0	−64.5	5.11	0.28	18.1	75.4	1.6
−156.0	−64.5	7.09	0.48	14.9	77.9	1.9
−171.0	−64.5	7.00	0.91	7.7	68.8	3.7
234.0	−49.5	7.74	0.82	9.4	−14.0	3.0
219.0	−49.5	2.41	0.61	4.0	42.0	7.2
204.0	−49.5	1.42	0.30	4.8	−0.1	6.0
189.0	−49.5	1.72	0.38	4.6	73.5	6.3
174.0	−49.5	1.39	0.46	3.0	−42.5	9.5
159.0	−49.5	1.47	0.39	3.8	−65.7	7.6
129.0	−49.5	2.88	0.48	6.0	−82.6	4.8
114.0	−49.5	2.97	0.46	6.4	71.5	4.5
99.0	−49.5	4.06	0.46	8.9	70.8	3.2

Table 6.3 (continued)

Δ R.A. (″)	Δ DEC. (″)	p (%)	dp (%)	σ_p	θ (°)	$d\theta$ (°)
84.0	−49.5	4.06	0.56	7.3	−85.0	3.9
69.0	−49.5	4.47	0.67	6.6	−71.8	4.3
54.0	−49.5	7.57	0.74	10.2	75.6	2.8
39.0	−49.5	7.18	0.62	11.5	81.4	2.5
24.0	−49.5	5.39	0.46	11.7	−82.3	2.4
9.0	−49.5	5.09	0.45	11.3	−67.5	2.5
−6.0	−49.5	3.51	0.71	4.9	67.4	5.8
−111.0	−49.5	6.93	0.62	11.2	−12.5	2.6
−141.0	−49.5	3.84	0.42	9.1	−87.1	3.1
−156.0	−49.5	10.14	0.70	14.4	−87.9	2.0
234.0	−34.5	3.63	0.49	7.4	2.4	3.9
219.0	−34.5	2.48	0.29	8.6	−16.0	3.3
204.0	−34.5	1.39	0.15	9.0	−26.4	3.2
189.0	−34.5	2.18	0.23	9.5	−52.6	3.0
174.0	−34.5	1.80	0.41	4.4	−45.6	6.5
159.0	−34.5	1.44	0.31	4.6	−53.0	6.2
144.0	−34.5	2.54	0.26	9.8	−56.1	2.9
129.0	−34.5	1.59	0.27	5.9	−55.9	4.9
114.0	−34.5	2.14	0.29	7.4	−72.6	3.9
99.0	−34.5	5.08	0.26	19.2	88.1	1.5
84.0	−34.5	1.43	0.31	4.7	55.2	6.2
69.0	−34.5	3.34	0.27	12.3	−72.6	2.3
54.0	−34.5	4.38	0.27	16.3	76.5	1.8
39.0	−34.5	5.37	0.32	16.9	81.8	1.7
24.0	−34.5	5.23	0.33	15.7	−89.6	1.8
9.0	−34.5	6.04	0.42	14.3	88.4	2.0
−6.0	−34.5	4.19	0.84	5.0	7.0	5.7
−126.0	−34.5	7.35	0.65	11.3	57.2	2.5
−141.0	−34.5	12.61	0.70	18.0	65.6	1.6
249.0	−19.5	4.22	0.86	4.9	−36.0	5.9
234.0	−19.5	5.38	0.57	9.4	6.0	3.0
219.0	−19.5	2.83	0.42	6.7	−19.0	4.3
204.0	−19.5	3.91	0.34	11.6	−52.7	2.5
189.0	−19.5	4.35	0.41	10.5	−56.9	2.7
174.0	−19.5	4.84	0.53	9.2	−60.0	3.1
159.0	−19.5	2.47	0.33	7.4	−74.4	3.9
144.0	−19.5	1.55	0.19	8.1	−67.2	3.5
129.0	−19.5	1.10	0.19	5.7	22.6	5.0
99.0	−19.5	3.64	0.24	15.1	−89.7	1.9
84.0	−19.5	2.84	0.31	9.2	−82.2	3.1

Table 6.3 (continued)

Δ R.A. ($''$)	Δ DEC. ($''$)	p (%)	dp (%)	σ_p	θ ($^\circ$)	$d\theta$ ($^\circ$)
69.0	−19.5	1.70	0.33	5.2	−78.0	5.6
54.0	−19.5	1.94	0.34	5.8	77.4	5.0
39.0	−19.5	9.12	0.39	23.5	−83.3	1.2
24.0	−19.5	5.51	0.48	11.5	87.3	2.5
9.0	−19.5	9.28	0.96	9.7	90.0	3.0
−96.0	−19.5	5.40	0.52	10.4	55.9	2.7
−111.0	−19.5	6.52	0.64	10.3	37.8	2.8
264.0	−4.5	5.51	0.95	5.8	39.6	5.0
249.0	−4.5	4.84	0.54	8.9	31.3	3.2
234.0	−4.5	4.28	0.53	8.0	15.5	3.6
219.0	−4.5	2.82	0.43	6.6	−39.5	4.3
204.0	−4.5	2.89	0.37	7.7	−73.0	3.7
189.0	−4.5	3.55	0.53	6.7	−88.2	4.3
174.0	−4.5	3.93	0.67	5.9	−47.0	4.9
144.0	−4.5	1.53	0.29	5.2	11.4	5.5
114.0	−4.5	1.75	0.35	5.0	−19.3	5.7
99.0	−4.5	3.05	0.25	12.0	−88.2	2.4
84.0	−4.5	1.66	0.28	6.0	76.1	4.7
54.0	−4.5	5.60	0.82	6.8	8.5	4.2
39.0	−4.5	7.16	0.88	8.1	−26.0	3.5
−96.0	−4.5	2.51	0.35	7.2	51.9	4.0
−111.0	−4.5	4.12	0.40	10.3	27.6	2.8
249.0	10.5	2.21	0.62	3.6	42.6	8.0
234.0	10.5	2.74	0.37	7.4	−67.2	3.9
219.0	10.5	3.06	0.26	11.5	−77.8	2.5
204.0	10.5	5.40	0.36	15.1	−62.1	1.9
189.0	10.5	10.42	0.72	14.4	−69.2	2.0
174.0	10.5	7.38	0.80	9.2	−60.9	3.1
159.0	10.5	5.88	0.73	8.1	−46.7	3.5
144.0	10.5	5.63	0.64	8.8	−59.5	3.3
129.0	10.5	3.20	0.45	7.1	−26.9	4.1
114.0	10.5	3.38	0.40	8.4	−45.9	3.4
99.0	10.5	1.90	0.29	6.5	−37.4	4.4
84.0	10.5	1.95	0.26	7.4	−72.2	3.9
−81.0	10.5	5.90	0.66	9.0	81.3	3.2
−96.0	10.5	3.76	0.36	10.5	55.4	2.7
−111.0	10.5	3.60	0.53	6.8	13.4	4.2
249.0	25.5	13.06	0.96	13.6	−7.9	2.1
234.0	25.5	6.99	0.53	13.2	−51.4	2.2

Table 6.3 (continued)

Δ R.A. ($''$)	Δ DEC. ($''$)	p (%)	dp (%)	σ_p	θ ($^\circ$)	$d\theta$ ($^\circ$)
219.0	25.5	6.16	0.31	20.1	−53.4	1.4
204.0	25.5	8.99	0.34	26.1	−65.6	1.1
189.0	25.5	17.07	0.70	24.5	−65.0	1.2
114.0	25.5	8.63	0.86	10.1	−33.3	2.8
99.0	25.5	2.83	0.56	5.0	−21.0	5.7
69.0	25.5	5.62	0.92	6.1	−53.3	4.7
−81.0	25.5	6.53	0.75	8.7	57.9	3.3
−96.0	25.5	2.93	0.52	5.6	64.0	5.1
−111.0	25.5	8.23	0.90	9.1	−31.6	3.1
234.0	40.5	8.20	0.77	10.6	−58.5	2.7
219.0	40.5	8.08	0.43	18.6	−64.5	1.5
204.0	40.5	15.63	0.51	30.5	−77.3	0.9
264.0	55.5	3.27	0.83	3.9	−88.3	7.3
249.0	55.5	6.25	0.58	10.8	−72.3	2.7
234.0	55.5	6.74	0.47	14.3	−49.5	2.0
219.0	55.5	6.48	0.54	12.1	−69.9	2.4
204.0	55.5	7.45	0.95	7.8	−84.8	3.7
249.0	70.5	6.72	0.73	9.2	−44.0	3.1
234.0	70.5	12.65	0.59	21.6	−59.1	1.3
219.0	70.5	15.56	0.93	16.7	−78.9	1.7

Bibliography

Aitken, D. K., Greaves, J., Chrysostomou, A., Jenness, T., Holland, W., Hough, J. H., Pierce-Price, D., & Richer, J., 2000. *ApJ Letters* **534**, L173.

Anthony-Twarog, B. J., 1982. *AJ* **87**, 1213.

Basu, S., 2000. *ApJ Letters* **540**, L103.

Carpenter, J. M., 2000. *AJ* **120**, 3139.

Coppin, K. E. K., Greaves, J. S., Jenness, T., & Holland, W. S., 2000. *A&A* **356**, 1031.

Crutcher, R. M., 1999. *ApJ* **520**, 706.

Crutcher, R. M., Troland, T. H., Lazareff, B., Paubert, G., & Kazès, I., 1999. *ApJ Letters* **514**, L121.

Dotson, J. L., Davidson, J., Dowell, C. D., Schleuning, D. A., & Hildebrand, R. H., 2000. *ApJS* **128**, 335.

Dowell, C. D., Hildebrand, R. H., Schleuning, D. A., Vaillancourt, J. E., Dotson, J. L., Novak, G., Renbarger, T., & Houde, M., 1998. *ApJ* **504**, 588.

Edwards, S. & Snell, R. L., 1984. *ApJ* **281**, 237.

Fiege, J. D. & Pudritz, R. E., 2000a. *MNRAS* **311**, 85.

Fiege, J. D. & Pudritz, R. E., 2000b. *ApJ* **544**, 830.

Gibb, A. G. & Little, L. T., 2000. *MNRAS* **313**, 663.

Gibb, A. G., Little, L. T., Heaton, B. D., & Lehtinen, K. K., 1995. *MNRAS* **277**, 341.

Girart, J., Crutcher, R. M., & Rao, R., 1999. *ApJ Letters* **525**, L109.

Greaves, J., Holland, W., Chrysostomou, A., & Jenness, T., 2000. Imaging the polarized interstellar medium. In *Imaging at Radio through Submillimeter Wavelengths. Edited by Jeff Mangum. Publisher: The Astronomical Society of the Pacific, Conference Series, 2000. The conference was held June 6-8, 1999, in Tucson, Arizona.*, pp. E18.

Greaves, J., Holland, W., Jenness, T., Moriarty-Schieven, G., Chrysostomou, A., Berry, D., Murray, A., Nartallo, R., Ade, P., Gannaway, F., Haynes, C., Tamura, M., Momose, M., & Morino, J., 2001. *MNRAS in preparation.*

Haschick, A. D., Moran, J. M., Rodriguez, L. F., & Ho, P. T. P., 1983. *ApJ* **265**, 281.

Hildebrand, R. H., 1988. *QJRAS* **29**, 327.

Hildebrand, R. H., Davidson, J. A., Dotson, J. L., Dowell, C. D., Novak, G., & Vaillancourt, J. E., 2000. *PASP* **112**, 1215.

Holland, W. S., Greaves, J. S., Ward-Thompson, D., & Andre, P., 1996. *A&A* **309**, 267.

Jenness, T., Lightfoot, J. F., & Holland, W. S., 1998. *Proc. SPIE* **3357**, 548.

Johnstone, D. & Bally, J., 1999. *ApJ Letters* **510**, L49.

Jones, B. F., Cohen, M., Wehinger, P. A., & Gehren, T., 1987. *AJ* **94**, 1260.

Krugel, E., Densing, R., Nett, H., Roser, H. P., Schafer, F., Schmid-Burgk, J., Schwaab, G., van der Wal, P., & Wattenbach, R., 1989. *A&A* **211**, 419.

Lada, E. A., Bally, J., & Stark, A. A., 1991. *ApJ* **368**, 432.

Lada, E. A., Evans, N. J., Depoy, D. L., & Gatley, I., 1991. *ApJ* **371**, 171.

Lada, E. A., Evans, N. J., & Falgarone, E., 1997. *ApJ* **488**, 286.

Launhardt, R., Mezger, P. G., Haslam, C. G. T., Kreysa, E., Lemke, R., Sievers, A., & Zylka, R., 1996. *A&A* **312**, 569.

Mannion, M. D. & Scarrott, S. M., 1984. *MNRAS* **208**, 905.

Matthews, B., Fiege, J., & Moriarty-Schieven, G., 2001. *ApJ in preparation.*

Matthews, B., Wilson, C., & Fiege, J., 2001. *ApJ accepted.*

Matthews, B. C. & Wilson, C. D., 2000. *ApJ* **531**, 868.

McKee, C. F., Zweibel, E. G., Goodman, A. A., & Heiles, C., 1993. Magnetic fields in star-forming regions - theory. In *Protostars and Planets III*, pp. 327.

McLaughlin, D. E. & Pudritz, R. E., 1996. *ApJ* **469**, 194.

Mezger, P. G., Chini, R., Kreysa, E., Wink, J. E., & Salter, C. J., 1988. *A&A* **191**, 44.

Mitchell, G., Johnstone, D., Moriarty-Schieven, G., Fich, M., & Tothill, N., 2001. *ApJ* **556**, 215.

Motte, F., André, P., Ward-Thompson, D., & Bontemps, S., 2001. *A&A* **372**, L41.

Mouschovias, T. C., 1987. Star formation in magnetic interstellar clouds. i - interplay between theory and observations. ii - basic theory. In *Physical Processes in Interstellar Clouds*, pp. 453.

Myers, P. C. & Goodman, A. A., 1988. *ApJ Letters* **326**, L27.

Padoan, P., Goodman, A., Draine, B., Juvela, M., Nordlund, A., & Rögnvaldsson, O., 2001. *ApJ submitted.*

Schleuning, D. A., 1998. *ApJ* **493**, 811.

Schleuning, D. A., Dowell, C. D., Hildebrand, R. H., Platt, S. R., & Novak, G., 1997. *PASP* **109**, 307.

Schulz, A., Guesten, R., Zylka, R., & Serabyn, E., 1991. *A&A* **246**, 570.

Sellgren, K., 1984. *ApJ* **277**, 623.

Walker, C. K., Schulz, A., Kruegel, E., & Gillespie, A. R., 1988. *A&A* **205**, 243.

Ward-Thompson, D., Kirk, J. M., Crutcher, R. M., Greaves, J. S., Holland, W. S., & André, P., 2000. *ApJ Letters* **537**, L135.

White, G. J. & Phillips, J. P., 1981. *MNRAS* **194**, 947.

White, G. J., Phillips, J. P., & Watt, G. D., 1981. *MNRAS* **197**, 745.

Zhao, B., Wang, M., Yang, J., Wang, H., Deng, L., Yan, J., & Chen, J., 1999. *AJ* **118**, 1347.

Chapter 7

Submillimetre Polarization of the Barnard 1 Dark Cloud

This chapter is a draft of the article "Magnetic Fields in Star-Forming Molecular Clouds V. Submillimetre Polarization of the Barnard 1 Dark Cloud" by B.C. Matthews and C.D. Wilson, which will be submitted for publication to The Astrophysical Journal.

Abstract

We present 850 μm polarimetry from the James Clerk Maxwell Telescope toward the dense cores of the dark cloud Barnard 1 in Perseus. Significant polarized emission is detected from across the mapped area, even in the absence of the embedded cores. This indicates the presence of aligned grains and hence a component of magnetic fields in the plane of the sky. Polarization vectors detected away from bright cores are strongly aligned at a position angle of $\sim 90°$, while vectors associated with bright cores show alignments of varying orientations. There is no direct correlation between the polarization angles measured in earlier optical polarimetry toward Perseus and the polarized submillimetre thermal emission. Depolarization toward high intensities is exhibited, but reaches a threshold toward the two brightest cores beyond which no further decrease is measured. The polarized emission data from the interior envelope are compared with previously published OH Zeeman data to estimate the total field strength and orientation under the assumption of a uniform (ordered) and non-uniform field component in the region. These results are rough estimates only due to the paucity of independent Zeeman measurements toward B1. The ordered field component is thus calculated to be $\mathbf{B}_0 = 29.8\ \mu\text{G}\ [\pm(0.81\hat{N} - 0.02\hat{E}) - 0.58\hat{z}]$.

7.1 Introduction

Evidence suggests that molecular clouds are in magnetic and virial equilibrium (Myers & Goodman 1988; Crutcher 1999; Basu 2000), and over the past decade, observational evidence for the presence of magnetic fields in molecular clouds and their role in star formation has grown dramatically. However, detection of magnetic fields is not synonymous with measuring their geometry or the total field strength. While models help interpret data, it is still very rare for evidence of Zeeman line splitting (which traces the line-of-sight field, B_{los}) and thermal dust polarimetry (which traces the plane-of-sky field, B_{pos}) both to exist toward regions of similar density in the same cloud.

The Perseus molecular cloud complex is one of the closest star-forming regions to the Sun. Its distance is the subject of some debate, but it is thought to be associated with the Per OB2 association at a distance of 334 ± 12 pc (Borgman & Blaauw 1964). However, the complex is likely in front of the OB association (Lynds 1969), and Cernicharo et al. (1985) suggest that there are in fact two clouds along the line of sight toward the complex, the second at a distance more comparable to Taurus at 200 pc. CO emission reveals that the complex is elongated, extending over 55 pc along its major axis (at $\sim 60°$ east of north), but just 15 pc along the minor axis (Sargent 1979). Along its length, six denser star-forming clouds (Barnard 1, Barnard 5, IC 348, L1448, L1455 and NGC 1333) are connected by low density molecular gas of $n \sim 10^2$ cm^{-3} (Bachiller & Cernicharo 1986).

The Barnard 1 cloud has been observed in many molecular transitions and modeled as a multi-phase cloud with a thin outer envelope, denser inner envelope and a central dense core. Bachiller & Cernicharo (1984) observed the cloud in several isotopes of CO and HCO^+ and a single transition from NH_3 and determined that temperatures are higher toward the outer edges of the cloud, indicating primarily external heating. Three optically visible young stellar objects, LkHα 327, LkHα 328, and LZK 21 are associated with the cloud, two of which show IRAS emission. Three additional IRAS sources are undetected optically; the presence of these sources indicates some recent star formation in B1. In the centre of the cloud, Bachiller et al. (1990) observe CS $J = 1 - 0$ emission from dense gas over a region ~ 2 pc $\times 5$ pc with an accompanying mass of 1200 $M_{\odot}$. NH_3 (1,1) and (2,2) emission toward the CS "main core" reveal substantial substructure within the gas, showing evidence for two or three condensations. IRAS 03301+3057 lies at the centre of the main core, but does not coincide directly with any of the ammonia peaks; it is located approximately $1'$ north of the south-western ammonia peak (the "southern clump" of Bachiller et al. (1990)).

High resolution observations of $H^{13}CO^{+}$ (Hirano et al. 1999) reveal a strong peak (B1-b) at the position of the south-east ammonia emission detected by Bachiller et al. (1990). As part of the same study, continuum emission at 850 and 350 μm from the JCMT and CSO respectively and at 3 mm with the Nobeyama Millimetre Array clearly identify two high density dust cores within the single molecular clump. Based on spectral energy distributions, Hirano et al. (1999) conclude that these objects are both extremely young protostars in the Class 0 phase (Andre et al. 1993). The masses of the central objects, called B1-bN and B1-bS are estimated to be no greater than 7×10^{-2} $M_{\odot}$, indicating extremely young ages of less than 2×10^{4} yr for both sources. No outflows were detected from either source.

One powerful outflow, associated with IRAS 03301+3057 (B1-IRS), was identified by Nakamura (1988). It is confined to a region of $40''$ (about 0.07 pc). The dynamical time estimated from the outflow is 10^{3} to 10^{4} years. Hirano et al. (1997) measured the small scale structure of the CO outflow from IRAS 03301+3057 and estimate that the driving source is very young and is observed in a pole-on configuration.

The masses of the YSOs seen optically and with IRAS range from 0.2 to 3 $M_{\odot}$

(Bachiller et al. 1990). Given these low stellar masses, the stellar to gas mass ratio in B1 is on the order of 0.5%, negligibly small even compared with Taurus where the star formation efficiency is $\sim 2\%$ (Shu et al. 1987). The observed rotation velocities within B1 are insufficient to support the cloud against collapse by a factor of ~ 8 (Bachiller et al. 1990). The ages of embedded but optically visible objects LkHα 327 and LkHα 328 are between 4-6 $\times 10^6$ yr (Cohen & Kuhi 1979). Based on this, Bachiller et al. (1990) conclude that a mechanism must be providing substantial support to the B1 cloud.

Polarization of background starlight from the Perseus cloud due to selective absorption from dust grains within the complex was measured by Goodman et al. (1990), who find that the distribution of polarization position angles measured is bimodal, with weaker vectors aligned along the cloud's projected major axis and stronger vectors lying roughly perpendicular to the first population. Goodman et al. (1990) hypothesized that two emitting clouds of differing magnetic field orientations could be superimposed along the line of sight. Previous evidence for a second gas cloud along the line of sight to Perseus and B1 at a distance of 200 pc was presented by Cernicharo et al. (1985).

The Barnard 1 cloud has been surveyed for evidence of Zeeman splitting in dense OH gas more extensively than any other dark cloud. Lang & Wilson (1979) estimated a 3σ limit of 90 μG toward LkHα 327, located approximately $4'$ away from B1's strong molecular peak. B1 was chosen by Goodman et al. (1989) as a strong candidate for magnetic field detections due to its atypically high non-thermal linewidth components. A field strength of -27 ± 4 μG was detected toward the position of the bright molecular core coincident with IRAS 03301+3057 (Goodman et al. 1989). Two other detections were made in the cloud: -12 ± 5 μG was measured $4\farcm2$ southwest of the IRAS source and -13 ± 6 μG was measured toward a fainter OH peak $12'$ north of the IRAS source (see Goodman et al. (1990) and Crutcher et al. (1994)). The negative sign indicates that the field is oriented toward the observer.

A survey of 12 dark clouds for evidence of Zeeman splitting yielded only one solid detection – toward B1 – with the 140 ft. Green Bank Telescope (Crutcher et al. 1993). In an observation toward the IRAS source 03301+3057, a field strength of -19 ± 4 μG was measured.

In order to supplement the Zeeman data toward the dense molecular gas of B1, we have measured polarized emission at 850 μm from dust toward the "main core" of B1 as identified in CS and NH_3, both tracers of high column densities. Emission from aligned, spinning dust grains is anisotropic and hence polarized. Unfortunately, polarization data reveal no direct information about the field strength, since the degree of polarization is dependent on other factors such as grain shape, composition and degree of alignment. The degree of polarization is in essence a measure of how effectively the grains have been "sped up" (Hildebrand et al. 1999). However, even though the grain spin is induced by mechanisms other than the magnetic field, such as the radiation field (Draine & Weingartner 1996) or the production of H_2 on the grain surface (Purcell 1979), the magnetic field is expected to provide the alignment. Because of this, continuum polarization data are the principal means of probing the geometry of the magnetic field. The very sensitive SCUBA detector now permits the observation of polarized emission from the ambient cloud surrounding dense cores.

This paper is the fifth in a series to examine the magnetic field geometries in star-forming molecular clouds using polarized emission. Barnard 1 is the first dark cloud we have observed, and these data are the first emission polarimetry toward this region. The observations and data reduction techniques are described in § 7.2. The polarization data are analyzed in § 7.3. We discuss the possible interpretations of these data and calculate an estimate three-dimensional structure for the mean field of B1 in § 7.4. Our findings are summarized in § 7.5.

7.2 Observations and Data Reduction

We have used the UK/Japan polarimeter with the Submillimetre Common User Bolometric Array (SCUBA) detector at the James Clerk Maxwell Telescope[1], to map polarized thermal emission from dust at 850 μm toward a dense region of the B1 dark cloud. The observations were taken from 11 to 13 October 1999. The polarizer and general reduction techniques are described in Greaves et al. (2000) and Greaves et al. (2001). To generate a polarization map, a 16-point jiggle map was made at each of 16 different half-waveplate positions. After each integration, the half-waveplate was rotated through 22.5° and the mapping repeated. The data were flat-fielded, corrected for extinction and dual-beam corrected using the general SCUBA software. Estimation of systematic errors due to chopping and sky subtraction can be found in Matthews, Wilson, & Fiege (2001). Unfortunately, there are no large scale scan maps of the B1 cloud in the literature. This made the identification of chop angles and sky removal candidate bolometers more difficult. The chop position angles (P.A.s) and throws for each field centre observed are summarized in Table 7.1. The level of precipitable water vapor was very stable over the course of the observations. The estimates of τ(225 GHz) from the CSO ranged from 0.055 to 0.075 over the observations, with 96% in the range 0.060 to 0.070.

Pointing Centre		Chop Throw	Chop P.A.	Number of
R.A. (J2000)	Dec. (J2000)	($''$)	(E of N)	Times Observed
$03^h33^m17\overset{s}{.}9$	$+31°09'32\overset{''}{.}3$	120	65°	16
$03^h33^m19\overset{s}{.}6$	$+31°08'28\overset{''}{.}25$	120	65°	12
$03^h33^m18\overset{s}{.}3$	$+31°07'3\overset{''}{.}8$	120	65°	30

Table 7.1: Observing Parameters for Jiggle Mapping of B1

These data were corrected for an error in the SCUBA clock which placed incor-

[1]The JCMT is operated by the Joint Astronomy Centre on behalf of the Particle Physics and Astronomy Research Council of the UK, the Netherlands Organization for Scientific Research, and the National Research Council of Canada.

rect LST times in the data headers during the period from July 1999 to May 2000. This error did not affect the telescope's acquisition or tracking, but affects data reduction since the elevation and sky rotation are calculated from the LST times in the data headers. The magnitude of this error over time can be evaluated and then corrected retroactively as described on the JCMT website. The error in timing after this adjustment is ±10s. The data were reduced using the Starlink software package POLPACK, designed specifically to include polarization data obtained with bolometric arrays.

After extinction correction, noisy bolometers identified for each night's data were flagged and removed from the data. Between 3 and 5 bolometers were removed per night. Prior to sky subtraction, images were made to examine the flux in each bolometer, since bolometers used for sky subtraction should not have negative values (produced if one has chopped onto a location with significant flux, for example). The data were sky subtracted using bolometers with mean values close to zero, but not those which were significantly negative. Between 1 and 4 bolometers were used to subtract the sky. The methods of sky subtraction are discussed in detail in Jenness et al. (1998). Finally, the instrumental polarizations (IPs) were removed from each bolometer. All the data sets were then combined to produce a final three dimensional map (I, Q and U). These three Stokes' parameters are then combined to yield the polarization percentage and polarization position angle in the map. The resultant vectors are plotted over the uncalibrated I map.

Before filtering the data to select reliable polarization vectors, it was necessary to estimate the effects of sidelobe polarization in the position of the main beam. This is a measure of the mimimal believable polarization, p_{crit}, given the potential for sources in sidelobes to produce artificial polarization signals in the central region of the map (see Greaves et al. 2001). For our worst case scenario in B1, the flux contributed at approximately $68''$ from the map centre is 16 times that at the centre. Examination of polarization maps of Saturn (which has only a small intrinsic polarization $\sim 0.6\%$, with a minimum of $\sim 0.2\%$) of 13 October 1999 reveal that the relative mean power $68''$ from the main beam centre is 0.0067 compared to the main beam itself. The mean polarization percentage in this region is 4.3%, which is a measure of the instrumental polarization. The p_{crit} value is given by:

$$p_{crit} \geq 2 \times 4.3\% \times 0.0067 \times 16 \tag{7.1}$$

which gives a minimum threshold polarization of 0.92%. Assuming the minimum intrinsic polarization of Saturn, this leaves $\sim 0.7\%$ arising from sidelobe polarization. We have thus selected vectors for which polarization percentage, $p > 1\%$, the uncertainty in polarization, $dp < 1\%$, and signal-to-noise in polarization $\sigma_p > 3\%$. To minimize the systematic effects arising from the possibility that we have chopped onto a region of polarized emission while observing, vectors are selected only if they are coincident with unpolarized intensity, I, $> 20\%$ of the faintest peak in our map. As discussed in Matthews, Wilson, & Fiege (2001), if the reference position has a flux level $\sim 10\%$ that of the source peak and polarized to the same level, in the final map the position angle at 20% the peak could be offset from the correct value by $\leq 10°$, while the p value is incorrect by < 2. For the brighter peaks, the effects would be considerably reduced.

7.3 850 μm Polarization Data

Figure 7.1 illustrates the polarization pattern detected across the B1 "main core" region as identified in CS and NH_3 by Bachiller et al. (1990). The polarization data are plotted on a greyscale map of the total, unpolarized intensity, estimated by summing together the fluxes detected at all waveplate positions. Four peaks are distinguishable, these are labelled B1-a to B1-d. B1-a and B1-b (N and S) follow the classification of Hirano et al. (1999) as identified in $H^{13}CO^+$ and 850 μm SCUBA emission. The presence of two sources within B1-b was confirmed by

3.0 mm observations with the Nobeyama interferometer (Hirano et al. 1999). NH_3 (1,1) and (2,2) emission was observed from peaks corresponding to B1-a, B1-b and B1-c by Bachiller et al. (1990). The B1-d 850 μm peak lies approximately $1'$ south of the B1-a molecular peak (Bachiller et al. 1990) which is likely associated with IRAS 03301+3057 (marked by a blue cross on Figure 7.1). No ammonia emission is concentrated at the B1-d position (Bachiller et al. 1990), although a very low signal-to-noise peak exists near this position in the $H^{13}CO^+$ map of Hirano et al. (1999).

7.3.1 Polarization Position Angles

Polarized emission is detected both on the bright cores and in regions of lower column density between them. The degree of alignment across the region is evidence for the presence of ordered magnetic fields within the main core of the B1 cloud. The data in high intensity regions have been binned to $6''$ sampling, while data in fainter regions are binned to $12''$ to improve signal-to-noise. The distributions of polarizations associated with faint emission and bright emission are plotted separately on Figure 7.2.

The distribution for faint I (dotted line) is approximately Gaussian. A fit to these data yields a mean of 91.3° (east of north) with a distribution width of 19.0°. A goodness of fit measure to the data yields $\chi^2_{red} = 0.6$. The statistical mean of the distribution is 88.3° (east of north) with a standard deviation of 27.7°. The distribution of vectors in regions of bright emission, however, cannot be fit effectively by a Gaussian (or even a series of Gaussians). The solid line of Figure 7.2 shows several peaks, each of which corresponds roughly to one of the bright peaks. We have indicated the peak sampled on the distribution.

Therefore, the polarization pattern in the ambient cloud material around the cores is defined by a mean polarization direction where the vectors are distributed

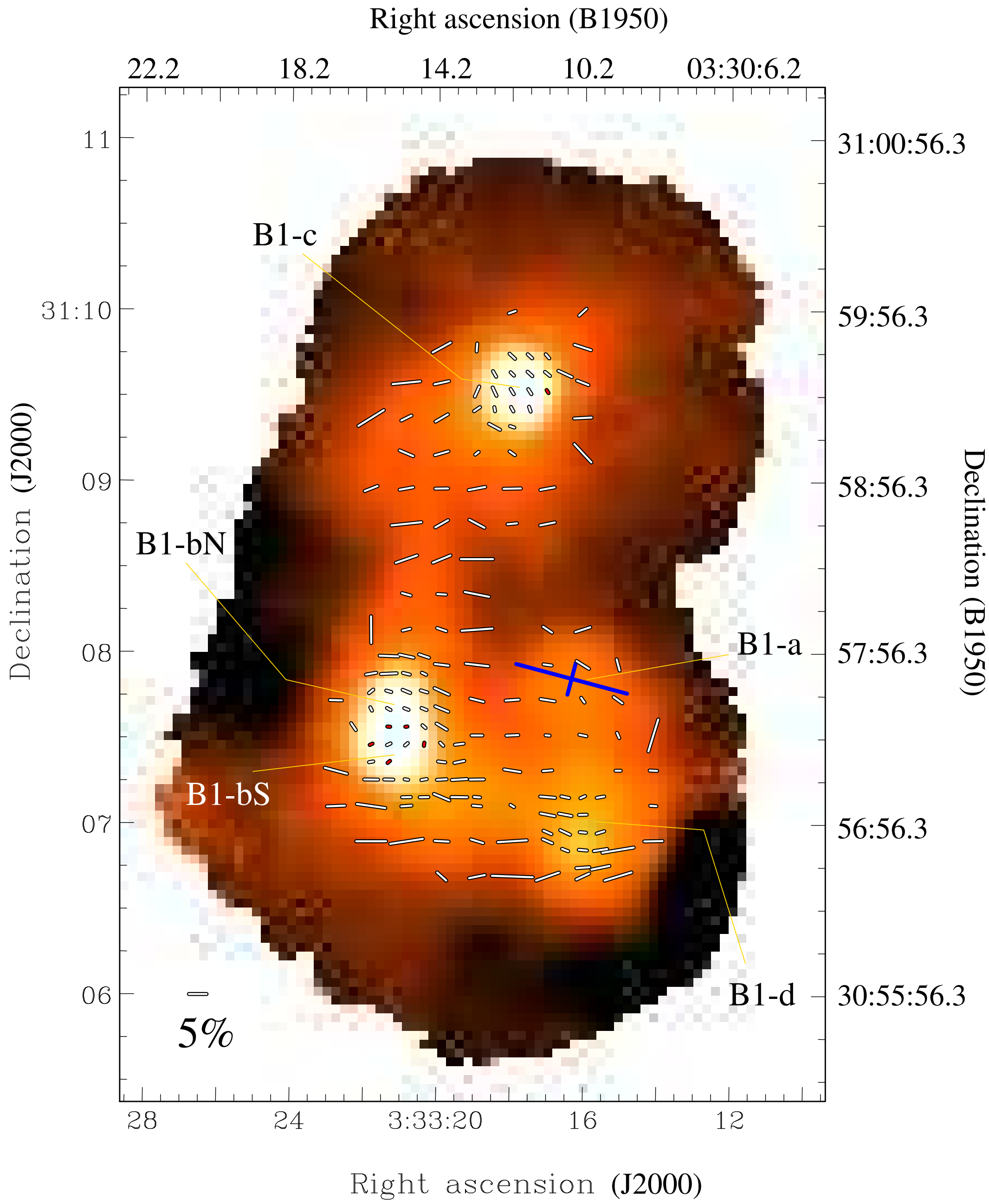

Figure 7.1: 850 μm Polarization Pattern toward the Centre of Barnard 1. The dust intensity greyscale is estimated by summing the polarization data at all waveplate positions. The greyscale range is -1σ to 3σ. Polarization data were sampled at $3''$ and have been binned to $6''$ (approximately half the JCMT beamwidth of $14''$) on the bright cores where signal-to-noise (σ_p) is high and $12''$ in the fainter regions. All vectors have intensity greater than 20% the B1-d peak flux, $\sigma_p > 3$, and an uncertainty in polarization percentage, dp, $< 1\%$. Red vectors have polarization percentage, p, $< 1\%$ and were not included in any analysis of the polarization pattern. The vectors are accurate in position angle to better than 10°. The peaks B1-a, B1-bN and B1-bS have been labelled according to the designations of Hirano et al. (1999). We have designated the other two peaks B1-c and B1-d. The position of IRAS 03301+3057 is marked in blue where the lines denote the extent of the error in the IRAS position. The mean polarization percentage of the plotted vectors is 3.6% with a standard deviation of 2.2%. Coordinates in J2000 and B1950 are shown.

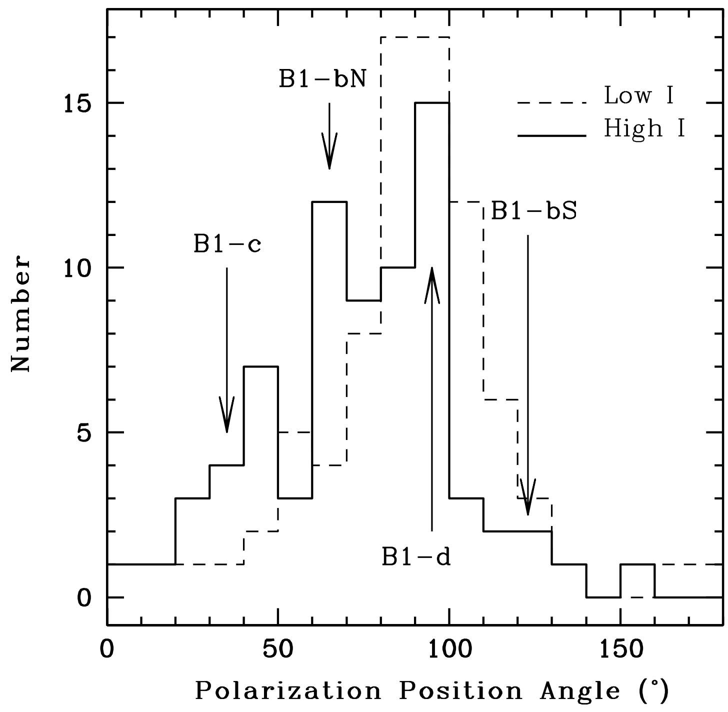

Figure 7.2: Distributions of θ in Regions of Low and High Unpolarized Intensity.
We have plotted histograms of the polarization angle measured toward faint (dashed) and bright (solid) regions separately. The threshold used to discriminate between faint and bright regions was an unpolarized intensity estimate of 330 mJy beam^{-1} (using the calibration factor discussed in §7.3.3. The vectors associated with lower column densities exhibit a Gaussian distribution with a mean of 91° and dispersion of 19°. The distribution of vectors toward the cores is not Gaussian, with each core dominating a different part of the total histogram. The position angles are labeled with the core dominating that peak.

about 90° (east of north), while the cores each exhibit different mean position angles. The core B1-b shows systematic variation in position angle. The northern core has $< \theta >\sim 65°$, while the southern core exhibits $< \theta >\sim 120°$. The B1-c core has $< \theta >\sim 35°$, and the B1-d core peaks around 90° east of north, in alignment with the fainter material in the cloud.

7.3.1.1 Correlations between Adjacent Vectors

To better examine the changes in the nature of the polarization data across the map, we have compared each vector to its closest eight neighbours, calculating the differences in polarization percentages and position angles for each pair of values. All the data of Figure 7.1 were used, except those values for which $p < 1\%$ (shown in red). Next, the results were smoothed onto $12''$ grid, by calculating the mean changes in polarization percentage and position angle. The resulting map is shown in vector form in Figure 7.3, where the vector magnitude is the mean change in polarization percentage in a grid and the vector angle is the mean change in orientation. No significant change in orientation is indicated by a vector at 0° east of north.

The locations of cores labeled on Figure 7.1 are indicated by red crosses on Figure 7.3. As expected, the changes within the cores are relatively small, excepting B1-a which is the faintest core in our map. Within the other cores, the position angles (and even polarization percentages) are consistent with relatively little change. Based on the histogram of the polarization data toward fainter regions shown in Figure 7.2, the vectors in this region were also expected to be well aligned, and the data of Figure 7.3 show that this is indeed the case. The large variations in adjacent data values are confined to the edge of the map and the boundaries between the B1-b and B1-c cores and the fainter material.

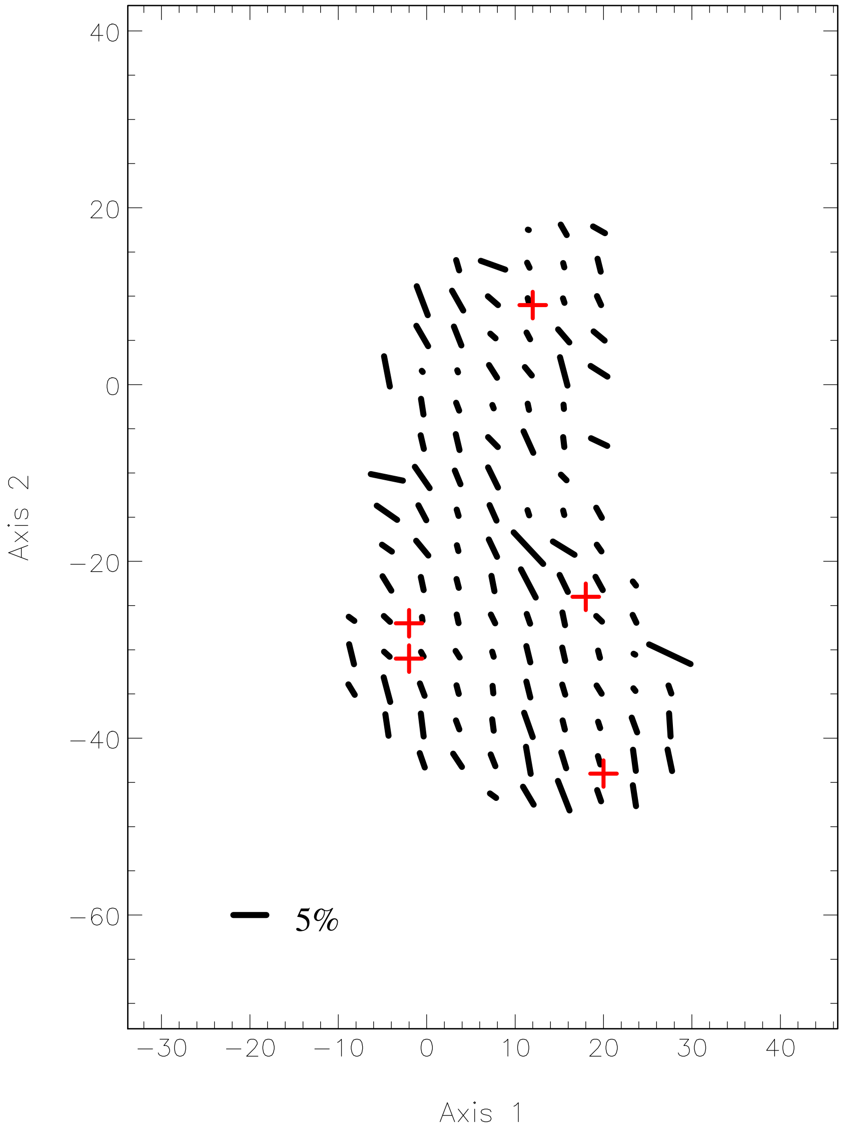

Figure 7.3: Variations between neighbouring vectors.
We have compared each vector to its nearest neighbours in eight directions to a maximum radial separation of 17″. The data were then smoothed to 12″ sampling. The length of the vectors plotted is the mean change Δp in the smoothed grid point, while the vector orientations indicate the mean change in direction $\Delta\theta$. Zero change in angle is indicated by 0° (east of north). The positions of the cores B1-a through B1-d are indicated by red crosses. These data reveal that within cores, and between them, the polarization percentages and position angles have a high degree of uniformity, while the large vectors offsets from 0° at the boundaries show where the changes in vector character occur.

7.3.2 Depolarization in Barnard 1

Figure 7.3 suggests that changes in polarization percentage are small within the cores of B1. The statistical means of the low intensity and high intensity vector populations are 4.5% and 2.6% in 81 and 74 values respectively. The standard deviations in these populations are 2.3% and 1.4%. In this case, the depolarization effect, declining polarization percentage with intensity, may be weak within parts of B1. The easiest way of examining the depolarization effect is to plot the p versus I for all values on a polarization map.

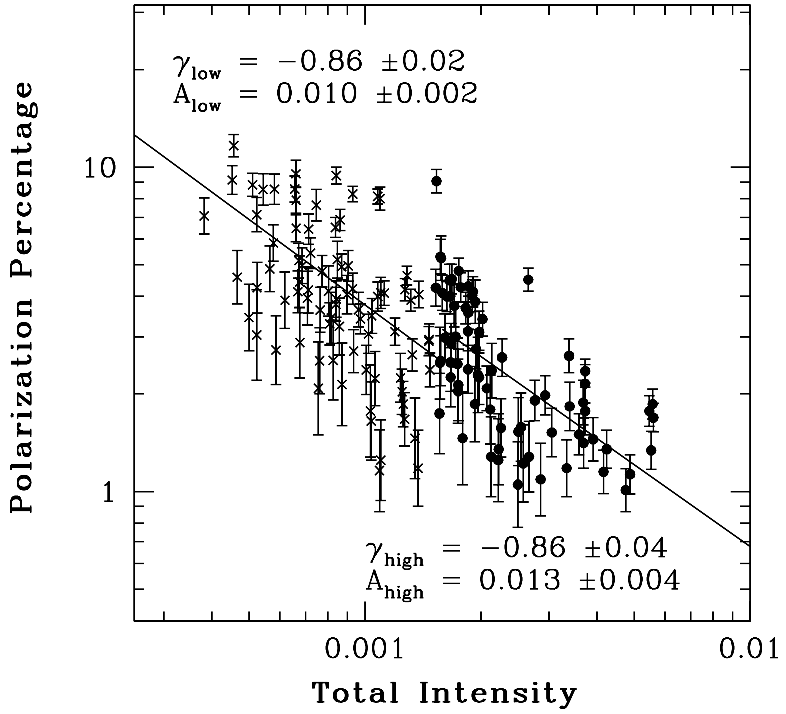

Figure 7.4: Depolarization in Regions of Low and High Column Density. Polarization is plotted against intensity on a log-log scale for our two populations of vectors. Low column density (intensity) data are plotted with crosses while circles illustrate vector magnitudes associated with the cores. The slopes derived from fits to the p versus I profiles yield the same power law index, γ (where $p = AI^{\gamma}$), plotted as the slope on the logarithmic scale. We note, however, that despite the scatter in the plot, the vectors at higher intensities seem to flatten in p.

In Figure 7.4, we present the data for the B1 region as presented in Figure 7.1, excluding only those data values with $p < 1\%$, plotted in red. The data exist in two populations, where the data at low intensities are binned to $12''$ (shown as crosses) and the data at high intensities are binned to 6″ (shown as circles). Although these plots are shown in log-log space, the fits to the data were done to profiles of p versus I by minimizing χ^2. This is a more effective treatment of the uncertainties since those for low values of p are exaggerated in log space. The fits to these two populations produce completely consistent slopes, indicating that both can be characterized by power laws of the form: $p = AI^\gamma$ with an index of $\gamma \approx -0.86$. At high values of I however, there is a slight thresholding of polarization percentage.

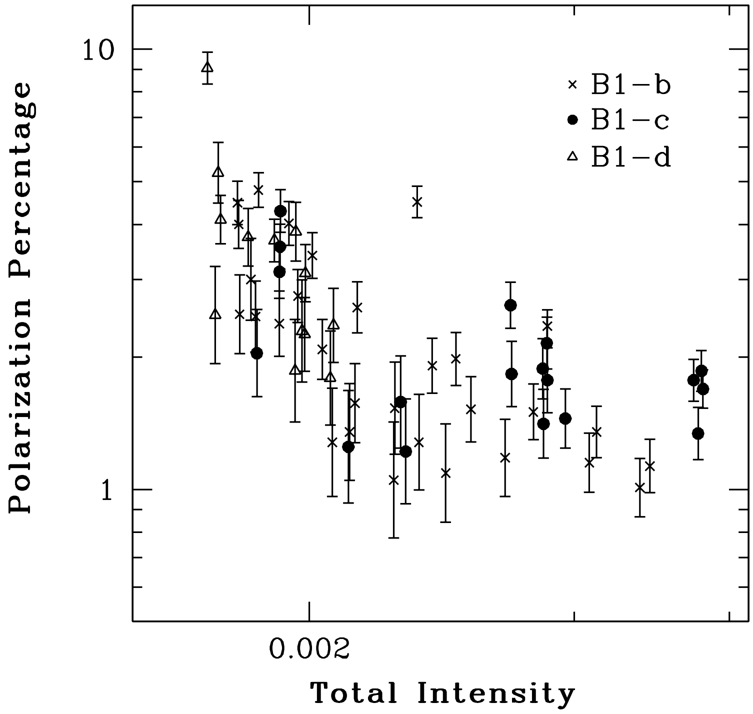

Figure 7.5: Depolarization toward individual cores.
To better examine the change in polarization percentage at high intensities, we plot log p versus log I for individual cores. Essentially, we take all vectors around each core above the intensity threshold discussed in Figure 7.1. By plotting the three bright cores separately, it is clear that B1-b and B1-c show flattening of p above an I threshold which corresponds to $\sim$ 30% of the peak of B1-c and $\sim$ 40% of B1-b.

To better illustrate this, in Figure 7.5 we show the same style plot for three cores: B1-b (north and south combined), B1-c and B1-d. Vectors toward the cores B1-b and B1-c show a distinct flattening at high intensities. Thus, the depolarization effect does not follow the usual trend of declining polarization percentage as intensity increases across these two cores. We note however, that several polarization vectors less than 1% were measured toward B1-b and still others were not used in the analysis due to poor signal-to-noise levels. The B1-d core, significantly fainter than the others, does exhibit depolarization at its peak, which is significantly lower in intensity than B1-b and B1-c. The B1-c core is well sampled and definitively exhibits a flat dependence of p on I down to 30% of that core's peak. To our knowledge, this is the first case of a bright core which has not exhibited depolarization over its whole intensity range.

7.3.3 Continuum Cores in B1

Of the four dense cores detected in our polarization map, two have not been observed previously in continuum emission. These are B1-c and B1-d, although the latter may have been confused with B1-a in large beams (i.e. IRAS) if they are at similar evolutionary stages. Absolute calibration is not part of the standard reduction of polarization data since the percentage polarization is a relative quantity only. However, from our Stokes' I map, we can estimate the fluxes in our map by using a reasonable flux conversion factor for 850 μm SCUBA data. This quantity is dependent on the chop throw used, and for 120″ throws, a reasonable conversion factor is 219 ± 21 Jy beam^{-1}V^{-1} according to the JCMT website. Hence, we have multiplied our Stokes' I map by 220 Jy beam^{-1}V^{-1}.

Core	RA (J2000)	DEC (J2000)	S_{peak} (Jy beam^{-1})	Notes
B1-a	$03^h33^m16\overset{s}{.}4$	$+31°07'51''$	0.31	IRAS 03301+3057
B1-b	$03^h33^m21\overset{s}{.}3$	$+31°07'28''$	1.15	double (Hirano et al. 1999)
B1-c	$03^h33^m17\overset{s}{.}7$	$+31°09'31''$	1.36	first continuum detection
B1-d	$03^h33^m16\overset{s}{.}2$	$+31°06'49''$	0.48	first continuum detection

Table 7.2: Peak flux densities at 850 μm

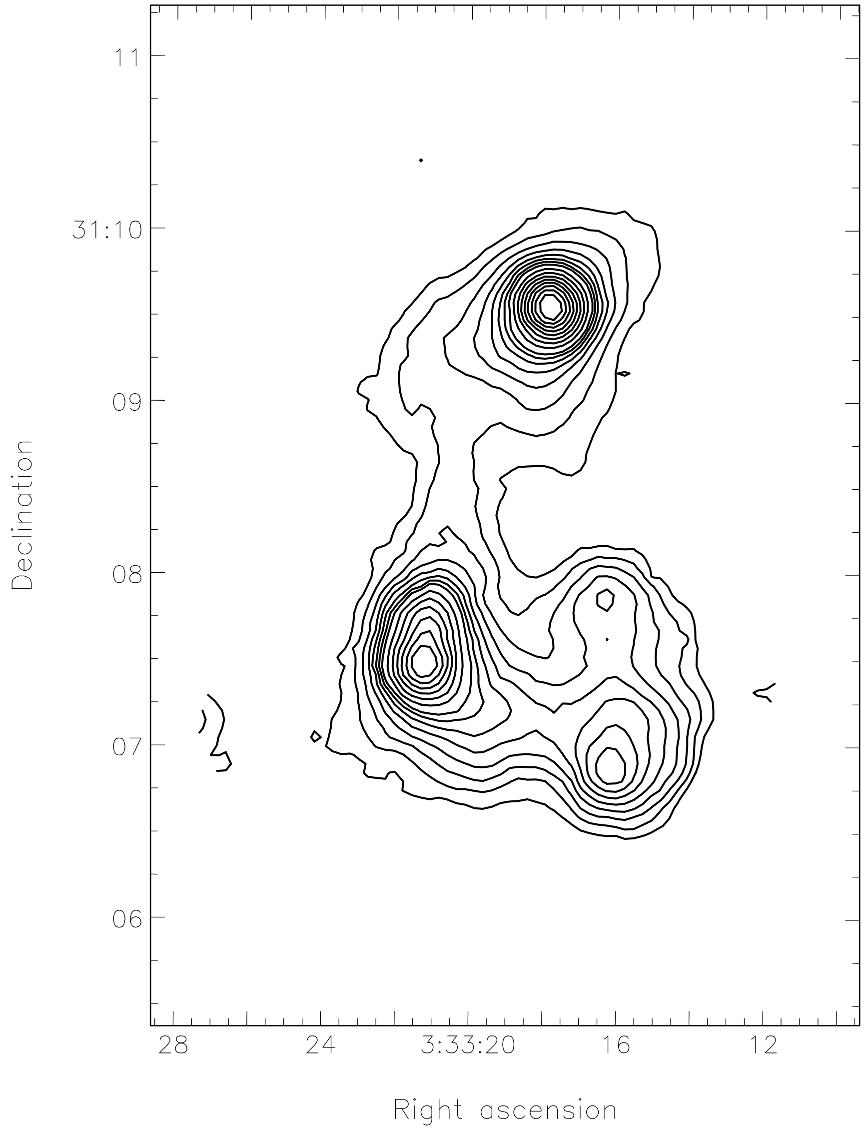

Figure 7.6: Continuum Cores in B1.

A contour plot of the total, unpolarized emission as estimated from the total of all polarizations is presented. We have done an approximate calibration using the mean flux calibration factor of 220 Jy beam^{-1}V^{-1} for SCUBA data at 850 μm with a 120$''$ chop throw; hence this calibration is approximate, and fluxes are uncertain by $\pm$ 10% based on the uncertainty in gain alone. Contours plotted are: 0.1 to 0.45 Jy beam^{-1} in steps of 0.05 Jy beam^{-1}, and 0.55 to 1.25 Jy beam^{-1} in steps of 0.1 Jy beam^{-1}.

Figure 7.6 is a contour map in Jy beam^{-1}. The brightest source is B1-c, not previously measured in continuum. We do not detect both peaks toward B1-b although Hirano et al. (1999) do in an earlier SCUBA map; their interferometic observation with the Nobeyama Millimeter Array clearly resolves two peaks toward this source. The slightly enhanced emission coincident with IRAS 03301+3057 is the faintest distinguishable peak at 850 μm. Table 7.2 summarizes the peak fluxes toward each of the four cores (B1-b is treated as a single core; this flux estimate likely includes some flux from both sources) and positions of these peaks.

7.4 Discussion

7.4.1 Interpreting the Polarization Pattern

Optical polarimetry using absorption of light from background stars was used to probe the magnetic field structure through dust at low extinctions in the Perseus cloud complex by Goodman et al. (1990). They found a bimodal distribution of polarization vector orientations toward the cloud such that the vectors lie roughly parallel and perpendicular to the major axis of the cloud at $\sim 60°$. They fit two Gaussians to their data set with means 71° and 145° east of north and 1 σ dispersions of 12° and 8°, respectively. Since there is no spatial distinction between the two populations and evidence in observations of molecular gas that two different clouds could lie along the same line of sight, they conclude that the two polarization populations are representative of two distinct clouds at different distances. The foreground cloud was predicted to have a low extinction ($A_V < 1$ mag). Bimodal distributions in polarization vectors had been previously noted by studies toward the Perseus clouds NGC 1333 (Turnshek et al. 1980; Vrba et al. 1976) and Barnard 5 (Joshi et al. 1985).

In the process of generating an evolutionary model for the B1 cloud, Crutcher et al. (1994) adopt a mean plane-of-sky field direction along the minor axis of the Perseus (and hence B1) cloud which corresponds to the polarization distribution centred on 145° east of north. In this case, the Goodman et al. (1990) vectors centred on 71° east of north would most likely be associated with the foreground cloud, at a distance of 200 pc (Cernicharo et al. 1985). If the interior of the dense B1 main core is threaded with the same field geometry as measured on the periphery of the B1/Perseus cloud, then a field of mean direction $145 \pm 12°$ should produce polarized emission from dust at a position angle of $55 \pm 12°$. Figure 7.2 demonstrates that there is no peak in the polarization data at 850 μm at 55°, although polarization vectors of B1-c and B1-bN fall roughly in the range of the optical polarization dispersion value. The second distribution measured by Goodman et al. (1990) peaked at 71°, which corresponds to an emission polarization angle of 161°. Thus, there is no component of position angle in our data set which corresponds to either population of the optical polarization data. Hence, based on our emission polarimetry, which is believed to arise only in the regions of dense, cold dust, we cannot conclude which optical polarization direction is more likely associated with the Perseus complex at 350 pc.

7.4.1.1 Vector Sums through Two Clouds

Since the thermal emission from dust is optically thin at 850 μm for all but the densest regions of protostellar cores (where $n > 10^6$ cm^{-3}), the vector sum measured would be the sum of the polarizations from all clouds along the line of sight. Thus, unless a single cloud dominated the emission, or the field structure in the dense regions is unrelated to that measured in the low column density dust probed by absorption polarimetry, then it is unlikely that we should measure a polarization direction corresponding to either of the field directions inferred from the optical observations of Goodman et al. (1990). As demonstrated in the previous section, this is indeed the case. We now investigate the possibility that the emission polarization data could be the sum of emission over two clouds along the line of sight.

The polarization data obtained in the regions of fainter dust emission between the cores of Figure 7.1 do exhibit a Gaussian distribution peaked roughly at 90°. A vector sum of clouds of polarization position angle 161° and 55° can produce a net vector of 90°, if the magnitude of the polarized intensity ($p \times I$) of the 55° cloud is twice that of the other cloud. In order for 1/3 of the total 850 μm emission between the cores of Figure 7.6 to arise in a foreground cloud, that cloud would be expected to have a column density N(H_2) $\sim 4 \times 10^{21}$ cm^{-2}, corresponding to an $A_V \sim$ 2-4 mag (assuming $T = 12$ K). The estimate of the extinction of a foreground cloud was $A_V \leq 1$ mag by Goodman et al. (1990). The second cloud could have an even lower column density if it were more polarized than B1. However, at this extinction, it is unlikely that dust grains could be cold enough to emit at 850 μm given the heating by the interstellar radiation field.

7.4.1.2 Complete Depolarization of the Cores?

The polarization vectors across the B1-d peak are aligned with the faint emission polarization angles of 90°, but the brighter peaks, B1-b and B1-c both exhibit different position angles. Given the previous observations of depolarization in bright peaks and the polarization plateau across these two cores, it would be tempting to think that the cores themselves are completely depolarized and that one might thus measure the polarization toward a different cloud along the line of sight at their positions. There are several reasons why this is unlikely to be the case.

Within cores, depolarization is a function of intensity, so the polarization percentage rarely reaches zero, and if it does become unmeasurably small, as it does at places in B1-b, then it does so at the highest intensities. Therefore, one might expect to see a varying position angle across cores that reflects the varying contribution of the core's polarized intensity to the vector sum with the second cloud, revealing the second cloud's position angle only toward the peak of the core. Furthermore, even in the case where the depolarization might atypically be complete across the core, this would effectively create a steeper than usual depolarization effect rather than a flat distribution of p with I as we particularly observe toward B1-c (see Figure 7.5). The reason is that if the polarized emission arose in a cloud other than B1 and were unassociated with the B1-c core (which we know to be in B1 through its molecular emission), the increasing contribution to the total intensity from the core (despite its contribution of zero polarized intensity) should produce a variation in p with I which varies exactly as the increase in intensity across the core. The only way this could be avoided would be if, as the intensity across the B1-c core increased, so did the polarized intensity in the second cloud. These increases would have to match each other exactly to produce the flat pattern we see. We dismiss this scenario as far-fetched.

In B1, we see not just a single core which exhibits a different position angle orientation than the ambient cloud, but instead there are two such cores, where B1-b includes systematic variation in θ from north to south. In order to see the optical polarizations from a foreground and background cloud in absorption, Goodman et al. (1990) point out that the extinction of the nearer cloud must be low ($A_V \leq 1$ mag) or have significant fluctuations in order to see through to the background cloud. If the extinction in the cloud is on the order of 1 mag, then the cloud is not self-gravitating and hence is an unlikely source of 850 μm emission (and certainly 850 μm polarized emission, which is at most 10% of the total flux). This leaves the possibility of a denser cloud with significant fluctuations in column density across its projected surface.

The distance between the B1-b and B1-c cores is approximately 2 arcminutes.

At a distance of 200 pc, which is the most probable location of a foreground cloud given previous molecular line observations, this corresponds to 0.12 pc, or about the scale of a self-gravitating core in a molecular cloud. Since we observe different position angles in the two bright cores (and a change in position angle within the B1 core itself), this would suggest that fields of varying orientations are exhibited in the foreground fluctuations in the nearby cloud. This implies that the fluctuations in the foreground cloud are comparable to or smaller than the scale of a starless core. Since the two bright cores associated with NH_3 emission are known to be within the B1 cloud at 350 pc, the fluctuations would have to vary on an angular scale similar to the separation of cores in B1, despite a distance nearly a factor of two smaller. We conclude that attributing the polarization seen against the bright cores B1-b and B1-c to a foreground cloud suggests an unlikely configuration for a nearby cloud not detected in any dense tracers such as CS and NH_3.

However, the polarization plateau in B1-c does suggest that this core is unusual in some way. Depolarization within cores is usually attributed to either changing grain or alignment physics with increasing density or varying magnetic field geometry. It is possible that no stellar condensation has formed at the centre of B1-c, in which case an essentially unidirectional B_{pos} field geometry may thread this core. Also, if no outflow is present, then theory suggests there should be no disk either, which means the field is unlikely to be tangled on small scales. Further study of this source to search for evidence of outflow or a protostellar condensation could provide some support for the suggestion that this is a starless core. It is interesting to note that all the starless cores observed thus far with SCUBA did exhibit depolarization toward their intensity peaks (Ward-Thompson et al. 2000). Those cores are all significantly closer than B1 (140-170 pc). The total flux from one of these cores (L183) is 2.8 Jy at 800 μm (Ward-Thompson et al. 1994). Therefore, cores of comparable brightness (> 1 Jy) both closer and further (i.e. LBS 23's cores, Matthews, Fiege, & Moriarty-Schieven 2001) than B1 do exhibit depolarization to the highest intensities. The polarization plateau of B1-c is thus not easily explained purely by differing resolutions.

7.4.1.3 Position Angles over the Cores

It is worth noting that the degree of alignment across the B1-a, B1-c, and B1-d cores is particularly strong. Figure 7.6 shows that these three cores are not significantly asymmetric, so the polarization patterns cannot be said to align with any preferred axes of the cores. The elongated core B1-b is the only one which exhibits systematic variation in polarization postion angle. Since this core is resolved into two sources, the polarization patterns could be different within each core and then we would observe their vector sum where the cores overlap.

Several models exist which predict the polarization patterns across cores depending on various physics. A recent publication by Padoan et al. (2001) predicts the continuum polarization for protostellar cores assembled via supersonic magnetized turbulent flows in models of molecular clouds. They find that the universally observed relationship between polarization percentage and intensity in star-forming cores can be reproduced by their model if grains are aligned only up to a threshold extinction ($A_v \sim 3$ mag in their simulation). We note that our observation of a core with a depolarization threshold and a high degree of alignment is contrary not only to this model, but all previous observations of polarization patterns toward star-forming cores. The fact that in this particular region, there is a potential for confusion between two clouds along the line of sight makes interpretation of the polarization data more complicated. However, constraints on the column density and spatial scale of potential variations in extinction of a second cloud suggest that the overwhelmingly predominant source of polarized emission is the B1 cloud and its associated cores. The models of Padoan et al. (2001) and Fiege & Pudritz (2000) relate to cores forming from lower density, filamentary structures. B1 is not a significantly elongated cloud (although the Perseus complex itself appears elongated on very large scales in projection), and its cores appear to be forming from density enhancements in its cold interior. A recent model of magnetized cores predicts a relation between the geometry of a core and the measured polarization position angles (e.g. Basu 2000). However, the B1 cores are not significantly elongated; the only asymmetry is in B1-b, which resolves into two sources with separate extended envelopes (Hirano et al. 1999).

7.4.2 An Estimate of the Total Field Strength and Direction in B1

Myers & Goodman (1991) describe a method by which the total field strength and direction can be estimated in a cloud toward which a series of independent Zeeman measurements of B_{los} and polarization measurements to infer B_{pos} have been made. Their formalism is described for absorption polarimetry, but is easily adapted to emission polarimetry if simple assumptions are made about the relation between the orientations of polarization vectors and the plane-of-sky magnetic field. A distribution of polarization data which can be fit by a single Gaussian is required. As described in § 7.3.1 above, the polarization vectors associated with the faint lower density gas off the B1 cores can be fit with a single distribution which has a mean of 91° (east of north) and a width of 19°. At 12″ sampling, these vectors are not completely independent (since the JCMT beamwidth is 14″), but we use them to get a rough estimate of the field properties. The B1 cloud has the most Zeeman data available of any dark cloud; this was one of the motivating factors for our 850 μm polarization observations. However, even in this cloud, the four Zeeman measurements are not completely independent and could also sample different populations of gas. For example, Goodman et al. (1990) report three B_{los} values for three positions in the B1 cloud measured with the Arecibo 305m telescope, but two exhibit very different field strengths than that toward the IRAS 03301+3057 core inside the so-called "main core" of dense gas (Bachiller et al. 1990). The fourth measurement was made with a much larger beam by Crutcher et al. (1993) and clearly samples a wider area and range of densities than the data of Goodman et al. (1990). To estimate the total field in the region, we have opted to take the mean and standard deviation of the three independent measurements made with Arecibo. We note that this is a dismally small sample on which to base an estimate of dispersion in the field strength along the line of sight, and the magnitude of B_{los} will likely be overestimated by the use of the high value measured toward the peak position of IRAS 03301+3057.

The model is based on the presence of both a uniform (B_0) and non-uniform (B_n) component to the field in the region. Non-uniform in this case refers to a disordered, possibly turbulent field component (as opposed to an ordered, unidirectional field). Given a distribution of polarization data with mean polarization angle Θ (in degrees) and dispersion, s, (in radians), and a series of Zeeman measurements with mean $\overline{B}_{0_z}$ and dispersion σ_{B_z}, the following quantities can be estimated: the inclination,

$$i = \arctan\left(\frac{\sigma_{B_z}}{s\overline{B}_{0_z}}\right); \tag{7.2}$$

the total uniform mean field strength,

$$B_0 = \frac{\overline{B}_{0_z}}{\cos i}; \tag{7.3}$$

and the dispersion in $\mathbf{B}$,

$$\sigma_B = \sigma_{B_z} N^{1/2} \tag{7.4}$$

where N is the number of correlation lengths of the non-uniform field component through the cloud. The correlation length is an expression of how quickly the non-uniform component of the field changes through the depth of the cloud. Values of B_n separated by less than a correlation length are likely to be correlated, while those more spatially separated than a correlation length are independent. They derive the relation:

$$N_{max} = 69 \left(\frac{A_V}{\mathrm{mag}}\right) \left(\frac{B}{\mu\mathrm{G}}\right)^{-1} \tag{7.5}$$

The maximum number of correlation lengths can be estimated under the assumption that the magnetic and gravitational energy densities are equal. Under this condition, $A_V/B \approx 0.17$ mag μG^{-1}, where B is the total field strength (Chandrasekhar & Fermi 1953; Myers & Goodman 1988). This estimate yields $N_{max} \approx 12$.

The r.m.s. field strength and the relative strengths of the non-uniform to uniform magnetic field energy densities can then be calculated according to the relations:

$$< B^2 >^{1/2} = \left(B_0^2 + 3\sigma_B^2\right)^{1/2}; \tag{7.6}$$

and

$$\frac{M_n}{M_u} = \frac{3\sigma_B^2}{B_0^2}. \tag{7.7}$$

Table 7.3 summarizes properties of the magnetic field in B1 based on equations (7.2), (7.3), (7.4), (7.6), and (7.7) for various numbers of correlation lengths. The non-uniform and uniform magnetic field energy densities are equal for the case where $N = 4.6$, very close to the values obtained for Lynds 204 by (Myers & Goodman 1991).

B_{0_z} (μG)	σ_{B_z} (μG)	Θ (°)	s (radians)	i (°)	B_0 (μG)	N	σ_B (μG)	$< B^2 >^{1/2}$ (μG)	$\mathbf{M}_n/\mathbf{M}_u$
17.3	8	91	0.33	54.5	29.8	3	13.8	38	0.64
						6	19.6	45	1.3
						9	24.0	51	1.9
						12	27.7	56	2.6

Table 7.3: Magnetic Properties of Barnard 1

Finally, the direction of the ordered component of the magnetic field can be estimated:

$$\hat{B}_0 = (\hat{N}\cos\Theta_B + \hat{E}\sin\Theta_B)\sin i + \cos i\hat{z}. \tag{7.8}$$

For emission polarization data, we assume the mean magnetic field direction, Θ_B, is related to Θ by $\pm 90°$. Emission local to each dust grain should be related to the local field direction in this manner, but for this to be the case in the vector averaged sum of all polarizations through the cloud (which is what we measure at the telescope) is to assume that the magnetic field orientation does not substantially vary through the depth of the cloud. This has been shown to be a poor assumption in some regions, where the polarization data support a more complex field geometry (i.e. OMC-3 in Orion A, Matthews, Wilson, & Fiege 2001; NGC 2024 in Orion B, Matthews, Fiege, & Moriarty-Schieven 2001; and NGC 2068, Matthews & Wilson 2001). However, B1 is a dark cloud and not part of a giant molecular cloud complex like Orion; therefore, a unidirectional field geometry (at least away from the cores) is not an unreasonable assumption here. We note however that in utilizing this relation in B1, we are also assuming that all the polarized emission is arising in the B1 core, as opposed to in a second cloud as discussed above.

Using equation (7.8), and $\Theta_B = \Theta \pm 90°$ with $i = 54.5°$ from the line of sight,

$$\mathbf{B}_0 = 29.8\mu G\left[\pm(0.81\hat{N} + 0.014\hat{E}) - 0.58\hat{z}\right]. \tag{7.9}$$

We note that in either case, the direction of the field along the line of sight is toward the observer.

The field components can also be expressed in terms of two dimensions, $\hat{x}$ and $\hat{z}$, where $\hat{x}$ lies along the plane-of-sky mean field direction, as estimated from the mean polarization direction. In this case,

$$B_{0_x} = B_{0_z}\tan i \tag{7.10}$$

and substitution of B_{0_z} and i gives:

$$\mathbf{B}_0 = B_{0_x}\hat{x} + B_{0_z}\hat{z} \tag{7.11}$$

$$= \pm 24.2\mu G\hat{x} - 17.3\mu G\hat{z}. \tag{7.12}$$

Based on comparisons with theoretical predictions based on the assumptions of equality of magnetic fields and kinetic energy and equivalence of magnetic and gravitational energies, Crutcher et al. (1993) found that the field measured in B1 agreed well with predicted values if the inclination of the field to the line of sight were close to zero. Furthermore, because B1 was the only cloud with a detected magnetic field out of 12 in their survey, there was a concern that B1 might have an atypically strong field. Based on statistical analysis, Crutcher et al. (1993) concluded that this need not be the case if the magnetic field in B1 lies nearly along the line of sight. Our crude estimates for the three-dimensional magnetic field properties suffer from a poorly sampled line-of-sight component. We noted earlier that it was quite likely that B_{0_z} was overestimated by the averaging of the three field strengths measured by Goodman et al. (1990). In such a case, i, B_0, B_{0_x}, and $< B^2 >^{1/2}$ are all overestimated. If both B_{0_z} and σ_{B_z} are overestimated, then the effects are less predictable.

However, our detection of ordered polarization vectors from dust associated with the main core of molecular gas in B1 indicates that at least some of the magnetic field in the region lies in the plane of the sky. Unfortunately, there is no way to determine unambiguously the plane-of-sky field strength from polarization data, since the degree of polarization may depend on grain size, shape, composition and degree of alignment or spin (Hildebrand et al. 2000). We note that the OH Zeeman measurements can effectively probe regions with densities as high as $n(H_2) \sim 10^4$ cm^{-3} (Crutcher et al. 1994), quite comparable to the densities associated with the dust emission. Assuming a temperature of 12 K for the main core (Bachiller et al. 1990), the 850 μm flux density (even in the faint area off the cores) implies a column density of $N(H_2) \sim 10^{22}$ cm^{-2}, which corresponds to a density of $n(H_2) \sim 5 \times 10^3$ cm^{-3} if the emitting dust extends over the main core diameter of 0.8 pc (Bachiller et al. 1990). In reality, the emitting region of dust may be more confined along the line of sight, which would imply even higher densities. This is certainly the case where flux densities are high. The column density toward B1-c is $N(H_2) \sim 10^{23}$ cm^{-2}. Since Zeeman data have been obtained toward regions of high density, it is possible that the OH Zeeman data and the dust emission polarimetry do not arise in precisely the same spatial regions of the cloud. They could, therefore, be sampling different field geometries, or at least different total field strengths.

7.5 Summary

We have detected polarized emission at 850 μm arising from the dense interior of the Barnard 1 dark cloud. Our observations are centred on the molecular "main core" observed by Bachiller et al. (1990), in which three ammonia peaks were identified. Submillimetre emission is detected coincident with each of the ammonia peaks. In total four dust cores are identified, one of which contains two sources. Two of the dust condensations, B1-c and B1-d, have not been observed previously in continuum. The B1-a core is likely the 850 μm counterpart of IRAS 03301+3057. This source appears quite faint at long wavelengths. We have done a rough calibration of our Stokes' I data using a standard flux calibration factor for SCUBA data at 850 μm. We note that the presence of two dense new dust condensations, plus the B1-b double sources identified as young Class 0 objects by Hirano et al. (1999), increases the number of YSOs or pre-protostellar objects in B1 by almost a factor of 2. This indicates that the star formation efficiency in B1 is likely much larger than the 0.5% estimate by Bachiller et al. (1990) since there may be other as yet unobserved pre-protostellar or protostellar cores in the cloud.

The polarized emission can be separated somewhat arbitrarily into two subgroups by the coincident total, unpolarized flux levels. Strong polarizations are measured toward faint dust emission regions where the mean polarization percentage is 4.5% (standard deviation 2.3%). The position angles are distributed about 90° (east of north) and can be fit by a Gaussian of mean 91.3° and dispersion 19°. The polarizations associated with high intensities (i.e. the cores) show smaller polarization percentages, with a mean of 2.6% and standard deviation 1.4%. The vectors show alignment across the cores, but each core does not exhibit the same mean position angle. A comparison of each vector to adjacent values shows that vectors are strongly aligned with their neighbours, both in polarization percentage and position angle. The largest discrepencies are observed at the "boundaries" between the dense cores and the lower column dust emission in which they are embedded.

Over the whole mapped area, we see evidence of the depolarization observed toward many star-forming cores. Interestingly, when the polarization percentages are plotted against intensity for individual cores, the depolarization effect is seen to plateau at 30% and 40% of the peak emission from the B1-c and B1-b cores, respectively. The B1-c core only exhibits one vector with a value of $p < 1\%$, and thus the thresholding in that core is real and not just an artifact of a lower limit on detectable polarizations. The observation of depolarization at the highest intensities of cores closer (Ward-Thompson et al. 2000) and further (Matthews, Fiege, & Moriarty-Schieven 2001) than B1 makes it unlikely that the plateau is directly related to our resolution of B1 at 350 pc.

None of the orientations of polarization vectors measured by SCUBA are directly related to the two mean magnetic field directions detected with optical polarimetry of the Perseus complex (Goodman et al. 1990). Since 850 μm emission is optically thin, we could be detecting the vector sum of polarization from two different clouds. However, in order to produce the 90° orientation we observe, the cloud threaded with a field of mean orientation 55° east of north must produce twice the polarized emission as the cloud with a mean field orientation of $\sim 160°$. Based on our 850 μm flux estimate, the second cloud should have extinctions of $A_V \sim$ 2-4, an estimate quite close to the $A_V \leq 1$ mag predicted based on optical polarimetry (Goodman et al. 1990). In the case where the B1 dense cores could be completely depolarized, the polarized emission along the line of sight to those cores would arise completely in the foreground cloud (proposed to be at 200 pc). If such a cloud contains fluctuations in extinction, those fluctuations must be on scales similar to the separation of cores in B1 at approximately half the distance. This is required to account for the differing orientations measured in the two bright cores, B1-b and B1-c. We dismiss this scenario as unlikely since, unless the polarized emission from the foreground cloud rises in such a way as to offset the increasing intensity toward the B1-c core peak, we should see a steeper depolarization toward B1-c than in typical cores, not the threshold we observe.

Finally, following the method of Myers & Goodman (1991), we have crudely estimated the net field geometry in the B1 main core using our polarized emission data toward faint regions (centred on 90° east of north) and three spatially uncorrelated measurements of the line-of-sight field toward B1 measured by Goodman et al. (1989). The results are quite uncertain due to the small numbers of independent Zeeman measurements in OH toward the region. However, as a crude estimate we find that the total ordered field component is described by:

$$\mathbf{B}_0 = 29.8\mu G \left[\pm(0.81\hat{N} - 0.02\hat{E}) - 0.58\hat{z}\right], \tag{7.13}$$

and the ratio of the magnetic energy of the non-uniform component of the field to the uniform component ranges from 0.6 to 2.6, depending on the number of correlation lengths of the non-uniform component through the cloud. This result is not consistent with the theoretical predictions based on virial and magnetic equilibrium in the cloud, for which the line-of-sight field was comparable to the total predicted field. Our result, coupled with the polarization data itself, suggest that some component (possibly a significant amount) of the magnetic field could lie in the plane of the sky.

The authors would like to thank J. Greaves, T. Jenness, and G. Moriarty-Schieven at the JCMT for their assistance with problems both large and small during and especially after observing. A. Goodman provided clarification regarding the status of Zeeman observations toward B1, and G. Petitpas and J. Wadsley provided helpful discussions on the most effective means of comparing adjacent vectors. The research of CDW is supported through grants from the Natural Sciences and Engineering Research Council of Canada. BCM acknowledges funding from Ontario Graduate Scholarships.

Appendix 7A – The Polarization Data

Table 7.4 contains the polarization data plotted in Figure 7.1. Positional offsets are given from the J2000 coordinates $\alpha = 03^{h}33^{m}20\overset{s}{.}9$ and $\delta = +31°09'03\overset{''}{.}7$ ($\alpha = 03^{h}30^{m}15\overset{s}{.}0$ and $\delta = +30°59'00\overset{''}{.}0$ in B1950). Vectors are binned to 12″ sampling above the chosen threshold in total intensity and 6″ sampling below. The threshold is a total intensity flux of 0.0015 volts (330 mJy beam^{-1} using the standard calibration factor of 220 Jy beam^{-1} V^{-1}. All vectors plotted have $\sigma_p > 3$, $p > 1\%$, and an absolute uncertainty in polarization percentage, $dp < 1\%$. The total intensity at each vector position exceeds 20% of the faintest compact peak, B1-d. This minimizes the chances of systematic effects from chopping to a reference position, as discussed in Appendix A of Matthews, Wilson, & Fiege (2001).

Table 7.4: Barnard 1 850 μm Polarization Data

Δ R.A. (″)	Δ DEC. (″)	p (%)	dp (%)	σ_p	θ (°)	$d\theta$ (°)
Vectors coincident with $I >$ threshold						
−58.5	−136.5	3.74	0.56	6.7	−85.3	4.3
−64.5	−136.5	5.24	0.83	6.3	−78.3	4.5
−52.5	−130.5	1.86	0.50	3.7	68.1	7.7
−58.5	−130.5	2.36	0.46	5.2	85.0	5.6
−64.5	−130.5	3.85	0.59	6.5	−80.9	4.4
−70.5	−130.5	9.06	0.76	11.9	−80.6	2.4
−46.5	−124.5	2.49	0.63	3.9	67.3	7.3
−52.5	−124.5	3.10	0.46	6.7	64.0	4.3
−58.5	−124.5	1.79	0.44	4.1	85.4	7.1
−64.5	−124.5	2.29	0.61	3.7	−72.8	7.6
−46.5	−118.5	4.10	0.52	7.9	79.3	3.6
−52.5	−118.5	3.68	0.41	9.0	79.8	3.2
−58.5	−118.5	2.25	0.43	5.2	−87.8	5.5
1.5	−112.5	2.50	0.51	4.9	−89.0	5.9
−4.5	−112.5	2.47	0.46	5.4	−88.7	5.3
−10.5	−112.5	4.79	0.43	11.0	66.7	2.6
−16.5	−112.5	4.52	0.48	9.5	89.1	3.0
−22.5	−112.5	1.74	0.50	3.5	85.6	8.2
−46.5	−112.5	4.25	0.55	7.7	84.6	3.7
−52.5	−112.5	2.25	0.47	4.8	78.3	6.0

Table 7.4 (continued)

Δ R.A. ($''$)	Δ DEC. ($''$)	p (%)	dp (%)	σ_p	θ (°)	$d\theta$ (°)
−58.5	−112.5	1.46	0.48	3.0	−66.1	9.5
−64.5	−112.5	2.13	0.54	3.9	−80.1	7.3
13.5	−106.5	4.00	0.50	8.0	89.8	3.6
7.5	−106.5	2.59	0.35	7.5	89.2	3.8
1.5	−106.5	1.05	0.32	3.3	81.9	8.7
−4.5	−106.5	1.57	0.32	4.8	−82.1	5.9
−10.5	−106.5	2.75	0.38	7.2	−86.7	4.0
−16.5	−106.5	4.26	0.44	9.7	−86.8	3.0
−22.5	−106.5	3.99	0.43	9.3	−89.1	3.1
13.5	−100.5	1.28	0.32	4.0	−80.5	7.2
−10.5	−100.5	2.08	0.33	6.4	83.2	4.5
−16.5	−100.5	2.86	0.41	7.0	−78.2	4.1
7.5	−94.5	1.13	0.16	7.2	−63.3	4.0
1.5	−94.5	1.01	0.15	6.6	−49.0	4.4
−10.5	−94.5	1.28	0.36	3.5	47.2	8.1
−16.5	−94.5	2.53	0.45	5.6	−82.8	5.1
19.5	−88.5	2.38	0.41	5.8	33.8	4.9
−4.5	−88.5	1.18	0.24	5.0	46.4	5.8
−10.5	−88.5	3.40	0.41	8.4	58.5	3.4
13.5	−82.5	1.09	0.28	3.9	28.0	7.4
7.5	−82.5	1.15	0.18	6.5	58.9	4.4
1.5	−82.5	1.35	0.18	7.4	67.5	3.9
−4.5	−82.5	1.52	0.26	5.8	68.0	4.9
−10.5	−82.5	4.02	0.46	8.8	66.9	3.3
13.5	−76.5	1.53	0.37	4.1	−50.2	6.9
7.5	−76.5	1.50	0.22	6.8	73.7	4.2
1.5	−76.5	2.35	0.20	11.9	66.6	2.4
−4.5	−76.5	1.91	0.27	7.0	71.2	4.1
−10.5	−76.5	4.48	0.51	8.8	65.5	3.2
13.5	−70.5	3.00	0.64	4.7	−80.1	6.1
7.5	−70.5	4.50	0.37	12.1	−87.4	2.4
1.5	−70.5	1.98	0.28	7.2	76.8	4.0
−4.5	−70.5	1.35	0.34	3.9	64.7	7.3
7.5	−64.5	5.30	0.65	8.2	87.8	3.5
1.5	−64.5	4.13	0.45	9.3	77.1	3.1
−4.5	−64.5	2.98	0.51	5.9	71.7	4.9
−28.5	13.5	3.56	0.42	8.5	61.2	3.4
−34.5	13.5	1.25	0.37	3.4	72.4	8.4
−22.5	19.5	2.04	0.47	4.4	−56.5	6.5
−28.5	19.5	1.22	0.33	3.7	9.7	7.8

Table 7.4 (continued)

Δ R.A. (″)	Δ DEC. (″)	p (%)	dp (%)	σ_p	θ (°)	$d\theta$ (°)
−34.5	19.5	1.41	0.25	5.6	27.9	5.1
−40.5	19.5	1.45	0.22	6.5	19.8	4.4
−22.5	25.5	3.12	0.43	7.2	−24.0	4.0
−28.5	25.5	2.62	0.31	8.3	24.8	3.4
−34.5	25.5	1.77	0.19	9.1	31.6	3.1
−40.5	25.5	1.69	0.17	9.9	31.9	2.9
−28.5	31.5	1.83	0.31	5.8	30.0	4.9
−34.5	31.5	1.34	0.18	7.4	44.9	3.9
−40.5	31.5	1.86	0.20	9.4	47.0	3.0
−46.5	31.5	1.88	0.30	6.3	50.3	4.5
−52.5	31.5	4.29	0.48	9.0	64.6	3.2
−34.5	37.5	2.15	0.29	7.4	47.1	3.9
−40.5	37.5	1.77	0.30	5.9	46.9	4.9
−46.5	37.5	1.58	0.38	4.1	40.6	6.9
Vectors coincident with $I <$ threshold						
−10.5	−139.5	3.44	0.81	4.2	47.8	6.8
−22.5	−139.5	4.58	0.87	5.3	−78.7	5.5
−34.5	−139.5	11.66	0.93	12.6	88.1	2.3
−46.5	−139.5	6.88	0.52	13.2	−70.8	2.2
−58.5	−139.5	4.05	0.38	10.6	−65.0	2.7
−70.5	−139.5	8.00	0.64	12.4	−73.1	2.3
13.5	−127.5	8.54	0.96	8.9	89.9	3.2
1.5	−127.5	9.42	0.57	16.5	−81.3	1.7
−10.5	−127.5	3.99	0.41	9.7	87.1	3.0
−22.5	−127.5	3.64	0.44	8.2	73.3	3.5
−34.5	−127.5	8.27	0.45	18.5	−86.2	1.5
−46.5	−127.5	2.94	0.33	8.9	67.2	3.2
−82.5	−127.5	5.19	0.68	7.7	−88.7	3.7
25.5	−115.5	5.15	0.64	8.0	−87.1	3.6
13.5	−115.5	8.13	0.43	18.7	82.0	1.5
1.5	−115.5	2.91	0.30	9.6	−85.2	3.0
−22.5	−115.5	2.37	0.28	8.3	84.0	3.4
−34.5	−115.5	1.18	0.32	3.7	56.5	7.7
−82.5	−115.5	1.77	0.58	3.1	86.0	9.4
25.5	−103.5	6.52	0.46	14.1	74.8	2.0
−34.5	−103.5	4.63	0.31	15.1	81.2	1.9
−46.5	−103.5	2.64	0.30	8.7	−85.3	3.3
−70.5	−103.5	1.46	0.42	3.5	−89.6	8.2
−82.5	−103.5	2.14	0.63	3.4	87.1	8.4
−22.5	−91.5	3.11	0.31	10.2	89.5	2.8

Table 7.4 (continued)

Δ R.A. ($''$)	Δ DEC. ($''$)	p (%)	dp (%)	σ_p	θ (°)	$d\theta$ (°)
−34.5	−91.5	3.41	0.36	9.4	−87.3	3.0
−46.5	−91.5	1.16	0.34	3.4	84.4	8.3
−58.5	−91.5	2.03	0.32	6.2	79.1	4.6
−70.5	−91.5	1.65	0.46	3.6	22.2	7.9
−82.5	−91.5	9.54	0.92	10.4	−17.0	2.7
25.5	−79.5	3.43	0.62	5.5	88.8	5.2
−22.5	−79.5	3.92	0.51	7.7	75.4	3.7
−34.5	−79.5	3.78	0.46	8.3	−85.8	3.4
−46.5	−79.5	4.09	0.36	11.5	80.9	2.5
−58.5	−79.5	1.67	0.32	5.3	35.8	5.5
−70.5	−79.5	3.06	0.43	7.2	54.1	4.0
−10.5	−67.5	3.89	0.31	12.7	83.2	2.3
−22.5	−67.5	6.48	0.62	10.5	83.5	2.7
−46.5	−67.5	2.37	0.41	5.7	82.5	5.0
−58.5	−67.5	4.19	0.33	12.8	57.9	2.2
−70.5	−67.5	3.29	0.49	6.7	15.0	4.3
13.5	−55.5	7.64	0.86	8.9	0.1	3.2
1.5	−55.5	2.23	0.43	5.2	−76.8	5.5
−10.5	−55.5	2.71	0.41	6.6	70.5	4.4
−22.5	−55.5	8.82	0.72	12.2	−85.7	2.3
−46.5	−55.5	3.04	0.98	3.1	56.5	9.2
−58.5	−55.5	4.43	0.81	5.4	−72.3	5.3
1.5	−43.5	2.54	0.72	3.5	74.5	8.1
−10.5	−43.5	2.53	0.59	4.3	86.9	6.7
−22.5	−43.5	7.08	0.90	7.8	78.9	3.7
1.5	−31.5	6.44	0.70	9.2	−70.8	3.1
−10.5	−31.5	5.43	0.59	9.1	−67.9	3.1
−22.5	−31.5	9.13	0.94	9.7	90.0	3.0
1.5	−19.5	8.57	0.79	10.9	−84.0	2.6
−10.5	−19.5	4.18	0.68	6.1	−60.5	4.7
−22.5	−19.5	4.86	0.79	6.1	61.7	4.7
−34.5	−19.5	2.73	0.67	4.1	−84.6	7.0
−46.5	−19.5	4.25	0.76	5.6	−78.6	5.1
13.5	−7.5	3.89	0.78	5.0	−68.9	5.7
1.5	−7.5	3.95	0.76	5.2	−80.3	5.5
−10.5	−7.5	3.63	0.58	6.3	−89.6	4.6
−22.5	−7.5	4.78	0.54	8.9	−79.0	3.2
−34.5	−7.5	4.93	0.45	11.0	−88.6	2.6
−46.5	−7.5	4.13	0.62	6.7	−79.5	4.3

Table 7.4 (continued)

Δ R.A. (″)	Δ DEC. (″)	p (%)	dp (%)	σ_p	θ (°)	$d\theta$ (°)
1.5	4.5	4.15	0.74	5.6	66.9	5.1
−10.5	4.5	4.05	0.55	7.3	−74.2	3.9
−22.5	4.5	1.25	0.36	3.5	−51.8	8.2
−34.5	4.5	1.86	0.30	6.2	54.0	4.6
−58.5	4.5	7.14	0.87	8.2	42.9	3.5
13.5	16.5	8.55	0.93	9.2	−58.2	3.1
1.5	16.5	3.23	0.65	5.0	−63.8	5.8
−10.5	16.5	4.10	0.45	9.1	−59.4	3.2
−58.5	16.5	4.97	0.63	7.9	−86.8	3.6
1.5	28.5	7.91	0.73	10.8	−84.6	2.6
−10.5	28.5	4.22	0.47	9.0	−77.2	3.2
−58.5	28.5	3.48	0.43	8.0	68.6	3.6
−10.5	40.5	5.84	0.76	7.7	−61.6	3.7
−22.5	40.5	2.24	0.39	5.8	−3.1	5.0
−58.5	40.5	4.96	0.54	9.1	72.1	3.1
−34.5	52.5	2.08	0.69	3.0	−71.1	9.5
−58.5	52.5	2.88	0.72	4.0	−47.1	7.2

Bibliography

Andre, P., Ward-Thompson, D., & Barsony, M., 1993. *ApJ* **406**, 122.

Bachiller, R. & Cernicharo, J., 1984. *A&A* **140**, 414.

Bachiller, R. & Cernicharo, J., 1986. *A&A* **166**, 283.

Bachiller, R., del Rio Alvarez, S., & Menten, K. M., 1990. *A&A* **236**, 461.

Basu, S., 2000. *ApJ Letters* **540**, L103.

Borgman, J. & Blaauw, A., 1964. *Bull. Astron. Inst. Netherlands* **17**, 358.

Cernicharo, J., Bachiller, R., & Duvert, G., 1985. *A&A* **149**, 273.

Chandrasekhar, S. & Fermi, E., 1953. *ApJ* **118**, 113.

Cohen, M. & Kuhi, L. V., 1979. *ApJS* **41**, 743.

Crutcher, R. M., 1999. *ApJ* **520**, 706.

Crutcher, R. M., Mouschovias, T. C., Troland, T. H., & Ciolek, G. E., 1994. *ApJ* **427**, 839.

Crutcher, R. M., Troland, T. H., Goodman, A. A., Heiles, C., Kazes, I., & Myers, P. C., 1993. *ApJ* **407**, 175.

Draine, B. T. & Weingartner, J. C., 1996. *ApJ* **470**, 551.

Fiege, J. D. & Pudritz, R. E., 2000. *ApJ* **534**, 291.

Goodman, A. A., Bastien, P., Menard, F., & Myers, P. C., 1990. *ApJ* **359**, 363.

Goodman, A. A., Crutcher, R. M., Heiles, C., Myers, P. C., & Troland, T. H., 1989. *ApJ Letters* **338**, L61.

Goodman, A. A., Myers, P. C., Bastien, P., Crutcher, R. M., Heiles, C., Kazes, I., & Troland, T. H., 1990. The magnetic field in the perseus molecular cloud complex. In *IAU Symp. 140: Galactic and Intergalactic Magnetic Fields*, Volume 140, pp. 319.

Greaves, J., Holland, W., Chrysostomou, A., & Jenness, T., 2000. Imaging the polarized interstellar medium. In *Imaging at Radio through Submillimeter Wavelengths. Edited by Jeff Mangum. Publisher: The Astronomical Society of the Pacific, Conference Series, 2000. The conference was held June 6-8, 1999, in Tucson, Arizona.*, pp. E18.

Greaves, J., Holland, W., Jenness, T., Moriarty-Schieven, G., Chrysostomou, A., Berry, D., Murray, A., Nartallo, R., Ade, P., Gannaway, F., Haynes, C., Tamura, M., Momose, M., & Morino, J., 2001. *MNRAS in preparation.*

Hildebrand, R. H., Davidson, J. A., Dotson, J. L., Dowell, C. D., Novak, G., & Vaillancourt, J. E., 2000. *PASP* **112**, 1215.

Hildebrand, R. H., Dotson, J. L., Dowell, C. D., Schleuning, D. A., & Vaillancourt, J. E., 1999. *ApJ* **516**, 834.

Hirano, N., Kamazaki, T., Mikami, H., Ohashi, N., & Umemoto, T., 1999. Discovery of two extreme young protostars in barnard 1. In *Star Formation 1999, Proceedings of Star Formation 1999, held in Nagoya, Japan, June 21 - 25, 1999, Editor: T. Nakamoto, Nobeyama Radio Observatory, p. 181-182*, pp. 181.

Hirano, N., Kameya, O., Mikami, H., Saito, S., Umemoto, T., & Yamamoto, S., 1997. *ApJ* **478**, 631.

Jenness, T., Lightfoot, J. F., & Holland, W. S., 1998. *Proc. SPIE* **3357**, 548.

Joshi, U. C., Kulkarni, P. V., Bhatt, H. C., Kulshrestha, A. K., & Deshpande, M. R., 1985. *MNRAS* **215**, 275.

Lynds, B. T., 1969. *PASP* **81**, 496.

Matthews, B., Fiege, J., & Moriarty-Schieven, G., 2001. *ApJ in preparation.*

Matthews, B. & Wilson, C., 2001. *ApJ in preparation.*

Matthews, B., Wilson, C., & Fiege, J., 2001. *ApJ accepted.*

Myers, P. C. & Goodman, A. A., 1988. *ApJ Letters* **326**, L27.

Myers, P. C. & Goodman, A. A., 1991. *ApJ* **373**, 509.

Padoan, P., Goodman, A., Draine, B., Juvela, M., Nordlund, A., & Rögnvaldsson, O., 2001. *ApJ submitted.*

Purcell, E. M., 1979. *ApJ* **231**, 404.

Sargent, A. I., 1979. *ApJ* **233**, 163.

Shu, F. H., Adams, F. C., & Lizano, S., 1987. *ARA&A* **25**, 23.

Turnshek, D. A., Turnshek, D. E., & Craine, E. R., 1980. *AJ* **85**, 1638.

Vrba, F. J., Strom, S. E., & Strom, K. M., 1976. *AJ* **81**, 958.

Ward-Thompson, D., Kirk, J. M., Crutcher, R. M., Greaves, J. S., Holland, W. S., & André, P., 2000. *ApJ Letters* **537**, L135.

Ward-Thompson, D., Scott, P. F., Hills, R. E., & Andre, P., 1994. *MNRAS* **268**, 276.

Chapter 8

Summary and Future Work

8.1 On Magnetic Field Geometries

I have observed the polarized emission at 850 μm toward six individual regions within three star-forming molecular clouds. Two of the clouds, Orion A and Orion B, are classified as Giant Molecular Clouds, while the third, Barnard 1, is a dark cloud.

8.1.1 Orion A

Before the research presented in this work, most polarization maps were interpreted in terms of a unidirectional field geometry (or constant B_{pos} direction), perhaps with some small perturbations due to collapsing gas (e.g. the hourglass field). Measurements toward various regions in Orion A suggested that a unidirectional field could thread the entire Orion A cloud, from low to high density gas (as discussed in §2.7.1). Our observations have revealed that, not only is there no single B_{pos} field direction implied along the Integral-shaped Filament within Orion A, but also that entire cloud cannot be threaded by a unidirectional field. Table 8.1 shows the updated summary of mean field directions determined by assuming an unchanging field structure through the depth of the cloud.

The polarization data along 75% of the length of OMC-3 shows strong alignment with the projected filament direction, inferring some relationship between the

Region	Mean θ (° E of N)	Mean Field Inferred (° E of N)	Method of Observation
M42	100	100	absorption (optical)
L1641	120	120	absorption (optical)
OMC-1	30	120	emission (100 and 350 μm)
OMC-3 (north)	130	40	emission (850 μm)
OMC-3 (centre)	160	70	emission (850 μm)
OMC-3 (south)	100	10	emission (850 μm)

Table 8.1: "Mean Field" Directions in Orion A
Polarization data toward Orion A. At least three subsets of OMC-3 must be defined to assign mean polarization position angles and field directions. These three directions alone infer that there is no mean field threading OMC-3. Additionally, none of the directions inferred agree with the data of OMC-1 20′ to the south, dismissing the notion of a unidirectional field across the Integral-shaped Filament. The OMC-3 directions also do not align with data near the periphery of the Orion A cloud. Hence, there is no unidirectional field threading the entire Orion A cloud.

local magnetic field and the dense filamentary structure itself. A recently developed model for filamentary clouds threaded by helical fields predicts polarization alignment with the filament axis in the case of a toroidally dominated field geometry (Fiege & Pudritz 2000a; Fiege & Pudritz 2000b). This model predicts depolarization toward the axis of filaments and the same radial density structure observed toward the Integral-shaped Filament (Johnstone & Bally 1999). Near the southern part of the filament, the observations reveal a mis-alignment of the Integral-shaped Filament and polarization data. Three possible explanations are proposed to interpret this mis-alignment in terms of the helical field model: the field may be poloidally dominated in this region; there may be a bend in the filament (i.e. a changing inclination on the plane of the sky); or a second filament may cross the Integral-shaped Filament near its southern boundary. Models are presented to demonstrate the polarization patterns predicted in each of the latter two cases. The polarization data are consistent with either of these helical field geometries.

8.1.2 Orion B

Four regions of the Orion B cloud have been observed in polarized emission. These data do not show a correlation in polarization position angle from region to region, which illustrates that a unidirectional magnetic field does not thread the Orion B cloud. The NGC 2024 region, which had been observed previously in polarization (100 μm) and Zeeman splitting of OH, exhibits the most ordered polarization pattern of the four regions. The 850 μm pattern is centred on a ridge of seven embedded cores and shows strong correlation with the earlier 100 μm data (Dotson et al. 2000), which suggests that the same dust grain population and field geometry are being sampled by both, even though the 100 μm data are likely sensitive to grains at higher temperatures. The Zeeman data of Crutcher et al. (1999) provide a strong constraint to the field geometry. Although a helical field model does a superlative job in reproducing the polarization pattern observed, it is not consistent with the Zeeman data, since a helical field should show a reversal in line of sight field direction across a filament (i.e. see Figure 2.24).

Taking into consideration the complex geometry of the region surrounding the NGC 2024 ridge, an alternative field geometry is proposed in which the field detected is that of the expanding ionization front of the associated HII region. The ionization front is known to be close to the ridge of embedded cores; the model proposed suggests that the ionization front is bending around the dense ridge and has bent further on the west side due to an increasing density gradient from west to east in the molecular cloud. This model can explain both the polarization pattern and the Zeeman data, which shows significant line-of-sight field components on only the west side of the ridge. A third possibility, that the Zeeman measurements are the sum of a helical field along the filament and a smooth field associated with the ionization front, could explain the Zeeman data. This geometry has yet to be modeled.

In the Orion B north cloud, patterns with varying degrees of ordering are observed. NGC 2071 is a massive core which exhibits polarization angles roughly aligned with its most powerful outflow and is the only region which could be described by a mean field with minor perturbations. However, unlike the massive OMC-1 core, there is no evidence of flattening perpendicular to field lines in NGC 2071. Furthermore, the inferred field direction obtained by rotating the polarization vectors would lie perpendicular to the outflow, which is not consistent with the typical theories of core collapse along field lines, in which the outflow should align with the field. Despite some evidence for contamination of 850 μm data by CO $J = 3 - 2$ emission, the idea that the polarization data throughout the core has been contaminated by the outflow without a corresponding effect on the gas and dust (i.e. flattening) is very unlikely. I conclude that the outflow direction of a single source within a massive core containing many sources is not solely determined by the large scale field geometry of the core.

The polarization pattern of NGC 2068 has a high degree of ordering, containing subsets of data with strong alignment. The pattern exhibits depolarization particularly toward the cores, which is in contrast to the OMC-3 region in which the pattern did not vary along the filament axis, independent of the presence or absence of dense cores. A field of constant B_{pos} direction is not consistent with the polarization from this region, but no other simple field geometry can explain the data either. I propose the answer to lie in the fact that comparison with optical data reveals that the filament is almost certainly inclined in the plane of the sky and part of it may lie on opposite sides of the associated reflection nebula. Hence the changing polarization angles could result from bends in a helically-threaded filament as illustrated toward OMC-3. Changing field geometries could also be the result of expansion of the nebula, in a similar manner to the model produced for the NGC 2024 ridge.

The LBS 23 region is the most poorly sampled of the four observed in Orion B. Without additional data along the associated southern cores, interpretation of the northern pattern would be difficult. The filamentary structure connecting these cores is much weaker than that of OMC-3, NGC 2024 and even NGC 2068, but is not inconsistent with a helical field geometry.

8.1.3 Barnard 1

Barnard 1 (B1) is the only dark cloud included in this study to date. As in the data toward the Orion clouds, variations in polarization position angle were noted across the observed region. The polarization data toward areas of fainter emission are consistent with an ordered, unidirectional ("uniform") field, and we have used these data to produce an estimate of the total strength and direction of this uniform field component using a model in which the dispersion in polarization vectors is attributed to a non-uniform field component (Myers & Goodman 1991). The use of this model is possible only because some Zeeman data (albeit a small sample) exists toward this region.

The cores of B1 each exhibit ordered and aligned vectors within their bounds, but only the two faintest are also aligned with the position angles toward the fainter emission. The two brightest cores exhibit different polarization position angles from each other and from the vectors associated with low intensities. Most interestingly, these two cores reach a threshold in polarization percentage and hence *do not* show the depolarization typified by all our other data.

8.2 The Future

8.2.1 Followup Polarization Work

I have obtained data toward regions in two other dark clouds. The first data set is toward the B2 core of ρ Ophiuchus (at a distance of 160 pc); the second set of observations is toward NGC 1333, a cloud within the Perseus complex not far from Barnard 1. The analysis of these data will provide a basis for comparison with the B1 cloud and signify whether a unidirectional field component is prominent in dark clouds. The data toward both these regions will be combined with data toward the ρ Ophiuchus A core and some additional NGC 1333 data belonging to Jane Greaves. The polarimetric study of more dark clouds in particular is vital since known alignment mechanisms may not be effective in their interiors.

The OMC-3 data produced several models whose veracity cannot be distinguished by the limitations of the first data set. I have already obtained (in collaboration with Christine Wilson, Jason Fiege and Jane Greaves) more spatially extensive data toward this region, using the recently commissioned scan-mapping polarimetry mode with SCUBA. These data, not yet reduced, will help discriminate between the models of a bent filament or two crossed filaments. They will also be used to test predictions of a recent model for core formation at the intersection of magnetized turbulent flows (Padoan et al. 2001). To determine how common helically threaded filaments are, more filamentary clouds must be observed. Two strong candidates are the IC 5146 and L977 clouds in Cygnus, which I plan to map with the JCMT.

Field geometry is not the only proposed method of producing the depolarization observed. Changes in dust grains are also suggested as a means of reducing polarized emission. Toward the MMS6 core of OMC-3, I (in collaboration with Richard Crutcher and Shih-Ping Lai at U. Illinois at Urbana-Champaign) have obtained high-resolution polarization data from the Berkeley-Illinois-Maryland Association (BIMA) interferometer at 1.3 mm. If these data continue to show polarized emission, this could be an indication that the helical field geometry continues to higher optical depths. If polarized emission is not detected, this could indicate that grain physics is changing. This could help to contribute to depolarization on scales observed with the JCMT as well.

In addition to the cores of Orion, there are several nearby candidates for interferometric polarimetry. These include the TMC-1 cloud in Taurus, which has shown signatures of infall (Hogerheijde 2000) and hence could exhibit an hourglass configuration in its polarization pattern as field lines are dragged inward with the gas. Zeeman splitting of OH has been observed toward L1544 and L1457S (the nearest star-forming cloud to the Sun at 65 pc) and hence there is information about the line-of-sight magnetic field toward these sources (Crutcher & Troland 2000). Recently, Zeeman splitting has been detected toward L1498 using the CCS molecule (Levin et al. 2000). All of these cores should now be observed in polarized emission, first through the JCMT and then with BIMA where the fluxes permit since these cores could contain field structure on small scales.

8.2.2 The Polarization Spectrum

Observations of polarized emission at multiple wavelengths provides an opportunity to measure the polarization spectrum, which varies according to the composition and shape of grain populations. In fact, no single object has been measured in polarized emission at all accessible wavelengths between 100 μm and 1.3 mm to date. In collaboration with Roger Hildebrand and members of his group at the University of Chicago, I will complete this set of observations toward the OMC-1 core in Orion in October 2001 at the JCMT. Growing interest in the polarization spectrum as a means of testing models of dust grains in the ISM will necessitate multi-wavelength polarization observations of a number of regions. The OMC-1 data will also be extensive enough to test whether the helical field geometry, supported by data in OMC-3, also predicts the large scale polarization pattern in OMC-1.

8.2.3 Zeeman Splitting Studies

The polarization work in this thesis has not been able to uniquely determine the magnetic field geometry in any region, although strong cases have been made for a helical field in OMC-3 and an expanding HII region in NGC 2024. In order to break the degeneracy in models of field geometry which can produce polarization patterns, information about B_{los} is very critical. For instance, the helical field predicts a specific behavior in B_{los}.

Obtaining information on B_{los} involves measurement of the Zeeman effect, most commonly acheived with HI or OH in emission or absorption. However, OH is only effective at tracing densities up to $\sim 10^4$ cm^{-3}, and the densities sampled by dust emission in GMCs is often more than 10 times denser. The CCS molecule has been successfully used to measure B_{los} in several regions. The CN molecule has also been used in Orion. I have undertaken a project at BIMA to measure the strength of CCS along OMC-3 in an attempt to locate regions where CCS is bright enough to attempt measurements of Zeeman splitting in this molecule. In lower density regions (like NGC 2068), detection of Zeeman splitting in OH will be attempted using the Very Large Array.

8.3 Concluding Remarks

The data compiled in this thesis represent the first emission polarization data toward the regions of OMC-3, NGC 2068, NGC 2071, LBS 23N and Barnard 1. The reasonably large spatial scales and detailed sampling achieved with the SCUBA polarimeter at the JCMT have provided data with which variations in polarization position angle are detectable across entire regions. These regions, which have been observed so effectively with this remarkable instrument, were in fact too faint to be feasibly observed on these spatial scales by the previous generation of polarimeters.

It is easy to see how observations toward bright cores alone have led to interpretations of unidirectional field geometries within molecular clouds and cores. However, in every region I have observed, fields aligned along a single B_{pos} direction cannot account for the entire polarization pattern. Comparison of polarization data to predicted patterns suggests that OMC-3 most likely contains a helical field which may thread the entire Integral-shaped Filament. A helical field may also explain the polarization pattern of NGC 2068, although more extensive modeling with Zeeman data may be required to completely understand this complex region. Information about B_{los} toward NGC 2024 does exist. These data are clearly very important in constraining field geometry, as they prompt me to dismiss a helical field geometry in this region in favour of a field associated with an expanding ionization front from the associated HII region. A unidirectional field may thread the Barnard 1 cloud itself, but its cores must contain a more complex geometry.

This thesis has shown that magnetic fields are actively aligning grains within all the regions observed, and it may be boldly extrapolated that magnetic fields are in fact present in most, if not all, molecular clouds. This is, after all, predicted by theories of energy equipartition and cloud support and substantiated by our observations with indicate fields are polarizing grains far from compact cores. The geometries of these fields are not simple and not generally unidirectional, particularly within GMCs. Whether dark clouds harbour more simplified fields is not yet certain, but the only evidence in our data set for a unidirectional field is associated with the lower column density dust in B1.

The recent and ongoing development of predicted polarization patterns arising from various model field geometries has been crucial to the interpretation of the polarization data presented in this thesis. The attempts at modeling the field geometries from polarization patterns show that simply rotating the vectors will in general completely misrepresent the global field structure. In fact, I have argued that each cloud must be modeled separately, taking into account the geometry of the region and the associated physics. I conclude that it is extremely unlikely that any single field geometry exists in all regions of all molecular clouds.

Bibliography

Crutcher, R. M., Roberts, D. A., Troland, T. H., & Goss, W. M., 1999. *ApJ* **515**, 275.

Crutcher, R. M. & Troland, T. H., 2000. *ApJ Letters* **537**, L139.

Dotson, J. L., Davidson, J., Dowell, C. D., Schleuning, D. A., & Hildebrand, R. H., 2000. *ApJS* **128**, 335.

Fiege, J. D. & Pudritz, R. E., 2000a. *MNRAS* **311**, 85.

Fiege, J. D. & Pudritz, R. E., 2000b. *ApJ* **544**, 830.

Hogerheijde, M. R., 2000. From infall to rotation in the envelopes around young stellar objects: Identification of a source with a transitional 2000 au radius disk. In *American Astronomical Society Meeting*, Volume 197, pp. 4706.

Johnstone, D. & Bally, J., 1999. *ApJ Letters* **510**, L49.

Levin, S. M., Langer, W. D., Kuiper, T. B. H., Velusamy, T., & Crutcher, R. M., 2000. Measuring the magnetic field strength in l1498 with zeeman splitting observations of ccs. In *American Astronomical Society Meeting*, Volume 197, pp. 1016.

Myers, P. C. & Goodman, A. A., 1991. *ApJ* **373**, 509.

Padoan, P., Goodman, A., Draine, B., Juvela, M., Nordlund, A., & Rögnvaldsson, O., 2001. *ApJ submitted.*